Catalytic Water Oxidation and Dehydrogenation of Formic Acid by Ruthenium-based Molecular Catalysts

BY

ADITI VATSA

(Admission no. 2015DR0080)

THESIS

SUBMITTED TO

INDIAN INSTITUTE OF TECHNOLOGY

(INDIAN SCHOOL OF MINES), DHANBAD

For the award of the degree of

DOCTOR OF PHILOSOPHY

September, 2021

Catalytic Water Oxidation and Dehydrogenation of Formic Acid by Ruthenium-based Molecular Catalysts

BY

ADITI VATSA

(Admission no. 2015DR0080)

THESIS

SUBMITTED TO

INDIAN INSTITUTE OF TECHNOLOGY

(INDIAN SCHOOL OF MINES), DHANBAD

For the award of the degree of

DOCTOR OF PHILOSOPHY

September, 2021

"I learned that courage was not the absence of fear, but the triumph over it.

The brave man is not he who does not feel afraid, but he who conquers that fear"

-Nelson Mandela

Form No: PH10

INDIAN INSTITUTE OF TECHNOLOGY (INDIAN SCHOOL OF MINES) DHANBAD

COPYRIGHT AND CONSENT FORM

(To be submitted at the time of Thesis Submission)

To ensure uniformity of treatment among all contributors, other forms may not be substituted for this form, nor may any wording of the form be changed. This form is intended for original material submitted to the IIT (ISM), Dhanbad and must accompany any such material in order to be published by the ISM. Please read the form carefully and keep a copy for your files.

TITLE OF THESIS: "Catalytic Water Oxidation and Dehydrogenation of Formic Acid by Ruthenium-based Molecular Catalysts"

AUTHOR'S NAME & ADDRESS: ADITI VATSA
Research Scholar
Department of Chemistry
IIT(ISM) Dhanbad, Jharkhand-826004, India

COPYRIGHT TRANSFER

1. The undersigned hereby assigns to Indian Institute of Technology (Indian School of Mines), Dhanbad all rights under copyright that may exist in and to: (a) the above Work, including any revised or expanded derivative works submitted to the ISM by the undersigned based on the work; and (b) any associated written or multimedia components or other enhancements accompanying the work.

CONSENT AND RELEASE

2. In the event the undersigned makes a presentation based upon the work at a conference hosted or sponsored in whole or in part by the IIT (ISM) Dhanbad, the undersigned, in consideration for his/her participation in the conference, hereby grants the ISM the unlimited, worldwide, irrevocable permission to use, distribute, publish, license, exhibit, record, digitize, broadcast, reproduce and archive; in any format or medium, whether now known or hereafter developed: (a) his/her presentation and comments at the conference; (b) any written materials or multimedia files used in connection with his/her presentation; and (c) any recorded interviews of him/her (collectively, the "Presentation"). The permission granted includes the transcription and reproduction of the Presentation for inclusion in products sold or distributed by IIT(ISM) Dhanbad and live or recorded broadcast of the Presentation during or after the conference.
3. In connection with the permission granted in Section 2, the undersigned hereby grants IIT (ISM) Dhanbad the unlimited,worldwide, irrevocable right to use his/her name, picture, likeness, voice and biographical information as part of the advertisement, distribution and sale of products incorporating the Work or Presentation, and releases IIT (ISM) Dhanbad from any claim based on right of privacy or publicity.
4. The undersigned hereby warrants that the Work and Presentation (collectively, the "Materials") are original and that he/she is the author of the Materials. To the extent the Materials incorporate text passages, figures, data or other material from the works of others, the undersigned has obtained any necessary permissions. Where necessary, the undersigned has obtained all third party permissions and consents to grant the license above and has provided copies of such permissions and consents to IIT (ISM) Dhanbad.

GENERAL TERMS

* The undersigned represents that he/she has the power and authority to make and execute this assignment.
* The undersigned agrees to indemnify and hold harmless the IIT (ISM) Dhanbad from any damage or expense that may arise in the event of a breach of any of the warranties set forth above.
* In the event the above work is not accepted and published by the IIT (ISM) Dhanbad or is withdrawn by the author(s) before acceptance by the IIT(ISM) Dhanbad, the foregoing copyright transfer shall become null and void and all materials embodying the Work submitted to the IIT(ISM) Dhanbad will be destroyed.
* For jointly authored Works, all joint authors should sign, or one of the authors should sign as authorized agent for the others.

Aditi Vatsa

Signature of the Author

Form No: PH11

INDIAN INSTITUTE OF TECHNOLOGY (INDIAN SCHOOL OF MINES) DHANBAD

CERTIFICATE FOR CLASSIFIED DATA

(To be submitted at the time of Thesis Submission)

This is to certify that the thesis entitled **"Catalytic Water Oxidation and Dehydrogenation of Formic Acid by Ruthenium-based Molecular Catalysts"** being submitted to the Indian Institute of Technology (Indian School of Mines), Dhanbad by **Ms. ADITI VATSA** for award of Doctor of Philosophy (Ph.D) Degree in **CHEMISTRY** does not contains any classified information. This work is original and yet not been submitted to any institution or university for the award of any degree.

Signature of Supervisor

Signature of Scholar

Form No: PH12

INDIAN INSTITUTE OF TECHNOLOGY (INDIAN SCHOOL OF MINES) DHANBAD

CERTIFICATE REGARDING ENGLISH CHECKING

(To be submitted at the time of Thesis Submission)

This is to certify that the thesis entitled **"Catalytic Water Oxidation and Dehydrogenation of Formic Acid by Ruthenium-based Molecular Catalysts"** being submitted to the Indian Institute of Technology (Indian School of Mines), Dhanbad by **Ms. ADITI VATSA**, Admission No. **2015DR0080**, for the award of Doctor of Philosophy (Ph.D.) Degree has been thoroughly checked for quality of English and logical sequencing of topics.

It is hereby certified that the standard of English is good and that grammar and typos have been thoroughly checked.

It is now worthy for evaluation by the panel of examiners.

Signature of Supervisor

Name: Dr. SUMANTA KUMAR PADHI

Date: 4th October 2021

Signature of Scholar

Name: ADITI VATSA

Date: 4th October 2021

Form No: PH13

INDIAN INSTITUTE OF TECHNOLOGY (INDIAN SCHOOL OF MINES) DHANBAD

CERTIFICATE FROM THE SUPERVISOR(S)

(To be submitted at the time of Thesis Submission)

This is to certify that the thesis entitled **"Catalytic Water Oxidation and Dehydrogenation of Formic Acid by Ruthenium-based Molecular Catalysts"** being submitted to the Indian Institute of Technology (Indian School of Mines), Dhanbad by **Ms. ADITI VATSA**, Admission No. **2015DR0080**, for the award of Doctor of Philosophy (Ph.D.) Degree is a bonafide work carried out by him/her, in the Department of **CHEMISTRY**, IIT (ISM), Dhanbad, under my/our supervision and guidance. The thesis has fulfilled all the requirements as per the regulations of this Institute and, in my/our opinion, has reached the standard needed for submission. The results embodied in this thesis have not been submitted to any other university or institute for the award of any degree or diploma.

_____

Signature of Supervisor (s)

Name: Dr. SUMANTA KUMAR PADHI

Date: 4th October 2021

Acknowledgement

I am deeply grateful to the God, the Almighty, for his shower of blessings, giving me strength and patience throughout my PhD to complete my thesis entitled as **'Catalytic Water Oxidation and Dehydrogenation of Formic Acid by Ruthenium-based Molecular Catalysts'** under the guidance of Prof. Sumanta Kumar Padhi, at IIT (ISM) Dhanbad. In this respect, I would wish to express my gratitude of thanks to everyone who helped me throughout my Ph.D journey and made this PhD thesis possible.

Foremost, I would like to express my deep and sincere gratitude to my research supervisor Prof. Sumanta Kumar Padhi for giving me opportunity to work in his lab and for his continuous support, encouragement and providing invaluable guidance throughout this research. His dynamism, vision, sincerity and motivation have deeply inspired me to work hard and be pateint in every situation. The thesis would not have been completed without his resourceful, timely advice, untiring supervision, meticulous scrutiny and encouragement to explore new ideas to make my work more meaningful in every aspects. Apart from many scientific lessons, he taught me to be focused and be honest toward my work. . It was a great privilege and honor to work and study under his guidance.

I am also thankful to Prof. Parthasarathi Das HOD (Chemistry Dept.), Prof. Mahendra Yadav and Prof. Devendra Deo Pathak, former HODs, Department of Chemistry, IIT (ISM) Dhanbad for creating professional ambiance in the department and their motivation for innovative research. I will be much obliged to my DSC members Prof. Devendra Deo Pathak, (Professor, Department of Chemistry, Chairman, DSC), Prof. Hari Pada Nayek (Associate Professor, Department of Chemistry, Member, DSC), and Prof. Suresh Pandian E. (Associate Professor, Department of Environmental Science and Engineering, Member of sister department, DSC), for their thoughtful comment and advice throughout my research work. I will be thankful to all the faculty members and staff members of the Department of Chemistry, IIT (ISM) Dhanbad, Library staffs and Administrative staffs for their kind cooperation during my research period.

I would especially thank to Prof. Ganesh Chandra Nayak (Associate Professor, Department of Chemistry, IIT (ISM) Dhanbad) for his helpful suggestions on XPS analysis, Prof. Chanchal Halder (Assistant Professor, Department of Chemistry, IIT (ISM) Dhanbad) for providing GC-

MS facility in his lab. I am very much grateful to Prof. Siddhartha Sengupta (Assistant Professor, Department of Chemical Engineering, IIT (ISM) Dhanbad) for providing Gas Chromatography facilities in his lab.

I would be thankful to SAIF IIT Madras for NMR and EPR analysis. IIT Bombay, IIT Ropar and IACS Kolkata, for Mass analysis. NIT Rourkela for the NMR facilities. CRF IIT (ISM) Dhanbad for single-crystal XRD, XPS, HRMS, HR-TEM as well as FESEM facilities, Department of Chemistry, IIT(ISM) Dhanbad for NMR facilities under DST (FIST) program.
I would like to thank my seniors Dr. Jully Patel, Dr. Ejaz Ahmad, and Dr. Karunamay Majee and my labmates Dr. Surabhi Rai, Manaswini Raj, Aman Mishra, Asit Pahari, Sk Samim Akhter and Dev Raj for their relentless support during my Ph.D and for creating a joyful environment in the laboratory. The time and every moment we spent together will always close to my heart and will make me smile whenever I miss them.

I am privileged to thank all the teachers in every stage of my life for making me proficient to complete this tough phase of my life. It can't be possible without their support.

I would like to thank my friends Bhawana, Nitika, Jyotsana, Kamini, for their love and support throughout my PhD. I would like to also thank Gourav, Samaresh, Pratap Bhaiya, Bikash, Bhola, Smruti, Abhinav, Krishna, Puja, Sidhartha, Manohar, Tithi, Neha, Rashmi, Vandana, and everyone who are there to make this life happier and easier.

I would like to especially thank my close friends Bhumika, Shiva, Shubhankar, Manaswini, Aman and Asit for bearing my anger and encouraging me to handle every hurdle came during this tough time. It couldn't be possible without all of you. You all are my strength in my happiness and in my difficult phase of life.

Lastly I would like to express my gratitude towards my family, who encouraged me in every phase of life and supported me whenever I am in trouble. I am very lucky to have a wonderful family. I am thankful to my cousins for their love and support. I am extremely grateful to my mother, father and my brothers for being my strength and who stood by me as pillars whenever I lost my patience and courage. I love to have you all. I love to thank my sisters in law for making me smile and to my little stress bombers Avi, Chhavi, Yash and Chandra.

Aditi Vatsa

Table of Contents

Index	Contents	Page No.
	Table of Contents	
	List of Tables and Scheme	
	List of Figures	
	List of Abbreviation	
	Abstract	i-vii
Chapter 1	Introduction	
1.1.	Origin	1
1.1.1.	Wind Energy	1
1.1.2.	Hydroelectric Energy	2
1.1.3.	Biomass Energy	2
1.1.4.	Geothermal Energy	2
1.1.5.	Photovoltaic Cell	2
1.2.	Natural Photosynthesis	3
1.2.1.	Photosystem II	3
1.2.2.	Water Oxidation Mechanism in PSII	5
1.3.	Artificial Photosynthesis	6
1.4.	Types of water oxidation catalysis	6-7
1.4.1.	Chemical water oxidation	7
1.4.2.	Electrocatalytic water oxidation	7
1.4.3.	Photocatalytic water oxidation	7
1.5.	Sacrificial oxidant	8
1.6.	Water oxidation catalysts	9
1.7.	The Mechanistic pathway for O-O bond formation and O_2 liberation	10
1.7.1.	Water nucleophilic attack (WNA) mechanism	10

1.7.2.	Interaction of two metal units (I2M)	10-11
1.8.	Ruthenium based water oxidation catalysts	11
1.8.1.	Multinuclear Ruthenium WOCs	11-16
1.8.2.	Mononuclear Ruthenium Polypyridyl Complexes	16-27
1.8.2.1.	Mononuclear Ruthenium Complexes Containing Neutral Ligands	16-24
1.8.2.2.	Mononuclear Ruthenium Complexes Containing Anionic Ligands	24-27
1.8.2.3.	Ruthenium based half – sandwich complexes	27-28
1.9.	Dehydrogenation of Formic acid	28-30
1.9.1.	Mechanism of Dehydrogenation of formic acid	30
1.9.2.	Mononuclear Ruthenium based catalysts for Dehydrogenation	30-38
1.9.3.	Mononuclear Iridium based catalysts for Dehydrogenation	38-40
1.10.	Current Challenges	40
1.11.	Aim of the Thesis	41
1.12.	References	41-54
Chapter 2	Catalytic Water Oxidation by a Single Site[Ru(Fc-tpy)(bpy)OH_2]$^{2+}$ Complex and its Mechanistic Study	
2.1.	Introduction	55-56
2.2.	Experimental	56
2.2.1.1.	Materials and method	56
2.2.1.2.	Optical Spectra	56
2.2.1.3.	NMR Spectroscopy and Mass Spectrometry	56
2.2.1.4.	Determination of p*K*a Value	57
2.2.1.5.	Cyclic Voltammetry	57
2.2.1.6.	Gas Evolution	57
2.2.1.7.	X-ray crystallographic analysis	57-58
2.2.2.	Synthesis	58
2.2.2.1.	Synthesis of [Ru(Fc-tpy)(bpy)Cl](PF_6)	58

2.2.2.2.	Synthesis of $[Ru(Fc\text{-}tpy)(bpy)(OH_2)](PF_6)_2$	59
2.3.	Results and Discussion	59
2.3.1.	Synthesis	59
2.3.2.	Optical spectra	60
2.3.3.	NMR and Mass Spectra	60
2.3.4.	Single crystal X-ray crystallography	61
2.3.5.	Acid-base equilibria	62
2.3.6.	Electrochemistry in organic medium	62
2.3.7.	Aqueous Electrochemistry and Pourbaix diagram	63-66
2.3.8.	Chemical water oxidation	66-68
2.3.9.	Catalytic Stability	68
2.3.10.	Kinetics and Plausible Mechanism	68-72
2. 4.	Summary	72
2.5.	References	73-74
	Appendix A	75-84
Chapter 3	Catalytic Water Oxidation by a RuII Half Sandwich Complex	
3.1.	Introduction	85
3.2.	Experimental	85
3.2.1.	Material and methods	85
3.2.1.1.	Materials	85-86
3.2.1.2.	Optical Spectra	86
3.2.1.3.	NMR Spectroscopy and Mass Spectrometry	86
3.2.1.4.	Determination of p*K*a	86
3.2.1.5.	Cyclic Voltammetry	86
3.2.1.6.	Controlled Potential Electrolysis	86-87
3.2.1.7.	Gas Evolution	87
3.2.1.8.	X-ray crystallographic analysis	87
3.2.1.9.	X-ray photoelectron spectroscopy	87-88
3.2.1.10.	High resolution transmission electron microscopy (HR-TEM)	88

3.2.1.11.	Field emission scanning electron microscopy (FE-SEM)	88
3.3.	Synthesis	88
3.4.	Results and Discussion	88
3.4.1.	Synthesis	89
3.4.2.	Optical Spectra	89
3.4.3.	NMR and Mass Spectra	89
3.4.4.	Single crystal X-ray crystallography	90
3.4.5.	Acid-Base Equilibria	91
3.4.6.	Electrochemistry	92
3.4.7.	Pourbaix Diagram	92-94
3.4.8.	Electrochemical Catalysis	94-95
3.4.9.	Controlled potential electrolysis (CPE)	95
3.4.10.	Charge transfer resistance (Rct) and TAFEL analysis	95-96
3.4.11.	Chemical Water Oxidation	96-98
3.4.12.	Morphological characterizations	98
3.4.13.	X- Ray photoelectron spectroscopy	98-100
3.5.	Summary	100
3.6.	References	100-102
	Appendix B	103-122
Chapter 4	Dehydrogenation of Formic Acid by a Ru^{II} Half Sandwich Catalyst	
4.1.	Introduction	123
4.2.	Experimental	123
4.2.1.	Material and methods	124
4.2.1.1.	Materials	124
4.2.1.2.	Optical Spectra	124
4.2.1.3.	NMR Spectroscopy and Mass Spectrometry	124
4.2.1.4.	Gas Evolution	124
4.2.1.5.	Gas chromatography mass spectrometer	124
4.2.1.6.	Gas chromatography analysis	124-125
4.3.	Results and Discussion	125

4.3.1.	Synthesis	125
4.3.2.	Dehydrogenation reactions	125-128
4.2.3.	Isotopic labelling kinetics of dehydrogenation reaction	128-129
4.2.4.	Activation Parameters	129-130
4.2.5.	pH variation for the decomposition of formic acid	131-132
4.2.6.	Stability of the catalyst	132-133
4.2.7.	Plausible Mechanism	133-134
4.4.	Summary	134-135
4.5.	References	135-136
	Appendix C	136-146
Chapter 5	Dehydrogenation of formic acid using mononuclear Ruthenium (II) [Ru(2py-tpy)(dqn)Cl]+ complex	
5.1.	Introduction	147
5.2.	Experimental	147
5.2.1.	Materials and methods	147
5.2.1.1.	Materials	148
5.2.1.2.	Optical Spectra	148
5.2.1.3.	NMR Spectroscopy and Mass Spectrometry	148
5.4.1.4.	Cyclic Voltammetry	148
5.2.1.5.	Gas Evolution	148
5.2.1.6.	X-ray crystallographic analysis	149
5.3.	Synthesis	149
5.3.1.	Synthesis of 2,3-di(pyridin-2-yl) quinoxaline (dqn) ligand	149
5.3.2.	Synthesis of [Ru(2py-tpy)(dqn)Cl](PF6)	149-150
5.4.	Results and Discussion	150
5.4.1.	Synthesis	150
5.4.2.	Optical and NMR spectra	150-151
5.4.3.	X-ray crystal structure	151
5.4.4.	Electrochemistry in organic medium	152-153
5.4.5.	Acid-base equilibria	153
5.4.6.	Dehydrogenation of formic acid	154-156

5.4.7.	Thermodynamical Analysis	156-158
5.4.8.	pH variation for the decomposition of formic acid	158-159
5.4.9.	Stability of the catalyst	159-160
5.5.	Plausible Mechanism	160-161
5.6.	Summary	161
5.7.	References	161-162
	Appendix D	163-174
Chapter 6	Dehydrogenation of Formic Acid by Half Sandwich $[Ru(\eta^6-benzene)(L)Cl]^+$ catalysts: L = 8-Hyroxyquinoline and 8-Hydroxy-2-methyl quinoline	
6.1.	Introduction	175
6.2.	Experimental	176
6.2.1.	Material and methods	176
6.2.1.1.	Materials	176
6.2.1.2.	Optical Spectra	176
6.2.1.3.	NMR Spectroscopy and Mass Spectrometry	176
6.2.1.4.	Gas Evolution	176
6.2.1.5.	X-ray crystallographic analysis	176-177
6.2.1.6.	Gas chromatography analysis	177
6.3.1.	Synthesis of $[Ru(\eta^6-benzene)(L)]$ complex	177
6.4.	Results and Discussion	177
6.4.1.	Synthesis	177
6.4.2.	Optical Spectra	178
6.4.3.	NMR and Mass Spectra	178-179
6.4.4.	X-ray crystal structure	179-180
6.4.5.	Dehydrogenation reactions	180-184
6.4.6.	Activation Parameters	184-186
6.4.7.	pH variation for the decomposition of formic acid	186-187
6.4.8.	Stability of the catalyst	187-189
6.5.	Plausible Mechanism	189
6.6.	Summary	190
6.7.	References	191-192

Appendix E 193-208

Chapter 7 Summary and Future scope

7.1. Summary 209-212
7.2. Future Scope 212-213

List of Tables and Schemes

Table No.	Table Caption	Page No.
Table 2.1.	Comparison between Ru centred single site WOCs having $[Ru(tpy)(bpy)(OH_2)]^{2+}$ scaffold.	71-72
Table A.1.	Crystal data and structure refinement for [Ru(Fc-tpy)(bpy)(Cl)](PF6).	82
Table A.2.	Selected Bond Lengths for [Ru(Fc-tpy)(bpy)(Cl)](PF6)**.**	83
Table A.3.	Selected Bond Lengths for [Ru(Fc-tpy)(bpy)(Cl)](PF6)**.**	83
Table B.1.	Crystal data and refinement for $[Ru(hdm)(Bz)]BF_4.2H_2O$.	121
Table B.2.	Selected bond lengths for $[Ru(hdm)(Bz)]BF_4.2H_2O$.	121
Table B.3.	Selected bond lengths for $[Ru(hdm)(Bz)]BF_4.2H_2O$.	122
Table 4.1.	Summary of experiments in different reaction conditions for dehydrogenation of formic acid	127
Table 4.2.	TON, TOF and volume of gas at different temperatures with deuterated and non-deuterated solvents	129
Table 4.3.	Calculations for Arrhenius plot and Eyring plot.	130
Table 4.4.	Decomposition of formic acid at different pH with 1.0 mM [Ru-hdm] in the presence of 10 mmol acid and 15 mmol of bases.	131
Table 5.1.	Summary of experiments in different reaction conditions for dehydrogenation of formic acid.	155
Table 5.2.	Calculations for Arrhenius plot.	157
Table 5.3.	Calculations for Eyring plot.	158
Table D1.	Crystal data and structure refinement for [Ru(dqn)].	173

Table D2.	Selected bond lengths for [Ru(dqn)].	173
Table D3.	Selected Bond Angles for [Ru(dqn)].	174
Table 6.1.	Summary of experiments in different reaction conditions for dehydrogenation of formic acid for complex **1**	182
Table 6.2.	Summary of experiments in different reaction conditions for dehydrogenation of formic acid for complex **2**	184
Table 6.3.	Calculations for Arrhenius plot and Eyring plot for complex **1**	185
Table 6.4.	Calculations for Arrhenius plot and Eyring plot for complex **2**	185
Table E1.	Crystal data and structure refinement for 1.	205
Table E2.	Selected Bond Lengths for 1.	205
Table E3.	Selected Bond Angles for 1.	206
Table E4.	Crystal data and structure refinement for 2.	207
Table E5.	Selected Bond Lengths for 2.	207
Table E6.	Selected Bond Angles for 2.	208

Scheme No.	**Scheme Caption**	**Page No.**
Scheme 1.1.	Different mechanistic paths of water oxidation in mononuclear complexes.	10
Scheme 1.2.	Catalytic cycle for FA hydrogen storage and release.	29
Scheme 1.3.	A general mechanism for catalytic decomposition of formic acid	30
Scheme 2.1.	Synthesis of Ru-Cl and Ru-OH_2 complex.	60
Scheme 2.2.	Acid-Base equilibria of Ru-OH_2 complex in Britton–Robinson buffer.	62
Scheme 2.3.	A plausible mechanism for water oxidation by **[Ru-OH_2]**.	71

Scheme 3.1.	Synthesis of **[Ru-hdm]** complex	89
Scheme 3.2.	Acid-base equilibria in **[Ru-hdm]** complex.	92
Scheme 4.1.	Plausible catalytic cycle involved in the dehydrogenation of formic acid.	134
Scheme 5.1.	Syntheses of the **dqn** ligand and **[Ru(dqn)]** complex.	150
Scheme 5.2.	The acid-base equilibria [Ru(dqn)] complex	153
Scheme 5.3.	Plausible mechanism for the catalytic cycle for dehydrogenation of HCOOH by **[Ru(dqn)]**.	161
Scheme 6.1	Syntheses of complexes **1** and **2**	178
Scheme 6.2.	Plausible mechanism for the catalytic cycles for complexes **1** and **2**.	189

List of Figures

Figure No.	Figure Caption	Page No.
Figure 1.1.	Photosynthesis changes sunlight into chemical energy, split water to liberate O_2, and fixes CO_2 into sugar.	3
Figure 1.2.	Simplified representation of natural photosynthesis.	4
Figure 1.3.	The Kok cycle	5
Figure 1.4.	Simplified representation of Artificial Photosynthesis	6
Figure 1.5.	The first molecular catalyst *cis,cis*-$[(bpy)_2(H_2O)Ru^{III}ORu^{III}(H_2O)(bpy)_2]^{4+}$ (**1**).	12
Figure 1.6.	The binuclear ruthenium complexes (**2-4**).	12
Figure 1.7.	Molecular structure of WOCs (**5a-5b**)	13
Figure 1.8.	Molecular structure of WOCs (**6-13**).	14
Figure 1.9.	Molecular structure of WOCs (**14-17**).	15
Figure 1.10.	Molecular structure of binuclear water oxidation catalyst (**18**).	16
Figure 1.11.	Molecular structure of WOCs (**19-24**).	17
Figure 1.12.	Molecular structure of WOCs (**25-27**).	18
Figure 1.13.	Molecular structure of WOCs (**28-48**).	19
Figure 1.14.	Molecular structure of WOCs (**49-53**).	20
Figure 1.15.	Molecular structure of WOCs (**54-62**).	21
Figure 1.16.	Molecular structure of WOCs (**63-66**).	22
Figure 1.17.	Molecular structure of complexes (**67-68**).	22-23
Figure 1.18.	Molecular structure of WOCs (**69-72**).	23
Figure 1.19.	Molecular structure of WOCs (**73-77**).	24
Figure 1.20.	Molecular structure of WOCs (**78-80**).	25
Figure 1.21.	Molecular structure of WOCs (**81-83**).	26
Figure 1.22.	Molecular structure of WOCs (**84-87**).	27

Figure 1.23.	Molecular structure of Half-sandwich water oxidation complex (**88-89**).	28
Figure 1.24.	Molecular structure of complex (**90**).	32
Figure 1.25.	Series of oligocationic aminomethyl-substituted triarylphosphines (**91-96**)For catalyzing dehydrogenation coupled with Ru (II) metal center.	32
Figure 1.26.	Molecular structure of Dehydrogenation catalysts (**97-106**)	34
Figure 1.27.	Molecular structure of Dehydrogenation catalysts (**107-113**).	35
Figure 1.28.	Molecular structure of Dehydrogenation catalysts (**114-122**).	36
Figure 1.29.	Molecular structure of Dehydrogenation catalysts (**123-132**).	36
Figure 1.30.	Molecular structure of Dehydrogenation catalysts (**133-137**).	38
Figure 1.31.	Molecular structure of Dehydrogenation catalysts (**138-140**).	39
Figure 1.32.	Molecular structure of Dehydrogenation catalysts (**141a-141f**).	39
Figure 1.33.	Molecular structure of Dehydrogenation catalysts (**142-143**).	40
Figure 2.1.	The 30 % probability Oak Ridge Thermal Ellipsoid plot of [Ru (Fc-tpy)(bpy)Cl]+.	61
Figure 2.2.	**(A)** CV of 0.50 mM Fc-tpy (red) and Ferrocene (black) in CH_3CN containing 0.1 M TBAP. **(B)** CV of 0.5 mM $[Ru(Fc\text{-}tpy)(bpy)Cl]^+$ (red) and $[Ru(tpy)(bpy)Cl]^+$ (black) in CH_3CN containing 0.1 M TBAP.	63
Figure 2.3.	(Left) Cyclic voltammogram of 0.5 mM $[Ru(tpy)(bpy)OH_2]^{2+}$ (black) and 0.5 mM	65

	$[Ru(Fc\text{-}tpy)(bpy)OH_2]^{2+}$ (red) in pH 1.0 CF_3SO_3H solution. (Right) CV of 0.5 mM $[Ru(tpy)(bpy)OH_2]^{2+}$ in Britton–Robinson buffer at pH 7.4.	
Figure 2.4.	Pourbaix diagram of $[Ru(Fc\text{-}tpy)(bpy)OH_2]^{2+}$ in Britton–Robinson buffer.	66
Figure 2.5.	Initial rate *vs.* [**Ru-OH$_2$**] (left) and ln (Initial rate of O_2 evolution) *vs.* ln [**Ru-OH$_2$**] (right) in pH 1.0 triflic acid.	67
Figure 2.6.	(A) O_2 evolution by $[Ru(Fc\text{-}tpy)(bpy)(OH_2)](PF_6)_2$ with various complex concentration at 100 mM CAN; (B) Comparison of O_2 evolution by 1.0 mM $[Ru(Fctpy)(bpy)(OH_2)](PF_6)_2$ with 1.0 mM $[Ru(tpy)(bpy)(OH_2)](PF_6)_2$ in presence of 100 mM CAN;(C) The reiteration of catalytic cycles with the addition of 100 mM CAN.	68
Figure 2.7.	(A) Spectra of the intermediate species extracted from the kinetics fitting; (B) Species distribution of the intermediate species.	70
Figure 3.1.	ORTEP (30% probability thermal ellipsoids) of **[Ru(η6-benzene)(hdm)]$^+$** complex.	90
Figure 3.2.	CV of 1.0 mM of **[Ru-hdm]** (red) and blank (black) in water using 0.1 M of $NaBF_4$ as supporting electrolyte (left) and CV and DPV of 1.0 mM **[Ru-hdm]** in water using 0.1 M $NaBF_4$ as supporting electrolyte(right).	93
Figure 3.3.	Pourbaix diagram of **[Ru-hdm]** complex in Britton-Robinson buffer.	93
Figure 3.4.	**(A)** The Nyquist plot of 1.0 mM of **[Ru-hdm]** in water using 0.1 M of $NaBF_4$ as supporting electrolyte. **(B)** Tafel plot of 1.0 mM **[Ru-hdm]** in water using 0.1 M of $NaBF_4$ as supporting electrolyte.	96

Figure 3.5.	**(a)** O_2 evolution by **[Ru-hdm]** with various CAN concentration at 4.0 mM Complex. **(b)** Rate of O_2 evolution *vs.* CAN in water.	98
Figure 3.6.	Fitted Ru(3d) XPS spectra for RuO_3 and RuO_2 in solution.	99
Figure 4.1.	**(A)** Gas evolution by **[Ru-hdm]** with a variety of acid concentrations in the presence of 1.0 mM of complex and 15 mmol of the base at 55 °C in water. **(B)** Rate of gas evolution *vs.* acid in water.	125
Figure 4.2.	**(A)** Gas evolution by **[Ru-hdm]** with the variation of temperature in the presence of 1.0 mM of complex, 10 mmol of the base, and 15 mmol of acid in water. **(B)** Rate of gasevolution *vs.* temperature in water.	126
Figure 4.3.	Gas evolution in H_2O and D_2O in 20 mmol of acid and 40 mmol of a base at 55°C in water.	128
Figure 4.4.	**(A)** Arrhenius plot for the complex [Ru-hdm] to estimate the activation energy. **(B)** Eyring plot for the complex [Ru-hdm] to estimate the $\Delta H^{\ddagger}$, $\Delta S^{\ddagger}$, and $\Delta G^{\ddagger}$.	130
Figure 4.5.	pH dependence of the initial TOF for the decomposition of formic acid with 1.0 mM complex, 10 mmol formic acid, and 15 mmol sodium formate in phosphate buffer.	132
Figure 4.6.	Catalytic cycles for the complex **[Ru-hdm]** with the iteration of 20 mmol of acid in the presence of 1.0 mM complex and 25 mmol bases in water.	133
Figure 4.7.	Mass spectrum of the complex in the presence of formic acid and formate [(Simulated; Top) and (Experimental; bottom)].	134

Figure 5.1.	ORTEP of $[Ru(2py\text{-}tpyH)(dqn)Cl]^{2+}$.	152
Figure 5.2.	CV of 1.0 mM of **[RuDqn]** in DMF using 0.1 M $^{n}Bu_4NClO_4$ (TBAP) as supporting electrolyte.	153
Figure 5.3.	**(a)** Gas evolution by **[Ru(dqn)]** with a variety of acid concentration in the presence of 1.0 mM of complex and 15 mmol of the base at 55 °C in water. **(b)** Rate of gas evolution *vs.* acid in water. **(c)** Gas evolution by **[Ru(dqn)]** with the variation of temperature in the presence of 1.0 mM of complex, 10 mmol of the base, and 15 mmol of acid in water. **(d)** Rate of gas evolution *vs.* temperature in water.	156
Figure 5.4.	Arrhenius plot for the complex **[Ru(dqn)]** to estimate the activation energy.	157
Figure 5.5.	Eyring plot for the complex **[Ru(dqn)]** to estimate the $\Delta H^{\ddagger}$, $\Delta S^{\ddagger}$, and $\Delta G^{\ddagger}$.	158
Figure 5.6.	pH dependence of the initial TOF for the decomposition of formic acid with 1.0 mM complex, 10 mmol formic acid, and 15 mmol sodium formate in phosphate buffer.!	159
Figure 5.7.	Catalytic cycles for the complex **[Ru(dqn)]** with the iteration of 20 mmol of acid in the presence of 1.0 mM complex and 25 mmol base in water.	160
Figure 6.1.	ORTEP of complexes **1** and **2**.	180
Figure 6.2.	(a) Gas evolution by complex 1 with a variety of base concentrations in the presence of 1.0 mM of complex and 10 mmol of the acid at 70 °C in water. (b) Rate of gas evolution *vs.* base in water. (c) Gas evolution by complex 1 with the variation of temperature in the presence of 1.0 mM of complex, 15	181

	mmol of the base, and 10 mmol of acid in water. (d) Rate of gas evolution *vs.* temperature in water.	
Figure 6.3.	**(a)** Gas evolution by complex **2** with a variety of acid concentrations in the presence of 1.0 mM of complex and 15 mmol of the base at 70 °C in water. **(b)** Rate of gas evolution *vs.* acid in water. **(c)** Gas evolution by complex **2** with the variation of complex concentration in the presence of 15 mmol of the base and 10 mmol of acid in water. **(d)** Rate of gas evolution *vs.* complex concentration in water.	183
Figure 6.4.	**(a)** Arrhenius plot for complex **1** to estimate the activation energy **(b)** Eyring plot for complex **1** to estimate the $\Delta H^{\ddagger}$, $\Delta S^{\ddagger}$, and $\Delta G^{\ddagger}$.. **(c)** Arrhenius plot for complex **2** to estimate the activation energy (d) Eyring plot for complex **2** to estimate the $\Delta H^{\ddagger}$, $\Delta S^{\ddagger}$, and $\Delta G^{\ddagger}$.	186
Figure 6.5.	**(a)** pH dependence of the initial TOF for the decomposition of formic acid with 1.0 mM complex **1**, 10 mmol formic acids, and 15 mmol sodium formate in phosphate buffer at 70 °C **(b)** pH dependence of the initial TOF for the decomposition of formic acid with 1.0 mM complex **2**, 10 mmol formic acids, and 15 mmol sodium formate in phosphate buffer at 85 °C	187
Figure 6.6.	Catalytic cycles for complex **1** with the iteration of 20 mmol of acid in the presence of 1.0 mM complex and 25 mmol bases in deionized water.	188
Figure 6.7.	Catalytic cycles for complex **2** with the iteration of 20 mmol of acid in the presence of 1.0 mM complex and 25 mmol bases in water.	188

List of Abbreviation

ATP	Adenosine triphosphate
bpm	2,2′-bipyrimidine
bpy	2,2′-bipyridine
bpyms	2,2’-bipyridine-5,5’-bis(methanesulfonate)
bpz	2,2′-bipyrazine
Btpyan	1,8-bis(2,2′:6′,2″-terpyridyl)-anthracene
COSY	Correlation spectroscopy
CAN	Ceric ammonium nitrate
CV	Cyclic voltammetry
CCDC	Cambridge Crystallographic Data Centre
CPE	Control potential electrolysis
DPV	Differential pulse voltammetry
DFT	Density functional theory
DMF	Dimethylformamide
DCM	Dichloromethane
DMA	Dimethylacetamide
DMSO	Dimethyl sulfoxide
DQN	2,3-di(pyridine-2-yl) quinoxaline
EA	Electron acceptor
ECEC	Electrochemical chemical electrochemical chemical
EDG	Electron donating group
EWG	Electron withdrawing group
ESI MS	Electrospray ionisation mass spectrometry

EDX	Energy –dispersive X-ray spectroscopy
FESEM	Field emission scanning electron microscope
FA	Formic acid
FID	Flame Ionization detector
FTIR	Fourier transform infrared spectroscopy
Fc-tpy	4-(2-ferrocenyl)-2,2:6,2”-terpyridine
GCE	Glassy carbon electrode
GC	Gas chromatography
GC-MS	Gas chromatography-mass spectrometry
GW	Giga watt
hdm	hydroxydi(pyridine-2-yl)methanolate
HRMS	High resolution mass spectrometry
HR-TEM	High resolution-transmission electron microscopy
ITO	Indium tin oxide
LSV	Linear sweep voltammetry
MLCT	Metal to ligand charge transfer
NADPH	Nicotinamide adenine dinucleotide phosphate
NHE	Normal hydrogen electrode
NMR	Nuclear magnetic resonance
OCP	Open circuit potential
OEC	Oxygen-evolving complex
ORTEP	Oak Ridge Thermal Ellipsoid Plot
PSI	Photosystem I
PSII	Photosystem II

PCET	Proton coupled electron transfer
PV	Photovoltaic
PPMV	Parts per million volume
SA	Sacrificial electron acceptor
SCE	Saturated calomel electrode
SF	Sodium formate
SHE	Standard hydrogen electrode
SVD	Singular Value Decomposition
TOF	Turn over frequency
TON	Turn over number
Tpy	2,2':6',2" terpyridine
TCD	Thermal conductivity detector
TBAP	Tetrabutylammonium perchlorate
TW	Tera watt
tyrz	Tyrosine
UV–vis	Ultraviolet-visible spectroscopy
WNA	Water nucleophilic attack
WOC	Water oxidation catalysis
WOCs	Water oxidation catalysis
XPS	X- ray photoelectron spectroscopy
XRD	X-ray diffraction

Catalytic Water Oxidation and Dehydrogenation of Formic Acid by Ruthenium-based Molecular Catalysts

ABSTRACT OF THE THESIS

Abstract of the Thesis

The thesis entitled "**Catalytic Water Oxidation and Dehydrogenation of Formic Acid by Ruthenium-based Molecular Catalysts"** deals with the development of the various proficient Ru-based polypyridine as well as Ru-based half sandwich catalysts for chemical and electrochemical water oxidation and also for studying the dehydrogenation of formic acid.

Challenges in designing the Water Oxidation and Dehydrogenation of Formic Acid Catalysts

- Catalyst should be cost-effective
- It should be soluble in both aqueous and organic medium.
- It should be stable in acidic, basic and aqueous medium.
- It should have a high turn over frequency (TOF) and high turn over number (TON).
- It should have low overpotential for water oxidation catalysis.

The Aim and objective of the work

- Study the effects of electron-donating and electron-withdrawing groups on ligands for low overpotential for water oxidation.
- Increase the catalytic stability and activity i.e. TON and TOF.
- Study the chemical water oxidation using different oxidants at different pH.
- Study the stability and activity of complexes towards dehydrogenation of formic acid from lower to a higher temperature and also by varying the concentration of acid, base and complex.

Outline of the Thesis

The present thesis consists of 7 chapters, Chapter 1 is the "Introduction" and Chapter 2 to 6 comprises of synthesis and catalytic activity of Ru-based complexes towards water oxidation and dehydrogenation of formic acid and Chapter 7 is "Conclusion and Future Scope".

Chapter 1: Introduction

This chapter illustrates the brief idea about artificial photosynthesis and its significance in the current framework. It also consists of an overview of natural photosynthesis and the component involved in the process of water oxidation i.e. photosystem II for the evolution of oxygen and how this system is followed for the development of artificial systems for water oxidation both chemically and electrochemically. The chapter describes about the different types of water oxidation like chemical, photochemical and electrochemical water oxidation. It also gives brief description of sacrificial oxidants used for the chemical and photochemical water oxidation reaction. The chapter also provides a literature review on ligand and complexes employed for water oxidation. The Ru-based mononuclear homogeneous polypyridyl as well Ru-based half sandwich complexes were employed for the evolution of oxygen from water electrochemically and by using oxidants in chemical water oxidation.

The chapter also gives the brief concept of dehydrogenation of formic acid in the presence of a base at a high temperature. The chapter provides a literature review on synthesis and catalytic activity of the Ru-based complexes as well as Ir-based complexes employed for the evolution

of hydrogen. The purpose of the present study is the development of an efficient and stable catalyst for the water oxidation and dehydrogenation reaction.

Chapter 2: Catalytic water oxidation by a single site $[Ru(Fc\text{-}tpy)(bpy)OH_2]^{2+}$ complex and its mechanistic study [1]

In this chapter, the novel complexes $[Ru(Fc\text{-}tpy)(bpy)Cl]PF_6$ and its corresponding aqua $[Ru(Fc\text{-}tpy)(bpy)OH_2](PF_6)_2$ complex (Fc-tpy = 4′-(2-ferrocenyl)-2,2′:6′2″-terpyridine) have been synthesized and characterized by various spectroscopic techniques. The utilization of $[Ru(Fc\text{-}tpy)(bpy)OH_2](PF_6)_2$ towards water oxidation is being discussed. This complex acts as an efficient water oxidation catalyst at pH = 1.0 in triflic acid using ceric ammonium nitrate (CAN) as a sacrificial electron acceptor. The complex exhibits a turnover number (TON) of 12 whereas the parent $[Ru(tpy)(bpy)(OH_2)]^{2+}$ complex exhibits a TON of 10 under similar conditions. The rate of evolution of O_2 for this complex is much higher as compared to parent $[Ru(tpy)(bpy)(OH_2)]^{2+}$ complex with 230 mV of lower onset potential. The complex follows the first-order reaction for O_2 evolution with complex as well as CAN concentration. The presence of the ferrocenyl group coupled with terpyridine has the potential to act as an electron donor and can stabilize the higher oxidation state of the ruthenium complex required towards chemical water oxidation. From the acid-base equilibria and electrochemical studies, it was observed that under strong acidic conditions the Fe(II) center of ferrocene moiety (Fc) undergoes protonation to generate Fe(IV)hydrido species Fe(IV)-H (FcH^+). The complex shows one p*K*a value at 10.0 due to the deprotonation of the aqua ligand. The rate of O_2 evolution is 1st order for the catalyst as well as oxidant (CAN) concentration. The mechanistic study for water oxidation was performed through stoichiometric addition of CAN in the complex at pH 1.0 and spectral changes observed were fitted in the kinetics fitting model using ReactLab Kinetics software. Based on the experimental and simulated result the interaction step between $[Fc^+\text{-}Ru^{IV}\text{-}O\text{-}OH]^{4+}$ and Ce^{4+} is the rate-determining step (RDS) in the catalytic oxygen evolution reaction, where $k = 6.0 \times 10^{-4}\ M^{-1}\ s^{-1}$.

Graphical synopsis of Chapter 2:

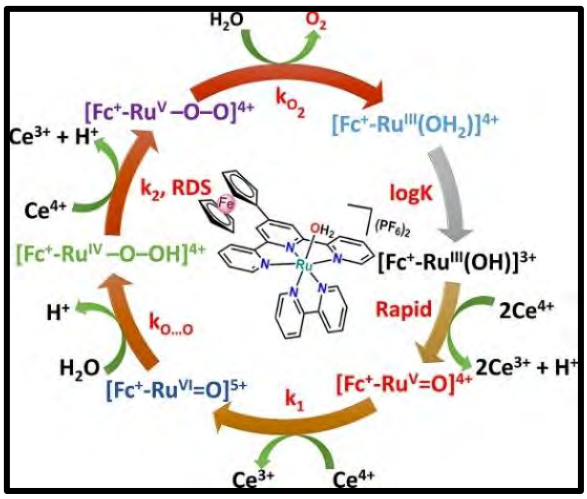

[1] This Chapter has been published in

Vatsa, A. and Padhi, S. K.* *Inorg. Chim. Acta*, 2020, *504*, 119444.

Chapter 3: Catalytic Water Oxidation by a Ru^{II} Half Sandwich Complex [2]

In Chapter 3, the synthesis, characterization and the catalytic water oxidation properties by a half-sandwich [Ru(η^6-benzene)(hdm)]BF_4 complex (hdm = hydroxydi(pyridine-2-yl)methanolate) has been discussed. This complex acts as an active precatalyst towards electrochemical and chemical water oxidation. The chemical water oxidation was performed in deionized water using ceric ammonium nitrate (CAN) as an oxidant. The experimental results reveal that the **[Ru-hdm]** catalyst having the **hdm** ligand, suffers decomposition under extreme harsh conditions of acidic pH, in the presence of an oxidant and doesn't exhibit O_2 evolution. The kinetics of chemical water oxidation reveals the 1st order dependency on CAN and catalyst concentration. The complex shows electrochemical water oxidation with 98 % Faradaic efficiency at pH 6.6 in phosphate buffer. The electrochemical water oxidation was performed in different complex concentrations and different pH. During the chemical water oxidation the complex undergoes decomposition resulting in the formation of insoluble particles due to highly acidic pH of 1.35 after the addition of CAN in deionized water. The formation of insoluble particles in the reaction mixture and also a coating over the surface of the silicone rubber septum has been observed and analyzed through FE-SEM, EDX, XPS, and HR-TEM analysis. From the XPS of the reaction mixture and the solid particles deposited over the septum, it was observed that catalyst remains in Ru^{IV}=O and Ru^{VI}=O during the water oxidation reaction.

Graphical synopsis of Chapter 3:

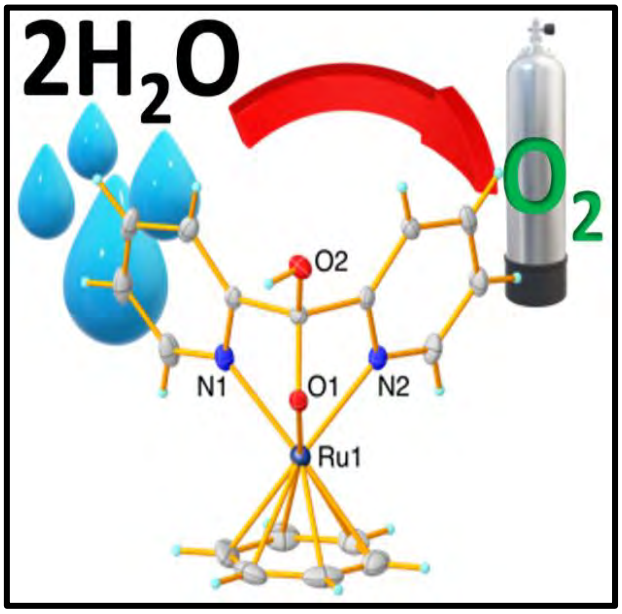

[2] This Chapter has been published in

Vatsa, A. and Padhi, S. K.*, *Eur. J. Inorg. Chem.*, 2021, *2021(34)*, 3499-3505.

Chapter 4: Dehydrogenation of Formic Acid by a Ru^{II} Half Sandwich Catalyst [3]

Chapter 4, describes the investigation of dehydrogenation of the formic acid into hydrogen and carbon dioxide in deionized water using sodium formate by $[Ru(\eta^6\text{-benzene})(hdm)]BF_4$. The dehydrogenation of formic acid was studied from lower to higher temperatures and it was observed that the rate of reaction is high at a higher temperature. In this case, the activation energy required for dehydrogenation of formic acid is calculated from the Arrhenius plot was 11.6 kJ/mol, whereas the reaction is endergonic with the $\Delta G = 81.642$ kJ at 298 K which was calculated from the Eyring plot. The kinetics of the dehydrogenation reaction was studied by varying the concentration of the complex, acid, and base through manometry. The dehydrogenation reaction was also studied at different pH and it was observed that the dehydrogenation of formic acid is efficiently shown gas evolution at pH 7.0. The stability of the catalyst towards dehydrogenation was examined by iterative addition of formic acid and sodium formate in a different set of reactions.

Graphical synopsis of Chapter 4:

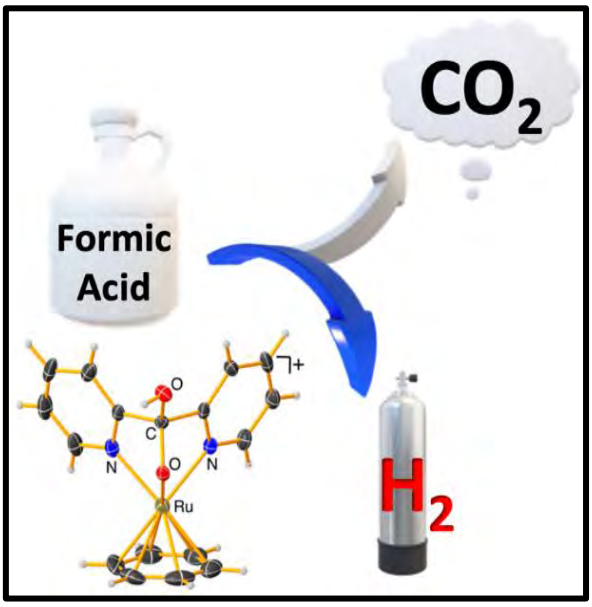

[3] This Chapter has been published in

Vatsa, A. and Padhi, S. K.*, *ChemistrySelect., 2021, 6(35),* 9447-9452.

Chapter 5: Dehydrogenation of formic acid using mononuclear Ruthenium (II) $[Ru(2py\text{-}tpy)(dqn)Cl]^{2+}$ complex [4]

In this chapter, the novel complex $[Ru(2py\text{-}tpy)(dqn)\ Cl]^{2+}$ (where dqn = 2,3-di(pyridine-2-yl) quinoxaline) has been synthesized and characterized by various spectroscopic techniques. The complex employed to study the dehydrogenation of formic acid using sodium formate as a base in deionized water. The dehydrogenation of formic acid was studied at different concentrations of acid, base and complex and from lower to higher temperature to determine the kinetics of the reaction. The dehydrogenation of formic acid was also performed at different pH values from 2.0 to 11.0. The dehydrogenation of formic acid at different temperatures reveals that activation energy required for the dehydrogenation of formic acid was 31.45 kJ / mol and ΔG was estimated to be 81.33 kJoules. The composition of gas was detected from the TCD and FID detectors of the Gas Chromatograph. The catalytic stability of the complex towards dehydrogenation was examined by iterative addition of formic acid and sodium formate in different set of reactions. The formation of the formate complex has confirmed through ESI-Mass spectra.

Graphical synopsis of Chapter 5:

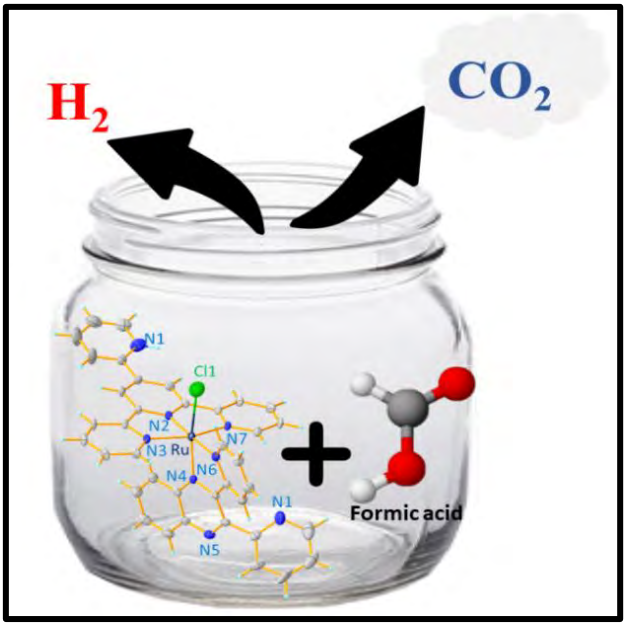

[4] Manuscript under preparation

Vatsa, A. and Padhi, S. K.* *Catalytic dehydrogenation of Formic Acid and Kinetic Studies by a Ru(II) Molecular catalyst*

Chapter 6: Dehydrogenation of Formic Acid by Half Sandwich [Ru(η^6-benzene)(L)Cl] catalysts [5]

In this chapter, two novel complexes [Ru(η^6-benzene)(L)Cl]$^+$ (where L = 2-Methyl 8-hydroxy quinoline **1** and 8-hydroxy quinoline **2**) were synthesized and characterized by different spectroscopic techniques. These complexes were utilized for the dehydrogenation of formic acid in the presence of sodium formate as a base in deionized water. The catalytic activity towards dehydrogenation of formic acid was compared between complexes **1** and **2**. For studying the kinetics of the dehydrogenation reaction, the reactions were performed with various concentration of acid, base and complex and by varying the temperature. The dehydrogenation of formic acid was also studied at different pH from highly acidic to highly basic medium. The dehydrogenation of formic acid at different temperatures reveals that activation energy required for the dehydrogenation of formic acid was 29.81 kJ / mol and ΔG was estimated to be 90 kJoules for the complex **1** and activation energy required for the dehydrogenation of formic acid was 29.83 kJ / mol and ΔG was found to be 83 kJoules for the complex **2**. The composition of gas was examined from the TCD and FID detectors of the Gas Chromatograph. The catalytic stability of the complex towards dehydrogenation was examined by repetitive addition of formic acid and sodium formate in different set of reactions. The formation of the formate complex has confirmed through ESI-Mass spectra. The Ru-H formation was noticed in NMR spectra.

Graphical synopsis of Chapter 6:

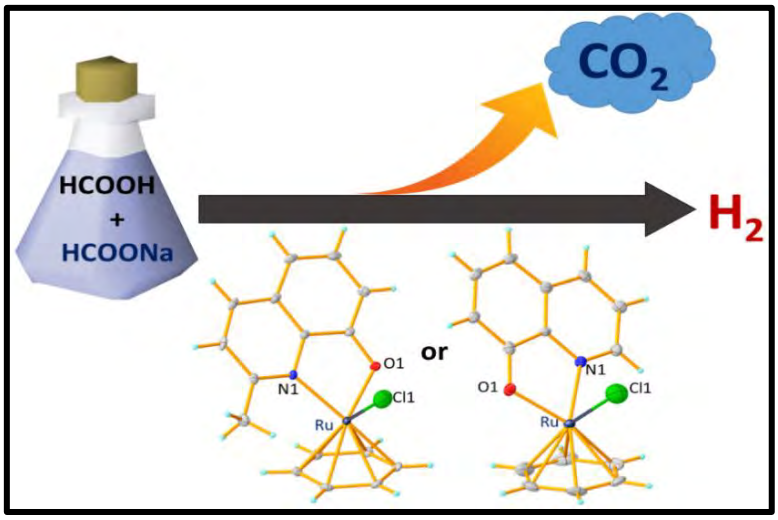

[5] Manuscript under preparation

Vatsa, A. and Padhi, S. K.* *Dehydrogenation of Formic Acid and Kinetic Studies by Half Sandwich Ru(II) molecular catalysts*

It has been concluded from the above investigations that:

- $[Ru(Fc\text{-}tpy)(bpy)OH_2]^{2+}$ and $[Ru(\eta^6\text{-benzene})(hdm)]BF_4$ complexes were successfully employed for the chemical water oxidation using ceric ammonium nitrate (CAN) as sacrificial oxidant. These catalysts also utilised for the electrochemical water oxidation.
- $[Ru(Fc\text{-}tpy)(bpy)OH_2]^{2+}$ complex shows chemical water oxidation at pH 1.0 in triflic acid and is highly active towards water oxidation as compared to the $[Ru(\eta^6\text{-benzene})(hdm)]BF_4$. The $[Ru(\eta^6\text{-benzene})(hdm)]BF_4$ complex undergoes decomposition after the addition of CAN as oxidant leading to the formation of insoluble particles.
- $[Ru(\eta^6\text{-benzene})(hdm)]BF_4$, $[Ru(2py\text{-}tpy)(dqn)Cl]^{2+}$ and $[Ru(\boldsymbol{\eta}^6\text{-benzene})(L)Cl]^{+}$ complexes were successfully catalysed the dehydrogenation of formic acid in the presence of sodium formate as base in deionized water. All the three complexes efficiently catalyse the dehydrogenation of formic acid in neutral pH rather than in highly acidic or basic pH.
- The introduction of electron donating groups enhances the catalytic activity of the catalysts.

These studies may encourage the researchers for designing the more efficient catalysts for the water oxidation by coordinating the electron donating groups on the ligand moiety to lower the overpotential and enhance the activity of the catalyst. It has also observed from these studies that half sandwich complexes shows low catalytic activity towards water oxidation as they are not stable in the highly acidic medium and in strong oxidising conditions. These studies also provides the path for studying and designing of Ru-based dehydrogenation of formic acid which is mostly catalysed by utilizing the Ir-based catalysts.

CHAPTER 1

This chapter is based on the literature survey

CHAPTER 1

INTRODUCTION

1. Introduction

1.1. Origin

The massive utilization of carbon-based energy fuels causes an increase in carbon dioxide levels in the atmosphere. Rise in the level of CO_2 causes various irreversible climatic changes, which include an increase in global temperature that results in warming of the earth resulting in the rise of sea level partially of 0.4-1.0 m is expected if CO_2 concentration exceeds 600 ppmv and exceeding up to 1000 ppmv of CO_2 concentration for 1.9 m. [1-2] At the same time, ice caps and glaciers are melting due to thermal expansion, which is responsible for rising sea levels that may affect some coastal regions. The abrupt changes in the atmosphere by various gaseous emissions cause a shift in rainfall in some areas because of global warming, increased sea surface and land temperature, and reduced surface humidity. Some other regions face a decrease in rains or low precipitation due to a rise in anthropogenic climatic changes. Day by day, global energy consumption rises, which is expected to double from 13.5 TW in 2001 to 27 TW by 2021. [3] Nature blessed us with a copious endowment in the form of different energy resources. With the increment in the exhaustion of these non-renewable energy sources, the demand for sustainable energy also increases. The increase in global warming due to CO_2 emissions is a concern for developing carbon-free or carbon-neutral resources for human well-being. Humans utilize various naturally available resources to overcome the energy crisis, such as wind energy, hydroelectric power, solar energy, biomass energy, and geothermal energy. These energies are sustainable renewable energy resources as well as economical. [4-5] The renewable energies were described below:

1.1.1. Wind Energy

Wind energy is the source that is utilized for the generation of electricity. The wind provides energy to turbines to rotate the propeller-like blades around a rotor for spinning the driveshaft to convert the kinetic energy into mechanical energy to turn on a generator that produces electrical energy. There are three key factors on which wind turbines utilize the maximum wind energy, i.e., wind speed, swept area, and air density. About 15% of the electricity produced by wind energy was consumed in Europe. The significant drawbacks of wind energy are a threat

to wildlife, visual and noise pollution, expensive setup, and energy can be harnessed only to selective locations. [6-7]

1.1.2. Hydroelectric Energy

The power is generated by utilizing flowing water upstream to downstream to drive the turbine to turn on the generator or produce electricity. Hydropower has about 16 to 17 % of total world electricity generation. The limitations of hydroelectric power are expensive, dangerous for aquatic life, is dependent on water availability, and may impact the flow and quality of water. [8-9]

1.1.3. Biomass Energy

Biomass is the energy produced by living organisms. Biomass energy mainly utilizes the materials generated by plants, woods, and waste. Biomass energy can be used in making heat, electricity and also used as biofuels. Biomass energy supplies less than 10% of the total energy in an industrialized country and about 20 – 30% in developing countries. In several countries, biomass contributes 50-90% of the total energy demand. The disadvantages of biomass energy are the size of land it requires, the requirement of storage room, biofuels are not completely clean as they still produce some greenhouse gases. The production of biomass is quite expensive. [10]

1.1.4. Geothermal Energy

Geothermal energy is the heat evolved from the sub-surface of the earth's crust which is clean and sustainable. Geothermal energy combines heat produced by the gravitational collapse and the radioactive decay of various isotopes. Geothermal energy is estimated to contribute about 3-5% of global energy demand in the form of renewable energy. The disadvantages of geothermal energy are the high-temperature requirement, emission of toxic gases, geothermal reservoirs are not permanent, etc. [11-13]

1.1.5. Photovoltaic Cell

Photovoltaic cells convert solar energy into electricity using semiconductor materials that interact with the photons coming from the sun through a process called the photovoltaic effect. The photovoltaic cell is the third renewable energy after wind and hydro powers in terms of

global capacity. According to the International Energy Agency, the growth of the PV cells is expected to rise 700-800 GW from 2019 to 2024. [14]

1.2. Natural Photosynthesis

Photosynthesis is one of the cleanest and sustainable biochemical processes that sustains life on earth by harvesting the sunlight into chemical energy in photosystem II that can be stored in chemical bonds in the form of carbohydrates needed to power life. Photosynthesis is performed by plants, algae, cyanobacteria, anoxygenic photosynthetic bacteria, and these organisms are called photoautotrophs. Photosynthesis is mainly responsible for producing and retaining the oxygen content on earth. [15-17]

$$\mathbf{6CO_2 + 6H_2O \xrightarrow{light} C_6H_{12}O_6 + 6O_2} \qquad \textbf{(1.1)}$$

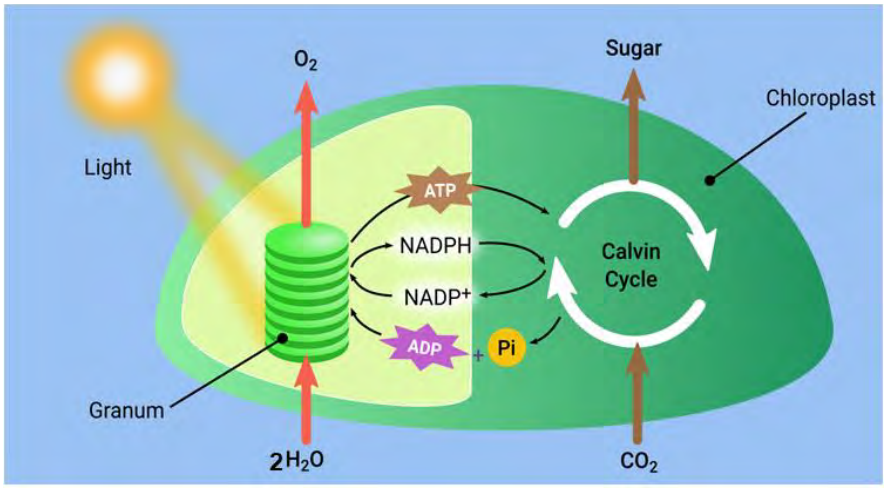

Figure 1.1. Photosynthesis changes sunlight into chemical energy, split water to liberate O_2, and fixes CO_2 into sugar.

1.2.1. Photosystem II

Photosystem II is located in the thylakoid membrane of plants, algae, and cyanobacteria. Photosystem II is the water-plastoquinone oxidoreductase, which is the protein enzyme in light-dependent reactions. In the photosystem, the role of the enzyme is to capture the photons from the sunlight to stimulate electrons that travel through various coenzymes and cofactors to reduce plastoquinone into plastoquinol. This drives the energized electrons to oxidize the water into an oxygen molecule and hydrogen ions.

$$\mathbf{2H_2O + 2Q + 4H^+_{stroma} \xrightarrow{h\vartheta} O_2 + 2QH_2 + 4H^+_{lumen}} \qquad \textbf{(1.2)}$$

The oxygen generated during the process is released as a byproduct in the atmosphere, and the reduced plastoquinol (QH_2) goes within the membrane and carries out the photosynthetic chain to cytochrome b_6f. The electron chain terminates at photosystem I. The generated hydrogen ions from water oxidation provide a potential gradient across the thylakoid membrane to the adenosine triphosphate synthase to generate ATP. The excited electron transported to the plastoquinone is eventually utilized to reduce the $NADP^+$ to NADPH. Both NADPH and ATP are needed for the final carbon fixation, light-independent reactions that reduce CO_2 to carbohydrates. The function of PSII is described based on four processes: (i) Light harvesting by the chlorophyll-proteins and transfer of excitation energy to the reaction center, (ii) excitation of the reaction center and separation of charge by creating hole-electron pair, (iii) electron transfer for the reduction of plastoquinone to plastoquinol across the membrane, and (iv) reduction of the reaction center by the Mn_4CaO_5 cluster, which in turn stocks oxidizing equivalents and oxidizes water. The chlorophyll photosynthetic pigments and cofactors in the PSII were utilized for the sequence of electron transfer for light-induced water oxidation in PSII (Figure 1.2). The P_{680i} is excited to P_{680}^* by absorbing energized photons transferred from the light-harvesting antenna chlorophylls and P_{680}^* via pheophytin (Phe), quinones A and B (Q_A and Q_B) transfers an electron to PSI, resulting in highly oxidized P_{680}^{*+}. The P_{680}^{*+} acts as an oxidant oxidizer having an oxidation potential of 1.2 V vs. NHE oxidizes tyrosine Z (Tyrz) into a Tyrz radical species. This Tyrz radical extricate an electron from the adjacent oxygen-evolving complex (OEC), which results in the oxidation of water when the four electrons are transferred. [18-19]

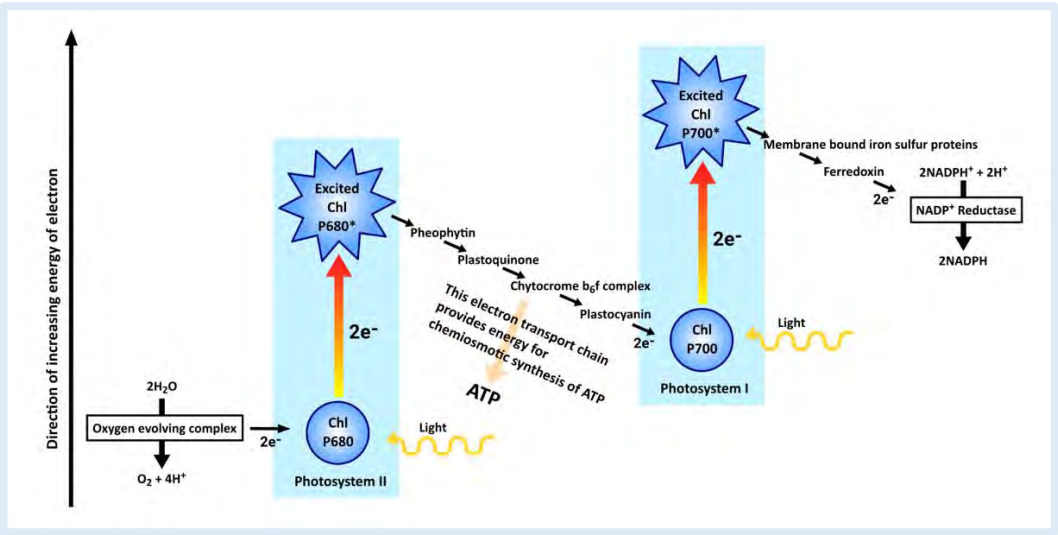

Figure 1.2. Simplified representation of natural photosynthesis.

The crystallographic studies and various spectroscopic techniques of PSII described the structure of OEC to be composed of the Mn_4CaO_5 cluster in which all the metal atoms and the neighboring ligands were placed unambiguously. The five oxygen atoms were found to provide oxy bridges connecting the five metal atoms, wherein three manganese and one calcium atom are linked through four oxygen atoms and form a cubane-like structure. The fourth manganese atom hanging outside the cubane and is connected through two oxygen atoms. The Mn_4CaO_5 cluster is coordinated with four water substrates in which two water molecules bind with dangling and two with calcium atoms. All the carboxylate ligands coordinate to the Mn_4CaO_5 cluster bidentate manner except the Glu 189 residue, which coordinates as a monodentate ligand. The Tyr 161 is bonded with one water molecule of the Mn_4CaO_5 cluster through hydrogen bonding and mediates the electron transfer between the Mn_4CaO_5 cluster and PSII. Asp 61 actively acts as a proton carrier and withdraws proton released from the cubane during the water oxidation. [20-21]

1.2.2. Water Oxidation Mechanism in PSII

In nature, the water oxidation process is catalyzed by OEC in PSII in the presence of light. The protons and electrons extracted from the water are transferred to the PSI, where reduction of CO_2 into carbohydrates takes place. The mechanism of water oxidation starts with four light-driven charge separation events leading to consecutive elimination of four electrons from the Mn ions of the OEC through oxidized Tyr161. At this stage, O_2 is evolved, and OEC reverts to its most reduced state. [22] The events occurring in the OEC for water oxidation are demonstrated in a catalytic cycle comprised of five intermediates known as the Kok cycle (Figure1.3). [23-24] The five intermediates are known as S states. The S_0 is the most reduced state of the array, S_1 is the dark-stable resting state, and S_4 is the most oxidized state. The S_4 is transient and decays spontaneously into reduced state S_0 by releasing O_2. [25]

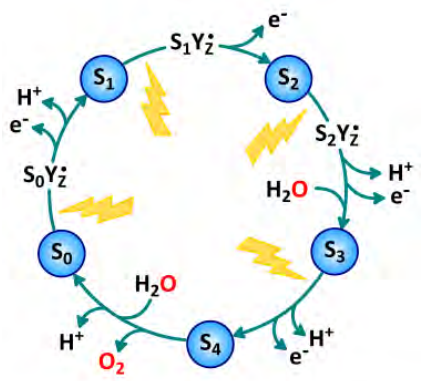

Figure 1.3. The Kok cycle

1.3. Artificial Photosynthesis

The worldwide increase in demand for energy led to the different scientific approaches towards developing an alternative energy source as artificial photosynthesis. [26-30] Artificial photosynthesis provides a clean, sustainable, and tremendous amount of energy resources by harnessing the sunlight for converting it into chemical products by imitating the process of natural photosynthesis of capturing and storing sunlight through artificial systems. [31-34] With the recent expansion in technologies, many efforts have been made towards the genesis of innovative approaches that led to significant advances in designing electrocatalysts related to light-driven charge separation systems. Based on the natural photosynthesis principle, researchers encounter the technologies for water splitting and hydrogen generation reactions by mimicking the OEC by converting sunlight into cost-effective, valuable chemical resources. Water oxidation is a thermodynamically exothermic reaction and requires highly proficient stable water oxidation catalysts to supply electrons for oxidizing water. [35-37] In an artificial system, the water oxidation reaction and hydrogen evolution reaction are photocatalyzed, and oxygen is evolved from the oxidation of water with the reduction of a proton into hydrogen. The artificial photosynthesis system is comprised of i) light-harvesting antennae for capturing photons and transfer the electrons into the photosynthetic chain and, ii) charge separation unit for proton-coupled electron transfer along the photosynthetic chain, and iii) multi-electron redox-active catalysts for utilizing the transferred electrons for oxidizing water into oxygen and reducing proton into the hydrogen (Figure 1.4). [38-41]

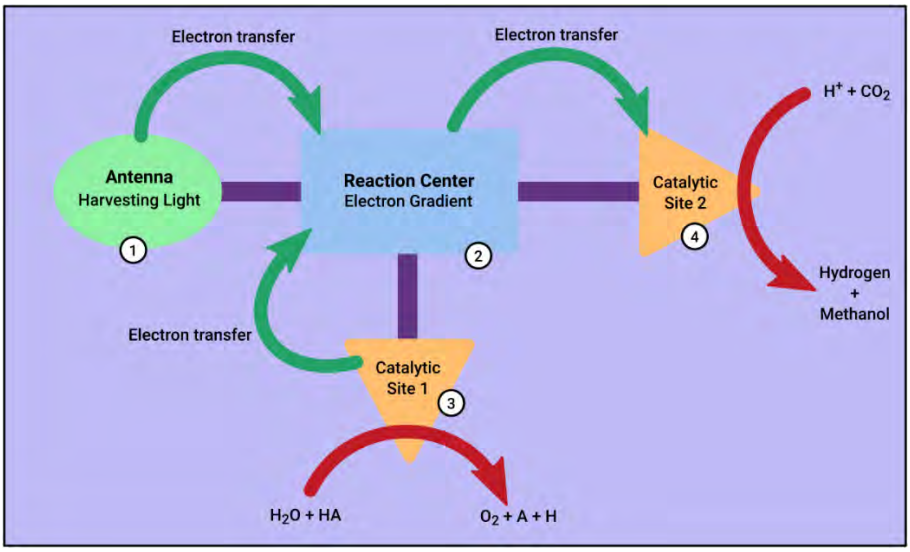

Figure 1.4. Simplified representation of Artificial Photosynthesis.

1.4. Types of water oxidation catalysis

Water oxidation is explored in different ways with varying reaction conditions. The different approaches examined in WOC are described below:

1.4.1.1. Chemical water oxidation

In the chemical water oxidation, the artificial metal catalyst is activated with a sacrificial oxidant at certain reaction conditions and pH for the evolution of oxygen from water. The commonly used one-electron oxidants are CAN and Ruthenium(III) tris(bipyridine) cation, mainly at a highly acidic pH. There are also some extensively used two-electron oxidants such as sodium periodate and oxone. The sacrificial oxidant enhances the catalyst's performance by increasing the rate of oxygen evolution and helps assess the reaction intermediates. The oxidant gets involved in the catalysis and is used up at the end of the reaction. [42]

1.4.2. Electrocatalytic water oxidation

Electrocatalytic water oxidation consists of two essential elements: the cathode for H_2 evolution and the anode for O_2 evolution. The energy production from the electrocatalytic WOC depends on the catalytic efficiency of the electrocatalysts. The electrochemical evolution of oxygen requires an external influence of three electrodes, first is the working electrode where the chemical reaction occurs. With the employment of the desired potential, it facilitates the transfer of electrons. The second one is a reference electrode with known reduction potential, which is used for measuring and controlling the electrode potential of the working electrode. The third one is a counter or auxiliary electrode, which passes all the current required to maintain the current at the working electrode for measuring the electrochemical activity of the catalyst towards water oxidation. In the electrochemical reaction, the highly sensitive instrumental and advanced techniques are employed to characterize electrocatalysts in diverse conditions such as highly acidic medium, in the presence of supporting electrolytes, and various instruments set up to increase the electroconductivity. In an oxygen-evolving reaction, the electrocatalyst must have low catalytic overpotential to enhance the efficacy of the electrochemical water oxidation.[43]

1.4.3. Photocatalytic water oxidation

Photocatalytic water splitting is to generate oxygen from water in the presence of natural or artificial light that provides photons to activate the photosensitizer. The photochemical water oxidation is carried out by employing a three-component system that consists of a molecular

WOC catalyst, a photosensitizer (P), and a sacrificial electron acceptor (SA). The most commonly used sacrificial electron acceptors are $S_2O_8^{2-}$ and $[Co(NH_3)_5Cl]^{2+}$, even $[Co(bpy)_3]^{3+}$ or $[Co(phen)_3]^{3+}$ have also been utilized. The $[Ru(bpy)_3]^{2+}$ and its derivatives are extensively used as the photosensitizers in photochemical water splitting. The $[Ru(bpy)_3]^{2+}$ are used as photosensitizer due to their peculiar properties, including strong absorption in the visible region, long-lived excited-state lifetime, reversible redox processes, and stability in excited as well as in their ground state. The P absorbs photons from the light, gets excited to P^*, and transfers the electron to the SA, generating an oxidized P^+ that triggers the oxidation of the WOC and building up a catalytic cycle. Thus the active form of WOC can evolve oxygen from the water. Further, many modifications have been executed by designing dyad or triad supramolecular assemblies. Two covalently linked metal complexes have a different chemical function, one act as a molecular catalyst and the other as a photosensitizer. In some cases, P and the WOC are anchored with the n-type semiconductor surface. [44]

1.5. Sacrificial oxidant

There are different types of sacrificial oxidants having distinctive properties are used along with water oxidation catalysts in water oxidation. Sacrificial oxidant abstracts electrons from the WOC, which further attain its higher oxidation state to catalyze the water oxidation. The sacrificial oxidant must have a sufficient reduction potential for oxidizing the catalyst. Ceric ammonium nitrate $(NH_4)_2Ce(NO_3)_6$ (CAN) is widely used as a primary oxidant for water oxidation, having a reduction potential of approximately 1.75 V vs. NHE. The characteristic properties of CAN which make it an extensively used oxidant for water oxidation are i) it is stable in acidic aqueous solution, ii) it is a one-electron oxidant, iii) CAN show a weak absorption band in the UV-Vis region, making it easy to track the progress of water oxidation reaction, and iv) CAN also found to be electrochemically active. The CAN is only stable in highly acidic conditions at low pH 1.0 and stable approximately up to pH 3.0. This limits the utilization of CAN for WOCs in artificial photosynthesis within neutral to alkaline media. [45-47]

$$\mathbf{4Ce^{IV} + 4e^{-} \rightarrow 4Ce^{III}} \qquad \mathbf{(1.3)}$$

$$\mathbf{2H_2O + 4Ce^{IV} \rightarrow O_2 + 4H^{+} + 4Ce^{III}} \qquad \mathbf{(1.4)}$$

Sodium periodate is also used as a two-electron oxidant for catalyzing WOCs within a wide range of pH from 2.0 to approximately pH 7.5; thus, it can catalyze the WOC in neutral conditions significant for the design of an artificial system. The reduction potential of sodium periodate is 1.6 V vs. NHE. The reduction of periodate into iodate requires one proton per electron, as in the water oxidation reaction. The sodium periodate can be an oxo transfer reagent, so oxygen produced during water oxidation must be characterized to confirm oxidation is occurring or not. [48-52] Ruthenium(III) tris(bipyridine) cation ($[Ru^{III}(bpy)_3]^{3+}$) is also a one-electron oxidant that can be employed as an alternative to CAN. The very low reduction potential of 1.21 V vs. SCE for $[Ru^{III}(bpy)_3]^{3+}$ is the main advantage. It provides a small overpotential for water oxidation based on the higher pH and reaction conditions. The drawbacks of ($[Ru^{III}(bpy)_3]^{3+}$ are that due to the low potential at low pH, it can drive the limited number of the water oxidation catalyst, which is stable at low pH, and ($[Ru^{III}(bpy)_3]^{3+}$ as oxidants are sensitive to decomposition and is quite expensive. [53-56]

$$\mathbf{4[Ru^{III}(bpy)_3]^{3+} + 4e^- \rightarrow 4[Ru^{III}(bpy)_3]^{2+}} \quad \mathbf{(1.5)}$$

1.6. Water Oxidation Catalysts

The water oxidation in PS II is a complicated process driven by the strong oxidizing oxo and carboxylate groups by stabilizing the higher oxidation state of Mn and lowering the redox potential of the OEC. Based on the activity and structural arrangement of the OEC, numerous families of synthetic water oxidation catalysts have been designed with optimal catalytic performance for the oxidation of water. The catalysts are based on transition metals by varying the substitution in the electron-donating ligands to enhance the activity of the catalyst by stabilizing the highest oxidation state of the metal center. The molecular catalysts for the water oxidation must have the following features:

- The catalyst must have a redox-active center
- Higher catalytic stability in reaction conditions can be referred to as TON
- The catalyst must be highly efficient towards water oxidation, i.e., high TOF
- Solubility and stability in aqueous acidic solution
- Undergo a multi-electron or multi-proton mechanism
- Production of oxygen with a higher rate
- Have small overpotential for easy transfer of electrons

The researchers take all of these features into account during the development of the water oxidation catalysts. Many high valent oxo, hydroxo, metal oxides, and polypyridyl complexes

were designed and synthesized with transition metals. There are various kinds of WOCs that have been evolved, including biological, homogeneous, heterogeneous, and hybrid catalysts.

1.7. The mechanistic pathway for O-O bond formation and O_2 liberation

The oxidation of water into the oxygen molecule requires the elimination of four electrons that means the catalyst undergoes transfer of four-electron and that's why an efficient and robust catalyst is needed for the O-O bond formation and O_2 liberation. Various pathways were reported earlier for different transition metal catalysts depending on their properties. The two routes based on the mechanistic studies have been established: i) Water nucleophilic attack on a metal-oxo (M-O) entity and ii) interaction of two metal-oxo (M-O) entities (I2M). As water oxidation involves the transfer of electrons and protons, the formation of intermediates goes through the proton-coupled electron transfer (PCET) mechanism. The two mechanistic pathways are described below:

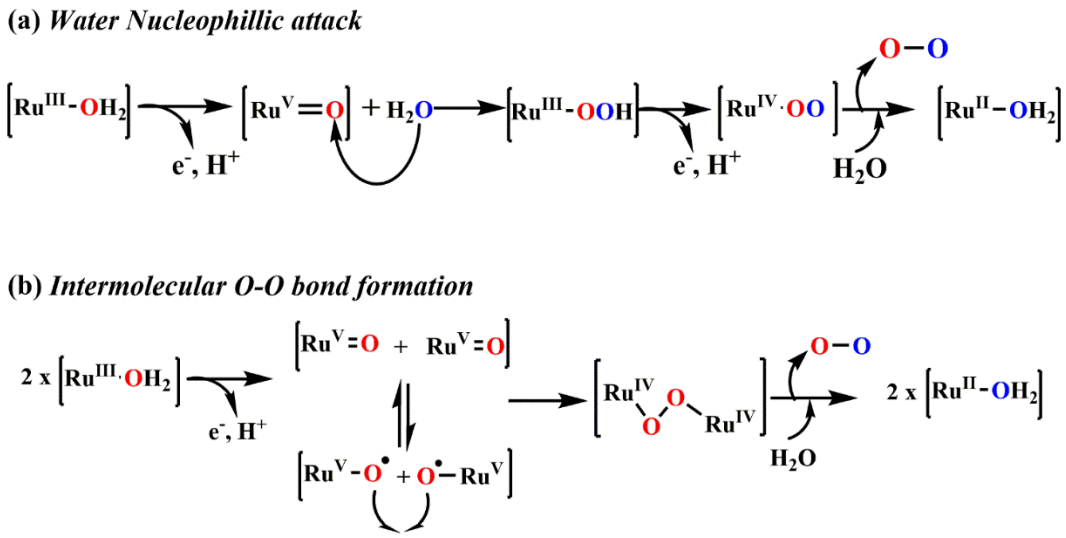

Scheme 1.1. Different mechanistic paths of water oxidation in mononuclear complexes.

1.7.1. Water nucleophilic attack (WNA) mechanism

In the WNA mechanism, the metal attains a higher oxidation state after sequential oxidation events, such as Ru(IV)-oxo or Ru(V)-oxo species, producing more electrophilic metal-oxo units. By the nucleophilic attack of water on the high-valent metal-oxo entity, there is a reduction of 2e- resulting in forming a metal hydroperoxide (M^n-OOH) species. The additional oxidation and deprotonation steps consequently give rise to an M^{n+1}-OO^- intermediate species, followed by the liberation of O_2.

1.7.2. Interaction of two metal units (I2M)

The two mono metal-oxo radicals undergone coupling intra- and intermolecularly, where the intramolecular coupling is feasible for multinuclear complexes. This mechanism involves the interaction of two metal-oxo units. One M-O oxyl radical coupled with another non-radical M-O unit to obtain a peroxo M-O-O-M intermediate with the consequent release of O_2.

1.8. Ruthenium based water oxidation catalysts

The transition metals with their distinctive catalytic properties are utilized to design catalysts for WOCs such as transition metals like Mn, Fe, Co, Cu, Ru, and Ir. Among these, multinuclear and mononuclear Ru complexes are widely used as an efficient catalysts in the study of water oxidation catalysis.

1.8.1. Multinuclear Ruthenium WOCs

The development of the first molecular catalyst *cis*, *cis*-$[Ru(bpy)_2(H_2O)]_2(\mu\text{-}O)^{4+}$ **(1)** by Meyer and co-workers in 1982 led to the beginning of using an efficient catalyst for chemical water oxidation. [57] This oxo ruthenium complex, because of its blue color called 'blue dimer,' undergoes water oxidation at pH 1.0 chemically and electrochemically by utilizing CAN as a sacrificial oxidant ($E_{1/2}$ = 1.6 V vs. NHE). The TON and TOF of the complex for the chemical water oxidation were 13.2 and 4.2 x 10^{-3} $s^{-1,}$ respectively. [58] The cyclic voltammetry studies of the **(1)** show some oxidation-reduction waves for various oxidation states and examined their pH dependence through the Pourbaix diagram, which mainly involves the transfer of electrons and protons. [59] The Ru in complex **(1)** undergoes a maximum Ru^V-O-Ru^V oxidation state with an oxidation potential of 1.46 V vs. SCE under the given catalytic conditions. The complex is very stable at its higher oxidation state. Still, at its lower oxidation state, it undergoes disproportionation to afford mononuclear analog, which was found to be inactive towards the water oxidation. [60-62] Several other groups have also been synthesized Ru-based WOCs and studied their mechanistic pathways. In 2000s Llobet and co-workers have reported the binuclear ruthenium complex $[Ru_2^{II}(bpp)(\mu\text{-}Cl)(terpy)_2]^{2+}$ (bpp = bis(2-pyridyl)pyrazolato, terpy = 2,2':6',2''-ter-pyridine). The μ-chloro bridge in this complex could be replaced by μ-acetato bridge resulting in $[Ru_2^{II}(\acute{\imath}\text{-}OAc)(bpp)(trpy)_2](PF_6)_2$. Under the acidic condition, the μ-acetato bridge could be replaced by two water molecules generating a di aqua complex $[Ru^{II}_2(bpp)(terpy)_2(H_2O)_2]^{3+}$ (**2**). [63] This complex undergoes Ce^{IV} driven chemical water oxidation resulting in a TON of 512 and TOF of 0.014 s^{-1}. Complex (**2**) shows several pH-dependent oxidation states that generate the high valent Ru^{IV}-Ru^{IV}, which was found to be the

active species for the O-O bond formation. [64] Later, in 2014, Llobet and Co-workers retailored complex (**2**) by substituting the C4 carbon of the pyrazole with methyl moiety in place of hydrogen. The resulting complex $\{[Ru^{II}(py\text{-}SO_3)_2(H_2O)]_2(\mu\text{-Mebbp})\}^-$ (**3**) consists of two axial pyridines functionalized with sulphonate groups for increasing the solubility of the complex (**3**) in aqueous media necessary for characterization and also for the insight of the reaction mechanisms. Catalyst (**3**) exhibits the TON of 22.6 and TOF of 0.068 s^{-1}. [65]

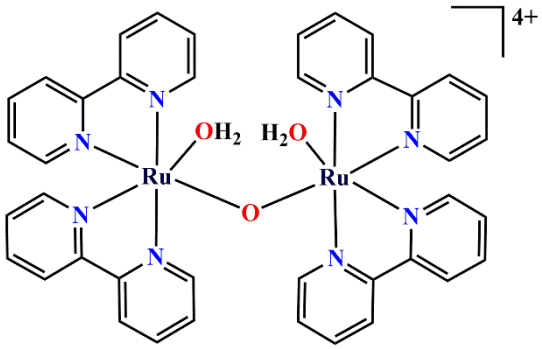

Figure 1.5. The first molecular catalyst *cis*, *cis*-$[(bpy)_2(H_2O)Ru^{III}ORu^{III}(H_2O)(bpy)_2]^{4+}$ (**1**).

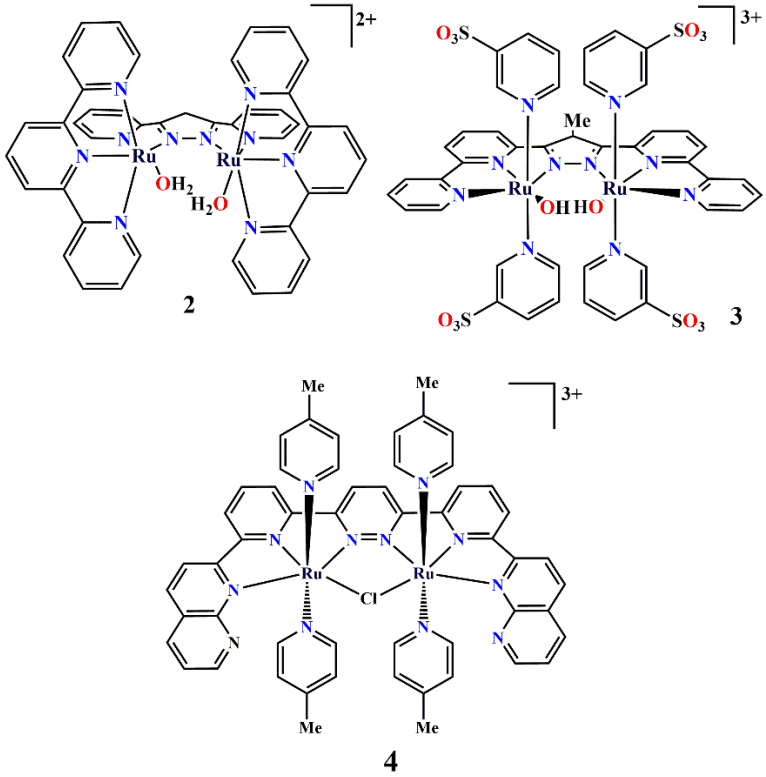

Figure 1.6. The binuclear ruthenium complexes (**2-4**).

Thummel and co-workers synthesized and studied several mononuclear and dinuclear ruthenium complexes by coordinating substituted pyridine axially and heteroatomic polynuclear ligand in the equatorial plane (**4**). After the chemical water oxidation reaction using

Ce^{IV} as an oxidant, the complex shows high catalytic activity with a TOF of 0.046 s^{-1} and TON of 538 after 20 h of catalysis. [66]

Sun *et al.* in 2010 reported two isomers of the dinuclear ruthenium complex by incorporating the carboxylate ligand. The *trans* isomer of the dinuclear complex (**5a**) shows a much lower TON of 4740 and TOF of 0.28 s^{-1} for catalyzing the water oxidation. They have synthesized the *cis* isomer of the dinuclear ruthenium complex with 1,4- bis(6'-COOH-pyrid-2'-yl)phthalazine ligand (**5b**) for better catalytic activity. The catalyst (**5b**) is efficient for chemical water oxidation showing a TON of 10400 and TOF of 1.2 s^{-1}. [67-68]

Tanaka and group reported a dinuclear ruthenium complex $[Ru^{II}_2(OH)_2(3,6\text{-}^tBu_2qui)_2(btpyan)](SbF_6)_2$ (**6**) using 3,6-^{t}Bu$_2$qui.3,6-di(tert-butyl)-1,2-benzoquinone as supporting ligand and 1,8-bis{(2,2':6',2")-terpyridyl}anthracene (btpyan) as bridging ligand between two ruthenium employed for converting the aqua into oxo ligands to form O-O bond. The indium-tin-oxide (ITO) electrode is utilized for catalyzing the oxidation of water showing the dependence on the pH of the medium. [69] The TON for the electrochemically oxidized water is 33500 by using $(SbF_6)^{2-}$ modified ITO electrode in the water at pH 4.0. [70]

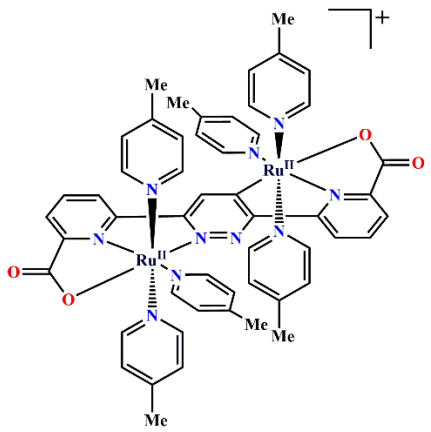

5a

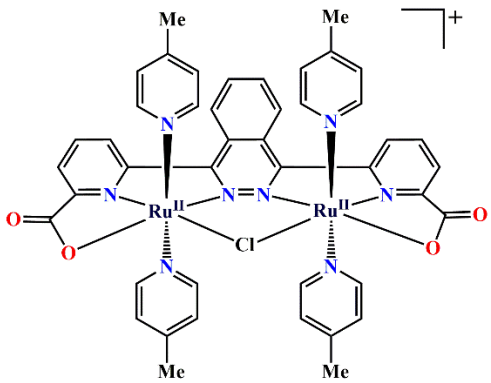

5b

Figure 1.7. Molecular structure of WOCs (**5a-5b**).

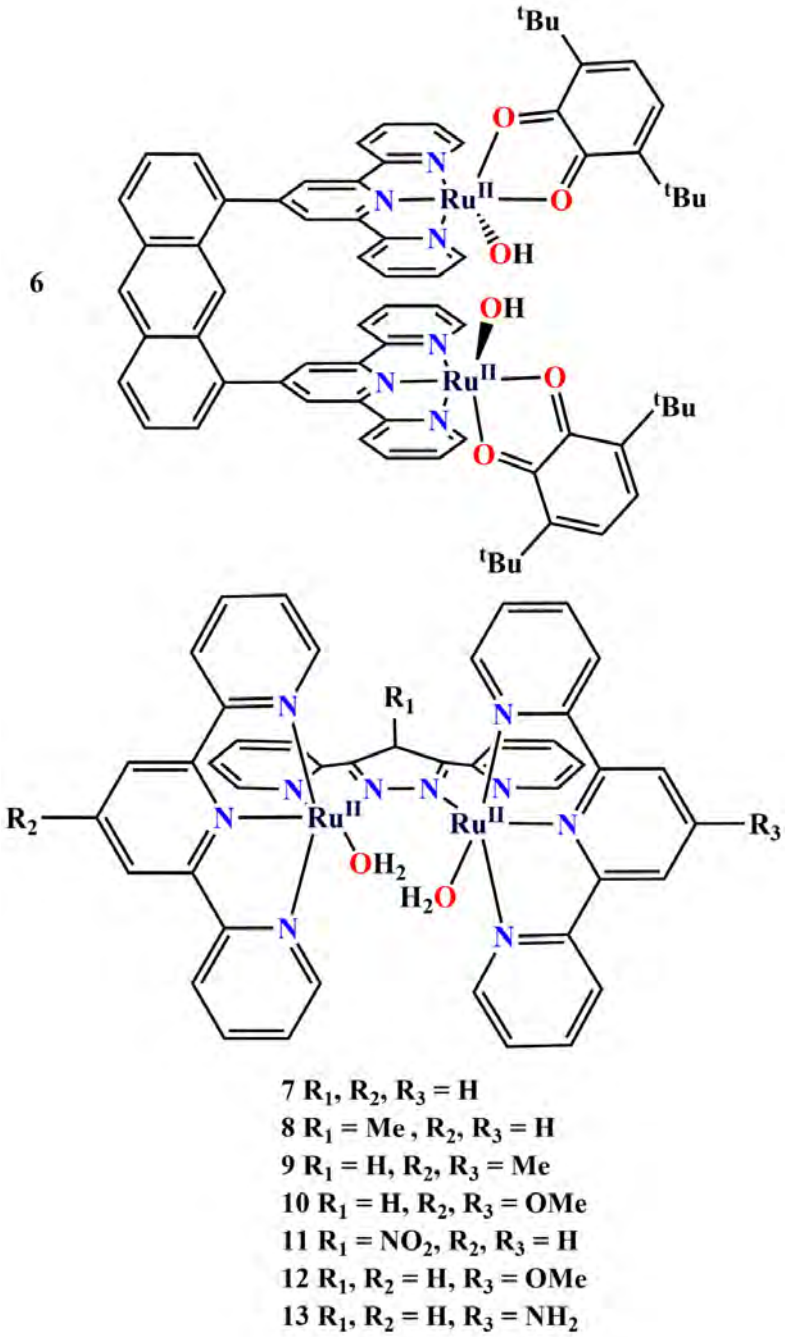

Figure 1.8. Molecular structure of WOCs (**6-13**).

In 2016, Llobet and group synthesized a series of symmetric and non-symmetric dinuclear Ru complexes by employing electron-withdrawing (EW) and electron-donating (ED) groups having general formula $\{[Ru(R^2\text{-tpy})(H_2O)][Ru(R^3\text{-tpy})(H_2O)](\mu\text{-}R^1\text{-bpp})\}^{3+}$ (**7-13**) where R^1, R^2, and R^3 are EW and ED groups such as Me, MeO, NH_2, and NO_2. They concluded that ED groups do not change the catalytic rates whereas EW groups taper the catalytic rate during water oxidation. [71]

Meyer *et al.* in 2015 reported a pyrazolate-based dinuclear ruthenium complex $[\{Ru(py)_2\}_2(\mu\text{-}L)(H_2O)_2]^+$ (**14**) (where L = 3,5-bis(6-hydroxymethylpyrid-2-yl)-1H-pyrazole) adjoined with

carboxylate ligand. Complex (**14**) shows the oxidation of water with low oxidation potential having an initial TOF of 1.4 s^{-1} and a TON of 24 (out of 25). [72]

In 2016, Araki *et al.* have synthesized a binuclear complex $[Ru_2(H_2O)_2(bpy)_2(tpy_2ph)](PF_6)_4$ (**15**) (tpy_2ph = 1,3-bis(4'-2,2':6',2''-terpyridin-4-yl)benzene) and the catalytic activity was examined by compairing with its mononuclear analogue $[Ru(H_2O)(bpy)(phtpy)](PF_6)_2$ (phtpy = 4'-phenyl-2,2':6',2''-terpyridine). The weakly coupled binuclear complex (**15**) have high reaction rate of 1.9×10^{-3} s^{-1} as compared to its mononuclear analogue having low O_2 production rate of 9.5×10^{-5} s^{-1}. [73]

Matias *et al.* in 2018 studied the catalytic activity of the polymeric binuclear poly-$[\{Ru(H_2O)(phen)\}_2(tpy_2ph)]$ (**16**) and also synthesized a binuclear complex linked through benzene ring at meta positions $[\{RuCl(Clphen)\}_2(tpy_2ph)]^{2+}$ (**17**) and its corresponding aqua $[\{Ru(H_2O)(Clphen)\}_2(tpy_2ph)]^{4+}$ (**16**) complex. The poly-$[\{Ru(H_2O)(phen)\}_2(tpy_2ph)]$ characterized by electrochemical and spectroscopic procedure indicates the formation of active $[Ru^{V}=O]$ species at potential 1.5 V with the rise of ruthenyl [Ru=O] confirmed through Raman spectra. Complex (**16**) shows faradaic efficiency of 39 % for oxygen evolution reaction. [74]

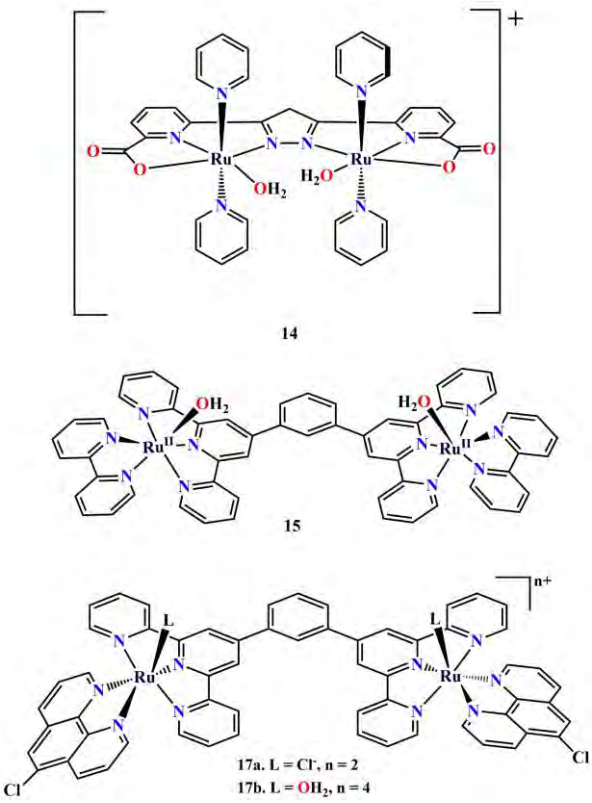

Figure 1.9. Molecular structure of WOCs (**14-17**).

In 2019 Matais and group have synthesized the chloro and aqua analogue of $[\{Ru(L)(bpz)\}_2(tpy_2ph)](PF_6)_n$ (where L = Cl, H_2O and n = 2, 4). The $[\{Ru(H_2O)(bpz)\}_2(tpy_2ph)](PF_6)_4$ (**18**) **is** employed for the water oxidation catalysis, and its

activity is compared with the bipyridine bpy as an ancillary ligand instead of bpz. The bpz ligand stabilizes the redox potential and lower oxidation state of the species relative to bpy. Still, this strong π– acceptor doesn't show any favorable effect on water oxidation activity as determined theoretically and experimentally by the reversal of the tendency in the formation of the catalytically active $[Ru^{V}=O]^{3+}$ species and decrease in spin density and oxyl character. [75]

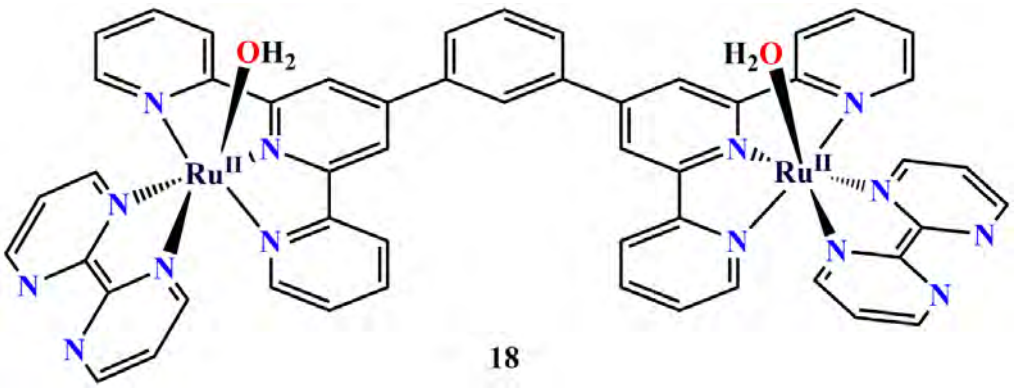

Figure 1.10. Molecular structure of binuclear water oxidation catalyst (**18**).

1.8.2. Mononuclear Ruthenium Polypyridyl Complexes

After the successful employment of multinuclear polypyridyl complexes for water oxidation, the discovery of mononuclear complexes has garnered much attention from researchers. In comparison to multinuclear complexes, mononuclear complexes have a simpler structure and distinct spectroscopic properties. The use of these catalysts provides a simpler platform to study the catalytic pathways experimentally and theoretically. [76-79] The mononuclear complexes were discussed below:

1.8.2.1. Mononuclear Ruthenium Complexes Containing Neutral Ligands

In 2005, Thummel and group had proposed the first family of mononuclear Ru aqua complex $[Ru(pbn)(4\text{-}R\text{-}Py)_2OH_2]^{2+}$ (**19-21**) (where pbn = 2,2'-(4-(tert-butyl)pyridine-2,6-diyl)bis(1,8-naphthyridine and Py = pyridine). The pyridine ligand was substituted at the 4th position with R (R = CF_3, NMe_2, and CF_3). The complex (**19**) substituted with dimethylamino group get protonated at pH = 1 and behave as strongest σ – donating group in the series giving highest catalytic activity ((**19**): TOF = 7.8 x 10^{-4} s^{-1}, (**20**): TOF = 3.5 x 10^{-4} s^{-1}, and (**21**): TOF = 3.5 x 10^{-4} s^{-1}) and having lower catalytic stability ((**19**): TON =50, (**20**): TON = 580 and (**21**): TON = 70). [80] Meyer and co-workers have reported Ru complexes $[Ru(NNN)(NN)(OH_2)]^{2+}$ (**22-24**) (where NNN = tpy is 2,2′:6′,2″-terpyridine or Mebimpy = 2,6-Bis(1-methylbenzimidazol-2-yl)pyridine and NN = bpm is 2,2′-bipyrimidine or bpz is 2,2′-bipyrazine) act as single-site catalyst for water oxidation. The complex (**23**) shows TON = 8 and TOF = 0.02 s^{-1}. They have

proposed the mechanistic pathways through electrochemical, and kinetics studies as well as through O^{18} labeling experiments showing the involvement of Ru^{V}=O intermediate and after an attack of water on the oxo group forms peroxo intermediate which gives terminal step of O-O bond formation for water oxidation. [81-82] They have also synthesized another series of mononuclear complexes by varying the ligand environment, and here $[Ru^{IV}=O]^{2+}$ formed as a key intermediate for water oxidation. [83]

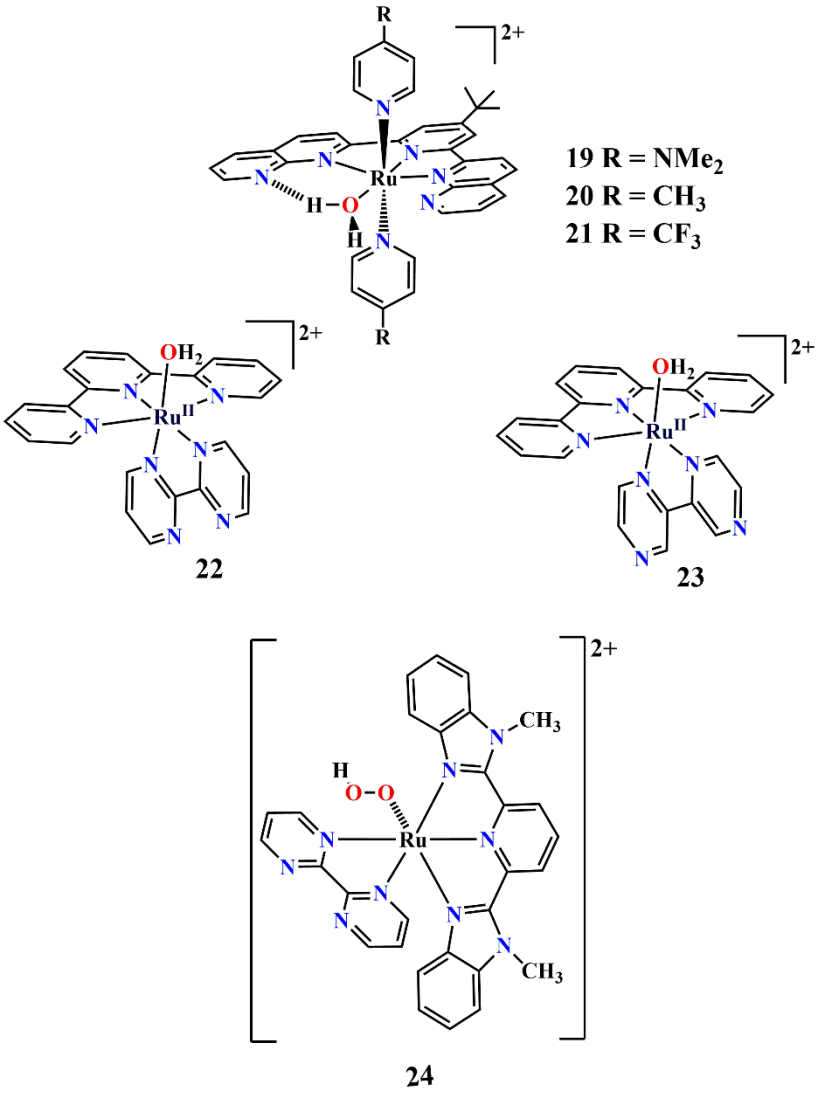

Figure 1.11. Molecular structure of WOCs (**19-24**).

Thummel [84-85] and Fujita *et al.* [86] proposed a series of mononuclear WOCs having the general formula $[Ru(NNN)(N_2)H_2O]$ (**25** – **27**) where NNN stands for tridentate and N for monodentate N-donating ligands and these complexes have aqua ligand at the equatorial position. They also proposed that the aqua group forms H-bond with the free nitrogen of the N-donating ligand at the equatorial plane.

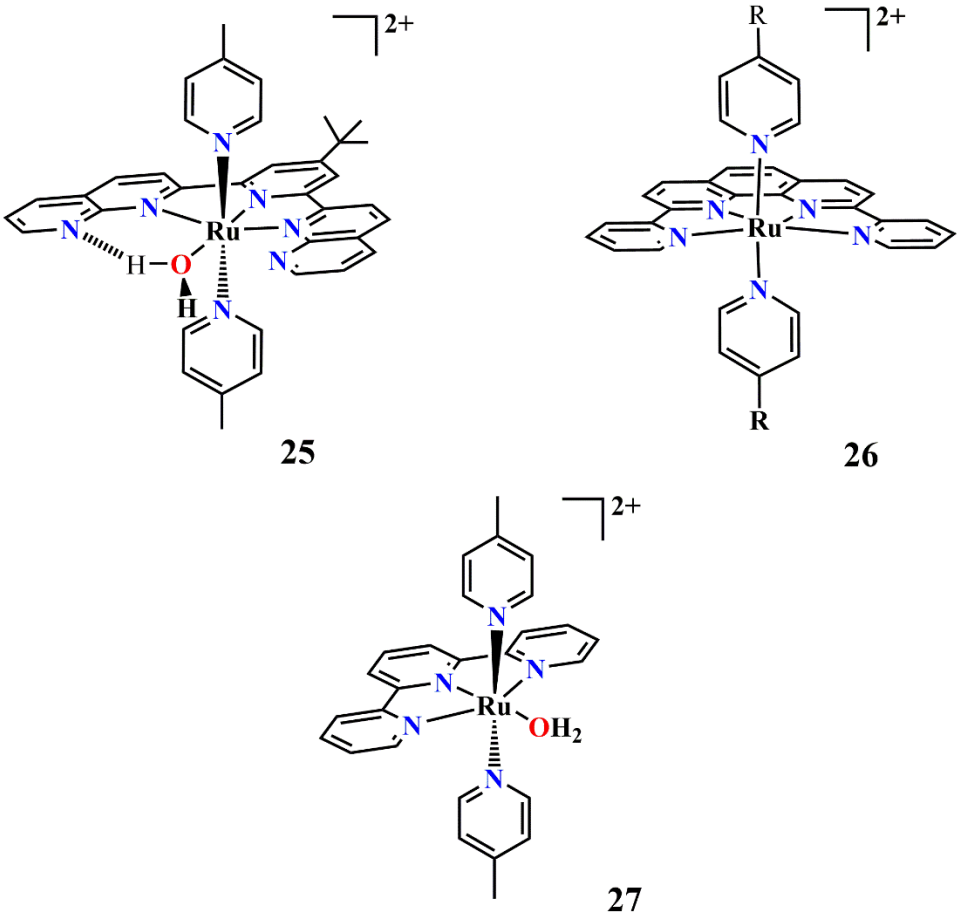

Figure 1.12. Molecular structure of WOCs (**25-27**).

Berlinguette and co-workers reported a series of chloride and their corresponding aqua complexes by substituting both bipyridine and terpyridine moieties with electron-withdrawing (-Cl, -COOH) and electron-donating groups (-OMe) having the general formula $[Ru(tpy\text{-}R^1)(bpy\text{-}R^2)L]^{n+}$ (**28 - 36**) (where tpy = 2,2′:6′,2″-terpyridine and bpy = 2,2′-bipyridine; when L = Cl, n = +1 and L = OH_2, n = +2) to study the influence of electronic parameters on the catalytic activity. The electron-withdrawing groups on the bpy suppress the catalytic activity and increase the catalytic stability, whereas electron-donating groups enhance the catalytic activity and decrease the catalytic TONs. They suggest that 2,2′-bipyridine N, N'- dioxide is produced in the presence of ceric ammonium nitrate in acidic media, causing the dissociation of bpy ligand, which is responsible for the catalyst's deactivation. They observed that aqua complexes have a short induction period as compared to the chloride complexes. They have proposed the mechanism of the water oxidation having numerous steps through WNA mechanism via PCET pathway indicating that $[Ru^V{=}O]$ plays a vital role as a key intermediate. [87-88]

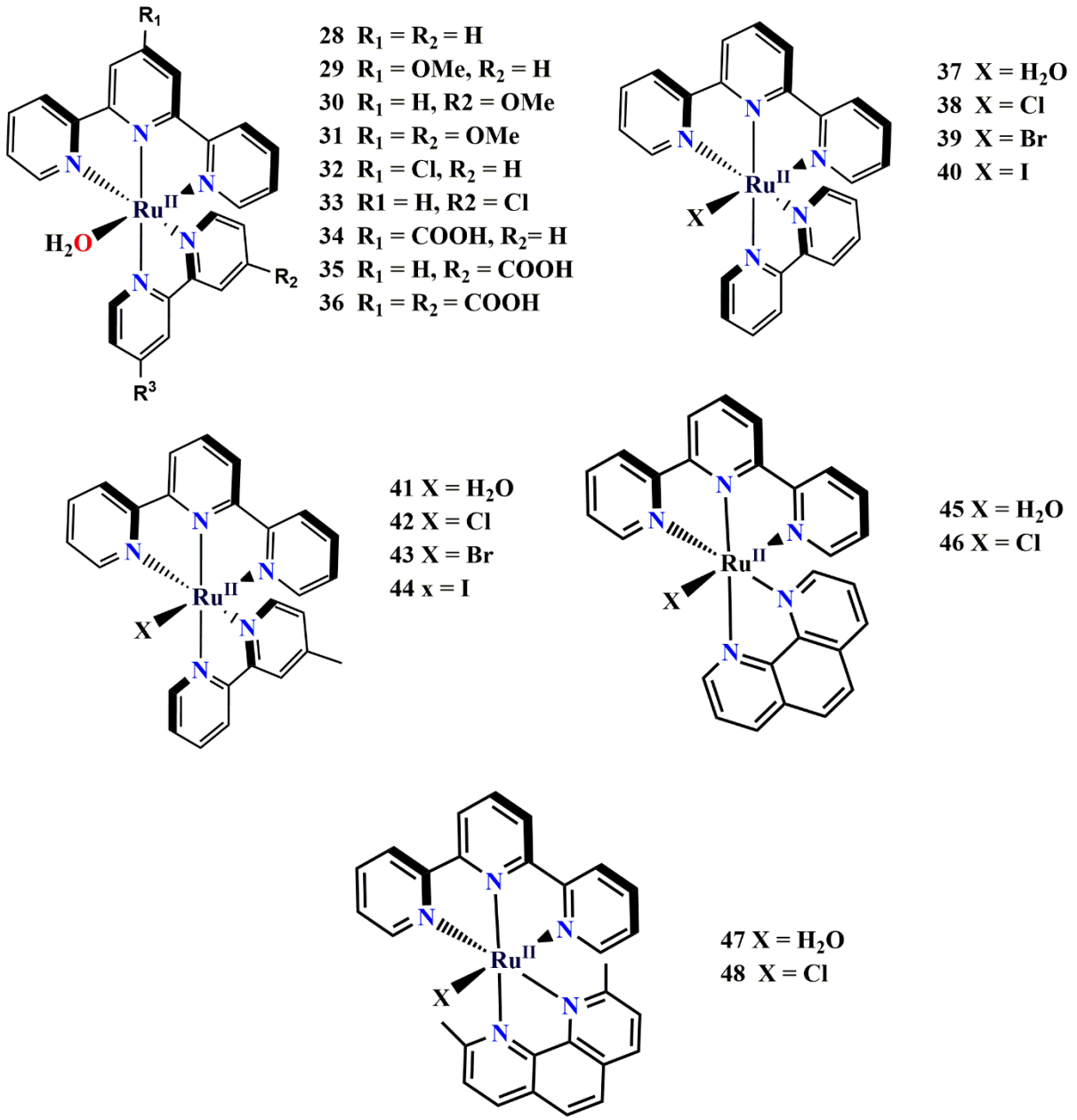

Figure 1.13. Molecular structure of WOCs (**28-48**).

Thummel and group have reported two different series of Ru (II) complexes (**37** – **53**), the 1st series have a general formula of $[Ru(NNN)(NN)X]^{n+}$ where NNN = tridentate polypyridyl ligand, NN = bidentate polypyridyl ligand, and X = halogen (Cl, Br, I) or water molecule and the second series have general formula $[Ru(NNN)(pic)_2X]^{n+}$ where NNN = tridentate polypyridyl ligand, pic = 4-picoline, and X = halogen or water. In the first series, the water molecule or halide group is coordinated at the axial position. In contrast, the water or halide group is coordinated at the equatorial position in the second series. The bromo- or chloro-complexes undergo water oxidation through halogen/water exchange. The iodo- catalyst

doesn't require water–halogen exchange for better catalytic activity because water oxidation proceeds through seven coordinated aqua intermediate formations. [89]

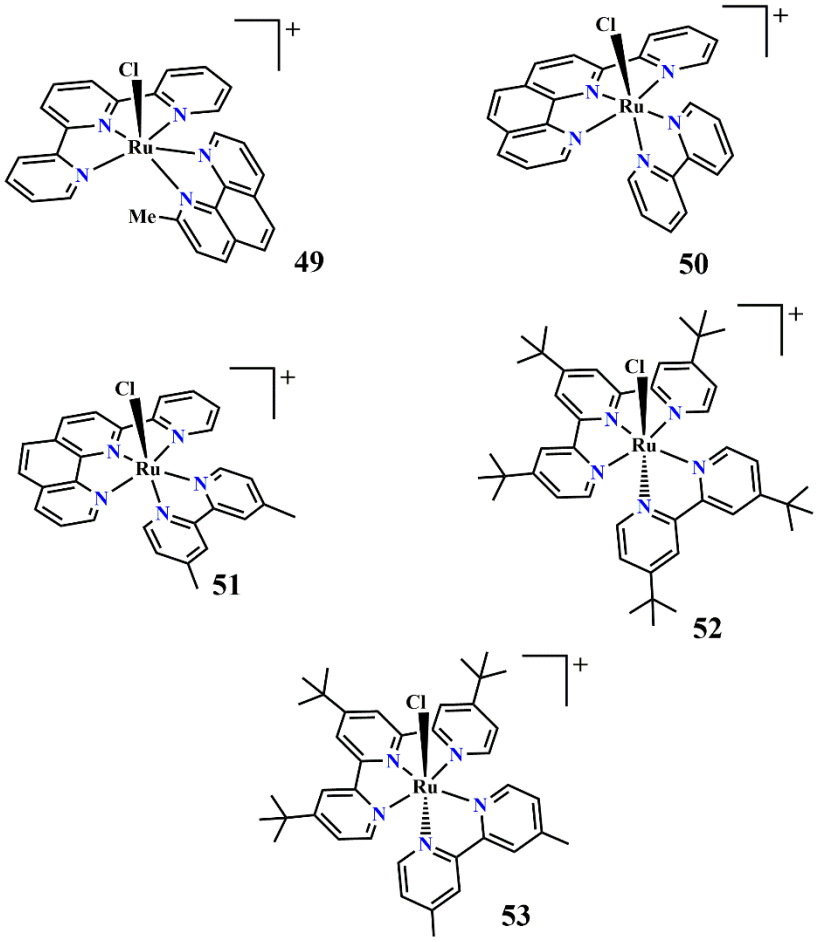

Figure 1.14. Molecular structure of WOCs (**49-53**).

Yagi and group have reported the $[Ru(R\text{-}tpy)(bpy)OH_2]^{2+}$ (**54-58**) complex, and terpyridine ligand is substituted with R = H, CH_3O, EtO, CH_3, and Cl group at 4th position. They have observed that the catalytic rate of reaction depends on the type of substitution on R-tpy ligand. The substitution with the strong electron-donating groups such as EtO and MeO shows a much higher catalytic rate than the weak electron-donating group CH_3 and electron-withdrawing Cl group. They have proposed that oxidation of Ru^{IV}=O to Ru^{V}=O is the rate-determining step instead of O-O bond formation by WNA mechanism. [90]

Thummel, Fujita and Yagi groups have reported the two photo-isomers *cis*-$[Ru(tpy)(pynap)(H_2O)]^{2+}$ and *trans*-$[Ru(tpy)(pynap)(H_2O)]^{2+}$ (**59-60**) (where pynap = 2-(pyrid-2'-yl)-1,8-naphthyridine). They have found that pynap ligand behaves as pendant base in *trans*-$[Ru(tpy)(pynap)(H_2O)]^{2+}$ and which shows higher catalytic activity towards water oxidation as compared to the *cis* isomer. In this case, the uncoordinated nitrogen of the naphthyridine forms hydrogen bonding with the aqua ligand. [91-92]

Llobet and group have reported the complex $[Ru(tpy)(bpy)H_2O]^{2+}$ (**61-62**) by incorporating F atom on bpy ligand framework to find out the effect of H- bonding and electronic environment on the water oxidation activity. They observed that the F atom shows interaction with the aqua ligand through H-bonding, which decreases the catalytic activity of the complex and lowers the TON. [93]

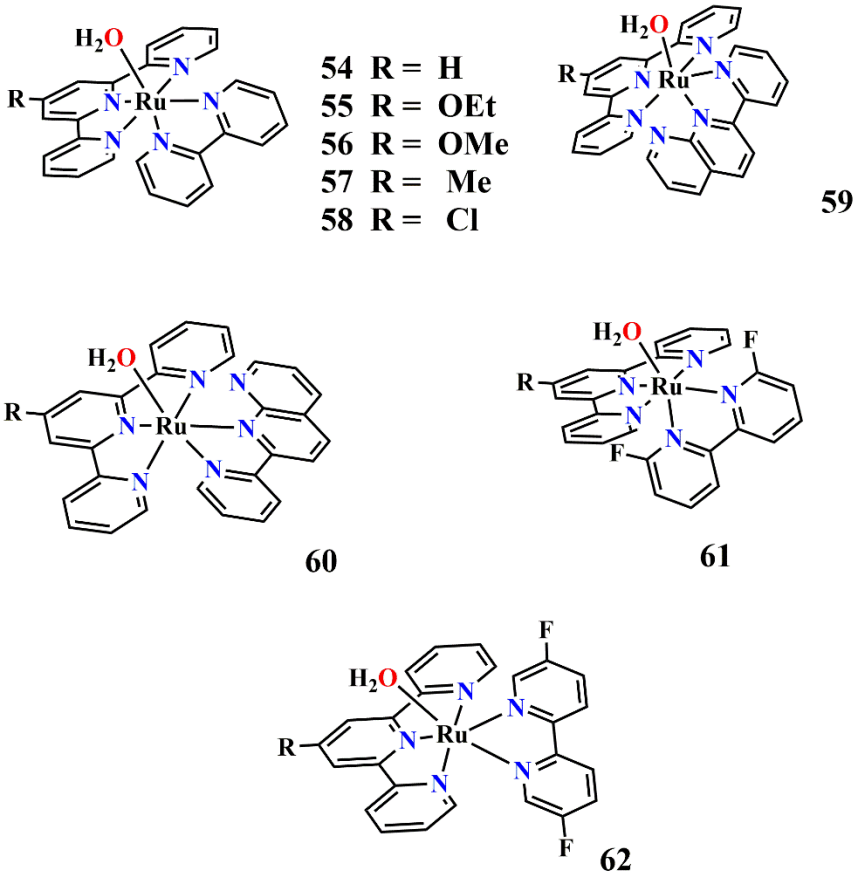

Figure 1.15. Molecular structure of WOCs (**54-62**).

Grotjahn and group have reported the $[Ru(tpy)(bpy)Cl]^{+}$ and $[Ru(tpy)(bpy)H_2O]^{2+}$ (**63-65**) by substituting the bpy ligand with electron-donating alkoxy (-OMe) and hydroxyl group (-OH). They observed that the methoxy group located *cis* to Cl atom is responsible for the ionization of the chloride ligand by the formation of hydrogen bonding with the aqua ligand in aqueous acetone. [94]

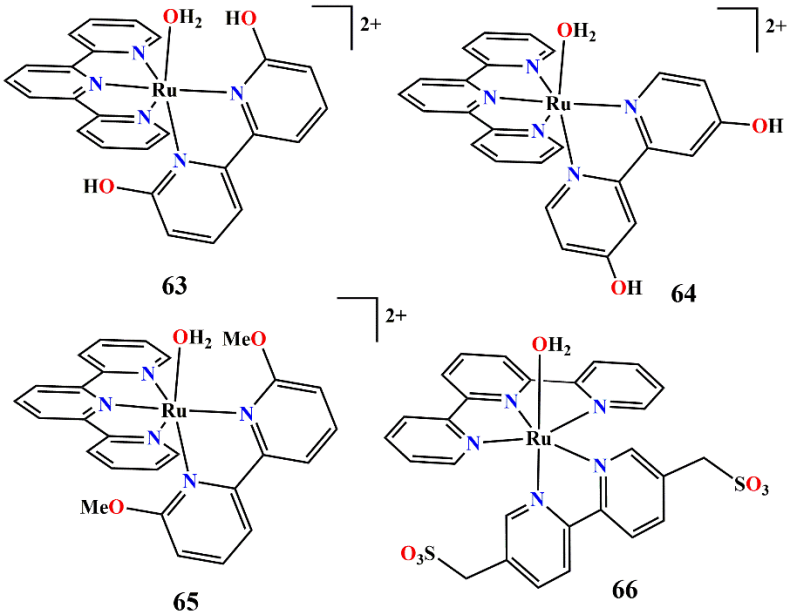

Figure 1.16. Molecular structure of WOCs (**63-66**).

Masaoka and group have reported the aqua complex [Ru(terpy)(bpyms)H_2O] (**66**) (where terpy = 2,2′:6′,2″-terpyridine and bpyms = 2,2'-bipyridine-5,5'-bis(methanesulfonate)) bearing SO_3^- as pendant base on bpy ligand framework for water oxidation in the presence of Ce^{4+} as an oxidant. They suggested that pendant SO_3^- groups coordinated to the catalyst enhance its activity by capturing Ce^{4+} for hetrometallic O-O bond formation due to its strong ability to coordinate Lewis-acid metal ions. The catalyst shows a TON of 47 with 94 % of conversion efficiency for catalysis. [95]

Wada and group introduced a mononuclear precursor complex [Ru(dpp)(bpy)Cl]Cl (**67**) (where dpp = 2,6-dipyridylphenyl, bpy=2,2'-bipyridine) which was easily hydrolysed in neutral medium to form hydroxo complex $[Ru(dpp)(bpy)OH]^+$ (**68**). This complex dpp ligand forms a covalent bond between Ru and C of the ligand's central phenyl group, which acts as a strong σ donor and is regarded as carbanion. This complex shows catalytic water oxidation in the presence of $[Ru(bpy)_3]^{3+}$ as the oxidant at pH 2.5 with a TON of 22. [96]

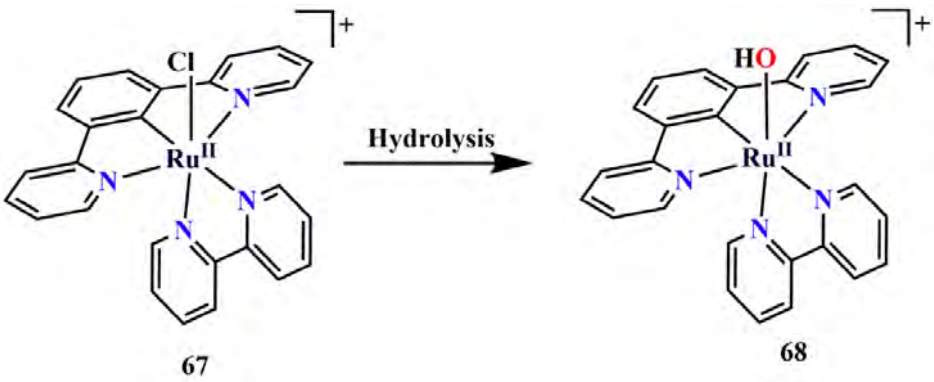

Figure 1.17. Molecular structure of complexes (**67-68**).

Kumbhar and group synthesized the mononuclear Ru complex $[Ru(tpy)(bpy)H_2O]^{2+}$ (**69-72**) by modifying backbone of bpy ligand with introduction of glycoluril group forming bpg ligand where bpg = 4b,5,7,7a-tetrahydro- 4b,7a-nepiminomethanoimino-6*H*-imidazo[4,5 *f*][1,10]phenanthro- line-6,13-dione. The O atom of the bpg ligand forms the H- bonding with the H atom of the aqua ligand, which favors the second-order coordination sphere. As a result, the availability of water molecules increases at the catalytic site. The complex shows a TON of 833 and TOF of 1.9 x 10^{-2} s^{-1} using Ce^{4+} as an oxidant. [97]

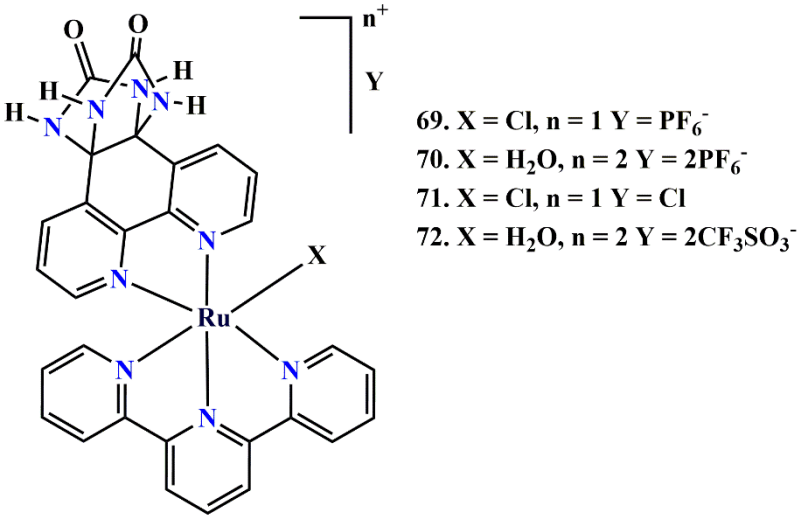

Figure 1.18. Molecular structure of WOCs (**69-72**).

Padhi and group have reported synthesis and water oxidation activity using Ce^{4+} as sacrificial oxidant of the various $[Ru(tpy)(bpy)(OH_2)]^{2+}$ based complexes such as $[Ru(n\text{-}py\text{-}tpy)(bpy)(OH_2)]^{2+}$ (**73-75**) (where n = 2,3,4), $[Ru(QCl\text{-}tpy)(bpy)(OH_2)]^{2+}$ (**76**) (where QCl= 2-4'-(2-chloroquinolin-3-yl)-2,2':6',2''-terpyridine) and $[Ru(Ql\text{-}tpy)(bpy)(OH_2)]^{2+}$ (**77**) (where Ql-tpy= (8-(2,6-di(pyridin-2-yl)pyridin-4-yl) quinoline) by incorporating electron-withdrawing and donating groups and studied their electronic effects on the tpy scaffold. It was observed that the catalytic activity of the catalyst decreases in the presence of the electron-withdrawing group. [98-100]

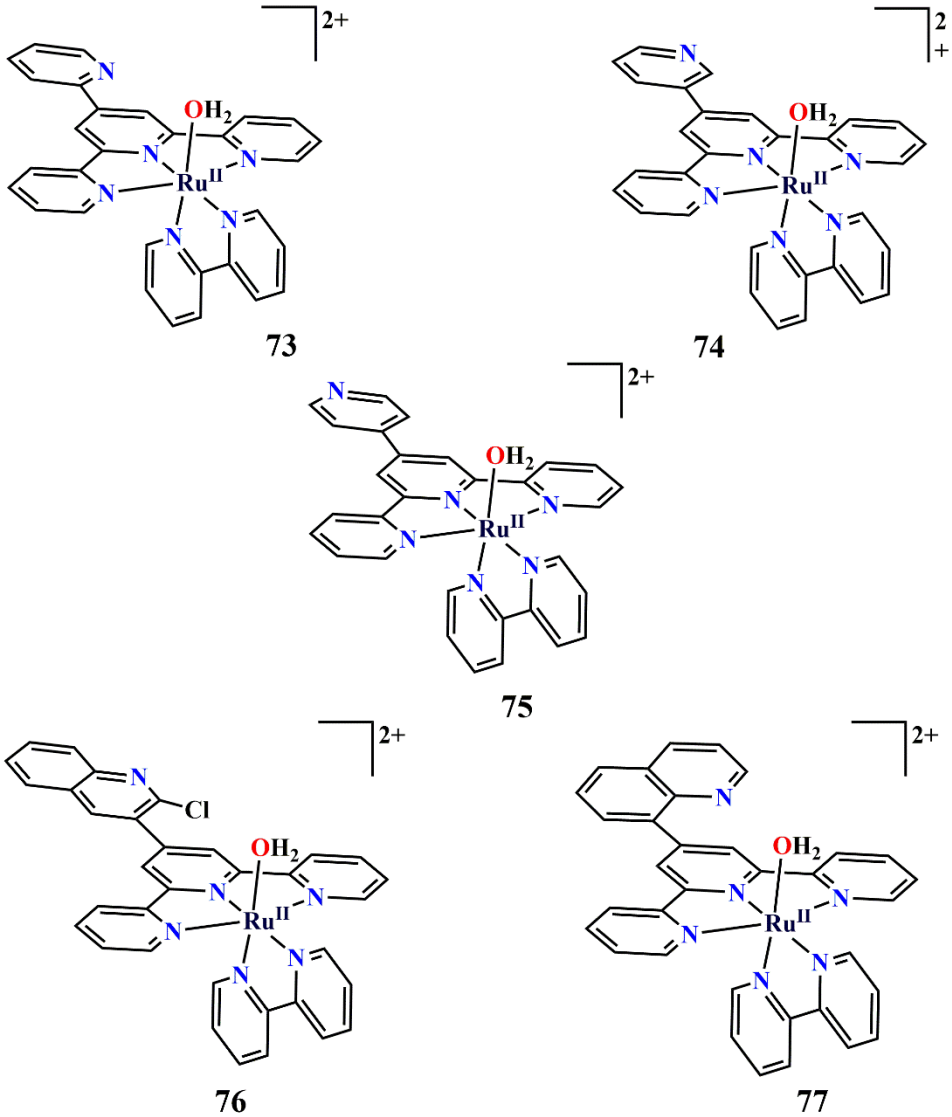

Figure 1.19. Molecular structure of WOCs (**73-77**).

1.8.2.2. Mononuclear Ruthenium Complexes Containing Anionic Ligands

The negatively charged ligand stabilizes the metal center in a high valent redox state and lowers the redox potential compared to the WOCs with neutral ligands. To overcome these limitations of Ru-based WOCs with neutral ligands, some negatively charged ligands were also employed for the chemical and photochemical water oxidation. Sun and group have studied the chemical water oxidation using CAN with [Ru (bda) L_2] (**78-80**) (where H_2bda =2,2'-bipyridine-6,6′-dicarboxylic acid, L = pyridazine, pyrimidine, and phthalazine). They observed that complex (**80**) with phthalazine axial ligand have the highest reaction rate of 286 s^{-1} and TON of 55400. [101]

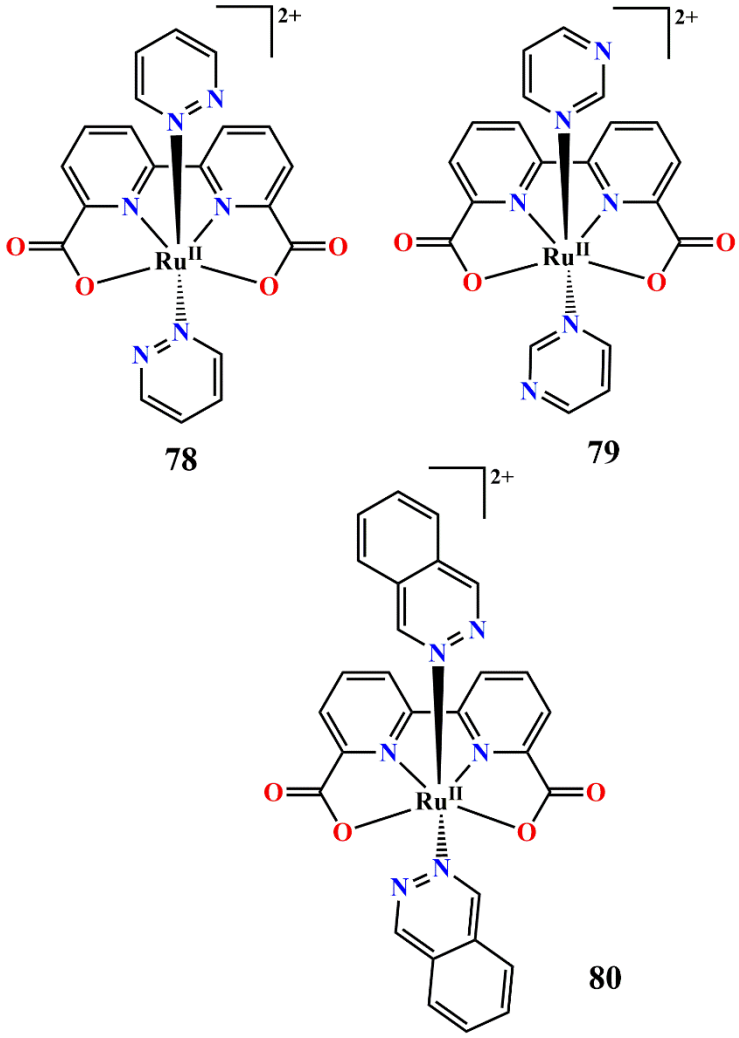

Figure 1.20. Molecular structure of WOCs (**78-80**).

Later Sun and the group have reported the water oxidation with [Ru (bda) $(isoq)_2$] (**81**) (where isoq = isoquinoline). The complex (**81**) catalyzes the water oxidation process efficiently with TOF of 300 s^{-1} due to the presence of a highly polarizable π –system of isoquinoline as axial ligand. They observed that water oxidation reaction proceeds with the formation of seven coordinated intermediate through the WNA mechanism. [102] Sun and group have synthesized $[Ru^{II}$ (bpc) (bpy) $OH_2]^+$ (**82**) (where bpc = 2,2′-bipyridine-6-carboxylate, bpy = 2,2′-bipyridine) and $[Ru^{II}(bpc)(pic)_3]^+$ (**83**) (where pic = 4-picoline) for catalysing water oxidation using Ce^{IV} at pH 1.0. They suggested that O-O bond formation occurs via the WNA mechanism with $[Ru^{V}=O]$ as an intermediate. The presence of negatively charged carboxylate ligand reduces the redox potential, lowers the overpotential for water oxidation, increases the rate of ligand exchange (H_2O / picoline), and thus facilitates the release of dioxygen from the ruthenium center. [103]

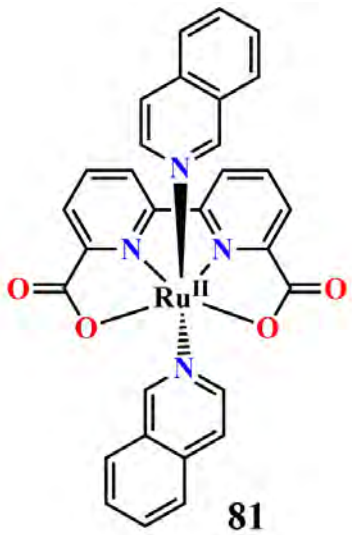

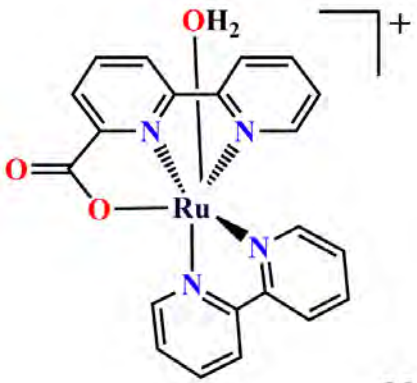

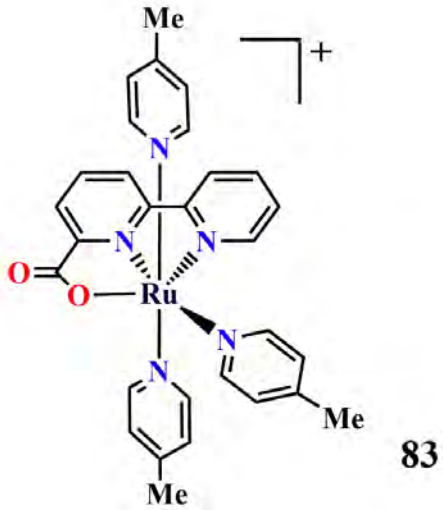

Figure 1.21. Molecular structure of WOCs (**81-83**).

Concepcion and group have reported a ruthenium complexes [$Ru^{II}(bpaH_2)(pic)_2$] (**84**) and [$Ru^{II}(bpaH_2)(isq)_2$] (**85**) (where $bpaH_2$ = 2,2'-bipyridine-6,6'-diphosphonic acid, pic = picoline and isoq = isoquinoline) with multifunctional bipyridyl diphosphonate ligands. Complexes (**84**) and (**85**) show Ce^{IV} driven water oxidation with TOF of 0.30 s^{-1} and 0.40 s^{-1} respectively. [104] Akermark and group have synthesized a [Ru (H_2pdca) $(pic)_3]^+$ (where H_2pdca = 2,6-pyridine-dicarboxamide) (**86**) complex showing chemical water oxidation using [Ru $(bpy)_3]^{3+}$ under mild conditions with TON of 400. [105] Mandal and group have reported the chemical water oxidation monitored by Ce^{IV} with [Ru(L)$(pic)_3$] (**87)** (H_3L = 2,2′-iminodibenzoic acid, pic = 4-methylpyridine). They proposed that negatively charged ligand stabilizes high valent oxidation state of ruthenium center and [Ru^{VII}=O] intermediate prompt the generation of molecular oxygen. [106]

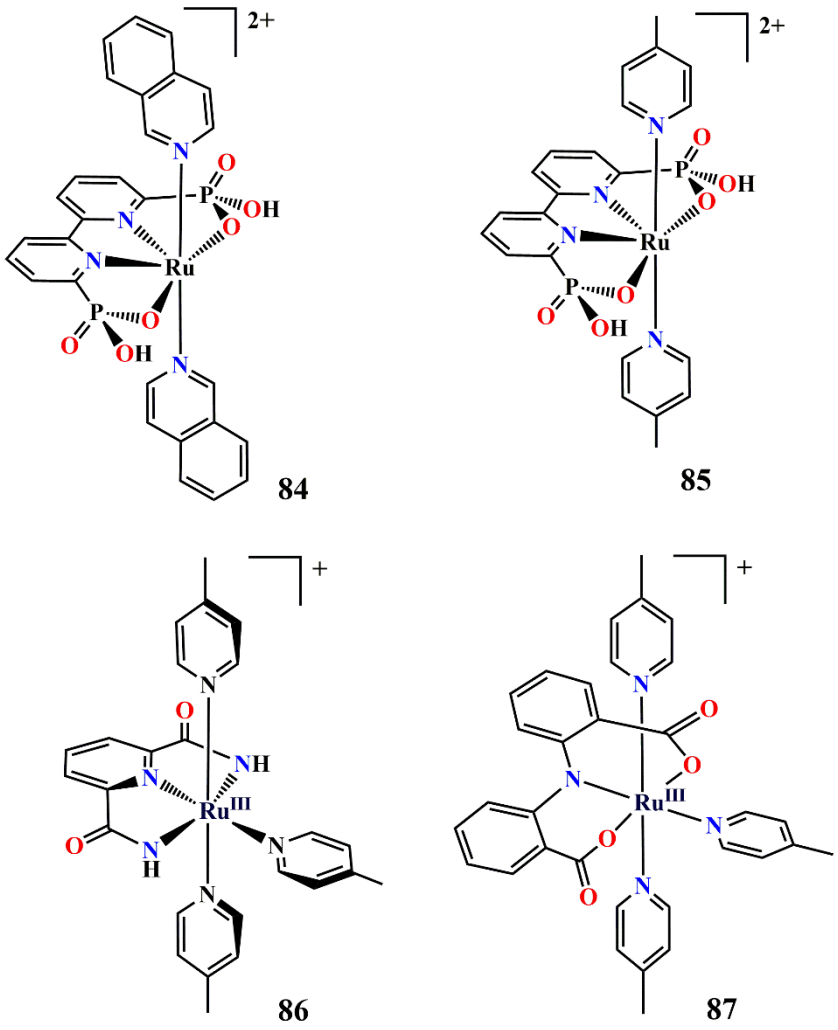

Figure 1.22. Molecular structure of WOCs (**84-87**)

1.8.2.3. Ruthenium based half – sandwich complexes

The organometallic complexes with polyhapto ligand bound with the metal center having other types of ligand are called half sandwich complexes. [107] Many iridium-based half sandwich complexes were reported and employed for the water oxidation catalysis. [108] A very few Ru-based half sandwich complexes were reported for the oxidation of water. The benzene, *p*-cymene, and Cp* as ligands provide strong-π donating ability and electron-rich environment to stabilize the high valent intermediates required to drive water oxidation. Groot and group have reported a series of mono site half sandwich ruthenium-based complexes $[(bpy)Ru(cy)(OH_2)]^{2+}$ (**88**) and studied their activity towards chemical and electrochemical water oxidation. They have also calculated the free energy difference from the electrochemical investigations. [109] Yu and group reported the Ru/Rh azo compounds $[\eta^5\text{-Cp*Rh(L)(MeOH)}]$ and $[\eta^6\text{-CyRu(L)}(H_2O)]$ (**89**) where L is an azo-dye compound of (p-(2-hydroxy-1-

naphthylazo)benzenesulfonic acid sodium salt) and observed that these complexes show good electronic properties for the electrochemical water oxidation. [110]

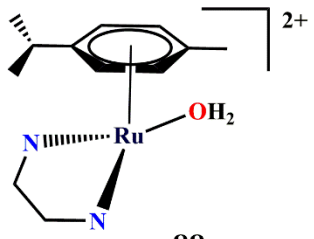

88

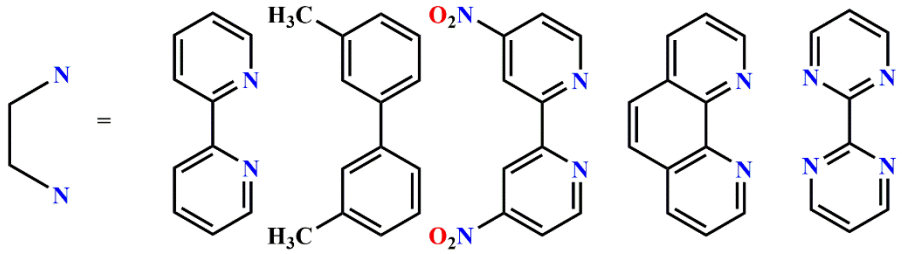

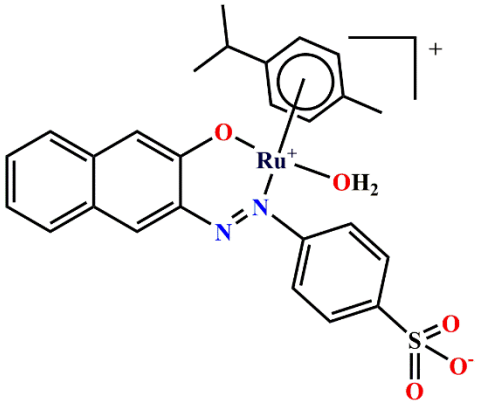

89

Figure 1.23. Molecular structure of Half-sandwich water oxidation complex (**88-89**).

1.9 Dehydrogenation of Formic acid

Hydrogen is one of the cleanest and sustainable alternative energy sources. Still, its storage is one of the major obstacles in using it directly as a possible energy source. The hydrogen can be stored either by physical method or by chemical methods. [111-116]. The physical method involves the storage of hydrogen in its molecular form in closed containers at high temperature and low pressure in cryo tanks or pressure tanks. The hydrogen is stored in a chemically bonded form in the chemical method rather than its molecular form. [117-121] Generally, hydrogen can be generated efficiently from suitable molecules such as methanol, methane, or formic acid (FA) having high hydrogen content via catalytic or non-catalytic processes. [122]

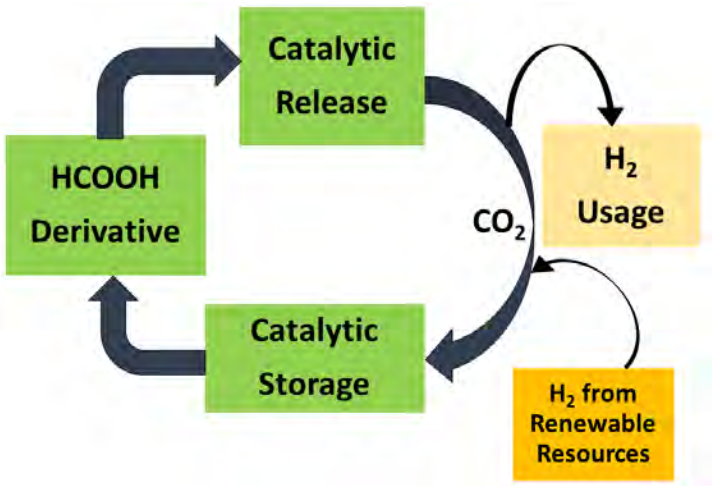

Scheme:1.2. Catalytic cycle for FA hydrogen storage and release

Formic acid is one of the most promising hydrogen storage materials. It contains 100 % hydrogen stored, which is available for catalytic storage compared to hydrogen stored in methanol (66 %) and methane (50 %). [123-124] The dehydrogenation of formic acid is a potential reaction for the production of H_2 that can be utilized as fuels in electricity production and green technologies with H_2O as by-products. The formic acid is kinetically stable, non-toxic, and easily stored in liquid form at room temperature. [125] The formic acid contains 4.4 weight % of hydrogen, being marginally below the desired target of the United States Department of Atomic Energy (DOE). The pure form of formic acid has 43.8 grams of H_2 per kilogram or 52 grams of H_2 per liter. Scheme 1.1 shows the formation and decomposition of formic acid. Dehydrogenation of formic acid into hydrogen and carbon dioxide is thermodynamically favorable with $\Delta G = -32.9\ \mathrm{kJ\ mol^{-1}}$ reaction at room temperature but kinetically blocked (equation (1.5)). [126-134]

$$\mathbf{HCOOH \rightarrow H_2 + CO_2 \quad \Delta G^{\circ} = -32.9\ kJ\ mol^{-1}} \qquad \mathbf{(1.5)}$$

$$\mathbf{HCOOH \rightarrow H_2O + CO\ \Delta G^{\circ} = -28.5\ kJ\ mol^{-1}} \qquad \mathbf{(1.6)}$$

The formation of H_2O and CO during the decomposition of formic acid is also thermodynamically feasible. The decomposition of formic acid without the formation of CO is essential for hydrogen storage by using formic acid. Therefore selective catalysis for the formation of hydrogen from the decomposition of formic acid and the conversion of CO_2 into formic acid or formate by a reduction in the presence of H_2 is necessary. Immense research has been done for the development of a suitable and efficient catalyst for the dehydrogenation reaction. Both homogeneous and heterogeneous catalysis has been studied for the decomposition of FA. The dehydrogenation reactions were investigated by studying the effect of different bases on the reaction rate, pH dependence of the dehydrogenation of FA,

temperature variation, and calculation of activation energy and use of appropriate solvent for facilitating the gas evolution. In recent years, many efficient homogeneous catalysts using noble metals like iridium, rhodium, platinum, palladium, and ruthenium have been studied to dehydrogenate formic acid. [135-138]

1.9.1. Mechanism of Dehydrogenation of formic acid

The general mechanism of dehydrogenation of formic acid involves the following steps:

- Deprotonation of formic acid either by itself or in the presence of a base to form formate
- Formation formate complex with the metal center
- $\beta -$ elimination of CO_2 and the formation of metal hydride complex.
- The final step involves the release of H_2 and CO_2.

The $\beta -$hydride elimination step is the rate-determining step for the dehydrogenation of the formic acid (Scheme 1.3.).

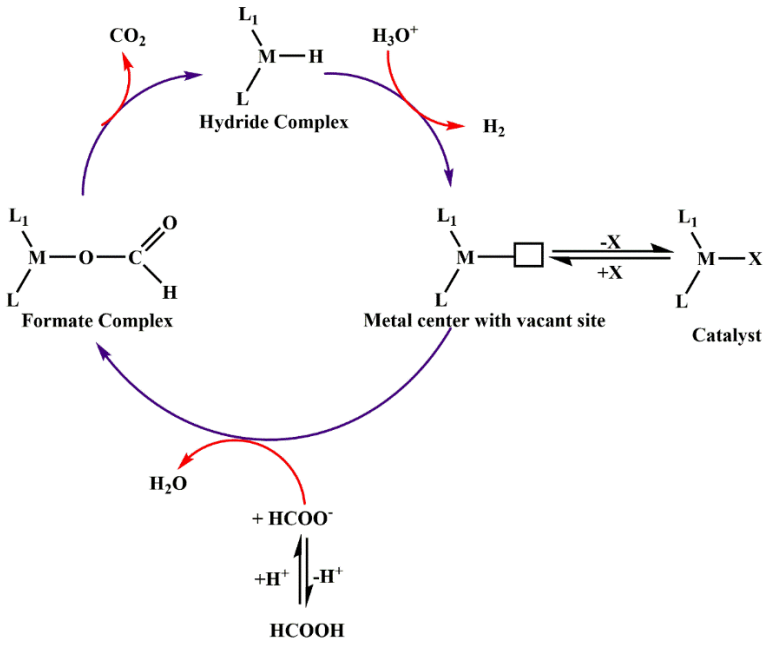

Scheme 1.3. A general mechanism for catalytic decomposition of formic acid

1.9.1. Mononuclear Ruthenium based catalysts for Dehydrogenation

In 1967 Coffey firstly discovered the decomposition of formic acid by utilizing soluble homogenous phosphine stabilized complexes of Pt, Pd, Ir, and Ru. Among all of these complexes, Ir and Ru complexes show the highest rate of selective decomposition of formic acid into H_2 and CO_2. [139]

Beller and group have studied the dehydrogenation of formic acid by utilizing commercially available [Ru $Cl_2(PPh_3)_3$] using 5HCOOH/2NEt_3 at room temperature. This catalyst gives high TOF of 417 and 302 h^{-1} after 2 and 3 hours, respectively, and 90 % conversion of formic acid after 3 hours. [140]

Laurenczy and group have reported the formation of H_2 and CO_2 from the decomposition of formic acid using commercially available $RuCl_3$ or $[Ru(H_2O)_6]^{2+}$ or $[Ru(H_2O)_6](tos)_2$ (tos=toluene-4-sulfonate) with highly soluble ligand in water TPPS (meta-trisulfonated triphenylphosphine). The complex $[Ru(H_2O)_6](tos)_2$ shows the production of H_2 and CO_2 with a TOF of 460 h^{-1} at 120 °C. [141] In 2008, Beller and group investigated the dehydrogenation of formic acid with Ru precursor catalysts such as [{$RuCl_2$(*p*-cymene)}$_2$] and [{$RuCl_2$(benzene)}$_2$] and [{RuI_2(*p*-cymene)}$_2$] with a variation of formic acid-ammine adducts. They have also studied the formation of H_2 and CO_2 with commercially available ruthenim phosphine complex [$RuCl_2(PPh_3)_3$]. They have performed the catalytic dehydrogenation by varying the phosphine ligand and observed that the [{$RuCl_2$(benzene)}$_2$] with dppe ligand (1,2-bis(diphenylphosphino)ethane) is the best catalytic system with the highest TON of TON = 1376 after 3 h. [142] Wills and group have studied the dehydrogenation of formic acid using [$RuCl_2(DMSO)_4$], [$RuCl_2(NH_3)_6$], or [$RuCl_3$] catalysts and observed that these complexes in the presence of FA/NEt_3 at 120 °C forms dimer [$Ru_2(HCO_2)_4(CO)_4$] during the reaction and they have isolated the stable complex after addition of triphenyl phosphine and proposed the mechanism shown in the scheme. This dimeric complex [$Ru_2(HCO_2)_4(CO)_4$] offers a TOF of 1.78 x 10^4 h^{-1} for the decomposition of the formic acid. [143] Fukuzumi and group reported a tunneling effect on the production of hydrogen through dehydrogenation of formic acid (HCOOH, HCOOD, DCOOD) using heterodinuclear iridium-ruthenium complex [Ir^{III}(Cp*)(H_2O)(bpm)$Ru^{II}(bpy)_2](SO_4)_2$ (**90**) where= η5-pentamethylcyclopentadienyl, bpm = 2,2′-bipyrimidine, bpy = 2,2′-bipyridine). They have studied the dependence of pH on dehydrogenation and observed that the catalyst shows the highest TOF of 426 h^{-1} at pH 3.8 using HCOONa as a base. The activation energy for the decomposition of FA was found to be 17 kcal mol^{-1}. They observed that the kinetic isotopic effect (KIE) increases with increasing pH, and by kinetic studies, they found that the rate-determining step is the production of hydrogen by the reaction of hydride complex [Ir^{III}(Cp*)(H)(bpm)$Ru^{II}(bpy)_2]^{3+}$ produced via β – elimination with H_3O^+. [144]

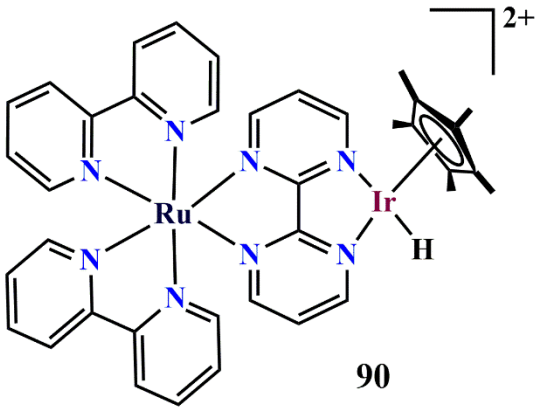

Figure 1.24. Molecular structure of the complex (**90**).

Laurenczy and group have proposed the Ru (II) catalyzed dehydrogenation reaction using a series of oligocationic aminomethyl-substituted triarylphosphines (**91-96**) as precatalyst in an aqueous solution under mild conditions. The tricationic triarylphosphine (**93a**) shows the highest TOF of 1950 h^{-1} and TON of 10000 using sodium formate as a base. These positively charged phosphine ligands show a higher rate of dehydrogenation than the negatively charged ligands under the same conditions. [145]

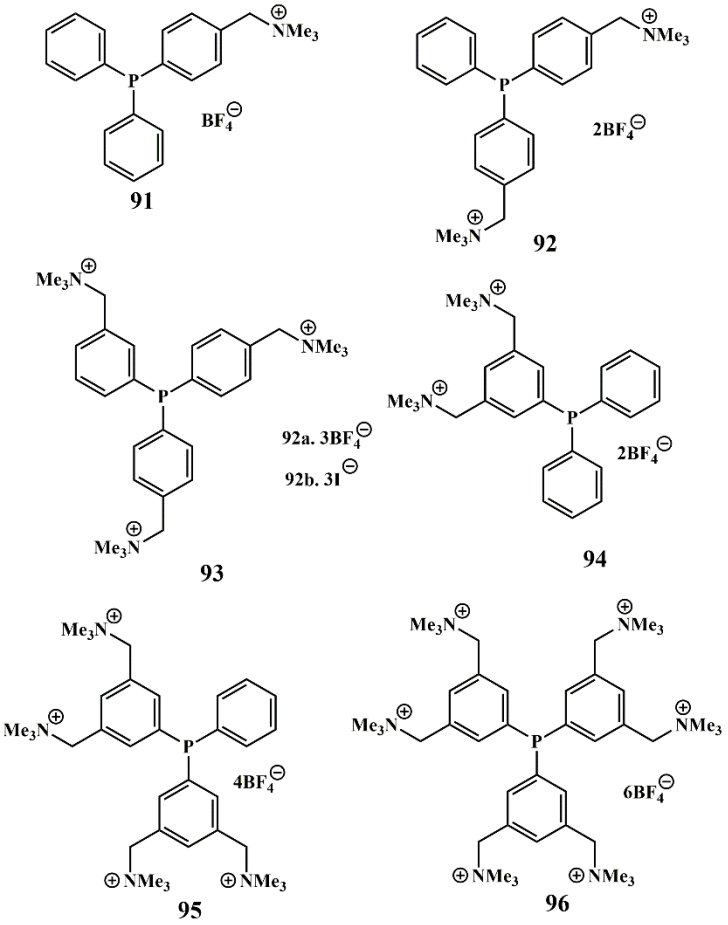

Figure 1.25. Series of oligocationic aminomethyl-substituted triarylphosphines (**91-96**) For catalyzing dehydrogenation coupled with Ru (II) metal center.

Huang and group have synthesized the unsymmetrically protonated PN^3 pincer type complex with ruthenium (**97-99**). The metal center binds with one nitrogen and two phosphorus atom and is employed for selective extraction dehydrogenation of the formic acid. The dehydrogenation reaction starts with the protonation of dearomatized ligand, and during this process oxidation state of the Ru center doesn't change, and this prevents the decarbonylation process and thus makes the dehydrogenation reaction selective without the formation of CO. This complex shows TON over one million with a long time of 150 hours. [146] Huang and group have synthesized the ruthenium complex containing 2,2′-biimidazoline ligand with $[Ru(p\text{-cymene})Cl_2]_2$ (**100**). This complex shows a selective dehydrogenation in water medium by using HCOOH/HCOONa (5:1) with TON and TOF of 350000 and 12000 h^{-1} respectively at 90 °C. The activation energy was 23 ± 0.5 kcal/mol by measuring the initial temperatures from 60 °C to 90 °C. The kinetic isotopic effect (KIE) studies proposed that cleavage of formyl C-H bond during decarboxylation is the rate-determining step (RDS) in the catalytic cycle. [147] Sasson and group have reported the dehydrogenation of formic acid by using precursor complex $[\{RuCl_2(p\text{-cymene})\}_2]$ with phosphine ligand DPPM (DPPM = Bis(diphenylphosphino)methane) as catalyst (**101**) upon pretreatment in DMF solvent before addition of formic acid. The TOF >600 h^{-1} and TON>530 were observed under mild conditions at 40 °C for catalyzing dehydrogenation of FA. [148]

The mechanistic study of complex (**101**) was further studied through DFT calculation, where they revealed the decomposition of formate species during the catalytic reaction.

Awasthi and group have utilized the Ru-arene-based catalysts (**102-104**) containing *N*-substituted iminopyridine ligands with hydrazine at 80 °C with a temperature variation, with different bases, and with different solvents or solvent combination. They have observed the highest catalytic activity with a TON of 37.0 and TOF of 58.5 h^{-1} in THF/methanol mixture as a solvent in the presence of KO^tBu (potassium tert-butoxide) as a base with ruthenium arene catalyst containing *N*-hydroxy iminopyridine as a ligand for the dehydrogenation of hydrazine. [149]

Beller and group have compared the catalytic activity of non-methylated and methylated ruthenium PNP-pincer type complexes $Ru(H)(Cl)(CO)(HN\{CH_2CH_2P(iPr)_2\}_2)$ (**105**) and $Ru(H)(Cl)(CO)(CH_3N\{CH_2CH_2P(iPr)_2\}_2)$ (**106**) respectively towards selective dehydrogenation of formic acid at different pH values. They suggested that these complexes achieved the highest catalytic performance at acidic pH 4.5. The *N*- methylated complex b shows the most increased catalytic activity towards dehydrogenation of formic acid compared to non-methylated complex. [150]

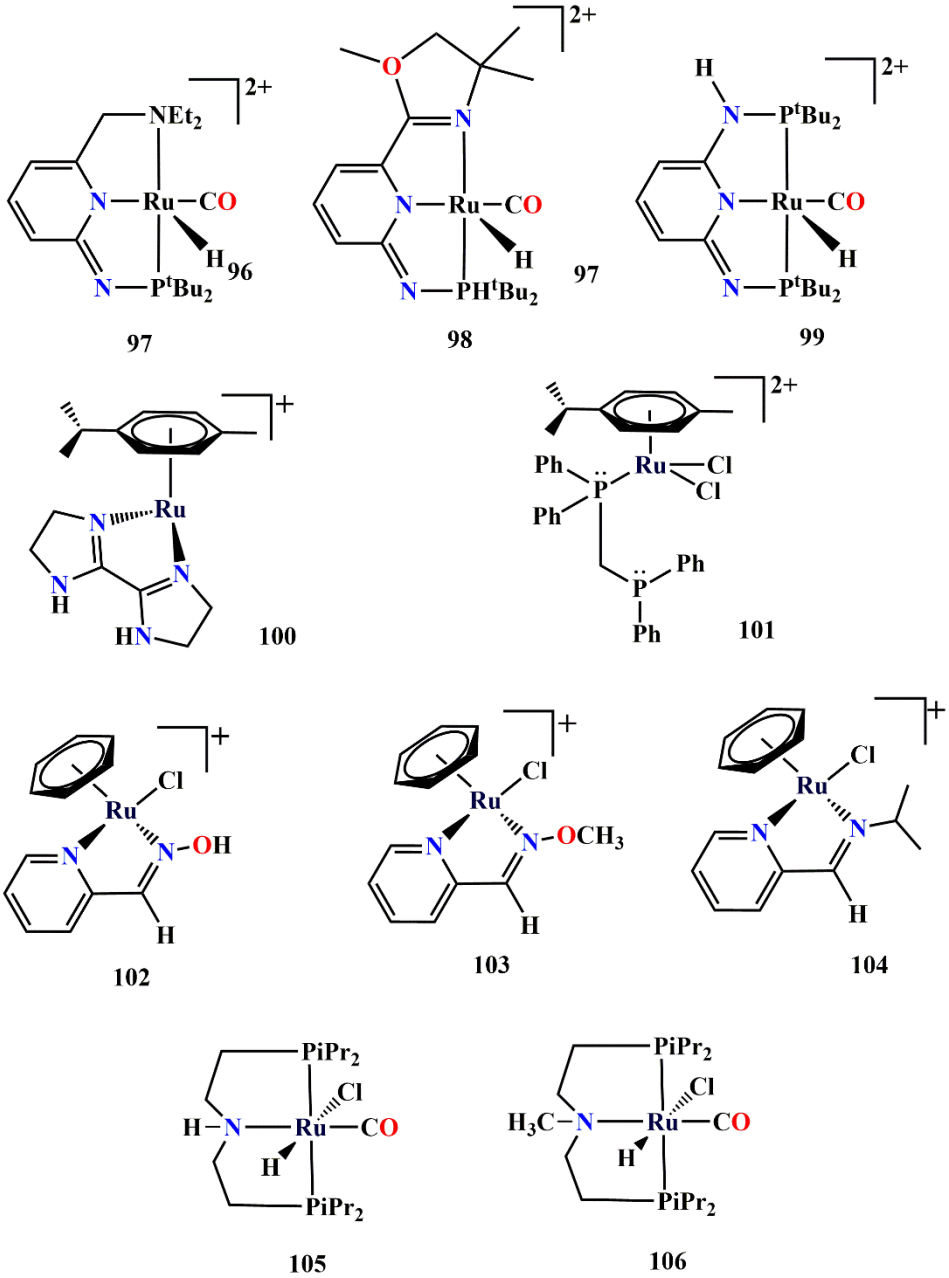

Figure 1.26. Molecular structure of Dehydrogenation catalysts (**97-106**).

Singh and co-workers reported several Ru-arene complexes (**107-113**) as catalysts for the dehydrogenation of formic acid in water at 90°C without any base addition. The catalytic system of (**110**) comprising of 8-(*N*-methylamino)quinoline ligand scaffold resulted in the highest TOF and TON value of 940 h^{-1} and 2248, respectively. The high catalytic behavior of (**110**) was ascribed to the presence of -NH moiety and its high stability in the water medium. They also provided strong evidence for the formation of several intermediates during the catalytic process by complex (**110**) using various spectroscopic techniques and kinetic studies.[151]

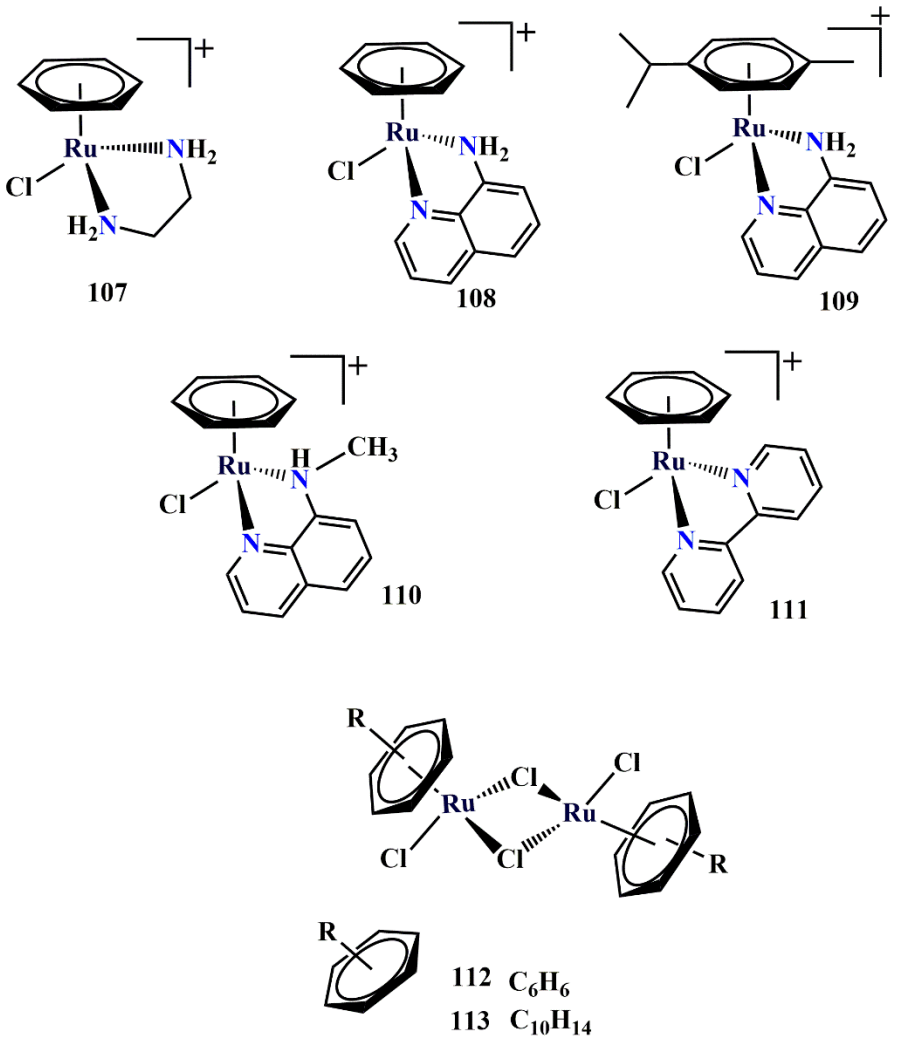

Figure 1.27. Molecular structure of Dehydrogenation catalysts (**107-113**).

Later on, the same group examined another series of pyridine-base Ru-arene complexes (**114-122**), which catalyzed the system generating dihydrogen from formic acid in an aqueous medium. The TOF and TON value for complex (**114**) was highest among all the complexes, and the value obtained was 1548 h^{-1} and 6050, respectively. Additionally, complex (**114**) could also produce dihydrogen from formaldehyde without any additives or base. The participation of oxygen atoms during the catalytic cycle in one of the protonation deprotonation processes is held responsible for displaying high catalytic activity by complex (**114**). NMR and mass spectroscopy techniques were employed for identifying the intermediate species involved during the dehydrogenation process. [152]

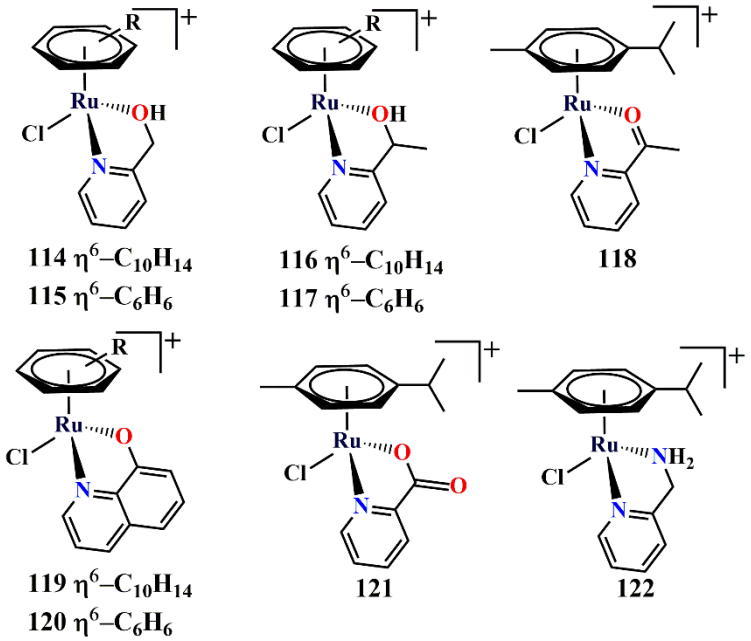

Figure 1.28. Molecular structure of Dehydrogenation catalysts (**114-122**).

Recently, they investigated a family of half-sandwich Ru-arene complexes coordinated to bis-imidazole methane-based ligand frameworks (**123-132**) for the dehydrogenation of formic acid in water. The Ru complex (**124**) linked with 4-methoxy phenyl substituted bis-imidazole methane ligand displayed high stability in the reaction medium and high catalytic activities yielding TOF and TON of 1545 h^{-1} and 8830, respectively. By utilizing several spectroscopic techniques and controlled experiments, they were able to identify the important intermediates responsible for driving the catalytic processes. They concluded regarding the role of Ru-formato in forming Ru-hydride species, which ultimately generates the dihydrogen as the product. [153]

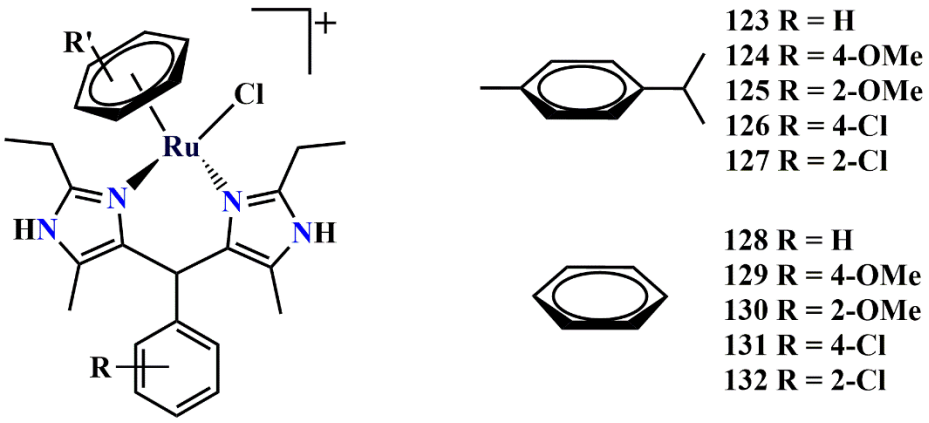

Figure 1.29. Molecular structure of Dehydrogenation catalysts (**123-132**).

Selective dehydrogenation of a Ru-based cyclometalated complex (**133**) was studied by Beller and co-workers. Notably, a TON of >10000 was obtained without a trace of CO formation throughout the dehydrogenation process. They even revealed that on increasing the temperature, the amount of H_2 and CO_2 evolved was found to be higher along with the liberation of CO. [154]

Louloudi and group examined a Ru-phosphine complex $RuP(CH_2CH_2PPh_2)_3$, (**134**) for dihydrogen evolution through dehydrogenation of formic acid. They operated the system in the atmospheric condition that yielded a TOF of 5670 h^{-1} and TON of 81090. Employing various spectroscopic techniques, they confirmed the conversion of Ru(III) to Ru(II) species to be vital for driving the catalytic process.[155]

Kar and the group prepared a Ru 9H-acridine pincer catalyst (**135**), which they successfully employed for dihydrogen liberation from HCOOH in the absence of any additives and solvents. A high TON of 1,701,150 was obtained. They operated the system for a total of 19 days in which dehydrogenation of 1.5 kgs of HCOOH led to a TON of >802,000 with a minimal libration of CO (<20 ppm). Further, the catalytic reaction was operated in a closed system to liberate the high pressure of 100 H_2 and CO_2 mixture bars. Additionally, the catalytic route involving the *cis* accessible bonding position was the major pathway for driving the system.[156]

Polydentate tripodal-based Ru complex $[Ru(\kappa^3\text{-triphos})(MeCN)_3](OTf)_2$, (**136**) designed and synthesized by Mellone and group displayed high catalytic activity with a TON of 8000 when performed with the addition of $OctNMe_2$ at 80°C for 14 h. The mechanistic studies monitored through spectroscopic techniques demonstrated the stabilization of short-lived Ru-hydrido intermediate species by NP_3 ligand scaffolds.[157]

Gonsalvi and the group utilized $RuCl_3.3H_2O$ as a precursor with several alkyl-biaryl, aryl-biaryl, and sulphonated phosphines derivatives as dehydrogenation catalyst in an aqueous medium at a temperature of 90°C without the presence of any additives. The formation of Ru-hydrido intermediates during the dehydrogenation process was also detected via high-pressure NMR. Moreover, in different sets of the experiment, another precursor complex $[Ru(\eta^6\text{-}C_6H_6)Cl_2]_2$ was also used, which, unlike the previous precursor, proved to be efficient for dehydrogenation.[158]

A binuclear Ru catalyst $[Ru_2(\mu\text{-}CO)(CO)_4(\mu\text{-}dppm)_2]$ (where dppm = $Ph_2PCH_2PPh_2$), (**137**) was also examined by Gao and group in acetone medium at a low temperature of 20°C affording turn over rate of 70 h^{-1}. They compared the catalytic activity with its mononuclear analogue $[RuHBr(CO)(PEt_2Ph)_3]$ under the refluxing CH_3COOH condition and found the turnover rate to be 4 h^{-1}. [159]

They further investigated the mechanistic route of complex 1 and identified the intermediate species taking part in the catalytic process to be ruthenium hydrido, ruthenium formato, and ruthenium unsaturated species.[160]

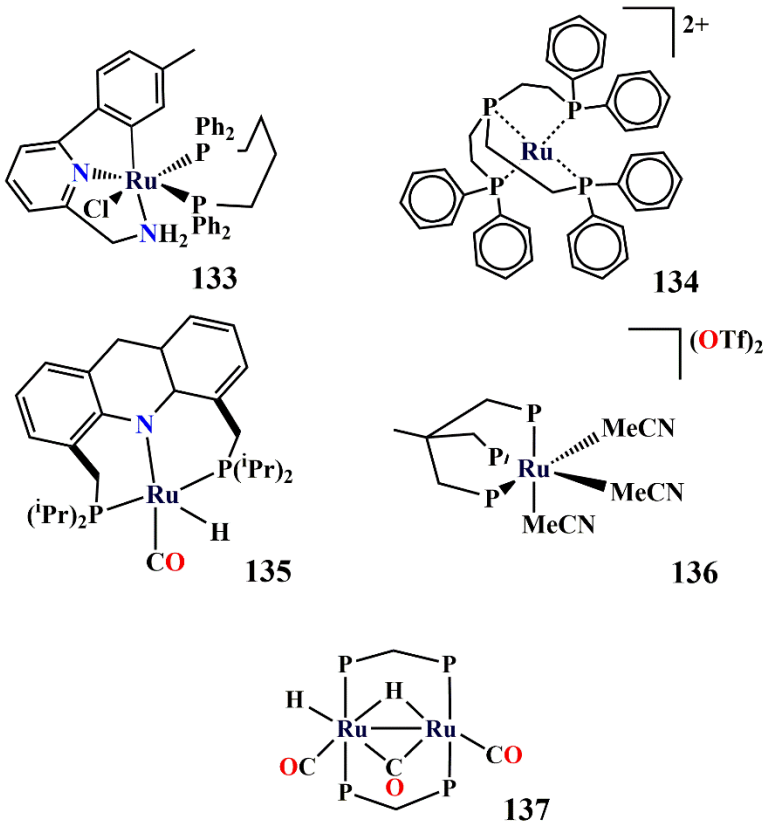

Figure 1.30. Molecular structure of Dehydrogenation catalysts (**133-137**).

1.9.2. Mononuclear Iridium based catalysts for Dehydrogenation

The organometallic iridium complexes were also employed for the dehydrogenation of the formic acid. Himeda and the group have reported a half sandwich Ir complex [Cp*Ir (OH_2) (LH_2)] (SO_4) (**138**) (where LH_2 = 4,4'-dihydroxy-2,2'-bipyridine) for the dehydrogenation of formic acid with the highest TOF of 2400 h^{-1}. [161] Himeda and the group have studied the dehydrogenation of formic acid with [Ir(Cp*)(TH4BPM)(H_2O)]SO_4 (**139**) (where TH4BPM: 2,2',6,6'-tetrahydroxyl-4,4'-bipyrimidine) complex. The complex (**139**) shows a high TOF of 39500 h^{-1} at 80 °C in a 1 M aqueous solution of HCOOH / HCOONa. [162] Li and group have synthesized a Ir complexes [Cp*Ir(L1)Cl]Cl (**140a**) (L1=2,2'-bi-2-imidazoline) and [Ir(L2)Cp*Cl_2]$_2$ (**140b**) (where L2 = 2,2'-bi-1,4,5,6-tetrahydropyrimidine (L2). The complex (**140a**) shows a TOF of 487500 h^{-1} at 90 °C, and the complex (**140b**) shows a TON of 2400000 at 80 °C for the dehydrogenation of the formic acid into H_2 and CO_2. [163]

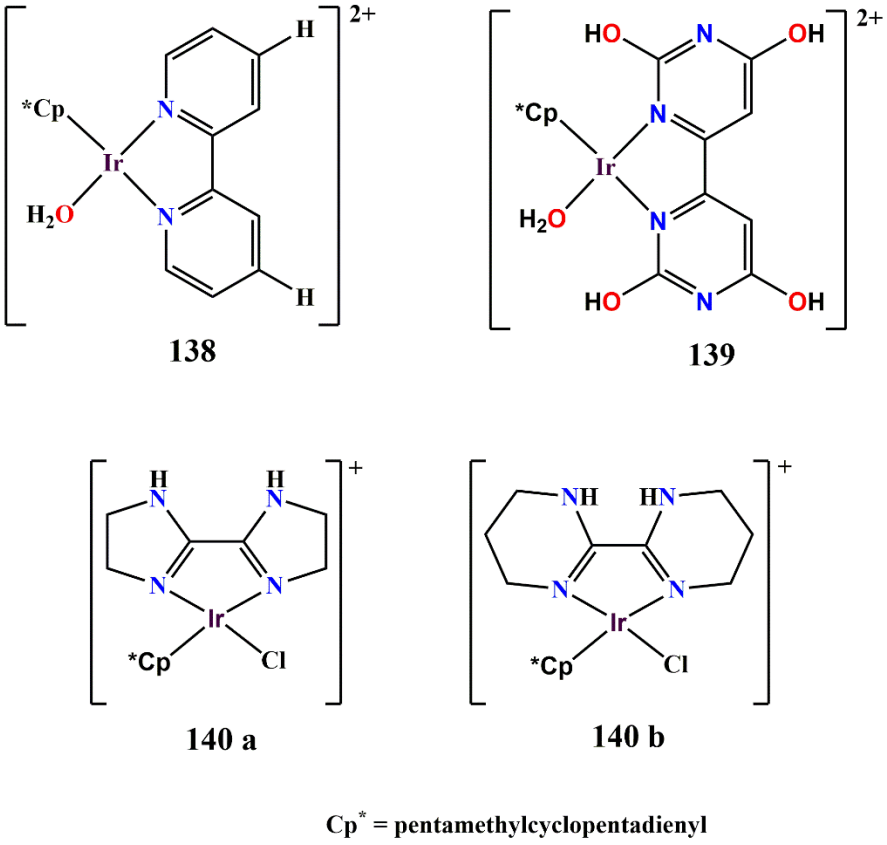

Figure 1.31. Molecular structure of Dehydrogenation catalysts (**138-140**).

Himeda and group have synthesized a group of Ir complexes with a bidentate pyridyl-imidazoline ligand (**141a-141f**). These complexes show dehydrogenation of formic acid without any additives at highly acidic conditions of pH 1.7. [164]

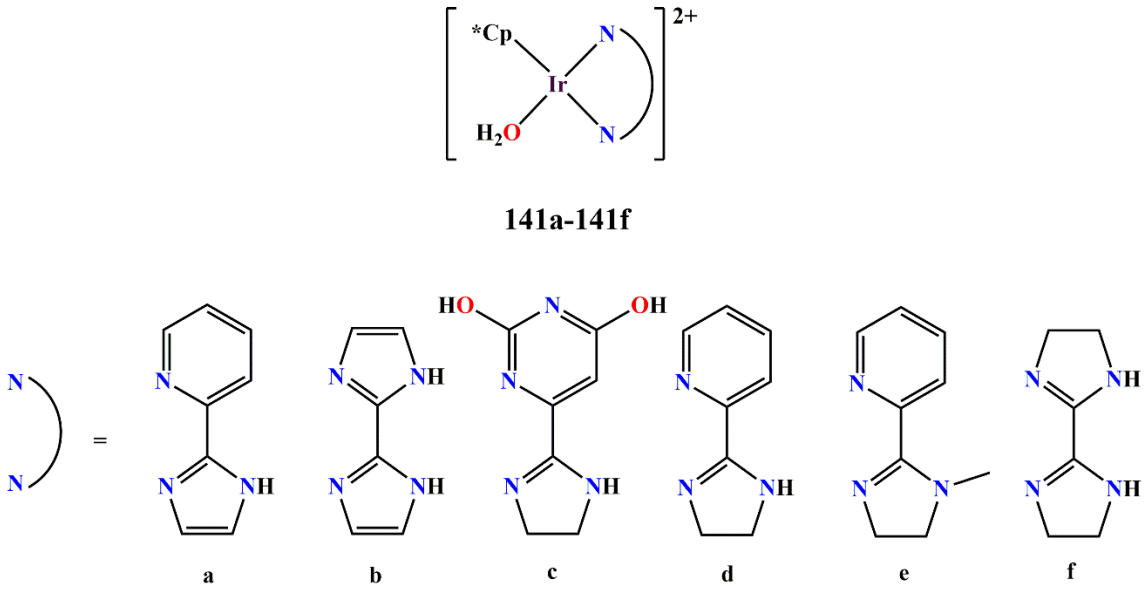

Figure 1.32. Molecular structure of Dehydrogenation catalysts (**141a-141f**).

Kawanami and group have studied the dehydrogenation of formic acid and kinetic isotope effects for reaction mechanism with water-soluble Ir complex bound with 4,4'-dihydroxy-2,2'-bipyridine ligand (**142**). [165] Ertem, Fujita, and Himeda group have reported Cp*Ir catalysts with picolinamidate ligands (**143**) having strong electron-donating properties through coordinated anionic nitrogen atom and localization of electron density. The complex (**143**) shows the highest TOF of 118000 h^{-1} for the decomposition of formic acid. [166]

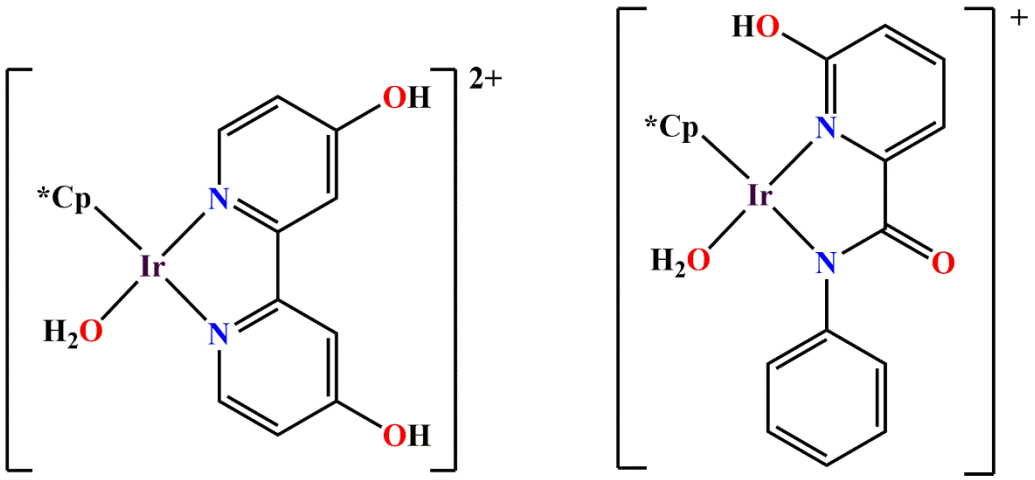

142 **143**

Figure 1.33. Molecular structure of Dehydrogenation catalysts (**142-143**).

1.10. Current Challenges

The water oxidation and dehydrogenation of formic acid processes contribute towards the generation of cleanest, sustainable, and environmentally friendly renewable energy sources. The water oxidation and dehydrogenation catalyzed by using transition metal complexes is one of the most effective methods for producing oxygen and hydrogen. Researchers face many challenges in designing efficient catalysts that should be overcome as soon as possible. The challenges are as follows:

- Stable in higher oxidation state
    - The metal center for designing the catalyst must undergo proton-coupled electron transfer to form high valent intermediates for the water oxidation.
- High turnover number and turnover frequency
    - The catalyst must undergo water oxidation with high TON and TOF to produce oxygen by chemical and electrochemical water oxidation. The catalyst must show dehydrogenation with high TON and TOF at various temperatures.
- Low overpotential

- The complex must show water oxidation with low overpotential and high faradaic efficiency.

- Recyclability
  - The robustness of the catalyst is also important for catalyzing the water oxidation, and dehydrogenation and catalyst must undergo catalysis for many folds for the production of O_2 and H_2 with high TON.
- Solubility in aqueous medium
  - The WOCs must be soluble in an aqueous medium as all the oxidizing agents for water oxidation have high solubility and stability for catalyzing the reaction. The dehydrogenation of formic acid is also favorable in an aqueous medium.

1.11. Aim of the Thesis

The present thesis outlined the synthesis and characterization of different types of ruthenium-based catalysts and their catalytic activity towards the water oxidation and dehydrogenation of the formic acid. The water oxidation was studied chemically in the presence of ceric ammonium nitrate as an oxidant and electrochemically in a three-electrode system. The dehydrogenation of formic acid was investigated in deionized water in sodium formate as a base. The aim of the thesis is as follows:

- To synthesize the catalyst having high stability in acidic and harsh conditions to prevent catalyst degradation during the reaction.
- To synthesize the catalyst with high TON and TOF for water oxidation and dehydrogenation.
- To study the water oxidation with low overpotential and high faradaic efficiency
- To observe the effect of substituting electron-withdrawing and electron-donating groups on ligand scaffolds to enhance the catalytic rate.

1.12. References

1. Schneider, S. H. Abrupt non-linear climate change, irreversibility and surprise, *Global Environmental Change.* **2004**, *14* (3), 245–258.
2. Solomona, S.; Plattnerb, G.-K.; Knuttic, R.; Friedlingstein, P. Irreversible climate change due to carbon dioxide emissions, *Proc. Natl. Acad. Sci. U.S.A.* **2009**, *106* (6), 1704-1709.
3. Chadwick, R.; Good, P.; Martin, G.; Rowell, D. P. Large rainfall changes consistently projected over substantial areas of tropical land, *Nat. Clim. Change,* **2016**, *6* (2016), 177-

181.

4. Reid, W. V.; Ali, M. K.; Field, C. B. The future of bioenergy, *Glob Chang Biol.* **2020**, *26* (1), 274–286.
5. Lewis, N. S.; Nocera, D. G. Powering the planet: Chemical challenges in solar energy utilization, *Proc. Natl. Acad. Sci. U.S.A.*, **2006**, *103* (43) 15729-15735.
6. Azad, A. K.; Rasul, M. G.; Islam, R.; Shishir, I. R. Analysis of wind energy prospect for power generation by three Weibull distribution methods, *Energy Procedia*, **2015**, *75* (75), 722-727.
7. Kumar, A.; Khan, M. Z. U.; Pandey, B. Wind Energy: A Review Paper, *Gyancity J. Eng. Technol.* **2018**, *4* (2), 29-37.
8. Hydroelectric Power, U.S. Department of the Interior Bureau of Reclamation Power Resources Office. **2005**.
9. Killingtveit, A. Managing Global Warming, *An Interface of Technology and Human Issues*. **2019**, 265-315.
10. Omer, A. M. Biomass energy resources utilisation and waste management, *J. Agric. Biotech. Sustain. Dev.* **2011**, *3* (8), 149-170.
11. Saibi, H.; Finsterle, S.; Bertani, R.; Nishijima, J. Geothermal Energy, *J. Kauffman, K.-M. Lee (eds.), Handbook of Sustainable Engineering* **2013**.
12. Kutscher, C. F. The Status and future of geothermal electric power, Presented at the American Solar Energy Society (ASES) Conference, Madison, Wisconsin, June 16-21, **2000**, 1-6.
13. Barbier, E. R. Nature and technology of geothermal energy: A review, *Renew. Sustain. Energy Rev.* **1997**, *1* (1-2), 1-69.
14. Eldin, A. A. H.; Refaey, M.; Farghly, A. A Review on Photovoltaic Solar Energy Technology and its Efficiency, *Conference: 17th International Middle-East Power System Conference (MEPCON'15*) At: Mansoura University, Egypt, **2015**.
15. Blankenship, R. E. Origin and early evolution of photosynthesis. *Photosynth Res.* **1992**, *33*, 91-111.
16. Voloshin, R. A.; Rodionova, M. V.; Zharmukhamedov, S. K.; Hou, H. J. M.; Shen, J. -R.; Allakhverdiev, S. I. Components of Natural Photosynthetic Apparatus in Solar Cells, Applied Photosynthesis - New Progress, *Mohammad Mahdi Najafpour, IntechOpen*, **2016**.
17. Janssen, P. J. D.; Lambreva, M. D.; Plumere, N.; Bartolucci, C. Antonacci, A.;

Buonasera, K.; Frese, R. N.; Scognamiglio, V.; Rea, G. Photosynthesis at the forefront of a sustainable life, *Front Chem.* **2014**, *2* (2) 36-58.

18. Blankenship, R. E. The Basic Principles of PhotosyntheticEnergy Storage, *Molecular Mechanisms of Photosynthesis* **2002**.
19. Krewald, V.; Retegan, M.; Pantazis, D. A. Principles of Natural Photosynthesis, *Top Curr. Chem*. **2015**, 371.
20. Zhang, J. Z.; Reisner, E. Advancing photosystem II photoelectrochemistry for semi-artificial photosynthesis, *Nat. Rev. Chem.* **2020,** *4* (2020), 6-21.
21. Umena, Y.; Kawakami, K.; Shen, J. -R.; Kamiya, N. Crystal structure of oxygen-evolving photosystem II at a resolution of 1.9 A, *Nature*,**2011**, *473* (2011), 55-60.
22. Askerka, M.; Brudvig, G. W.; Batista, V. S. The O_2-Evolving Complex of Photosystem II: Recent Insights from Quantum Mechanics/Molecular Mechanics (QM/MM), Extended X-ray Absorption Fine Structure (EXAFS), and Femtosecond X-ray Crystallography Data, *Acc. Chem. Res.* **2017**, *50* (1), 41-48.
23. Zhang, B.; Sun, L. Why nature chose the Mn_4CaO_5 cluster as water-splitting catalyst in photosystem II: a new hypothesis for the mechanism of O-O bond formation, *Dalton Trans.*, **2018**, *47* (41), 14381-14387.
24. Lubitz, W.; Chrysina, M.; Cox, N. Water oxidation in photosystem II, *Photosynth. Res.* **2019**, *142* (2019), 105-125.
25. Pantazis, D. A.; Cox, N.; Lubitz, W.; Neese, F. Oxygen-evolving Photosystem II, *Encyclopedia of Inorganic and Bioinorganic Chemistry*, **2014**.
26. Ye, S.; Ding, C.; Li, C. Artificial photosynthesis systems for catalytic water oxidation, *Adv. Inorg. Chem.* **2019**, *74*, 3-59.
27. Gust, D.; Moore, T. A.; Moore, A. L. Artificial photosynthesis, *Theor. Exp. Plant Physiol.*, **2013**, *25* (3), 182-185.
28. Solar fuels and Artificial Photosynthesis, Science and Innovation to change our future options, *Royal Society Chemistry*, **2012**.
29. Purchase, R.; Groot, H. D.; Harmsen, P. Artificial photosynthesis for the conversion of sunlight to fuel, Biosolar cell, Netherlands, **2015**, 1-53.
30. Benniston, A. C.; Harriman, A. Artificial photosynthesis, *Mater.Today*, **2008**, *11* (12), 26-34.
31. Dau, H.; Fujita, E.; Sun, L. Artificial Photosynthesis: Beyond Mimicking Nature, *ChemSusChem* **2017**, *10* (22), 1-9.
32. Dogutan, D. K.; Nocera, D. G. Artificial Photosynthesis at Efficiencies Greatly

Exceeding That of Natural Photosynthesis, *Acc. Chem. Res.* **2019**, *52* (11), 3143-3148.

33. Muckerman, J. T.; Fujita, E. Artificial Photosynthesis, *Chemical Evolution II: From the Origins of Life to Modern Society* **2009**, Chapter 15, 283-312.
34. Kuang, T. A breakthrough of artificial photosynthesis. *National Science Review*, **2016**, *3*, 2-4.
35. Su, J.; Vayssieres, L. A Place in the Sun for Artificial Photosynthesis? *ACS Energy Lett.* **2016**, *1* (1), 121-135.
36. Ye, S.; Ding, C.; Chen, R.; Fan, F.; Fu, P.; Yin, H.; Wang, X.; Wang, Z.; Du, P.; Li, C. Mimicking the Key Functions of Photosystem II in Artificial Photosynthesis for Photoelectrocatalytic Water Splitting, *J. Am. Chem. Soc.* **2018**, *140* (9), 3250-3256.
37. Zhang, B.; Sun, L. Artificial photosynthesis: opportunities and challenges of molecular catalysts, *Chem. Soc. Rev.*, **2019**, *48* (7), 2216-2264.
38. Cogdell, R. J.; Brotosudarmo, T. H.; Gardiner, A. T.; Sanchez, P. M.; Cronin, L. Artificial photosynthesis – solar fuels: current status and future prospects, *Biofuels*, **2010**, *1* (6), 861-876.
39. Whang, D. R.; Apaydin, D. H. Artificial Photosynthesis: Learning from Nature, *Chemphotochem*, **2017**, *2* (3), 148-160.
40. Hou, H. J. M.; Allakhverdiev, S. I.; Najafpour, M.; Govindjee, M. Current challenges in photosynthesis: From natural to artificial, Frontiers Media SA, **2014**.
41. Barber, J.; Tran, P. D. From natural to artificial photosynthesis, *J. R. Soc. Interface.* **2012**, *10* (81) 20120984-20120984.
42. Tong, L.; Thummel, R. P.; Mononuclear ruthenium polypyridine complexes that catalyze water oxidation, *Chem. Sci.*, **2016**, *7* (11), 6591-6603.
43. Bofill, R.; Antón, J. G.; Escriche, L.; Sala, X. Chemical, Electrochemical and Photochemical Molecular Water Oxidation Catalysts, *J. Photochem. Photobiol. B*, **2015**, *152*, 71-81.
44. Puntoriero, A.; Sartorel, M.; Orlandi, G.; Ganga, L.; Serroni, S.; Bonchio, M.; Scandolac, F.; Campagnaa, S. Photoinduced water oxidation using dendrimeric Ru(II) complexes as photosensitizers, *Coord. Chem. Rev.* **2011**, *255* (21-22), 2594-2601.
45. Nair, V.; Deepth, A. Cerium (IV) Ammonium Nitrates-A Versatile Single-Electron Oxidant, *Chem. Rev.* **2007**, *107* (5), 1862-1891.
46. Wadsworth, E.; Duke, F. R.; Goetz, C. A. Present Status of Cerium(IV)-Cerium(III) Potentials, *Anal. Chem.* **1957**, *29* (12), 1824-1825.
47. Ohno, A. I.-; Tsushima, S.; Hennig, C.; Yaita, T.; Bernhard, G. Dinuclear complexes of

tetravalent cerium in an aqueous perchloric acid solution, *Dalton Trans.*, **2012**, *41* (24), 7190-7192.

48. Hetterscheid, D. G. H.; Reek, J. N. H. Periodate as an Oxidant for Catalytic Water Oxidation: Oxidation via Electron Transfer or O-Atom Transfer?, *Eur. J. Inorg. Chem.* **2014**, *2014* (4) 742-749.
49. Parent, A. R.; Crabtree, R. H.; Brudvig, G. W. Comparison of primary oxidants for water-oxidation catalysis, *Chem. Soc. Rev.*, **2013**, *42* (6), 2247-2252.
50. Andralojc, A. L.; Polyansky, D. E.; Wang, C. -H.; Wang, W.-H.; Himeda, Y.; Fujita, E. Efficient water oxidation with organometallic iridium complexes as precatalysts, *Phys. Chem. Chem. Phys.*, **2014**, *16* (24), 11976-11987.
51. Liu, Y.; Xiang, R.; Du, X.; Ding, Y.; Ma, B. An efficient oxygen evolving catalyst based on a μ-O diiron coordination complex, *Chem. Commun.*, **2014**, *50* (84), 12779-12782.
52. Mills, A.; Hazafy, D.; Elouali, S.; O'Rourke, C. Periodate-an alternative oxidant for testing potential water oxidation catalysts, *J. Mater. Chem. A*, **2016**, *4* (8), 2863-2872.
53. Ghosh, P. K.; Brunschwig, B. S.; Chou, M.; Creutz, C.; Sutin, N.; Thermal and Light-Induced Reduction of Ru(bpy)$_3^{3+}$ in Aqueous Solution, *J. Am. Chem. Soc.* **1984**, *106* (17), 4772-4183.
54. Das, B.; Orthaber, A.; Ott, S.; Thapper, A. Iron Pentapyridyl Complexes as Molecular Water Oxidation Catalysts: Strong Influence of a Chloride Ligand and pH in Altering the Mechanism, *ChemSusChem.* **2016**, *9* (10), 1178-1186.
55. Chen, G.; Chen, L.; Ng, S.-M.; Man, W.-L.; Lau, T.-C. Chemical and Visible-Light-Driven Water Oxidation by Iron Complexes at pH 7-9: Evidence for Dual-Active Intermediates in Iron-Catalyzed Water Oxidation, *Angew. Chem. Int. Ed.* **2013**, *52* (6), 1789-1791.
56. Hong, D.; Mandal, S.; Yamada, Y.; Lee, Y.-M.; Nam, W.; Llobet, A.; Fukuzumi, S. Water Oxidation Catalysis with Nonheme Iron Complexes under Acidic and Basic Conditions: Homogeneous or Heterogeneous?, *Inorg. Chem.* **2013**, *52* (16), 9522-9531.
57. Gersten, S. W.; Samuels, G. J.; Meyer, T. J. Catalytic Oxidation of Water by an Oxo-Bridged Ruthenium Dimer. *J. Am. Chem. Soc.* **1982**, *104* (14), 4030-4032.
58. Gilbert, J. A.; Eggleston, D. S.; Murphy, Jr. W. R.; Geselowitz, D. A.; Gersten, S. W.; Hodgson, D. J.; Meyer, T. J. Structure and redox properties of the water-oxidation catalyst $[(bpy)_2(OH_2)RuORu(OH_2)(bpy)2]^{4+}$. *J. Am. Chem. Soc.* **1985**, *107* (13), 3855-3864.
59. Collin, J. P.; Sauvage, J. P.; Synthesis and Study of Mononuclear Ruthenium(I1)

Complexes of Sterically Hindering Diimine Chelates. Implications for the Catalytic Oxidation of Water to Molecular Oxygen. *Inorg. Chem.* **1986**, *25* (2), 135-141.

60. Doppelt, P.; Meyer, T. J. Synthesis and Redox Properties of the Unsymmetrical, Oxo-Bridged Complex $[(bpy)_2(py)Ru^{III}ORu^{III}(H_2O)(bpy)_2]^{4+}$. *Inorg. Chem.* **1987**, *26* (13), 2027-2034.
61. Ramaraj, R.; Kira, A.; Kaneko, M. Electrochemistry and stability studies of oxo-bridged dinuclear ruthenium(III) complexes for water oxidation. *J. Chem. Soc., Faraday Trans. 1*, **1986**, *82* (11), 3515-3524.
62. Ramaraj, R.; Kira, A.; Kaneko, M. Oxygen evolution by water oxidation with polynuclear ruthenium complexes. *J. Chem. Soc., Faraday Trans. 1*, **1987**, *83* (5), 1539-1551.
63. Sens, C.; Romero, I.; Rodrıguez, M.; Llobet, A.; Parella, T.; Buchholz, J. B. A New Ru Complex Capable of Catalytically Oxidizing Water to Molecular Dioxygen. *J. Am. Chem. Soc.* **2004**, *126* (25), 7798-7799.
64. Bozoglian, F.; Romain, S.; Ertem, M. Z.; Todorova, T. K.; Sens, C.; Mola, J.; Rodrıguez, M.; Romero, I.; Buchholz, J. B.-; Fontrodona, X.; Cramer, C. J.; Gagliardi, L.; Llobet, A. The Ru-Hbpp Water Oxidation Catalyst. *J. Am. Chem. Soc.* **2009**, *131* (42), 15176-15187.
65. Neudeck, S.; Maji, S.; Lopez, I.; Meyer, S.; Meyer, F.; Llobet, A.; New Powerful and Oxidatively Rugged Dinuclear Ru Water Oxidation Catalyst: Control of Mechanistic Pathways by Tailored Ligand Design. *J. Am. Chem. Soc.* **2014**, *136* (1), 24-27.
66. Deng, Z.; Tseng, H.-W.; Zong, R.; Wang, D.; Thummel, R.; Preparation and Study of a Family of Dinuclear Ru(II) Complexes That Catalyze the Decomposition of Water. *Inorg. Chem.* **2008**, *47* (6), 1835-1848.
67. Xu, Y.; Akermark, T.; Gyollai, V.; Zou, D.; Eriksson, L.; Duan, L.; Zhang, R.; Akermark, B.; Sun, L. A New Dinuclear Ruthenium Complex as an Efficient Water Oxidation Catalyst. *Inorg. Chem.* **2009**, *48* (7), 2717-2719.
68. Xu, Y.; Fischer, A.; Duan, L.; Tong, L.; Gabrielsson, E.; Akermark, B.; Sun, L. Chemical and Light-Driven Oxidation of Water Catalyzed by an Efficient Dinuclear Ruthenium Complex. *Angew. Chem. Int. Ed.* **2010**, *49* (47), 8934-8937.
69. Wada, T.; Tsuge, K.; Tanaka, K. Electrochemical Oxidation of Water to Dioxygen Catalyzed by the Oxidized Form of the Bis(ruthenium-hydroxo) Complex in H_2O. *Angew. Chem.* **2000**, *39* (8), 1479-1482.
70. Wada, T.; Tsuge, K.; Tanaka, K. Syntheses and Redox Properties of Bis(hydroxoruthenium) Complexes with Quinone and Bipyridine Ligands. Water-

Oxidation Catalysis. *Inorg. Chem.* **2001**, *40* (2), 329-337.

71. Roeser, S.; Bozoglian, F.; Richmond, C. J.; League, A. B.; Ertem, M. Z.; Francàs, L.; Miro, P.; Buchholz, J. B.-; Cramer, C. J.; Llobet, A. Water Oxidation Catalysis with Ligand Substituted Ru-bpp-type Complexes. *Catal. Sci. Technol.* **2016**, *6* (13), 5088-5101.
72. Sander, A. C.; Maji, S.; Francàs, L.; Böhnisch, T.; Dechert, S.; Llobet, A.; Meyer, F. Highly Efficient Binuclear Ruthenium Catalyst for Water Oxidation. *ChemSusChem*, **2015**, *8* (10), 1697-1702.
73. Matias, T. A.; Mangoni, A. P.; Toma, S. H.; Rein, F. N.; Rocha, R.C.; Toma, H. E.; Araki, K. Catalytic Water-Oxidation Activity of a Weakly Coupled Binuclear Ruthenium Polypyridyl Complex. *Eur. J. Inorg. Chem.* **2016**, *2016* (36), 5547-5556.
74. Matias, T. A.; Parussulo, A. L. A.; Benavides, P. A.; Guimaraes, R. R.; Dourado, A. H. B.; Nakamura, M.; de Torresi, S. C.; Bertotti, M.; Araki, K. Polymeric Binuclear Ruthenium Complex as Efficient Electrocatalyst for Oxygen Evolution Reaction. *Electrochimica Acta*, 2018, *283*, 18-26.
75. Matias, T. A.; Rein, F. N.; Rocha, R. C.; Formiga, A. L. B.; Toma, H. E.; Araki, K. Effects of a strong π-accepting ancillary ligand on the water oxidation activity of weakly coupled binuclear ruthenium catalysts. *Dalton Trans.* **2019**, *48* (9), 3009-3017.
76. Kikuchi, T.; Tanaka, K.; Mechanistic Approaches to Molecular Catalysts for Water Oxidation. *Eur. J. Inorg. Chem.* **2013**, *2013* (4), 607-618.
77. Hetterscheid, D. G. H.; Reek, J. N. H.; Mononuclear Water Oxidation Catalysts. *Angew. Chem. Int. Ed.* **2012**, *51* (39), 2-10.
78. Cao, R.; Lai, W.; Du, P. Catalytic water oxidation at single metal sites. *Energy Environ. Sci.* **2012**, *5* (8), 8134-8157.
79. Wasylenko, D. J.; Palmer, R. D.; Berlinguette, C. P. Homogeneous water oxidation catalysts containing a single metal site. *Chem. Commun.* **2013**, *49* (3), 218-227.
80. Zong, R.; Thummel, R. P.; A New Family of Ru Complexes for Water Oxidation. *J. Am. Chem. Soc.* **2005**, *127* (37), 12802-12803.
81. Concepcion, J. J.; Jurss, J. W.; Templeton, J. L.; Meyer, T. J. One Site is Enough. Catalytic Water Oxidation by $[Ru(tpy)(bpm)(OH_2)]^{2+}$ and $[Ru(tpy)(bpz)(OH_2)]^{2+}$. *J. Am. Chem. Soc.* **2008**, *130* (49), 16462-16463.
82. Concepcion, J. J.; Tsai, M.-K.; Muckerman, J. T.; Meyer, T. J. Mechanism of Water Oxidation by Single-Site Ruthenium Complex Catalysts. *J. Am. Chem. Soc.* **2010**, *132* (5), 1545-1557.

83. Concepcion, J. J.; Jurss, J. W.; Norris, M. R.; Chen, Z.; Templeton, J. L.; Meyer, T. J. Catalytic Water Oxidation by Single-Site Ruthenium Catalysts. *Inorg. Chem.* **2010**, *49* (4), 1277-1279.

84. Zhang, G.; Zong, R.; Tseng, H.-W.; Thummel, R. P.; Ru(II) Complexes of Tetradentate Ligands Related to 2,9-Di(pyrid-2′-yl)-1,10-phenanthroline. *Inorg. Chem.* **2008**, *47* (3), 990-998.

85. Tseng, H.-W.; Zong, R.; Muckerman, J. T.; Thummel, R. Mononuclear Ruthenium(II) Complexes That Catalyze Water Oxidation. *Inorg. Chem.* **2008**, *47* (24), 11763-11773.

86. Badiei, Y. M.; Polyansky, D. E.; Muckerman, J. T.; Szalda, D. J.; Haberdar, R.; Zong, R.; Thummel, R. P.; Fujita, E. Water Oxidation with Mononuclear Ruthenium(II) Polypyridine Complexes Involving a Direct RuIV=O Pathway in Neutral and Alkaline Media. *Inorg. Chem.* **2013**, *52* (15), 8845-8850.

87. Wasylenko, D. J.; Ganesamoorthy, C.; Koivisto, B. D.; Henderson, M. A.; Berlinguette, C. P. Insight into Water Oxidation by Mononuclear Polypyridyl Ru Catalysts, *Inorg. Chem.* **2010**, *49* (5), 2202-2209.

88. Wasylenko, D. J.; Ganesamoorthy, C.; Henderson, M. A.; Koivisto, B. D.; Osthoff, H. D.; Berlinguette, C. P. Electronic Modification of the $[RuII(tpy)(bpy)(OH_2)]^{2}$+ Scaffold: Effects on Catalytic Water Oxidation. *J. Am. Chem. Soc.* **2010,** *132* (45), 16094-16106.

89. Kaveevivitchai, N.; Zong, R.; Tseng, H.-W.; Chitta, R.; Thummel, R. P. Further Observations on Water Oxidation Catalyzed by Mononuclear Ru(II) Complexes. *Inorg. Chem.* **2012**, *51* (5), 2930-2939.

90. Yagi, M.; Tajima, S.; Komi, M.; Yamazaki, H. Highly active and tunable catalysts for O_2 evolution from water based on mononuclear ruthenium(II) monoaquo complexes. *Dalton Trans.*, **2011**, *40* (15), 3802-3804.

91. Yamazaki, H.; Hakamata, T.; Komi, M.; Yagi, M. Stoichiometric Photoisomerization of Mononuclear Ruthenium(II) Monoaquo Complexes Controlling Redox Properties and Water Oxidation Catalysis. *J. Am. Chem. Soc.* **2011**, *133* (23), 8846-8849.

92. Boyer, J. L.; Polyansky, D. E.; Szalda, D. J.; Zong, R.; Thummel, R. P.; Fujita, E. Effects of a Proximal Base on Water Oxidation and Proton Reduction Catalyzed by Geometric Isomers of $[Ru(tpy)(pynap)(OH_2)]^{2+}$. *Angew. Chem.* **2011**, *123* (52), 12808 -12812.

93. Maji, S.; Lopez, I.; Bozoglian, F.; Buchholz, J. B.-; Llobet, A. Mononuclear Ruthenium-Water Oxidation Catalysts: Discerning between Electronic and Hydrogen-Bonding Effects. *Inorg. Chem.* **2013**, *52* (7), 3591-3593.

94. Marelius, D. C.; Bhagan, S.; Charboneau, D. J.; Schroeder, K. M.; Kamdar, J. M.;. McGettigan, A. R; Freeman, B. J.; Moore, C. E.; Rheingold, A. L.; Cooksy, A. L.; D. K. Smith, Paul, J. J.; Papish, E.T.; Grotjahn, D. B. How Do Proximal Hydroxy or Methoxy Groups on the Bidentate Ligand Affect [(2,2';6',2"-Terpyridine)Ru- (N,N)X] Water-Oxidation Catalysts? Synthesis, Characterization, and Reactivity at Acidic and Near Neutral pH. *Eur. J. Inorg. Chem.* **2014**, *2014* (4), 676-689.

95. Yoshida, M.; Kondo, M.; Torii, S.; Sakai, K.; Masaoka, S. Oxygen Evolution Catalyzed by a Mononuclear Ruthenium Complex Bearing Pendant SO_3^- Groups. *Angew. Chem. Int. Ed.* **2015**, *54* (27), 7981-7984.

96. Wada, T.; Hiraide, T.; Miyazato, Y. Water Oxidation Catalyzed by a Ruthenium Complex with a Ru-C Bond. *ChemistrySelect* **2016**, *1* (12), 3045-3048.

97. Mane, V. S.; Kumbhar, A. S.; Thummel, R. P. A ruthenium water oxidation catalyst containing a bipyridine glycoluril ligand. *Dalton Trans.*, **2017**, *46* (38), 12901-12907.

98. Patel, J.; Majee, K.; Ahmad, E.; Das, B.; Padhi, S. K. Effect of Pyridyl Substitution on Chemical and Photochemical Water Oxidation by $[Ru(terpyridine)(bipyridine)(OH_2)]^{2+}$, Scaffolds. *Eur. J. Inorg. Chem.* **2017**, *2017* (1), 160-171.

99. Patel, J.; Majee, K.; Ahmad, E.; Vatsa, A.; Das, B.; Padhi, S. K. Electronic Effect on Catalytic Water Oxidation by Single Site $[Ru(QCl–tpy)(bpy)(OH_2)]^{2+}$ Catalyst. *ChemistrySelect* **2017**, *2* (1), 123-129.

100. Patel, J.; Majee, K.; Raj, M.; Vatsa, A.; Rai, S.; Padhi, S. K. Effect of Quinoline Substitution on Water Oxidation by $[Ru\ (Ql\text{-}tpy)(bpy)(OH_2)](PF_6)_2$. *ChemistrySelect* **2017**, *2* (10), 3053-3059.

101. Duan, L.; Araujo, C. M.; Ahlquist, M. S. G.; Sun, L. Highly efficient and robust molecular ruthenium catalysts for water oxidation. *Proc. Natl. Acad. Sci. U S A.* **2012,** *109* (39), 15584-15588.

102. Duan, L.; Bozoglian, F.; Mandal, S.; Stewart, B.; Privalov, T.; Llobet, A.; Sun, L. A molecular ruthenium catalyst with water-oxidation activity comparable to that of photosystem II. *Nature Chem,* **2012**, *4*, 418-423.

103. Tong, L.; Inge, A. K.; Duan, L.; Wang, L.; Zou, X.; Sun, L. Catalytic Water Oxidation by Mononuclear Ru Complexes with an Anionic Ancillary Ligand. *Inorg. Chem.* **2013**, *52* (5), 2505-2518.

104. Xie, Y.; Shaffer, D. W.; Andralojc, A. L.; Szalda, D. J.; Concepcion, J. J.; Water Oxidation by Ruthenium Complexes Incorporating Multifunctional Bipyridyl Diphosphonate Ligands. *Angew. Chem. Int. Ed.* **2016**, *55* (28), 1-6.

105. Rabten, W.; Akermark, T.; Kärkäs, M. D.; Chen, J.; Sun, P.; Andersson, G.; Akermark, B. A ruthenium water oxidation catalyst based on a carboxamide ligand. *Dalton Trans.*, **2016**, *45 (8)*, 3272-3276.
106. Kundu, A.; Dey, S. K.; Dey, S.; Anoop, A.; Mandal, S. Mononuclear Ruthenium-Based Water Oxidation Catalyst Supported by Anionic, Redox-Non-Innocent Ligand: Heterometallic O-O Bond Formation via Radical Coupling Pathway. *Inorg. Chem.* **2020**, *59* (2), 1461-1470.
107. Elschenbroich, C. *Organometallics*. Weinheim: Wiley-VCH, **2006**.
108. Blakemore, J. D.; Schley, N. D.; Balcells, D.; Hull, J. F.; Olack, G. W.; Incarvito, C. D.; Eisenstein, O.; Brudvig, G. W.; Crabtree, R. H. Half-Sandwich Iridium Complexes for Homogeneous Water-Oxidation Catalysis. *J. Am. Chem. Soc.* **2010**, *132* (45), 16017–16029.
109. Joya, K. S.; de Groot, H. J. M. Mono Ruthenium Catalysts for Water Splitting **2011**. In *Eur. Conf. Chem. Life Sci., 4th* (pp. 51-54).
110. Yu, W. -B.; He, Q.-Y.; Shi, H. –T.; Jia, J. –Y.; Wei, X. Azo-conjugated half-sandwich Rh/Ru complexes for homogeneous water-oxidation catalysis. *Dalton Trans.* **2014**, *43* (17), 6561–6566.
111. Schlapbach, L.; Züttel, A. Hydrogen-storage materials for mobile applications. *Nature* **2001**, *414*, 353-358.
112. Graetz, J. New approaches to hydrogen storage. *Chem. So. Rev.*, **2009**, *38* (1), 73-82.
113. Demirci, U. B.; Miele, P. Chemical hydrogenstorage: 'material' gravimetric capacity *versus* 'system' gravimetric capacity. *Energy Environ. Sci.*, **2011**, *4* (9), 3334-3341.
114. Makowski, P.; Thomas, A.; Kuhn, P.; Goettmann, F. Organic materials for hydrogenstorage applications: from physisorption on organic solids to chemisorption in organic molecules. *Energy Environ. Sci.* **2009**, *2* (5), 480-490.
115. Grasemann, M.;' Laurenczy, G. Formic acid as a hydrogen source-recent developments and future trends. *Energy Environ. Sci.*, **2012**, *5* (8), 8171-8181.
116. Fujita, E.; Muckerman, J. T.; Himeda, Y. Interconversion of CO_2 and formic acid by bio-inspired Ir complexes with pendent bases. *Biochimica et Biophysica Acta* **2013**, *1827*, 1031-1038.
117. Julien, P.; Bergthorson, J, M. Enabling the metal fuel economy: green recycling of metal fuels. *Sustainable Energy Fuels*, **2017**, *1* (3), 615-625.
118. Lan, R.; Irvine, J. T. S.; Tao, S. Ammonia and related chemicals as potential indirect hydrogen storage materials. *Int. J. Hydrog. Energy*, **2012**, *37* (2), 1482-1494.

119. Huang, Z.; Autrey, T. Boron-nitrogen-hydrogen (BNH) compounds: recent developments in hydrogen storage, applications in hydrogenation and catalysis, and new syntheses. *Energy Environ. Sci.*, **2012**, *5* (11), 9257-9268.

120. Crabtree, R. H. An Organometallic Future in Green and Energy Chemistry?. *Organometallics*. **2011**, *30* (1), 17-19.

121. Mandal, T. K.; Gregory, D. H. Hydrogen storage materials: present scenarios and future directions. *Annu. Rep. Prog. Chem., Sect. A: Inorg. Chem.* **2009**, *105*, 21-54.

122. Boddien, A.; Loges, B.; Gartner, F.; Torborg, C.; Fumino, K.; Junge, H.; Ludwig, R.; Beller, M. Iron-Catalyzed Hydrogen Production from Formic Acid. *J. Am. Chem. Soc.* **2010**, *132* (26), 8924-8934.

123. Loges, B.; Boddien, A.; Gartner, F.; Junge, H.; Beller, M. Catalytic Generation of Hydrogen from Formic acid and its Derivatives: Useful Hydrogen Storage Materials. *Top Catal.* **2010**, *53*, 902-914.

124. Nielsen, M.; Alberico, E.; Baumann, W.; Drexler, H. –J.; Junge, H.; Gladiali, S.; Beller, M. Low-temperature aqueous-phase methanol dehydrogenation to hydrogen and carbon dioxide. *Nature*, **2013**, *495*, 85-89.

125. Guan, C.; Pan, Y.; Zhang, T.; Ajithaa, M. J.; Huanga, K.-W. An update on Formic Acid Dehydrogenation by Homogeneous Catalysis. *Chem. Asian J.* **2020**, *15* (7), 937-946.

126. Eppinger, J.; Huang, K.-W. Formic Acid as a Hydrogen Energy Carrier. *ACS Energy Lett.* **2017**, *2* (1), 188-195.

127. Moriarty, P.; Honnery, D. A hydrogen standard for future energy accounting. *Int. J. Hydrog. Energy* **2010**, *35* (22), 12374-12380.

128. Turner, J. A. Sustainable Hydrogen Production. *Science*. **2004**, *304* (5686), 972-974.

129. Armaroli, N.; Balzani, V. The Hydrogen Issue. *ChemSusChem.* **2011**, *4* (1), 21-36.

130. Felderhoff, M.; C. Weidenthaler, R.von Helmolt, U. Eberle, Hydrogen storage: the remaining scientific and technological challenges. *Phys. Chem. Chem. Phys.* **2007**, 9 (21), 2643-2653.

131. Suh, M. P.; Park, H. J.; Prasad, T. K.; Lim, D.-W. Hydrogen Storage in Metal-Organic Frameworks. *Chem. Rev.* **2012**, *112* (2), 782-835.

132. Mura, M. G.; Luca, L. D.; Giacomelli, G.; Porcheddu, A. Formic Acid: A Promising Bio-Renewable Feedstock for Fine Chemicals. A. *Adv. Synth. Catal*, **2012**, *354* (17), 3180-3186.

133. Hietala, J.; Vuori, A.; Johnsson, P.; Pollari, I.; Reutemann, W.; Kieczka, H. Formic acid. *Ullmann's Encyclopedia of Industrial Chemistry*, doi.org/10.1002/14356007.a12-

013.pub3.

134. Mellmann, D.; Sponholz, P.; Junge, H.; Beller, M. Formic acid as a hydrogen storage material -development of homogeneous catalysts for selective hydrogen release. *Chem. Soc. Rev.* **2016**, *45* (14), 3954-3988.
135. Singh, A. K.; Singh, S.; Kumar, A. Hydrogen Energy Future with Formic Acid: A Renewable Chemical Hydrogen Storage System. *Catal. Sci. Technol.* **2016**, *6* (1), 12-40.
136. Celaje, J. J. A.; Lu, Z.; Kedzie, E. A.; Terrile, N. J.; Lo, J. N.; Williams, T. J. A prolific catalyst for dehydrogenation of neat formic acid. *Nat Commun*. **2016**, *7*, 1-6.
137. Fukuzumi, S., Kobayashi, T., Suenobu T. 'Efficient Catalytic Decomposition of Formic Acid for the Selective Generation of H_2 and H/D Exchange with a Water-Soluble Rhodium Complex in Aqueous Solution', *ChemSusChem.* **2008**, *1* (10), 827 – 834.
138. Qiao, X.-C. Qiu, D.-C.; Lin, N.; Zhu, J.-W.; Deng, W.; Yao, Z. J. Half-sandwich ruthenium-based versatile catalyst for both alcohol oxidation and catalytic hydrogenation of carbonyl compounds in aqueous media. *Appl Organometal Chem.* **2019**, *33* (5) 1-13.
139. Coffey, R. S. The Decomposition of Formic Acid catalysed by Soluble Metal Complexes. *Chem. Commun.* **1967**, (18) 923-924.
140. Loges, B.; Boddien, A.; Junge, H.; Beller, M., Controlled Generation of Hydrogen from Formic Acid Amine Adducts at Room Temperature and Application in H_2/O_2 Fuel Cells. *Angew. Chem. Int. Ed.* **2008**, *47* (21), 3962-3965.
141. Fellay, C.; Dyson, P. J.; Laurenczy, G., A Viable Hydrogen-Storage System Based On Selective Formic Acid Decomposition with a Ruthenium Catalyst. *Angew. Chem. Int. Ed.* **2008**, *47* (21), 3966-3968.
142. Boddien, A.; Loges, B.; Junge, H.; Beller, M.; Hydrogen Generation at Ambient Conditions: Application in Fuel Cells. *ChemSusChem.* **200**8, *1* (8-9), 751-758.
143. Morris, D. J.; Clarkson, G. J.; Wills, M., Insights into Hydrogen Generation from Formic Acid Using Ruthenium Complexes. *Organometallics*. **2009**, *28* (14), 4133-4140.
144. Fukuzumi, S.; Kobayashi, T.; Suenobu, T.; Unusually Large Tunneling Effect on Highly Efficient Generation of Hydrogen and Hydrogen Isotopes in pH-Selective Decomposition of Formic Acid Catalyzed by a Heterodinuclear Iridium-Ruthenium Complex in Water. *J. Am. Chem. Soc.* **2010**, *132* (5), 1496-1497.
145. Gan, W.; Snelders, D. J. M.; Dyson, P. J. Laurenczy, G., Ruthenium(II)-Catalyzed Hydrogen Generation from Formic Acid using Cationic, Ammoniomethyl-Substituted Triarylphosphine Ligands. *ChemCatChem.* **2013**, *5* (5), 1126-1132.
146. Pan, Y.; Pan, C.-L.; Zhang, Y.; Li, H.; Min, S.; Guo, X.; Zheng, B.; Chen, H.; Anders,

A.; Lai, Z.; Zheng, J.; Huang, K.-W., Selective Hydrogen Generation from Formic Acid with Well-Defined Complexes of Ruthenium and Phosphorus-Nitrogen PN^3-Pincer Ligand. *Chem. Asian J.* **2016**, *11* (9), 1357-1360.

147. Guan, C.; Zhang, D.-D.; Pan, Y.; Iguchi, M.; Ajitha, M. J.; Hu, J.; Li, H.; Yao, C.; Huang, M.-H.; Min, S.; Zheng, J.; Himeda, Y.; Kawanami, H.; Huang, K.-W.; Dehydrogenation of Formic Acid Catalyzed by a Ruthenium Complex with an N,N′-Diimine Ligand. *Inorg. Chem.* **2017**, *56* (1), 438 - 445.
148. Treigerman, Z.; Sasson, Y., Further Observations on the Mechanism of Formic Acid Decomposition by Homogeneous Ruthenium Catalyst. *ChemistrySelect,* **2017**, *2* (21), 5816-5823.
149. Awasthi, M. K.; Tyagi, D.; Patra, S.; Rai, R. K.; Mobin, S. M.; Singh, S. K.; Ruthenium Complexes for Catalytic Dehydrogenation of Hydrazine and Transfer Hydrogenation Reactions. *Chem. Asian J.* **2018**, *13* (11), 1424-1431.
150. Agapova, A., Alberico, E., Kammer, A., Junge, H., Beller, M., Catalytic Dehydrogenation of Formic Acid with Ruthenium-PNP-Pincer Complexes: Comparing N-Methylated and NH-Ligands. *ChemCatChem*. **2019**, *11* (7), 1910-1914.
151. Patra, S., et al., Dehydrogenation of Formic Acid Catalyzed by Water-Soluble Ruthenium Complexes: X-ray Crystal Structure of a Diruthenium Complex. *European Journal of Inorganic Chemistry*, **2019**, *2019* (7), 1046-1053.
152. Patra, S.; S.K. Singh, Hydrogen production from formic acid and formaldehyde over ruthenium catalysts in water. *Inorganic chemistry*, **2020**, 59 (7), 4234-4243.
153. Patra, S.; Deka, H.; Singh, S.K., Bis-Imidazole Methane Ligated Ruthenium (II) Complexes: Synthesis, Characterization, and Catalytic Activity for Hydrogen Production from Formic Acid in Water. *Inorganic Chemistry*, **2021**, *60* (18), 14275-14285
154. Léval, A.; Junge, H.; Beller, M., Formic Acid Dehydrogenation by a Cyclometalated κ3-CNN Ruthenium Complex. *European Journal of Inorganic Chemistry*, **2020**. *2020* (14), 293-1299.
155. Theodorakopoulos, M.; Solakidou, M.; Deligiannakis, Y.; Louloudi, M., A Use-Store-Reuse (USR) Concept in Catalytic HCOOH Dehydrogenation: Case-Study of a Ru-Based Catalytic System for Long-Term USR under Ambient O_2. *Energies*, **2021**. *14* (2), 481.
156. Kar, S.; Rauch, M.; Leitus, G.; David, Y. B.-; Milstein, D., Highly efficient additive-free dehydrogenation of neat formic acid. *Nature Catalysis*, **2021**, *4* (3), 193-201.
157. Mellone, I.; Peruzzini, M.; Rosi, L.; Mellmann, D.; Junge, H.; Beller, M.; Gonsalvi, L.

Formic acid dehydrogenation catalysed by ruthenium complexes bearing the tripodal ligands triphos and NP_3. *Dalton Transactions*, **2013**, *42* (7), 2495-2501.

158. Guerriero, A.; Bricout, H.; Sordakis, K.; Peruzzini, M.; Monflier, E.; Hapiot, F.; Laurenczy, G.; Gonsalvi, L. Hydrogen production by selective dehydrogenation of HCOOH catalyzed by Ru-Biaryl Sulfonated Phosphines in aqueous solution. *ACS Catalysis*, **2014**, *4* (9), 3002-3012.
159. Gao, Y.; Kuncheria, J.; Yap, G.P. A.; Puddephatt, R. J. An efficient binuclear catalyst for decomposition of formic acid. *Chem. Comm.*, **1998** (21), 2365-2366.
160. Gao, Y.; Kuncheria, J. K.; Jenkins, H. A.; Puddephatt, R. J.; Yap, G. P. A. The interconversion of formic acid and hydrogen/carbon dioxide using a binuclear ruthenium complex catalyst. *Journal of the Chemical Society, Dalton Transactions*, **2000** (18). 3212-3217.
161. Wang, W.-H.; Hull, J. F.; Muckerman, J. T.; Fujita, E.; Hirose, T.; Himeda, Y. Highly efficient D2 generation by dehydrogenation of formic acid in D2O through H+/D+ exchange on an iridium catalyst: application to the synthesis of deuterated compounds by transfer deuterogenation. *Chem. Eur. J.*, **2012**. 18 (30), 9397-9404.
162. Wang, W.-H.; Xu, S.; Manaka, Y.; Suna, Y.; Kambayashi, H.; Muckerman, J. T.; Fujita, E.; Himeda, Y., Formic acid dehydrogenation with bioinspired iridium complexes: a kinetic isotope effect study and mechanistic insight. *ChemSusChem*, **2014**, ***7*** (7), 1976-1983.
163. Wang, Z.; Lu, S. –M.; Li, J.; Wang, J.; Li, C., Unprecedentedly High Formic Acid Dehydrogenation Activity on an Iridium Complex with an N, N′-Diimine Ligand in Water. *Chem. Eur. J.* **2015**, *21* (36), 12592-12595.
164. Onishi, N.; Ertem, M. Z.; Xu, S.; Tsurusaki, A.; Manaka, Y.; Muckerman, J. T.; Fujita, E.; Himeda, Y.; Direction to practical production of hydrogen by formic acid dehydrogenation with Cp* Ir complexes bearing imidazoline ligands. *Catalysis Science & Technology*, **2016**, *6* (4), 988-992.
165. Iguchi, M.; Zhong, H.; Himeda, Y.; Kawanami, H., Kinetic Studies on Formic Acid Dehydrogenation Catalyzed by an Iridium Complex towards Insights into the Catalytic Mechanism of High-Pressure Hydrogen Gas Production. *Chem. Eur. J.*, 2017. **23**(67): p. 17017-17021.
166. Kanega, R.; Ertem, M. Z.; Onishi, N.; Szalda, D. J.; Fujita, E., Himeda, Y., CO2 hydrogenation and formic acid dehydrogenation using Ir catalysts with amide-based ligands. *Organometallics*, **2020**, *39* (9), 1519-1531.

CHAPTER 2

This chapter is published in

Vatsa, A. and Padhi, S. K.*, Inorg. Chim. Acta, 2020, 504, 119444.

Chapter 2

Catalytic Water Oxidation by a Single Site $[Ru(Fc\text{-}tpy)(bpy)OH_2]^{2+}$ Complex and its Mechanistic Study

2.1 Introduction

Artificial photosynthesis is one of the most promising fields of research for developing an alternative source of sustainable energy for overcoming the energy crisis in the future. The oxidation of water into molecular oxygen is proven to be an excellent source in the form of a chemical bond that can be utilized from solar energy.[1-2] Several mononuclear ruthenium-based molecular water oxidation catalysts (WOCs) have been reported and are discussed in Chapter 1. Few ruthenium-based mononuclear polypyridine complexes are reported with electron-donating (EDG) and electron-withdrawing group (EWG) in the ligand framework. Thummel and group synthesized a $[Ru(pbn)(4\text{-}R\text{-}Py)_2OH_2]^{2+}$ by substituting the 4th position of pyridine with electron-donating (EDG) and electron-withdrawing groups (EWG).[3] Meyer and group reported a series of Ru complexes having the general formula $[Ru(NNN)(NN)(OH_2)]^{2+}$ where NNN = tpy is 2,2′:6′,2″-terpyridine or Mebimpy = 2,6-Bis(1-methylbenzimidazol-2-yl)pyridine and NN = bpm is 2,2′-bipyrimidine or bpz is 2,2′-bipyrazine). They have studied the influence of the ligand environment on the rate of O_2 evolution and suggested the formation of Ru^V=O as an intermediate and release of O_2 from peroxo intermediate. [4-5] Berlinguette and group examined water oxidation by studying the electronic effect of substitution of EDGs and EWGs like OMe, Cl, COOH on both 'tpy' and 'bpy' framework of $[Ru(tpy)(bpy)OH_2]^{2+}$ based complexes. They suggested that EDG substitution increases the catalytic TON and TOF, and EWG increases the catalytic stability.[6-7] Yagi and group have reported a $[Ru(R\text{-}tpy)(bpy)OH_2]^{2+}$ complex by substituting the 'tpy' scaffold with R = H, CH_3O, EtO, CH_3, and Cl group at 4th position. The complex substituted with strong EDGs has a high catalytic rate as compared to complexes substituted with EWGs. They observed that Ru^{IV}=O to Ru^V=O oxidation is the rate-determining step instead of O-O bond formation by WNA mechanism.[8] Masaoka and group have reported the aqua complex $[Ru(terpy)(bpyms)H_2O]$ **57** (where terpy = 2,2′:6′,2″-terpyridine and bpyms = 2,2'-bipyridine-5,5'-bis(methanesulfonate)) bearing SO_3^- as pendant base on bpy ligand framework for water oxidation using Ce^{4+} as an oxidant having a TON of 47 with 94 % of conversion efficiency for catalysis.[9]

Kumbhar et al. reported the synthesis of mononuclear $[Ru(tpy)(bpg)H_2O]^{2+}$ complex (where bpg = 4b,5,7,7a-tetrahydro-4b,7a-nepiminomethanoimino-6*H* - imidazo [4, 5 – *f* [1,10]

phenanthroline 6,13- dione) where 'bpy' scaffold is substituted with the glycoluril group and studied the electronic effect of the functionalized bipyridine ligand that enhances the rate and activity of the complex towards water oxidation.[10]

In this chapter, the synthesis and characterization of [Ru(Fc-tpy)(bpy)Cl]PF_6 **(Ru-Cl)** and [Ru(Fc-tpy)(bpy)(OH_2)](PF_6)$_2$ **(Ru-OH_2)** complexes and the catalytic activity of the complex **Ru-OH_2** towards chemical water oxidation (where Fc-tpy= 4'-(2-ferrocenyl)-2,2':6'2''-terpyridine) are discussed. Herein the effect of the electron-donating ferrocene group on the terpyridine scaffold was investigated towards water oxidation for O_2 evolution as compared to the parent [Ru(tpy)(bpy)(OH_2)]$^{2+}$ complex in the presence of CAN as the sacrificial electron acceptor.

2.2 Experimental

2.2.1. Materials and methods

2.2.1.1. Materials

All the chemicals for the synthesis and experimental analysis used in this work were of reagent grade. Ferrocene-2-carbaldehyde, 2-acetylpyridine, and CF_3SO_3H were purchased from Alfa Aesar and used without further purification. $RuCl_3.xH_2O$, $AgPF_6$, and $(NH_4)_2Ce(NO_3)_6$ (>99.99 %) were purchased from Sigma-Aldrich and used without further purification. The solvents like acetone, diethyl ether, DMSO, and ethanol were purchased from Merck and dried before use. The distilled water purified from the Milli-Q purification system was utilized throughout the work. The ligand Fc-tpy and precursor complex [Ru^{II}(bpy)(DMSO)$_2$$Cl_2$] were synthesized according to a published procedure. [11-12]

2.2.1.2. Optical Spectra

All the UV-Vis spectroscopic-related analyses were carried out with an Agilent Cary 8454 photodiode array UV-Vis spectrophotometer.

2.2.1.3. NMR Spectroscopy and Mass Spectrometry

The ^{1}H and ^{13}C NMR spectra were recorded with 400 MHz Bruker Ultrashield NMR spectrometer at room temperature. High-resolution ESI mass spectroscopy (HRMS) was carried out with Waters UPLC TQD and Bruker micrOTOF-Q II instruments.

2.2.1.4. Determination of pK_a Value

The Acid-Base pH titration was carried out using UV-Visible spectroscopy in aqueous phosphate buffer solution within the pH range 1.62 to 13.0 to determine the pK_a of the complex **Ru-OH2**. The pH of the buffer solution containing **Ru-OH2** was adjusted by the minimum addition of saturated KOH solution. The change in absorbance vs pH was plotted, and the pK_a was determined by fitting the value of absorbance at selective wavelength using equation 2.1.

$$\boldsymbol{A = A_0 + K_a \left[\frac{A_\infty - A_0}{K_a + 10^{-pH}}\right]} \qquad \textbf{(2.1)}$$

2.2.1.5. Cyclic Voltammetry

Electrochemical measurements were conducted with an ALS/CHI model 1140C electrochemical analyzer, and all the experiments were carried out under an inert gas atmosphere at room temperature. All the cyclic voltammetry and differential pulse voltammetry techniques were carried out with three-electrode systems consisting of a glassy carbon electrode as working, a platinum wire as auxiliary, and saturated calomel electrode as the reference electrode.

2.2.1.6. Gas Evolution

The manometric studies were conducted in a 5 mL jacketed reaction vessel containing 2 mL of the reaction mixture solution and 3 mL of headspace volume. The reference 5 mL jacketed reaction vessel was filled with 2 mL of the pH 1 triflic acid solution with the same headspace volume as the working compartment. The yield of oxygen was calculated in micromoles using the ideal gas equation PV = nRT to calculate the number of moles of the gas evolved, which is converted into the micromoles. In this experiment 2 µmol of catalyst and 100 equivalent of ceric ammonium nitrate (CAN) as sacrificial oxidant were used in 2mL of triflic acid solution at pH 1.0. The pressure of evolved O_2 was measured by using a differential pressure manometer of TESTO 521 with a range 0 to 100 hPa, 0.1 hPa accuracy was used. The O_2 evolution was tested in the absence and presence of the catalyst using CAN. The generated O_2 was quantified and detected using an oxygen FOXY sensor probe of NeoFox Ocean Optics with 80 ppm O_2 % resolution in gas and monitored by NeoFox Viewer using NeoFox phase fluorometer systems.

2.2.1.7. X-ray crystallographic analysis

A suitable single crystal of [Ru(Fc-tpy)(bpy)Cl](PF_6) complex was mounted on a Rigaku SuperNova G8910B EosS2 single-crystal X-ray diffractometer using Mo Kα radiation (λ = 0.71073 Å). An EosS2 CCD detector was used for the collection of Frames and the data collected by the instrument were processed by using CrysAlis^{Pro} software.[13] The data was collected at 293 K and solved through Olex2 software utilizing the Charge Flipping solution program. The data refinement for the crystal structure was carried out through Gauss-Newton minimization using the Olex2 refinement package.[14] The disordered solvent molecules appeared in the asymmetric unit, and the voids were eliminated by SQUEEZE tool by means of PLATON. The crystal data and refinement parameters are listed in Table S1.

2.2.2. Synthesis

2.2.2.1. Synthesis of [Ru(Fc-tpy)(bpy)Cl](PF_6) (Ru-Cl)

A precursor complex [Ru(bpy)$(DMSO)_2Cl_2$] (500 mg, 1.03 mmol) was dissolved in 40ml of ethanol and 1.2 equivalent of $AgPF_6$ (313 mg, 1.23 mmol) was added to it. The reaction mixture was allowed to stir for one hour at 80 °C. An off-white precipitate of AgCl appeared in the reaction mixture which was filtered using celite and the complex was collected after evaporating the filtrate. The collected complex was dissolved in a minimum amount of ethanol, and one equivalent of Fc-tpy ligand (431 mg, 1.03 mmol) was added to it. The reaction mixture was refluxed for 12 hours at 80 °C. The resulting product was collected by evaporating the solvent, and it was further purified by column chromatography over neutral alumina eluting with $CHCl_3$/MeOH (95:5) mixture. The purple-colored band was collected and evaporated to dryness. The desired product was isolated as a purple coloured solid (Yield: 164 mg, 0.23 mmol, 22 %). The dark pink colored crystals suitable for Single-crystal X-ray Crystallography were grown in DMF and isolated after two weeks. Calculated mass for $[C_{35}H_{27}ClN_5FeRu]^+$: m/z = 710.034; found: 710.041 m/z. The 400 MHz ^{1}H NMR (δ, (*J*, Hz), CD_3CN): 4.20 (5H, s), 4.60 (2H, s), 5.16 (2H, s), 6.94-6.97 (1H, t, 12), 7.20-7.24 (3H, t, 8), 7.33-7.35 (2H, d, 8), 7.63-7.67 (1H, q), 7.94-7.97 (3H, t, 12), 8.23-8.30 (1H, m), 8.40-8.47 (2H, m), 8.57-8.59(4H, d, 8), 10.126 (1H, d, 8). The 100.62 MHz ^{13}C NMR {δ, (J, Hz), DMSO-D_6}: 68.18, 70.51, 71.42, 80.97, 119.31, 123.92, 124.17, 124.38, 126.95, 127.32, 127.95, 135.83, 136.82, 137.34, 148.31, 152.14, 152.35, 152.51, 156.32, 157.42, 158.93, 159.18 for 10 carbon of ferrocene moiety (2 x 2, 1 x 5 and one C connected tpy), 10 carbons of bipyridine moiety and 15 carbons of terpyridine (2 x 7 equivalent carbons and 01 C connected to ferrocene) i.e. a total of 22 ^{13}C signals appeared.

2.2.2.2. Synthesis of $[Ru(Fc\text{-}tpy)(bpy)(OH_2)](PF_6)_2$ (Ru-OH_2)

To a solution of $[Ru(Fc\text{-}tpy)(bpy)Cl](PF_6)$ (100 mg, 0.140 mmol) in 20 mL of EtOH/H_2O (3:1, v/v), 2.2 equivalent of $AgPF_6$ (65mg, 0.257mmol) was added and the reaction mixture was stirred for 4 hours at 80 °C. An off-white precipitate was filtered through celite, and the red-brown colored filtrate was collected by evaporating the solvent. The collected complex was dissolved in the minimum amount of solvent and precipitated by adding a saturated solution of KPF_6. The brown-colored precipitate was washed with ice-cold water several times, followed by diethyl ether (Yield: 94 mg, 0.095 mmol, 82 %). Calculated mass for $[C_{35}H_{27}N_5FeRu]^{2+}$ $[[Ru(Fc\text{-}tpy)(bpy)OH_2]\text{-}H_2O]^{2+}$: 338.04 m/z; found: 337.95 m/z and $[C_{35}H_{28}N_5OFeRu]^{+}$ $[[Ru(Fc\text{-}tpy)(bpy)OH]+Na]^{2+}$: 358.03 m/z; found: 358.47 m/z. ^1H NMR (δ, (*J*, Hz), CD_3COCD_3): 4.02 (2H, t, 12), 4.18 (2H, t, 16), 4.36 (1H, t, 16), 4.71 (2H, s), 6.25 (2H, s), 7.11 (1H, d, 8), 7.58 (2H, t, 12), 7.87-7.92 (3H, m), 8.05 (1H), 9.44-9.558.15-819 (1H,m), 8.26 (1H, d, 8), 8.53 (1H, t, 12), 8.64(1H, d, 8), 8.91-9.0 (2H, m), 9.10 (1H, t, 20),9.44-9.55(3H, m), 9.83 (1H, s). The NMR spectrum was obtained after the addition of ascorbic acid to the solution of $[Ru(Fc\text{-}tpy)(bpy)(OH_2)](PF_6)_2$ in acetone-D_6.

2.3. Results and Discussion

2.3.1. Synthesis

The Fc-tpy ligand and the precursor complex $[Ru(bpy)(DMSO)_2Cl_2]$ were synthesized according to the published procedures. [13-14] The syntheses of Ru-Cl and Ru-OH_2 are depicted in Scheme 2.1. The $[Ru(Fc\text{-}\ tpy)(bpy)Cl](PF_6)$ was synthesized from the reaction of one equivalent of Fc-tpy ligand with one equivalent of precursor complex $[Ru(bpy)\ (DMSO)_2Cl_2]$ in the presence of $AgPF_6$ in ethanol at 80 °C. Single crystals of $[Ru(Fc\text{-}tpy)(bpy)Cl](PF_6)$, suitable for X-ray crystallography were grown in DMF and isolated after two weeks. The $[Ru(Fc\text{-}tpy)(bpy)OH_2]\ (PF_6)_2$ complex was synthesized from $[Ru(Fc\text{-}tpy)(bpy)Cl](PF_6)$ by adding 2.2 equivalents of $AgPF_6$ as dechlorinating agent in EtOH/H_2O (4:1 v/v) medium and the reaction mixture was refluxed for 4 h at 80 °C. The AgCl precipitate was filtered out, and the product was precipitated by adding saturated KPF_6 solution after evaporation.

.

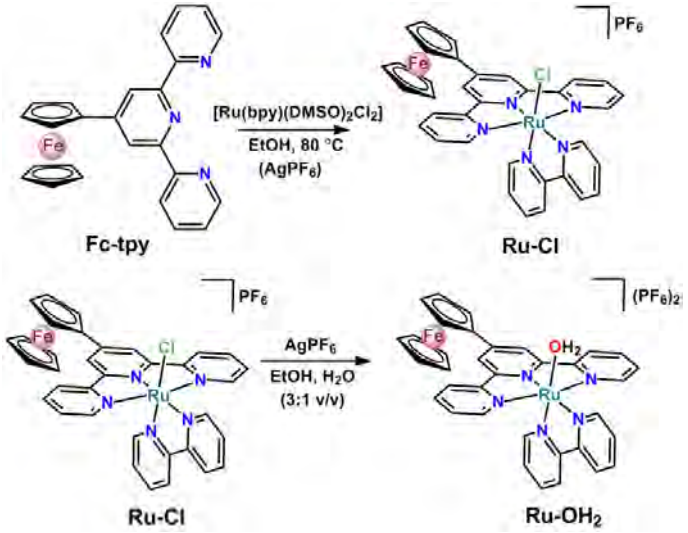

Scheme 2.1. Synthesis of Ru-Cl and Ru-OH_2 complex.

2.3.2. Optical Spectra

The UV-Vis Spectra of **Ru-Cl** and **Ru-OH_2** in methanol shown in Figure A1. In the Ulta Voilet region of both the **Ru-Cl** and **Ru-OH_2** complexes, the absorption band at 315 nm (ε = 11220 M^{-1} cm^{-1}) was ascribed to π→ π* transition for tpy moiety and the absorption band at 355 nm (ε = 3640 M^{-1} cm^{-1}) was ascribed to π→ π* transition for ferrocene moiety. In the visible region, a broad MLCT absorption band at 500 nm (ε = 3910 M^{-1} cm^{-1}) and a shoulder at 535 nm (ε = 3640 M^{-1} cm^{-1}) appeared in **Ru-Cl** complex, whereas a MLCT band at 500 nm (ε = 3910 M^{-1} cm^{-1}) was appeared in **Ru-OH_2** complex.

2.3.3. NMR and Mass Spectra

The NMR and mass spectra of the **Ru-Cl** and **Ru-OH_2** are provided in Figure A2-A6. A broad NMR spectrum of the $[Ru(Fc\text{-}tpy)(bpy)OH_2](PF_6)_2$ complex was observed in deuterated acetone, which may be due to aerial oxidation of the complex from Ru(II) to Ru(III). NMR spectra of the complex were resolved after the addition of ascorbic acid as a reducing agent. The mass spectra of **Ru-OH_2** complex was recorded in methanol, wherein the calculated and found mass for the base peak $[C_{35}H_{27}N_5FeRu]^{2+,}$ i.e. $[[Ru(Fc\text{-}tpy)(bpy)OH_2]\text{-}H_2O]^{2+}$ is 338.04 m/z; and 337.95 m/z respectively and another peak with calculated and found mass for $[C_{35}H_{28}N_5OFeRu]^{+,}$ i.e. $[Ru(Fc\text{-}tpy)(bpy)OH]+Na]^{2+}$is 358.03 m/z and 358.47 m/z respectively.

2.3.4. Single crystal X-ray crystallography

Dark pink-colored block-shaped single crystals of the complex [Ru(Fc-tpy)(bpy)Cl](PF_6) were isolated from the DMF solution obtained through the slow evaporation method. The complex [Ru(Fc-tpy)(bpy)Cl](PF_6) crystallizes in a P ĩ space group. There is a center of inversion with [-x,-y,-z] symmetry operation at [0,0,0]. The asymmetric unit of the crystal consists of a monocationic unit of $[Ru(Fc\text{-}tpy)(bpy)Cl]^+$ and a PF_6^- ion. A perspective view of the Oak Ridge Thermal Ellipsoid Plot (ORTEP) of the cationic unit $[Ru(Fc\text{-}tpy)(bpy)Cl]^+$ is displayed in Figure 2.1. A list of selected bond lengths and bond angles are provided in Table A2 and A3, respectively. The Ru center in $[Ru(Fc\text{-}tpy)(bpy)Cl]^+$ has an octahedral geometry wherein three meridional sites are occupied by the tridentate Fc-tpy ligand generating two 5 membered bite-angles of N_2C_2 rings. The other meridional plane perpendicular to the plane Fc-tpy ligand is consists of a bipyridine (bpy) ligand and a Cl^- ion coordinated to the Ru center. In this case, the bpy ligand coordinates as a bidentate ligand generating a 5 membered RuN_2C_2 ring. The Cp^- rings in the ferrocene moiety of Fc-tpy ligand are almost eclipsed conformation. The Ru–N(central pyridine ring of Fc-tpy) distance is comparatively shorter than the Ru–N (oppositely pyridine ring in Fc-tpy) because of the more effective overlap of the t_{2g} orbitals of Ru^{2+} with the π* orbitals of the central pyridine ring. The $\angle N_{Fc\text{-}tpy}–Ru–N_{bpy}$ [173.7(2)°] and $\angle N_{bpy}–Ru–Cl$ [173.7(2)°] slightly deviate from linearity. Whereas opposite N-atoms in the Fc-tpy ligand in the same meridional plane drastically deviate from linearity [91.6(2)°]. The two meridional planes generated by the (Fc-tpy) ligand and the (bpy and Cl^-) are nearly at right angle [88.2(2)°]. A significant π···π stacking interaction (3.339 Å) was observed between the ferrocene moieties of $[Ru(Fc\text{-}tpy)(bpy)Cl]^+$ units.

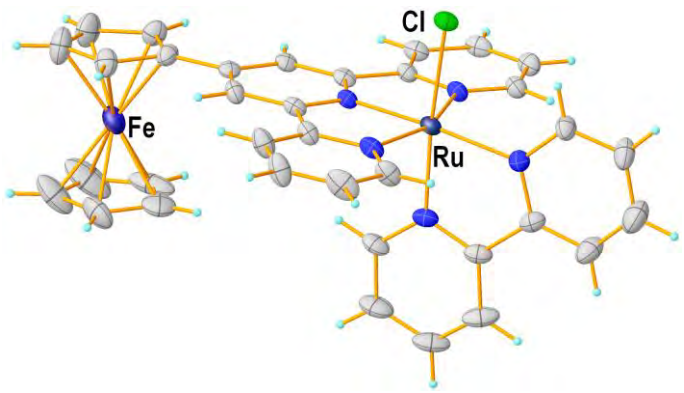

Figure 2.1. The 30 % probability Oak Ridge Thermal Ellipsoid plot of [Ru (Fc-tpy) (bpy)Cl]$^+$.

2.3.5. Acid-base equilibria.

The acid-base equilibria properties of the complex **Ru-OH$_2$** were investigated using UV–Visible spectroscopy in Britton–Robinson buffer solution within the pH span 2.0–12.0 (Scheme 2.2). Under strong acidic conditions, the Fe(II) centre of ferrocene moiety (Fc) undergoes protonation to generate Fe(IV)hydrido species Fe(IV)H (FcH$^+$).[15-16] Under such conditions, the [Ru(Fc-tpy)(bpy)(OH$_2$)]$^{2+}$ species converts into [Ru (FcH-tpy)(bpy)(OH$_2$)]$^{3+}$. The MLCT spectra at 486 nm were observed for [Ru(FcH-tpy)(bpy)(OH$_2$)]$^{3+}$ complex at pH 2.0. No significant changes were observed between the pH 2.0–7.0 band intensity at 486 nm (Figure A7). A substantial decrease in band intensity at 486 nm was observed due to deprotonation from the aqua group coordinated to the complex within the pH range 7.0–13.0 (Figure A8). An increase in pH gives rise to two new peaks at 383 nm and 518 nm, having two isosbestic points at 430 nm and 510 nm. The isosbestic point at 510 nm was observed for the deprotonation of the aqua group [Ru(FcH-tpy)(bpy)(OH$_2$)]$^{3+}$ [Ru(FcH-tpy)(bpy)(OH)]$^{2+}$. The change in absorbance at 486 nm and 518 nm were plotted with respect to pH, and the p*K*a was found to be 10 (Figure A9).

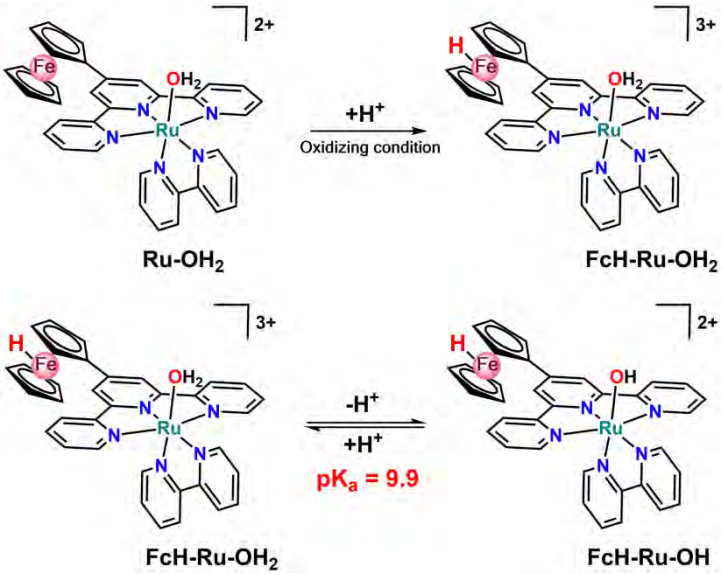

Scheme 2.2. Acid-Base equilibria of Ru-OH$_2$ complex in Britton–Robinson buffer.

2.3.6. Electrochemistry in organic medium.

The electrochemical measurements of the Fc-tpy ligand have been carried out in CH_3CN containing 0.1 M nBu_4NClO_4 (TBAP) as supporting electrolyte, under inert atmosphere. The cyclic voltammogram (CV) of the Fc-tpy ligand exhibits two quasi reversible peaks under anodic scan (Figure 2.2(A)). The redox couple with $E_{1/2}$ = +0.57 V *vs.* SCE (E_{pa} = 0.61 V and

E_{pc}= 0.53 V *vs.* SCE) was attributed to the Fe^{III}/Fe^{II}, whereas another one at $E_{1/2}$ = +1.13 V *vs.* SCE (E_{pa} = 1.18 V and E_{pc} = 1.07 V *vs.* SCE) was due to the Fc-tpy/Fc-tpy$^{\bullet+}$. The ligand shows the resting potential of 0.39 V *vs.* SCE that indicates oxidation state of iron in ferrocene moiety remains in Fe^{II} state. Under the same condition the Fe^{III}/Fe^{II} redox couple of the reference ferrocene appears at $E_{1/2}$ = +0.39 V *vs.* SCE (E_{pa} = 0.43 V and E_{pc} = 0.35 V *vs.* SCE) in presence of 0.1 M nBu$_4$NClO$_4$ (TBAP) as supporting electrolyte (Figure 2.2(A)). A comparison of the CV of [Ru(Fc-tpy)(bpy)Cl]$^+$ (red) and [Ru(tpy)(bpy)Cl]$^+$ (black) is displayed in Figure 2.2(B). The CV of [Ru(tpy)(bpy)Cl]$^+$ indicates the Ru^{III}/Ru^{II} and Ru^{IV}/Ru^{III} redox couples at $E_{1/2}$ = 0.80 V *vs.* SCE (E_{pa} = 0.83 V and E_{pc} = 0.77 V *vs.* SCE) and $E_{1/2}$ = 1.18 V *vs.* SCE (E_{pa} = 1.22 V and E_{pc} = 1.13 V *vs.* SCE) respectively. Whereas the CV of [Ru(Fc-tpy)(bpy)Cl]$^+$ shows the Fc-tpy based Fe^{III}/Fe^{II} redox couple at $E_{1/2}$ = 0.54 V *vs.* SCE (E_{pa} = 0.57 V and E_{pc} = 0.51 V *vs.* SCE) and Ru^{III}/Ru^{II} and Ru^{IV}/Ru^{III} redox couples were appeared at $E_{1/2}$ = 0.84 V *vs.* SCE (E_{pa} = 0.86 V and E_{pc} = 0.82 V *vs.* SCE) and $E_{1/2}$=1.26 V *vs.* SCE (E_{pa}=1.30 V and E_{pc}=1.22 V *vs.* SCE) respectively. The complex shows the resting potential of +0.41 V *vs.* SCE that indicates compound remains in Fe^{II} state.

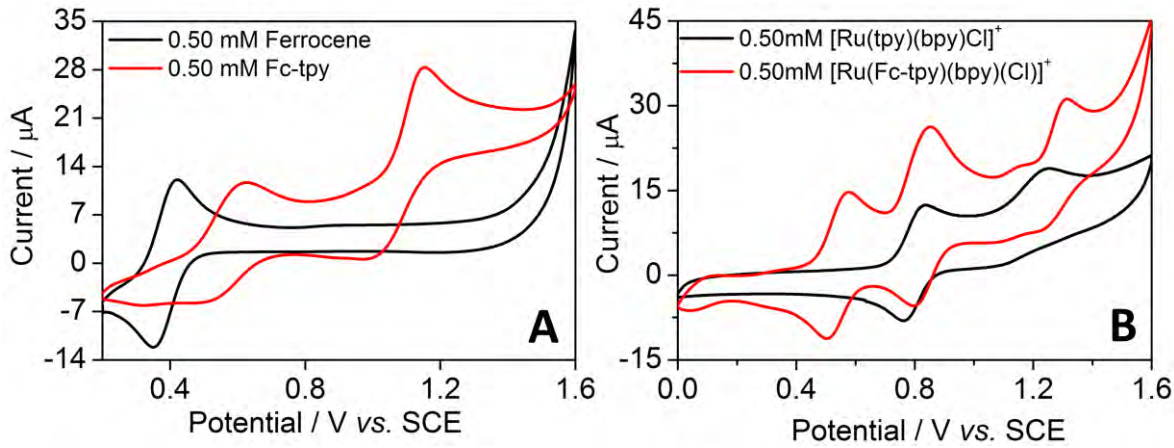

Figure 2.2. (A) CV of 0.50 mM Fc-tpy (red) and Ferrocene (black) in CH_3CN containing 0.1 M TBAP. **(B)** CV of 0.5 mM [Ru(Fc-tpy)(bpy)Cl]$^+$ (red) and [Ru(tpy)(bpy)Cl]$^+$ (black) in CH_3CN containing 0.1 M TBAP.

2.3.7. Aqueous Electrochemistry and Pourbaix diagram

The cyclic voltammogram of [Ru(tpy)(bpy)OH$_2$]$^{2+}$ (black) and [Ru(FcH-tpy)(bpy)OH$_2$]$^{3+}$ (red) were recorded in CF_3SO_3H solution at pH 1.0 (Figure 2.3). The [Ru(FcH-tpy)(bpy)OH$_2$]$^{2+}$ complex exhibits the Ru^{IV}/Ru^{III} redox couple at $E_{1/2}$ = 0.76 V *vs.* SCE, whereas the RuIII/RuII redox couple for the [Ru(tpy)(bpy)OH$_2$]$^{2+}$ was observed at 0.32 V *vs.* SCE. In the case of [Ru(FcH-tpy)(bpy)OH$_2$]$^{3+,}$ the Ru^{III}/Ru^{II} redox couple was apparently observed at 0.32 V vs.

SCE. In both the cases a catalytic current was observed in the anodic direction, which suggests the oxidation of water. The complex $[Ru(tpy)(bpy)OH_2]^{2+}$ shows an increase in catalytic current with onset potential of 1.20 V *vs.* SCE that indicates the electrocatalytic water oxidation. However, in case of $[Ru(FcH\text{-}tpy)(bpy)OH_2]^{3+}$ the onset potential for the catalytic current towards water oxidation is 230 mV lower than that of the $[Ru(tpy)(bpy)OH_2]^{2+}$ complex along with a significantly higher intensity of catalytic current is indicative of a better water oxidizing catalyst (WOC) as compared to $[Ru(tpy)(bpy)OH_2]^{2+}$. The cyclic voltammetry and differential pulse voltammetry of aqua complex $[Ru(FcH\text{-}tpy)(bpy)(OH_2)]^{3+}$ were performed in phosphate buffer at pH 1.62. The cyclic voltammogram of the 0.50 mM complex shows a quasi-reversible peak for redox couple Ru^{IV}/Ru^{III} at 0.74 V *vs.* SCE (E_{pa} = 0.77 V and E_{pc} = 0.72 V *vs.* SCE), and for redox couple, Ru^{IV}/Ru^{V} was not observed at this pH. The Ru^{IV}/Ru^{V} was clearly observed in Britton Robinson buffer between pH 7.0 to 12.0 (Figure 2.3 and A12). The resting potential of the $[Ru(FcH\text{-}tpy)(bpy)OH_2]^{3+}$ complex in phosphate buffer at pH 1.62 was found at 0.71 V *vs.* SCE, which indicates the Ru is in 3+ oxidation state. With the addition of ascorbic acid into 0.5 mM $[Ru(Fc\text{-}tpy)(bpy)OH_2]^{2+}$ in phosphate buffer at pH 1.62, an irreversible peak with anodic oxidation at 0.68 V *vs.* SCE appeared, which may be due to the Fe^{II}/Fe^{III} oxidation. The resting potential of the same reaction mixture was found at 0.26 V *vs.* SCE (Figure A11). The resting potential before the addition of ascorbic acid was at 0.71 V *vs.* SCE indicates that the Fe centre of ferrocene moiety is in Fe^{III} state and the Ru centre is in Ru^{III} state, whereas after the addition of ascorbic acid, it appeared at 0.26 V vs. SCE, and the Fe centre of ferrocene moiety is in Fe^{II} state (Fe(II) + H^+ under acidic condition), and Ru center is in Ru^{II} state. After multiple scans with addition of ascorbic acid, it was noticed that the cyclic voltammogram reverts back to the original one as it was without the addition of ascorbic acid. These results clearly indicate that the Fe centre in the complex **Ru-OH$_2$** is in Fe^{III} state under aqueous conditions, and Ru centre is in Ru^{III} state. The presence of Fe^{III} and Ru^{III} causes the broadening of ^{1}H NMR spectra (*vide supra*), whereas, after the addition of ascorbic acid, the NMR of ^{1}H NMR spectra was resolved.

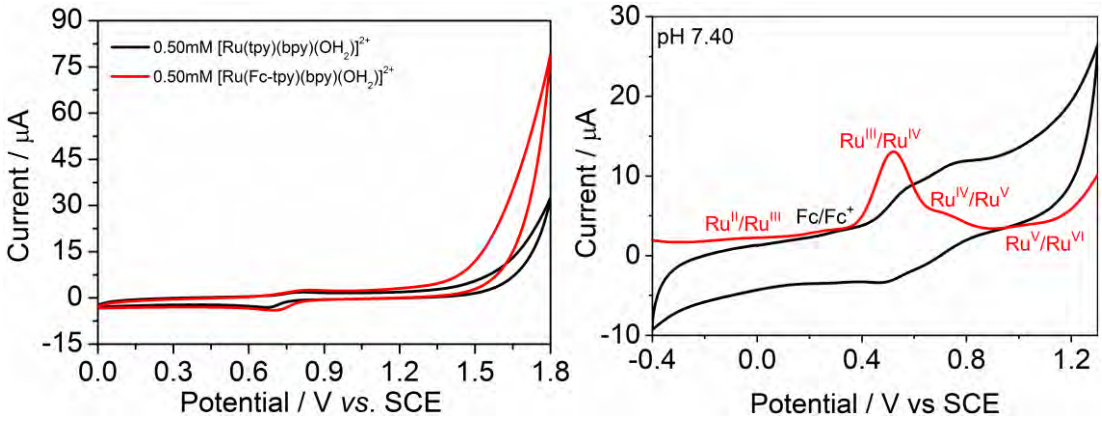

Figure 2.3. (Left) Cyclic voltammogram of 0.5 mM $[Ru(tpy)(bpy)OH_2]^{2+}$ (black) and 0.5 mM $[Ru(Fc\text{-}tpy)(bpy)OH_2]^{2+}$ (red) in pH 1.0 CF_3SO_3H solution. (Right) CV of 0.5 mM $[Ru(tpy)(bpy)OH_2]^{2+}$ in Britton–Robinson buffer at pH 7.4.

The Pourbaix diagram (Figure 2.4) for the complex $[Ru(Fc\text{-}tpy)(bpy)OH_2]^{2+}$ was studied in the Britton Robinson buffer. The details of the changes in DPV and CV are provided in Figure A12. In this case, the ligand-centered oxidation features could not be identified in aqueous buffer media. At pH 2.0 the $[Ru(Fc\text{-}tpy)(bpy)OH_2]^{2+}$ undergoes protonation at Fe(II) center under oxidizing conditions to generate $[Ru^{II}(FcH\text{-}tpy)(bpy)(OH_2)]^{3+}$ (*vide supra*).[15-16] Within the pH span 2.0–3.2, a potential gradient was horizontal, indicating an electron transfer between $[RuII(FcH\text{-}tpy)(bpy)(OH_2)]^{3+} \rightleftarrows [Ru^{III}(FcH\text{-}tpy)(bpy)(OH_2)]^{4+} + 1e^-$. Within the pH span 3.2–10.0 a potential gradient of −60 mV/pH was observed for $[Ru^{II}(FcH\text{-}tpy)(bpy)(OH_2)]^{3+} \rightleftarrows [Ru^{III}(FcH\text{-}tpy)(bpy)(OH)]^{3+} + 1H^+ + 1e^-$. The potential almost remains constant beyond pH 10, indicating the acid-base equilibria for $[Ru^{II}(FcH\text{-}tpy)(bpy)(OH_2)]^{3+} \rightleftarrows [Ru^{II}(FcH\text{-}tpy)(bpy)(OH)]^{2+}$ at a p*K*a of 10. This is in agreement with the p*K*a value that has been determined using UV–Vis spectroscopy with the consideration of a change in absorbance *vs.* pH (*vide supra*). The $[Ru^{III}(FcH\text{-}tpy)(bpy)(OH)]^{3+}$ species undergoes a proton-coupled one electron transfer to generate $[Ru^{III}(Fc^+\text{-}tpy)(bpy)(OH)]^{3+}$ i.e. $[Ru^{III}(FcH\text{-}tpy)(bpy)(OH)]^{3+} \rightleftarrows [Ru^{III}(Fc^+\text{-}tpy)(bpy)(OH)]^{3+} + 1H^+ + 1e^-$. Within pH 2.0–4.5, the $[Ru^{III}(Fc^+\text{-}tpy)(bpy)(OH)]^{3+}$ species undergo a proton-coupled $2e^-$ transfer forming $[Ru^{V}(Fc^+\text{-}tpy)(bpy)(=O)]^{4+}$. However, $[Ru^{III}(Fc^+\text{-}tpy)(bpy)(OH)]^{3+}$ species undergoes a proton-coupled $1e^-$ transfer to generate $[Ru^{IV}(Fc\text{-}tpy)(bpy)(=O)]^{3+}$ within pH span of 4.5–12.0. The horizontal lines were observed at potential 0.7 V *vs.* SCE and 1.0 V *vs.* SCE, which suggests the $1e^-$ transfer process generating $[Ru^{IV}(Fc^+\text{-}tpy)(bpy)(=O)]^{3+} \rightleftarrows [Ru^{V}(Fc+\text{-}tpy)(bpy)(=O)]^{4+}$ and $[Ru^{V}(Fc^+\text{-}tpy)(bpy)(=O)]^{4+} \rightleftarrows [Ru^{VI}(Fc^+\text{-}tpy)(bpy)(=O)]^{5+}$ respectively. The DPV at and the CV in Figure A12 at 1.0 V *vs.* SCE suggests that the Ru^{VI}=O is the active species for catalytic water oxidation.

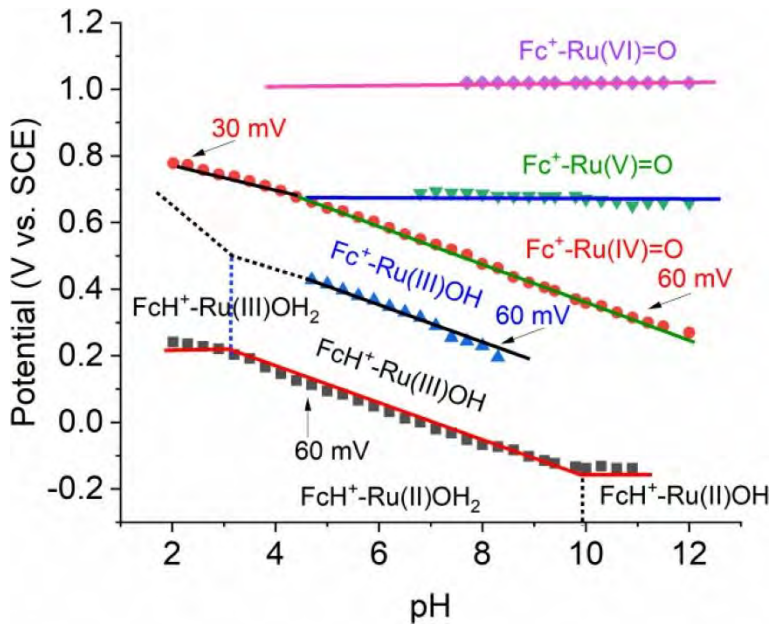

Figure 2.4. Pourbaix diagram of $[Ru(Fc\text{-}tpy)(bpy)OH_2]^{2+}$ in Britton–Robinson buffer.

2.3.8. Chemical water oxidation

Chemically driven water oxidation was studied in pH 1.0 CF_3SO_3H solution using ceric ammonium nitrate (CAN) as the sacrificial electron acceptor in the presence of the Ru-OH_2 catalyst for the evolution of oxygen from the water (Figure A13 and A14). The chemical water oxidation of the complex was conducted in a 5 mL double-jacketed reaction vessel having a catalyst at room temperature. A specific equivalent of CAN solution in CF_3SO_3H as compared to the catalyst was injected through a rubber septum cap. The amount of oxygen evolved was monitored by the differential pressure manometer. The generated dioxygen was also detected by an oxygen sensor. The overall chemical water oxidation reaction by CAN was represented as in equation (2.2).

$$2H_2O + 4Ce^{IV} \rightarrow O_2 + 4Ce^{III} + 4H^+ \qquad (2.2)$$

For kinetics studies, two different sets of experiments were conducted. In the first set of experiments, the catalyst concentration was varied from 0.25 mM to 1.0 mM while keeping the concentration of CAN 100 mM (Rate = $k[Cat]^x$) Figure 2.5(A), and in the second set of the experiment, the concentration of CAN was varied from 75 mM to 200 mM while keeping the concentration of catalyst 1.0 mM (Rate = $k[Ce^{IV}]^y$). The rate of water oxidation to evolve O2 was determined by using equation (2.3)

$$\text{Rate} = k_{cat}\,[cat]^x\,[Ce^{IV}]^y \qquad (2.3)$$

The initial rates are considered for determining the rate of the O_2 evolution at either various catalysts or CAN concentrations. It was observed from the kinetics plot that the initial rate of oxygen evolution at pH 1.0 follows first-order kinetics relative to catalyst, wherein k_{obs} = 0.15 ± 0.01 x 10^2 µmol s^{-1} (Figure A15 and 2.5) at 100 mM CAN concentration. Whenever the concentration of CAN was varied with 1.0 mM catalyst (Figure A16), the initial rate for oxygen evolution at pH 1.0 is first order with respect to [CAN] and k_{obs} = 2.4 ± 0.1 × 10^{-1} µmol s^{-1} (Figure A17 and A18). The plot of ln (initial rate) *vs.* ln[Ru-OH2] (Figure 2.5) and ln (initial rate) *vs.* ln[CAN] (Figure A18) reveals the 1st order dependency of the rate on [Ru-OH_2] and 1.5th order with respect to [CAN]. Hence the rate law for the whole catalytic process can be expressed as rate = kcat $[cat]^{1.0}[Ce^{IV}]^{1.5}$, and k_{cat} was found to be 3.16 ± 0.1 × 10^{-2} s^{-1}.

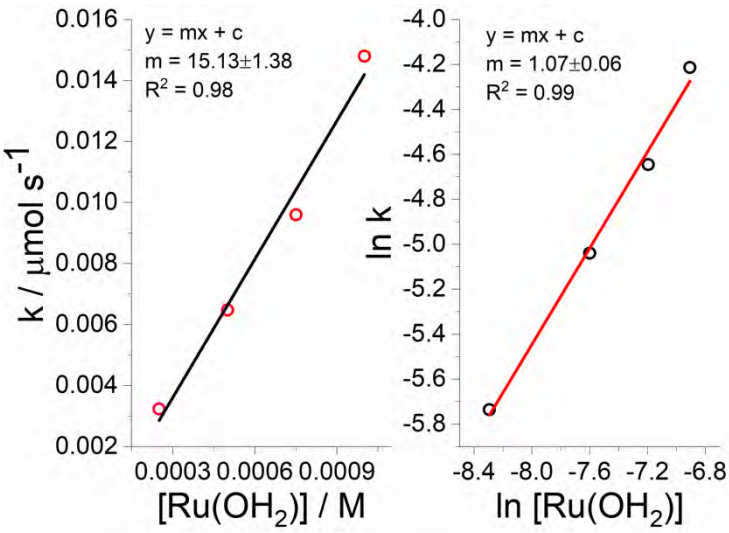

Figure 2.5. Initial rate *vs.* [**Ru-OH2**] (left) and ln (Initial rate of O_2 evolution) *vs.* ln [**Ru-OH2**] (right) in pH 1.0 triflic acid.

The pressure increased was converted into the number of moles by using the Ideal gas equation PV = nRT. The highest number of moles of oxygen evolved is ≈ 23 µmol in 4000 s (Figure 2.6(A)). This catalyst is very much active towards the catalytic water oxidation and shows the highest TON of 12 and initial TOF of 0.006 $s^{-1,}$ which is greater than the observed TON 10 and initial TOF 0.002 s^{-1} of the parent catalyst [Ru(tpy)(bpy)(OH_2)](PF_6)$_2$. Figure 2.6(B) indicates that [Ru(Fc-tpy)(bpy)(OH_2)](PF_6)$_2$ was a much stable and rate enhancing catalyst in comparison to [Ru(tpy)(bpy)(OH_2)](PF_6)$_2$. The TON was calculated by using the equation; TON = O_2 produced / catalyst used in moles.

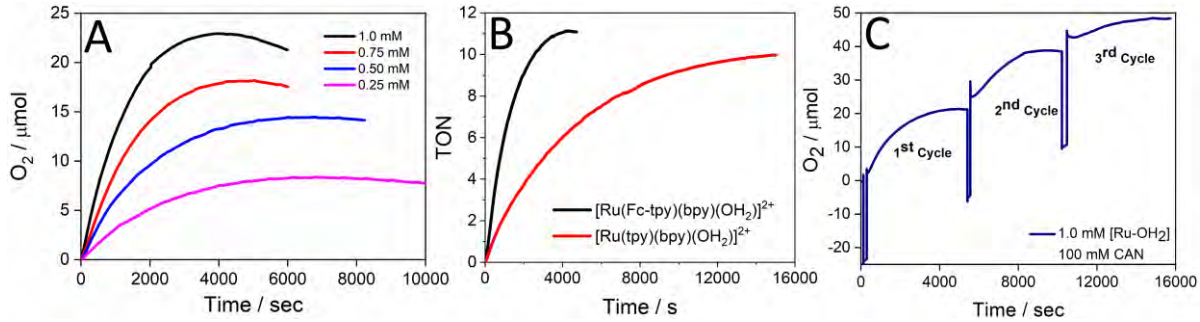

Figure 2.6. (A) O_2 evolution by $[Ru(Fc\text{-}tpy)(bpy)(OH_2)](PF_6)_2$ with various complex concentration at 100 mM CAN; (B) Comparison of O_2 evolution by 1.0 mM $Ru(Fc\text{-}tpy)(bpy)(OH_2)](PF_6)_2$ with 1.0 mM $Ru(tpy)(bpy)(OH_2)](PF_6)_2$ in presence of 100 mM CAN; (C) The reiteration of catalytic cycles with the addition of 100 mM CAN.

2.3.9. Catalytic Stability

The stability and reproducibility of the complex were determined based on the regeneration of the catalyst that occurred in the system. The plot Figure 2.6(C) shows the oxygen evolution by 1.0 mM of the catalyst with iterative addition of 100 mM of CAN up to three cycles (after the third cycle continuously with the measurement of O_2 pressure goes beyond the sensitivity of differential pressure manometer, that's why only three cycles were displayed in the plot Figure 2.6(C). This plot Figure 2.6(C) reveals that the oxidant CAN exhausts in the catalytic process, whereas the catalyst remains stable in the medium. The initial rate of the O_2 evolution is nearly the same in each of the repeated cycles. The stability of the catalyst was also verified by UV-Vis spectroscopy (Figure A19). In this case, a solution of 0.175 mM $[Ru(tpy)(bpy)(OH_2)](PF_6)_2$ was added with 10 equiv. of CAN. The change in absorbance of $[Ru(Fc\text{-}tpy)(bpy)(OH_2)](PF_6)_2$ upon oxidation was regained to Ru^{II} state with the addition of 10 equiv. of ascorbic acid. In order to confirm the reproducibility of the complex open circuit potential measurement *vs*. time (Figure A20) was conducted by taking 0.50 mM of the complex in triflic acid at pH 1.0. It was observed that the resting potential for Ru^{III} state was 0.40 V *vs.* SCE and after the addition of 6 equivalent of CAN, potential of the complex becomes 0.91 V *vs.* SCE i.e. for Ru^{V} state. After a certain period, the potential starts decreasing towards the resting potential of the Ru^{III} state. That indicates the catalyst remains stable in the acidic medium and reverts to its initial state.

2.3.10. Kinetics and Plausible Mechanism

2.3.10.1. Stoichiometric CAN titration

The stoichiometric addition of CAN into the 0.1 mM of **Ru-OH$_2$** solution in pH 1.0 triflic acid was carried out to determine several oxidation states of ruthenium. The changes in the absorbance *vs.* pH were monitored by UV–Vis spectroscopy (Figure A21–A23). After addition of one equivalent of CAN to **Ru-OH$_2$** (λmax = 486 nm), it oxidizes to $[Ru^{III}(Fc\text{-}tpy)(bpy)(OH_2)]^{2+}$ (λ_{max} = 486 nm). The addition of another equivalent of CAN generates $[Ru^{IV}{=}O]^{2+}$ (λ_{max} = 362 nm). No significant change was observed after adding further equivalents of CAN at 486 nm spectral band, whereas the increase at 362 nm spectral band was observed. It was difficult to identify the presence of $[Ru^{V}{=}O]^{3+}$ and $[Ru^{VI}{=}O]^{4+}$from the changes in absorbance from $[Ru^{III}\text{-}OH]^{2+}$ species. The kinetic studies for the water oxidation were carried out with the addition of 7 equiv. CAN into the 0.15 mM **Ru-OH$_2$** in pH 1.0 triflic acid (Figure A22 and A23). The evolution of the spectra with time during the interaction of CAN with **Ru-OH$_2$** was monitored by ReactLab Kinetics Software. The model (Eqs. (2.4) to (2.9)) was fitted with six species like $[Fc^{+}\text{-}Ru^{V}{=}O]^{4+}$, $[Fc^{+}\text{-}Ru^{VI}{=}O]^{5+}$, $[Fc^{+}\text{-}Ru^{IV}\text{-}O\text{-}OH]^{4+}$, $[Fc^{+}\text{-}Ru^{V}\text{-}O\text{-}O]^{4+}$, $[Fc^{+}\text{-}Ru^{III}\text{-}OH_2]^{4+}$, and $[Fc^{+}\text{-}Ru^{III}\text{-}OH]^{3+}$ along with six parameters k_1, $k_{O...O}$, k_2, k_{O2} and, logK. The changes in absorbance and the species distribution have been provided in Figure 2.7(A and B). The interaction step between $[Fc^{+}\text{-}Ru^{IV}\text{-}O\text{-}OH]^{4+}$ and Ce^{4+} is the rate-determining step (RDS).

$$[Fc^{+}\text{—}Ru^{II}(OH_2)]^{3+} + 3Ce^{4+} \xrightarrow{\text{Rapid}} [Fc^{+}\text{—}Ru^{V}{=}O]^{4+} + 3Ce^{3+} + 2H^{+} \tag{2.4}$$

$$[Fc^{+}\text{—}Ru^{V}{=}O]^{4+} + Ce^{4+} \xrightarrow[1.8\times10^{-2}\ M^{-1}S^{-1}]{k_1} [Fc^{+}\text{—}Ru^{VI}{=}O]^{5+} + Ce^{3+} \tag{2.5}$$

$$[Fc^{+}\text{—}Ru^{VI}{=}O]^{5+} + H_2O \xrightarrow[8.1\times10^{-4}\ S^{-1}]{k_{O.....O}} [Fc^{+}\text{—}Ru^{IV}\text{—}O\text{—}OH]^{4+} + H^{+} \tag{2.6}$$

$$[Fc^{+}\text{—}Ru^{IV}\text{—}O\text{—}OH]^{4+} + Ce^{4+} \xrightarrow[6.0\times10^{-4}\ M^{-1}S^{-1}]{k_2} [Fc^{+}\text{—}Ru^{V}O\text{—}O]^{4+} + Ce^{3+} + H^{+} \tag{2.7}$$

$$[Fc^{+}\text{—}Ru^{V}\text{—}O\text{—}O]^{4+}\ H_2O \xrightarrow[8.9\times10^{-4}\ S^{-1}]{k_{O_2}} [Fc^{+}\text{—}Ru^{III}(OH_2)]^{4+} + O_2 + H^{+} \tag{2.8}$$

$$[Fc^{+}\text{—}Ru^{III}(OH_2)]^{4+} \underset{-3.18}{\overset{\log K}{\rightleftharpoons}} [Fc^{+}\text{—}Ru^{III}(OH)]^{3+} + H^{+} \tag{2.9}$$

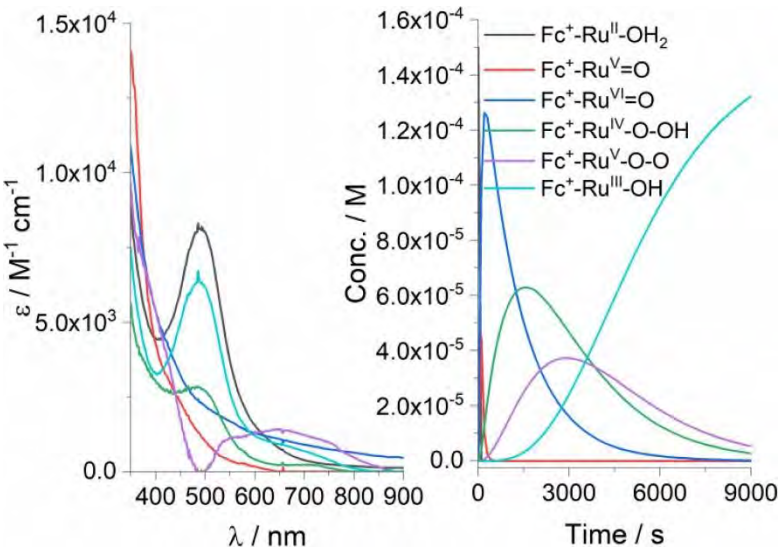

Figure 2.7. (A) Spectra of the intermediate species extracted from the kinetics fitting; (B) Species distribution of the intermediate species.

Based on the experimental results and the fitted model as per Eqs. (2.4) to (2.9), the plausible mechanism has been reported in Scheme 2.3. The catalytic cycle for the water oxidation process in **Ru-OH₂** follows the sequence $[Fc^{+}\text{-}Ru^{II}\text{-}OH_2]^{3+} \rightarrow [Fc^{+}\text{-}Ru^{V}{=}O]^{4+} \rightarrow [Fc^{+}\text{-}Ru^{VI}{=}O]^{5+} \rightarrow [Fc^{+}\text{-}Ru^{IV}\text{-}O\text{-}OH]^{4+} \rightarrow [Fc^{+}\text{-}Ru^{V}\text{-}O\text{-}O]^{4+} \rightarrow [Fc^{+}\text{-}Ru^{III}\text{-}OH_2]^{4+} \rightarrow [Fc^{+}\text{-}Ru^{III}\text{-}OH]^{3+}$. From the Pourbaix diagram, it was inferred that at pH 1.0, Considering the $[Fc^{+}\text{-}Ru^{II}\text{-}OH_2]^{3+} \rightarrow [Fc^{+}\text{-}Ru^{V}{=}O]^{4+}$ from the sudden changes in the spectra Figure A21–A23, the rest of the processes in equations 2.5–2.9 were considered for the model fitting. The $[Fc^{+}\text{-}Ru^{V}{=}O]^{4+} \rightarrow [Fc^{+}\text{-}Ru^{VI}{=}O]^{5+} + e^{-}$ was a faster process, wherein $k_1 = 1.8 \times 10^{-2}\ M^{-1}\ s^{-1}$. The catalytic current starts after $[Fc^{+}\text{-}Ru^{VI}{=}O]^{5+}$ (Figure 2.3); hence the active species is $[Fc^{+}\text{-}Ru^{VI}{=}O]^{5+}$ species. Therefore, the formation of $[Fc^{+}\text{-}Ru^{IV}\text{-}O\text{-}OH]^{4+}$ intermediate *via* $[Fc^{+}\text{-}Ru^{VI}{=}O]^{5+}$ species in the presence H_2O has been considered. This step is the O···O bond formation step, where $k_{O\cdots O} = 8.1 \times 10^{-4}\ M^{-1}\ s^{-1}$. The $[Fc^{+}\text{-}Ru^{IV}\text{-}O\text{-}OH]^{4+}$ undergoes a slow formation of $[Fc^{+}\text{-}Ru^{V}\text{-}O\text{-}O]^{4+}$ in the presence of Ce^{4+} and generates Ce^{3+} with the loss of $1H^{+}$, which the rate-determining step with $k_2 = 6.0 \times 10^{-4}\ M^{-1}\ s^{-1}$. The $[Fc^{+}\text{-}Ru^{V}\text{-}O\text{-}O]^{4+}$ in the presence of H_2O releases O_2 and reverts into $[Fc^{+}\text{-}Ru^{III}\text{-}OH_2]^{4+}$, wherein $k_{O2} = 8.9 \times 10^{-4}\ s^{-1}$. However, the final species spectrum is similar to $[Fc^{+}\text{-}Ru^{III}\text{-}OH]^{3+}$; hence it is expected that $[Fc^{+}\text{-}Ru^{III}\text{-}OH_2]^{4+}$ may undergo acid-base equilibria to revert into the original $[Fc^{+}\text{-}Ru^{III}\text{-}OH]^{3+}$, wherein the K was found to be 6.6×10^{-4}. The experimental and simulated result shows that the interaction step between $[Fc^{+}\text{-}Ru^{IV}\text{-}O\text{-}OH]^{4+}$ and Ce^{4+} is the rate-determining step (RDS) in the catalytic oxygen evolution reaction. The rate of O_2 evolution was found to be $k_{O2} = 8.9 \times 10^{-4}\ s^{-1}$.

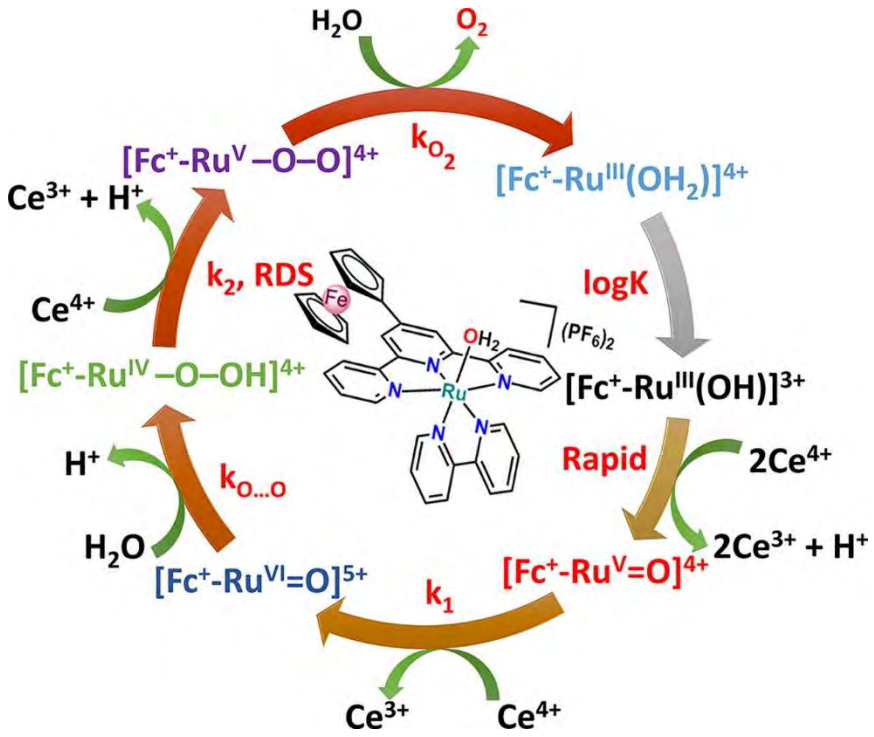

Scheme 2.3 A plausible mechanism for water oxidation by **[Ru-OH$_2$]**.

A comparison Table 2.1 has been provided based on the Ru-centered single-site water oxidation catalysts having $[Ru(tpy)(bpy)(OH_2)]^{2+}$ scaffold. Table 2.1 reveals that **Ru-OH$_2$** is an active, stable, and catalytically sound WOC and at par the reported catalysts having $[Ru(tpy)(bpy)(OH_2)]^{2+}$ scaffold in terms of TOF and k_{O2}.

Table 2.1. Comparison between Ru centred single site WOCs having $[Ru(tpy)(bpy)(OH_2)]^{2+}$ scaffold.

WOCs	$E_{1/2}$ Ru^{II}/Ru^{III} (V *vs.* SCE)	pK_a	k_{O2}	TON	TOF	Reference
$[Ru(Fc\text{-}tpy)(bpy)(OH_2)]^{2+}$	0.28	10	6.6×10^{-4}	12[a]	6.0×10^{-3}	This Work
$[Ru(tpy)(bpy)(OH_2)]^{2+}$	0.73	-	0.6×10^{-4}	10[a]	2.0×10^{-3}	This Work, [7]
$[Ru(OEt\text{-}tpy)(bpy)(OH_2)]^{2+}$	0.74	10.4	-	690[b]	1.1×10^{-1}	[17]
$[Ru(OMe\text{-}tpy)(bpy)(OH_2)]^{2+}$	-	9.5	-	375[b]	-	[17]
$[Ru(Me\text{-}tpy)(bpy)(OH_2)]^{2+}$	-	9.4	-	96[b]	-	[17]
$[Ru(Cl\text{-}tpy)(bpy)(OH_2)]^{2+}$	-	8.5	-	67[b]	-	[17]
$[Ru(2py\text{-}tpy)(bpy)(OH_2)]^{2+}$	0.50	9.8	-	16[a]	5.3×10^{-3}	[18]
$[Ru(3py\text{-}tpy)(bpy)(OH_2)]^{2+}$	0.50	9.8	-	13[a]	4.6×10^{-3}	[18]
$[Ru(4py\text{-}tpy)(bpy)(OH_2)]^{2+}$	0.50	9.8	-	17[a]	5.8×10^{-3}	[18]
$[Ru(QCl\text{-}tpy)(bpy)(OH_2)]^{2+}$	0.80	10.2	-	19[a]	1.4×10^{-3}	[19]
$[Ru(Ql\text{-}tpy)(bpy)(OH_2)]^{2+}$	0.79	10.5	-	18[a]	0.3×10^{-3}	[20]

$[Ru(tpy)(bpy\text{-}OMe)(OH_2)]^{2+}$	0.69	11.2	1.5×10^{-4}	9[c]	1.1×10^{-2}	[7]
$[Ru(tpy)(bpy\text{-}CO_2H)(OH_2)]^{2+}$	0.94	10.4	6.9×10^{-4}	2[c]	5.6×10^{-4}	[21]
$[Ru(tpy)(bpm)(OH_2)]^{2+}$	-	-	7.4×10^{-4}	7.8[d]	6.9×10^{-3}	[7]
$[Ru(tpy)(bpg)(OH_2)]^{2+}$	0.83	10.3	2.7×10^{-4}	833[e]	1.9×10^{-3}	[10]

[a] TON calculated with respect to 100 equiv. of CAN; [b] TON calculated with respect to 5000 equiv. of CAN; [c] TOF calculated for 10 min; [d] TON calculated with respect to 30 equiv. of CAN; [e] TON calculated with respect to 10^8 equiv. of CAN.

2.4. Summary

In summary, herein the $[Ru(Fc\text{-}tpy)(bpy)Cl]PF_6$ (**Ru-Cl**) and its corresponding aqua $[Ru(Fc\text{-}tpy)(bpy)OH_2](PF_6)_2$ (**Ru-OH$_2$**) complexes have been synthesized. The **Ru-OH$_2$** complex has been employed as a water oxidation catalyst (WOC) in pH 1.0 triflic acid in the presence of the sacrificial electron acceptor CAN. Under strong acidic conditions, the Fe(II) centre of ferrocene moiety (Fc) undergoes protonation to generate the Fe(IV)hydrido species Fe(IV)-H (FcH^+). In this case, the resting potential of **Ru-OH$_2$** complex in pH 1.62 phosphate buffer indicates that the Fe center in ferrocene is in Fe^{III} state, and the Ru center is in Ru^{III} state. The introduction of the ferrocene moiety in the 'tpy' scaffold behaves as an electron-donating group due to the oxidation of Fe^{II} to Fe^{III}. The onset potential for the catalytic water oxidation is 230 mV less as compared to the parent $[Ru(tpy)(bpy)OH_2]^{2+}$ complex. During the catalysis, it was found that the rate of O_2 evolution of **Ru-OH$_2$**, is quite high as compared to $[Ru(tpy)(bpy)OH_2]^{2+}$ complex. The Pourbaix diagram indicates the existence of $H^+/2e^-$ PCET at pH 1.0 between $[Fc^+\text{-}Ru^{III}\text{-}OH]^{3+} \rightarrow [Fc^+\text{-}Ru^{V}{=}O]^{4+} + H^+ + 2e^-$. The stoichiometric changes in the absorbance spectra of the intermediate species involved in the water oxidation catalytic process were predicted through the SVD analysis with an appropriate model fitting in ReactLab kinetics Bundle version 1.1 software. This case indicates that $[Ru^{VI}{=}O]^{3+}$ is active species in the kinetic process for O_2 evolution. The open-circuit potential test reveals that the final species rests at Ru^{III} state. The spectra evolved from the reaction mixture indicated that $[Fc^+\text{-}Ru^{VI}{=}O]^{5+}$ generates $[Fc^+\text{-}Ru^{IV}\text{-}O\text{-}OH]^{4}+$ in the presence of H_2O. Further $[Fc^+\text{-}Ru^{IV}\text{-}O\text{-}OH]^{4+}$ converts into $[Fc^+\text{-}Ru^{V}\text{-}O\text{-}O]^{4+}$ in the presence of Ce^{4+}, which is the rate-determining step (RDS) with $k_{RDS} = 6.0 \times 10^{-4}\ M^{-1}\ s^{-1}$. The $[Fc^+\text{-}Ru^{V}\text{-}O\text{-}O]^{4+}$ species releases O_2 in the presence of H_2O. The rate of O···O bond formation ($k_{O\cdots O}$) and O_2 evolution (k_{O2}) are $8.1 \times 10^{-3}\ s^{-1}$ and $8.9 \times 10^{-4}\ s^{-1}$.

2.5 References

1. Cox, C.R., Lee, J. Z., Nocera, D. G., Buonassisi, T. Ten - Percent solar-to-fuel conversion with nonprecious materials, *Proc. Natl. Acad. Sci. U. S. A.* **2014**, *111* (39), 14057-14061.
2. Su, J., Vayssieres, L. A Place in the Sun for Artificial Photosynthesis? *ACS Energy let.* **2016**, *1* (1), 121-135.
3. Zong, R., Thummel, R. P. A New Family of Ru Complexes for Water Oxidation , *J. Am. Chem. Soc.* **2005**, *27* (37), 12802-12803.
4. Concepcion, J. J., Tsai, M. -K., Muckerman, J. T., Meyer, T. J. Mechanism of Water Oxidation by Single-Site Ruthenium Complex Catalysts, *J. Am. Chem. Soc.* **2010**, *132* (5) 1545-1557.
5. Concepcion, J. J., Jurss, J. W., Norris, M. R., Chen, Z., Templeton , J. L., Meyer, T. J. Catalytic Water Oxidation by Single-Site Ruthenium Catalysts. *Inorg. Chem*. **2010**, *49* (4), 1277–1279.
6. Wasylenko, D. J., Ganesamoorthy, C., Koivisto, B. D., Henderson, M. A., Berlinguette, C. P. Insight into Water Oxidation by Mononuclear Polypyridyl Ru Catalysts, *Inorg. Chem.* **2010**, *49* (5), 2202–2209.
7. Wasylenko, D. J., Ganesamoorthy, C., Henderson, M. A., Koivisto, B. D., Osthoff, H. D., Berlinguette, C. P. Electronic Modification of the [RuII(tpy)(bpy)(OH2)]2+ Scaffold: Effects on Catalytic Water Oxidation. *J. Am. Chem. Soc.* **2010**, *132* (45), 16094–16106.
8. Yamazaki, H., Hakamata, T., Komi, M., Yagi, M. Highly active and tunable catalysts for O2 evolution from water based on mononuclear ruthenium(II) monoaquo complexes', *J. Am. Chem. Soc.* **2011**, *133* (15), 8846–8849.
9. Yoshida, M., Kondo, M., Torii, S., Sakai, K., Masaoka, S. Oxygen Evolution Catalyzed by a Mononuclear Ruthenium Complex Bearing Pendant SO_3^- Groups. *Angew. Chem. Int. Ed.* **2015**, *54* (27), 7981 –7984.
10. Mane, V. S., Kumbhar, A. S., Thummel, R. P. A ruthenium water oxidation catalyst containing a bipyridine glycoluril ligand. *Dalton Trans.* **2017**, *46* (38) 12901-12907.
11. Juneja, A., Macedo, T. S., Moreira, D. R. M., Sores, M. B. P., Liete, A. C. L., Neves, J. K. de A. L., Pereira, V. R. A., Aveulla, F. A., Azam, A. Synthesis of 4'-(2-ferrocenyl)-2,2':6;2"-terpyridine: Characterization and antiprotozoal activity of Mn(II), Co(II), Ni(II), Cu(II) and Zn(II) complexes. *Eur. J. Med.* **2014**, *75*, 203-210.

12. Toyama, M., Inoue, K., Iwamatsu, S., Nagao, N. Syntheses and Crystal Structures of Mono (2,2'-bipyridine)dichlorobis-(dimethyl sulfoxide-S)ruthenium(II) Complexes, [$RuCl_2$(bpy)(dmso-S)$_2$] *Bull. Chem. Soc. Jpn.* **2006**, *79* (10), 1525-1534.
13. Sheldrick, G.M., SADABS, Software for Empirical Absorption Corrections, University of Gottingen, Gottingen, **1996**.
14. Bourhis, L.J., Dolomanov, O.V., Gildea, R.J., J.A.K. Howard, H. Puschmann, The anatomy of a comprehensive constrained, restrained refinement program for the modern computing environment - Olex2 dissected, *Acta Cryst. A.* 2015, *71*, 59–75.
15. Astruc, D., 'Why is Ferrocene so Exceptional?' *Eur. J. Inorg. Chem.* **2017**, *2017* (1), 6-29.
16. Malischewski, M., Seppelt, K., Sutter, J., Heinemann, F. W., Dittrich, B., Meyer, K., Protonation of Ferrocene: A Low-Temperature X-ray Diffraction Study of [Cp_2FeH](PF_6) Reveals an Iron-Bound Hydrido Ligand. *Angew. Chem. Int. Ed.* **2017**, *56* (43), 13372 – 13376.
17. Yagi, M., Tajima, S., Komi, M., Yamazaki, H. Highly active and tunable catalysts for O_2 evolution from water based on mononuclear ruthenium(II) monoaquo complexes, *Dalton Trans.* **2011**, *40* (15), 3802–3804.
18. Patel, J., Majee, K., Ahmad, E., Das, B., Padhi, S. K. Effect of Pyridyl Substitution on Chemical and Photochemical Water Oxidation by [Ru(terpyridine)(bipyridine)(OH_2)]$^{2+}$ Scaffolds. *Eur. J. Inorg. Chem*. **2017**, *2017* (1), 160-171.
19. Patel, J., Majee, K., Ahmad, E., Vatsa, A., Das, B. Padhi, S. K. Electronic Effect on Catalytic Water Oxidation by Single Site [Ru(QCl–tpy)(bpy)(OH_2)]$^{2+}$ Catalyst. *ChemistrySelect.* **2017**, *2* (1), 123-129.
20. Patel, J., Majee, K., Raj, M., Vatsa, A., Rai, S., Padhi, S. K. Effect of Quinoline Substitution on Water Oxidation by [Ru(Ql–tpy)(bpy)(OH_2)](PF_6)$_2$', *ChemistrySelect*., **2017**, *2* (10), 3053-3059.
21. Concepcion, J.J., Jurss, J.W., Templeton, J.L., Meyer, T.J. One Site is Enough. Catalytic Water Oxidation by [Ru(tpy)(bpm)(OH_2)]$^{2+}$ and [Ru(tpy)(bpz)(OH_2)]$^{2+}$. *J. Am. Chem. Soc.* **2008**, *130* (49) 16462–16463.

Appendix A

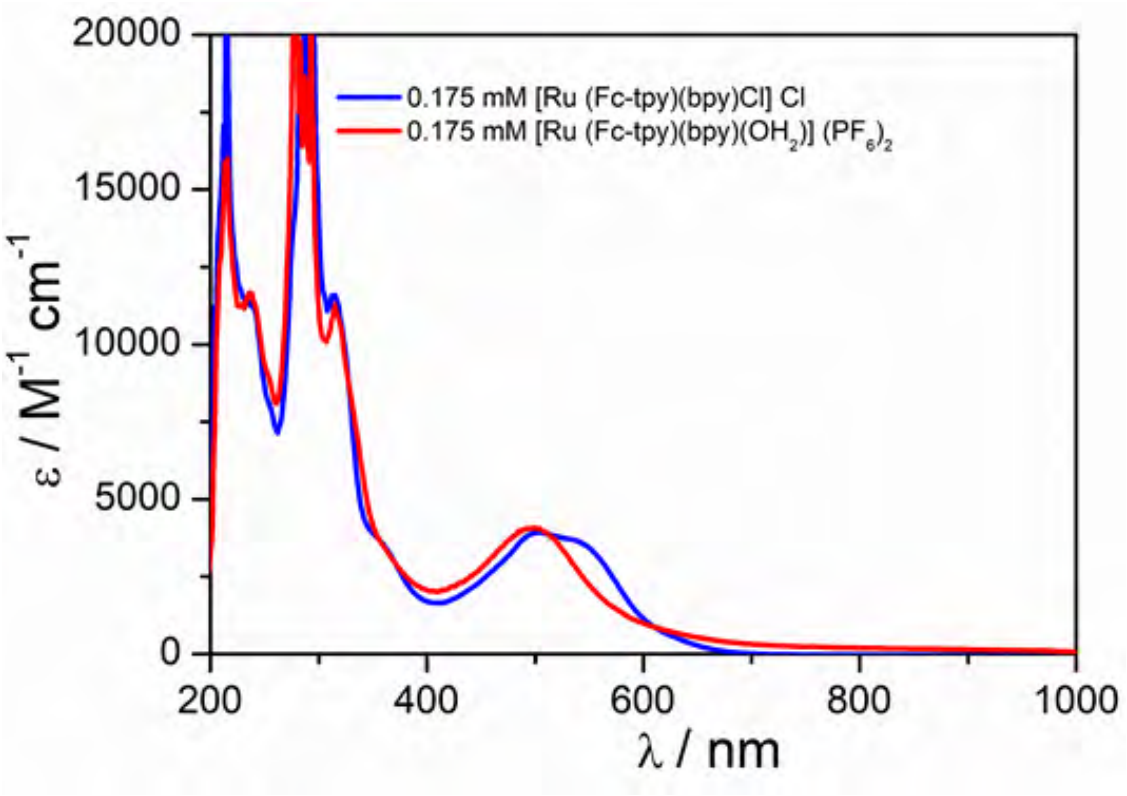

Figure A1. UV-Visible spectra of **Ru-Cl** and **Ru-OH$_2$** in MeOH.

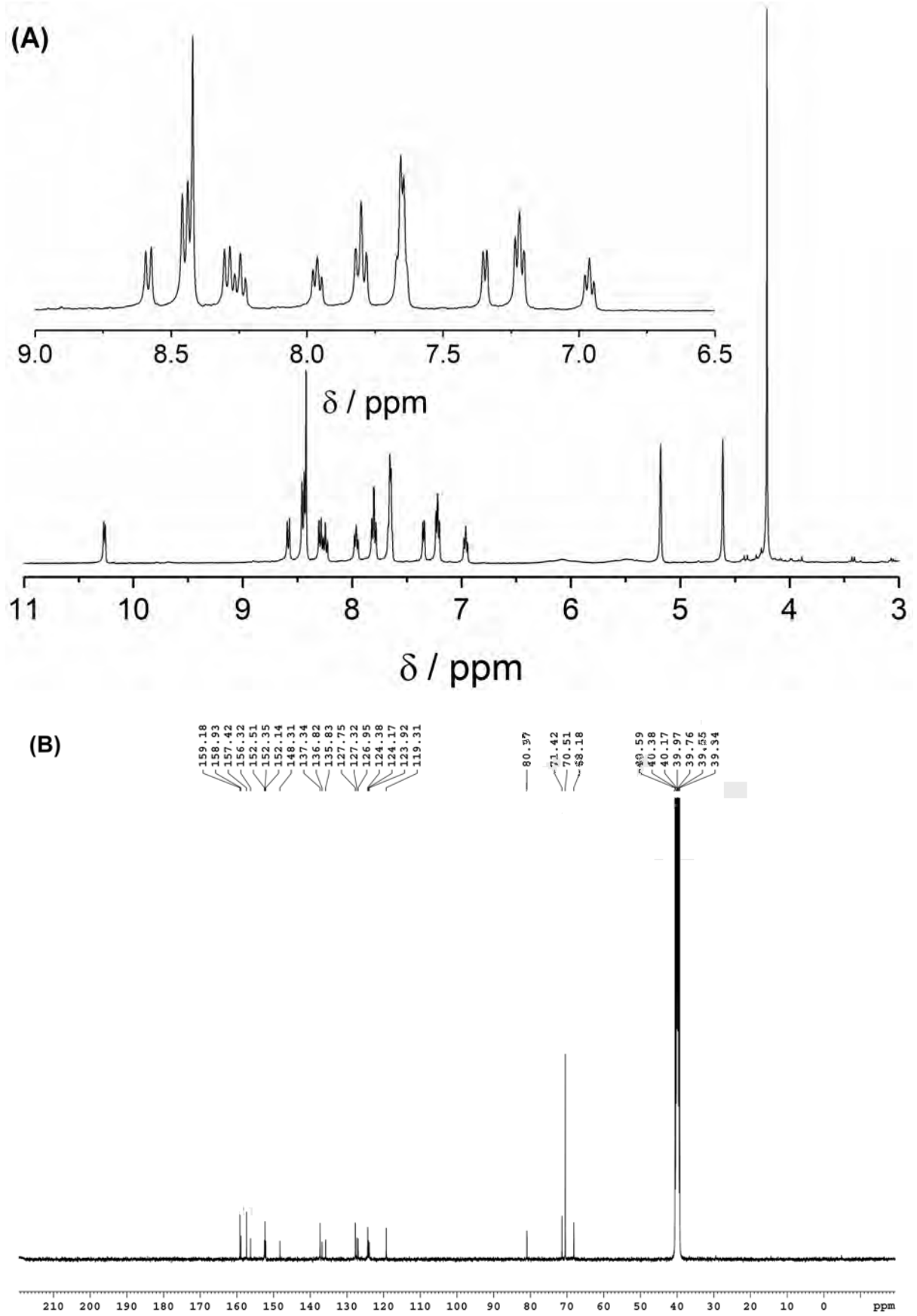

Figure A2. (A) ^{1}H NMR of **Ru-Cl** in CD_3CN; (B) ^{13}C NMR in CD_3SOCD_3.

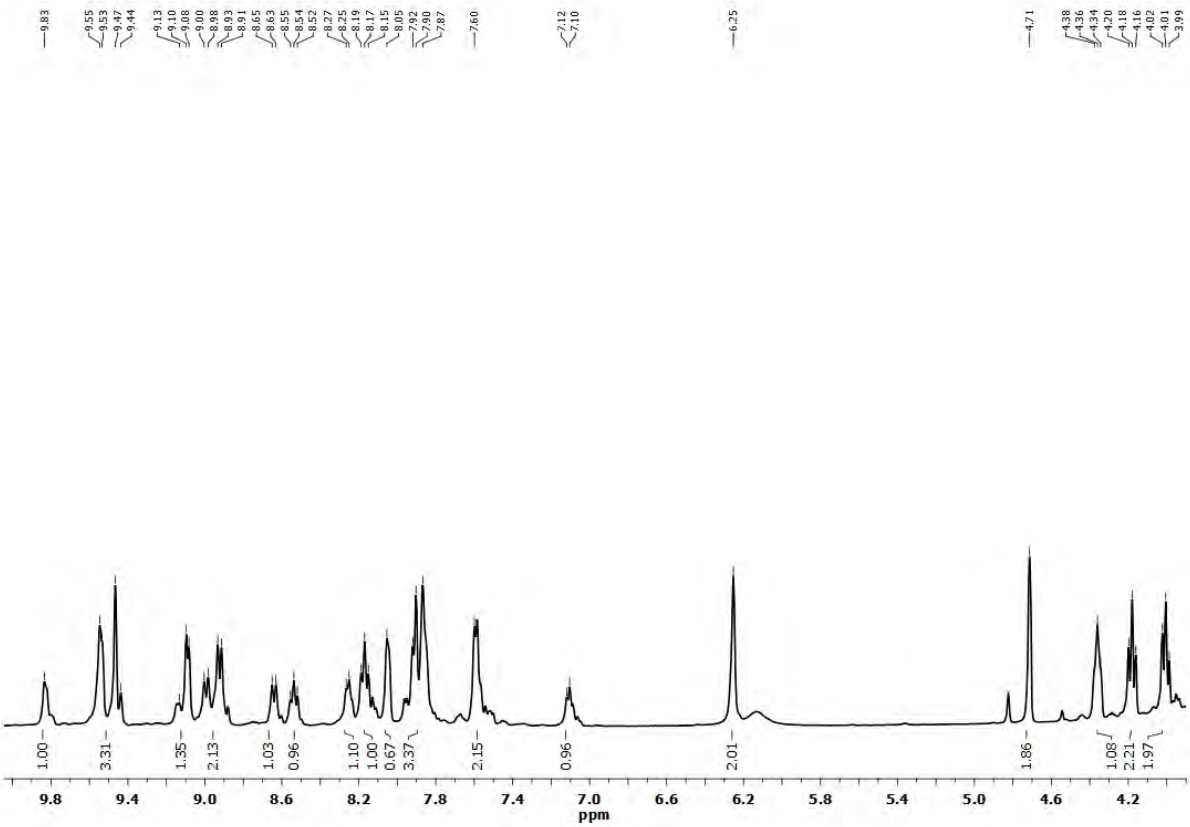

Figure A3. ^{1}H NMR of **Ru-OH$_2$** in $(CD_3)_2CO$ in presence of ascorbic acid.

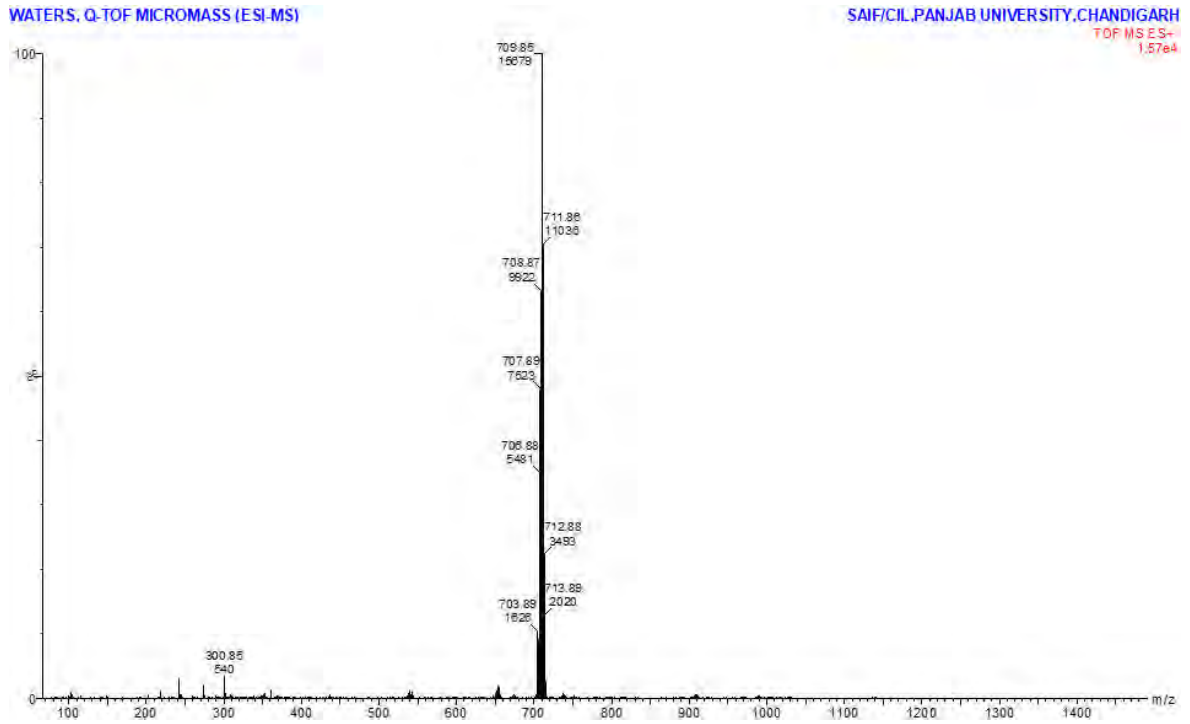

m/z

Figure A4. ESI-MS Spectra of **Ru-Cl** in MeOH.

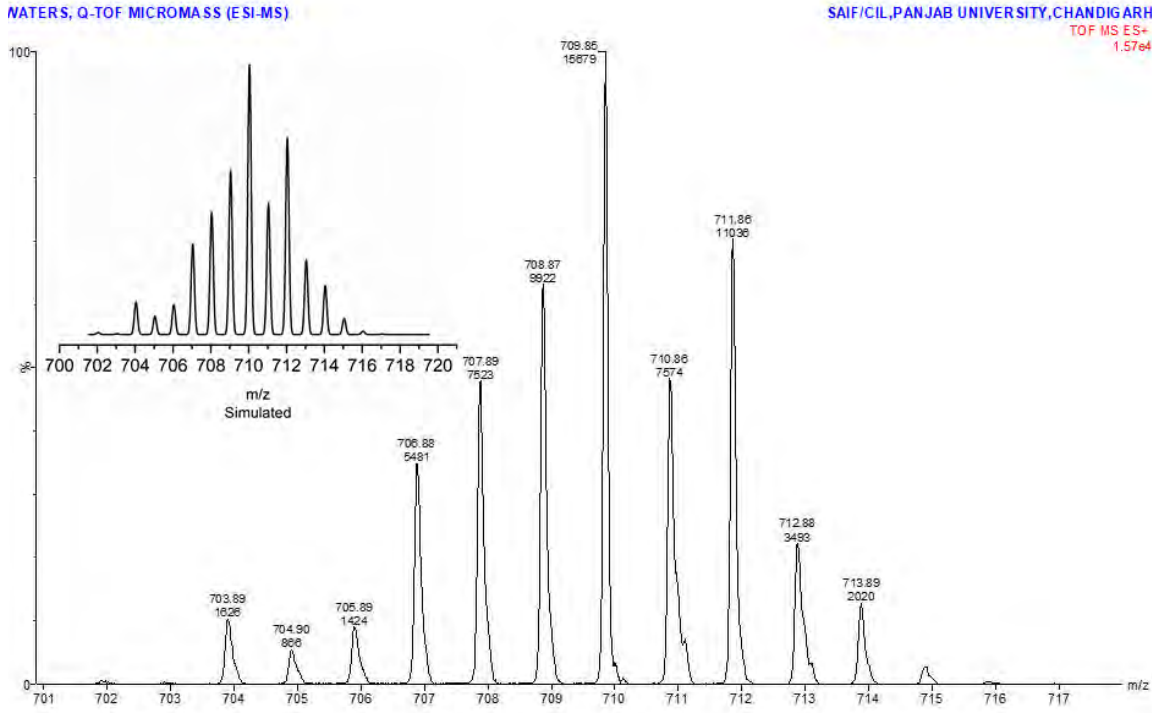

Figure A5. Zoomed region in ESI-MS of the **Ru-Cl.**

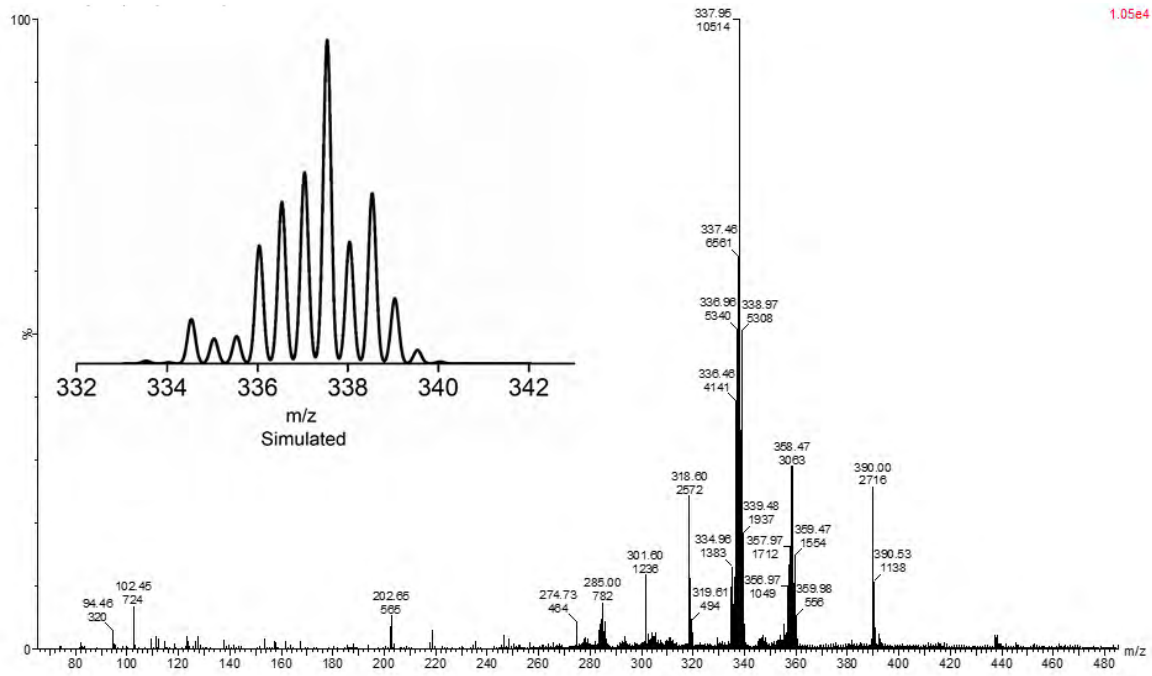

Figure A6. ESI-MS of **Ru-OH$_2$** complex in MeOH.

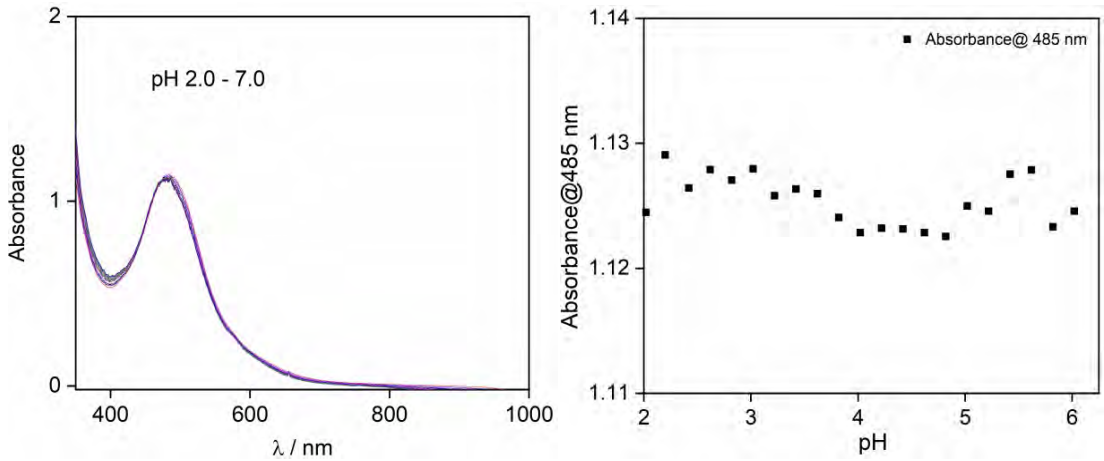

Figure A7. Change in UV-Visible spectra of **Ru-OH$_2$**. (left) and the changes in absorbance vs. pH (right) in Britton– Robinson buffer from pH 2.0 to 7.0.

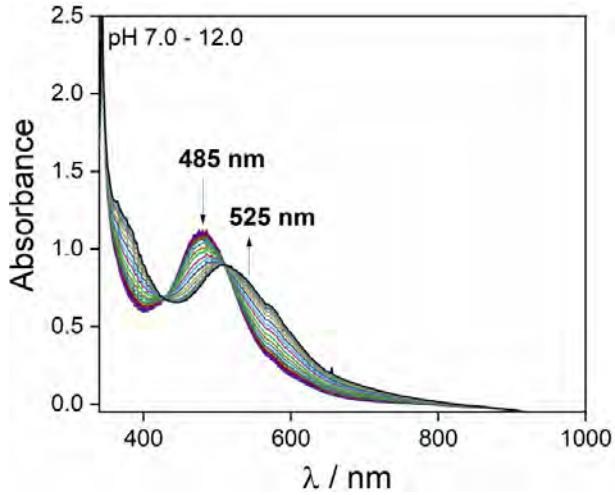

Figure A8. Change in UV-Visible spectra of **Ru-OH$_2$** in Britton–Robinson buffer from pH 7.0 to 12.0.

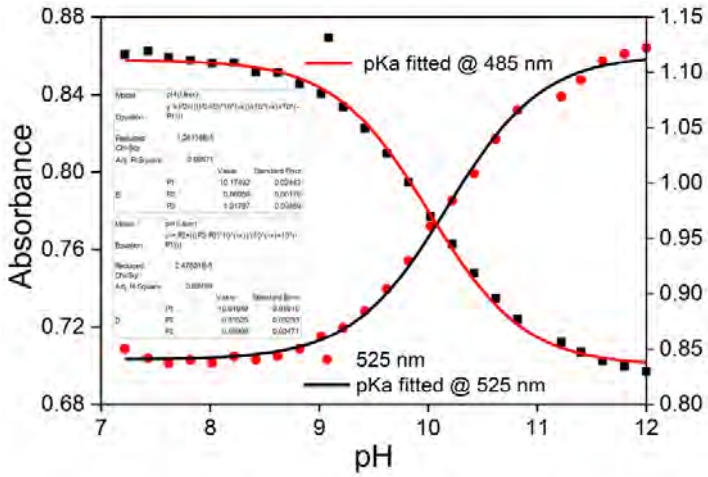

Figure A9. Absorbance vs. pH profile of **Ru-OH$_2$** within the pH 7.0-12.0.

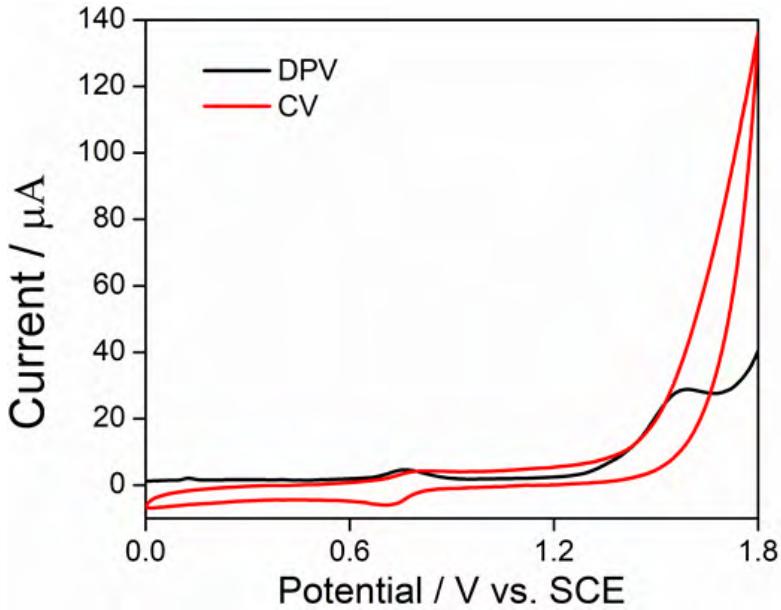

Figure A10. Cyclic voltammetry (Red) and Differential Pulse Voltammetry (Black) of 0.50 mM of **Ru-OH$_2$** complex in phosphate buffer at pH 1.62.

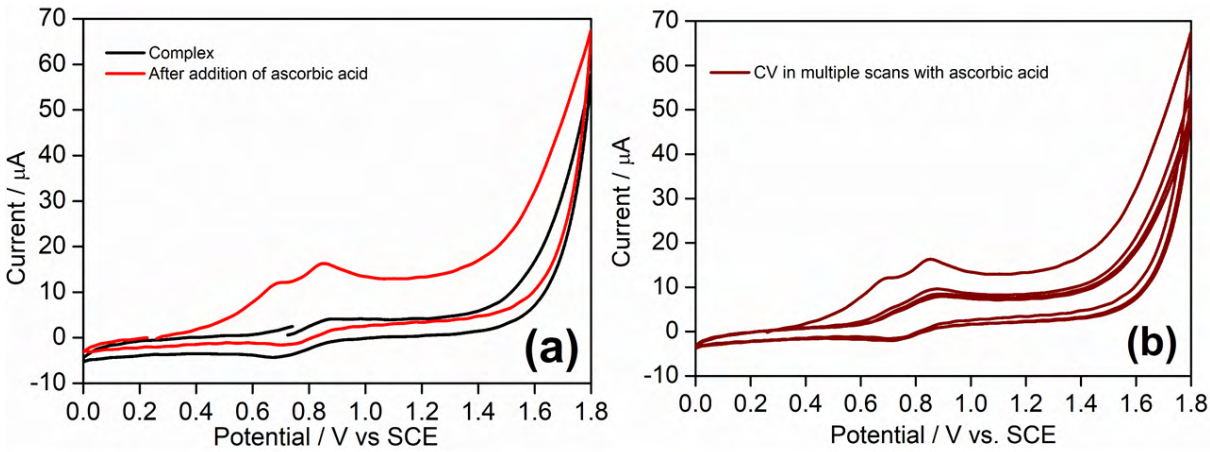

Figure A11. Cyclic voltammetry of **Ru-OH$_2$** complex (a) before (black) and after addition (red) of ascorbic acid in Phosphate buffer at pH 1.62 (b) Cyclic voltammetry of complex with ascorbic acid in multiple scan.

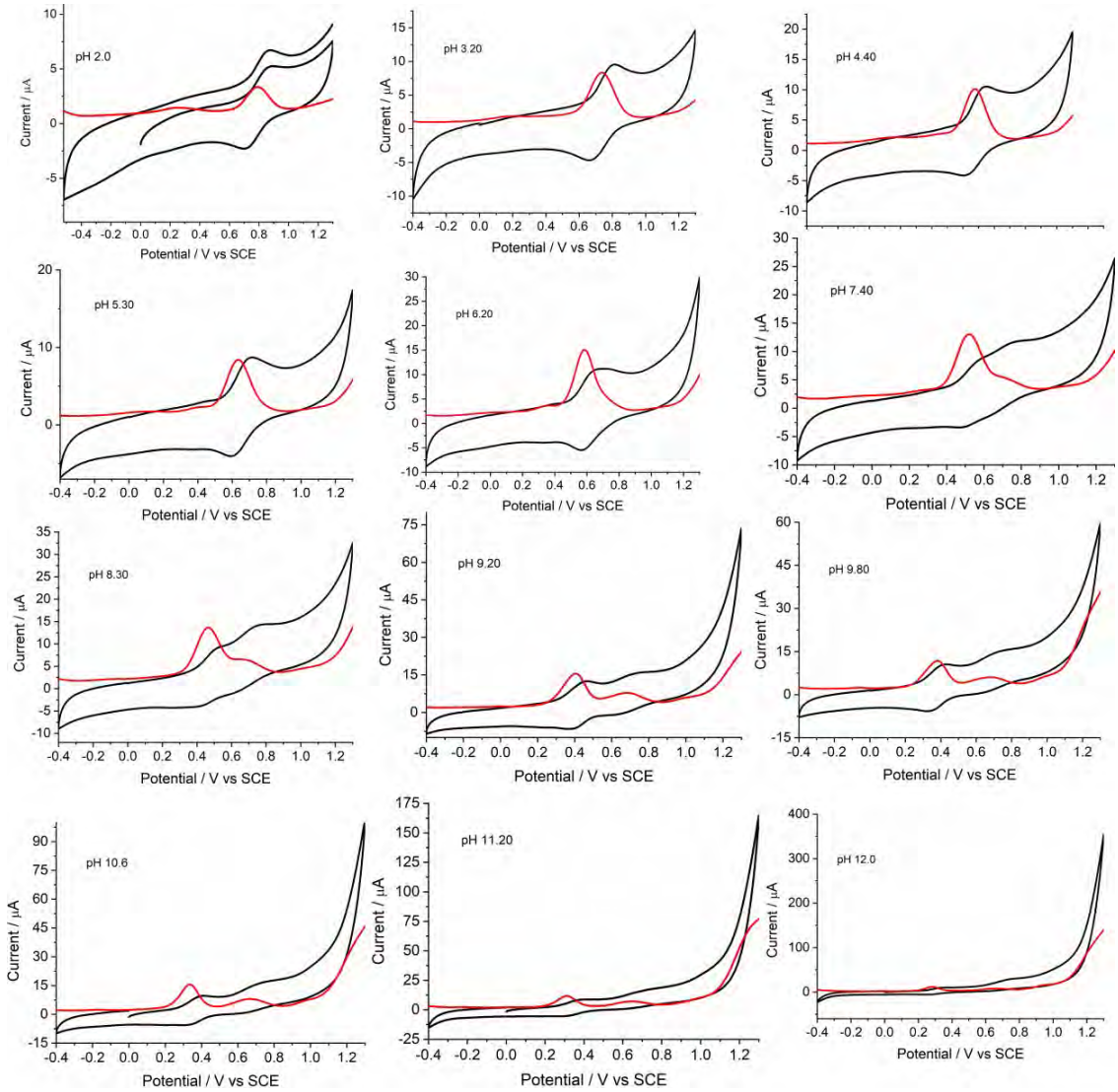

Figure A12. CV and DPV of 0.5 mM in Ru-OH2 in Britton–Robinson buffer from pH 2.0 to 12.0.

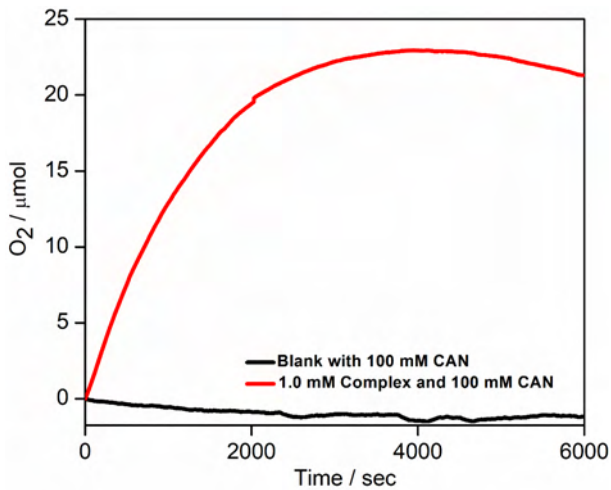

Figure A13. O_2 evolution in pH 1.0 triflic acid in presence of 100 mM of CAN (red) and in presence of 1.0 mM of catalyst (black).

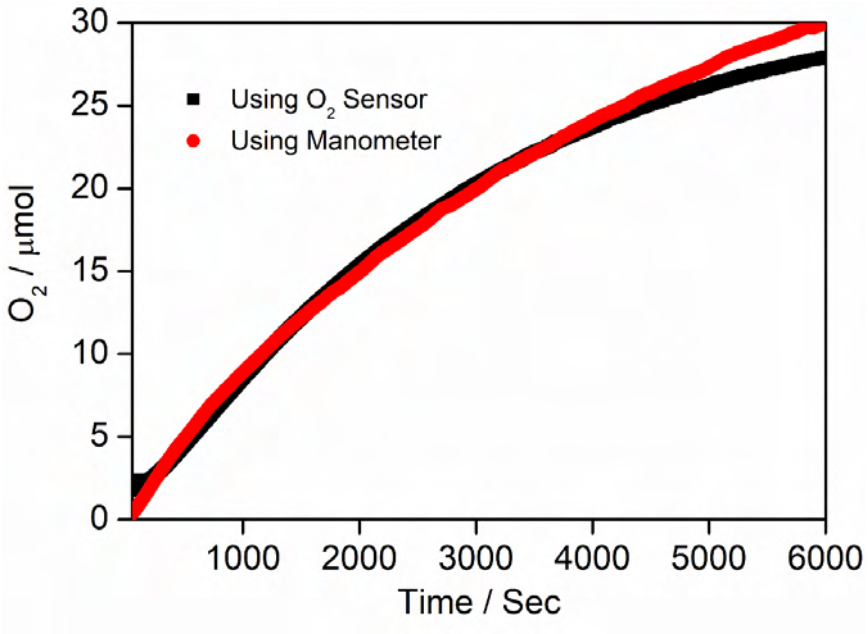

Figure A14. Comparison of Oxygen sensor and Manometry results with 1.0mM complex and 100mM CAN.

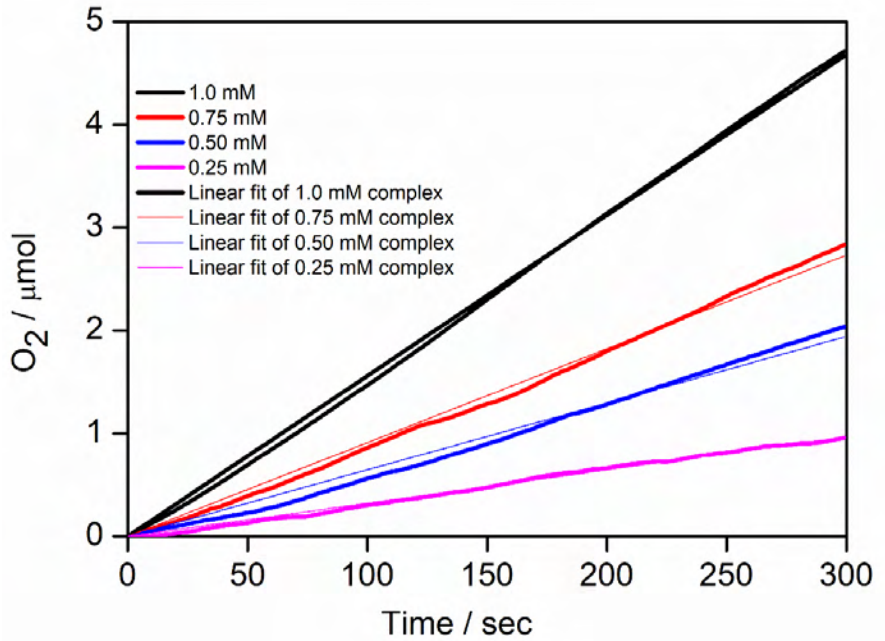

Figure A15 Initial rate upon variation of concentration of the **Ru-OH$_2$** complex in presence of 100 mM CAN.

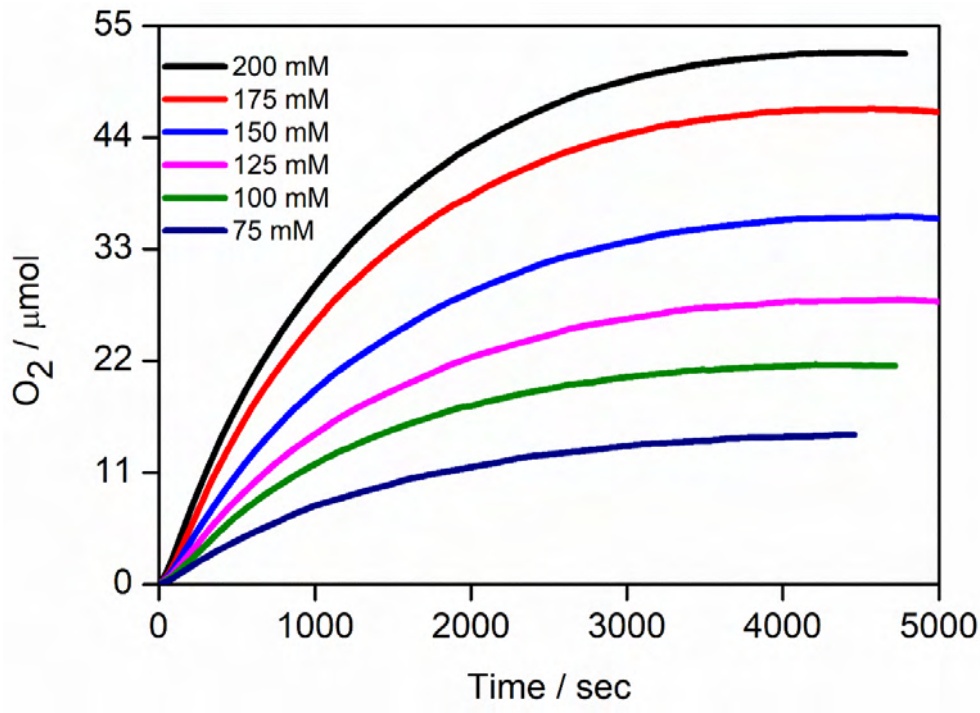

Figure A16. O_2 evolution by **Ru-OH$_2$** with various CAN concentration at 1.0 mM Complex.

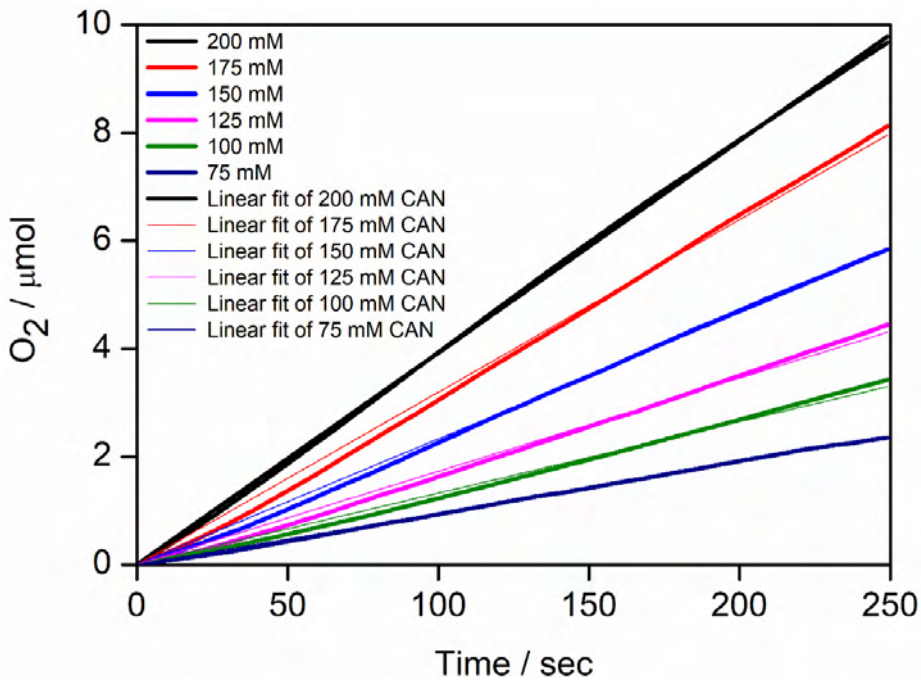

Figure A17. Initial rate upon variation of concentration of the CAN.

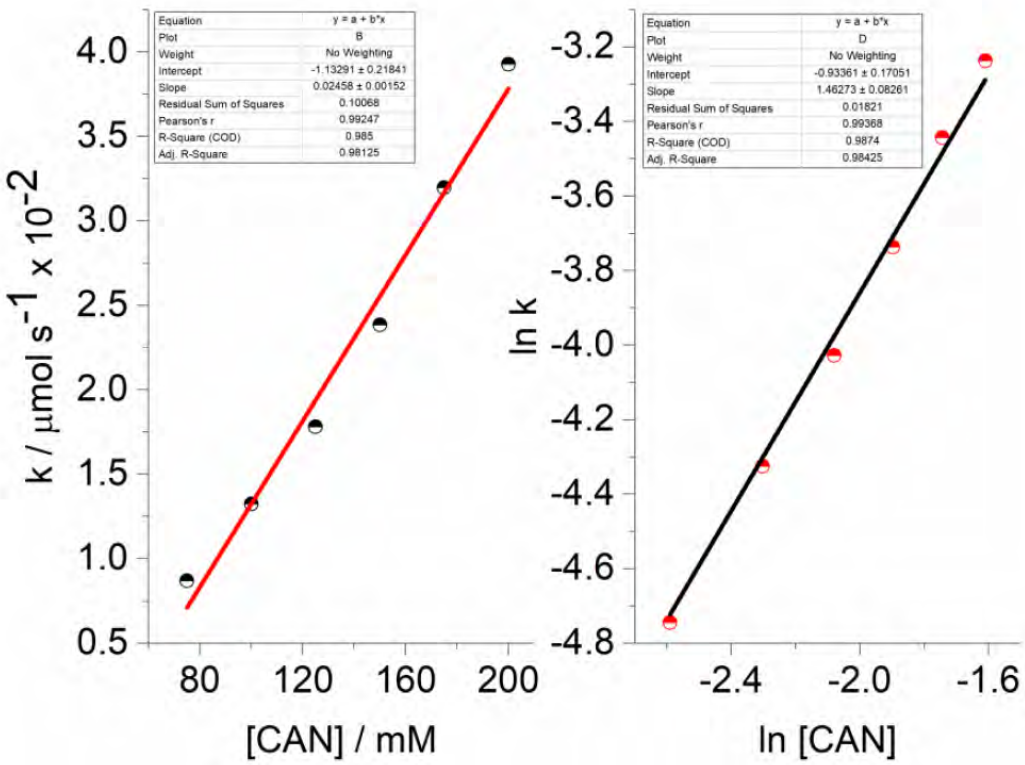

Figure A18. Initial rate *vs.* [CAN] (left) and ln (Initial rate of O2 evolution) *vs.* ln [CAN] (right) in pH 1.0 triflic acid.

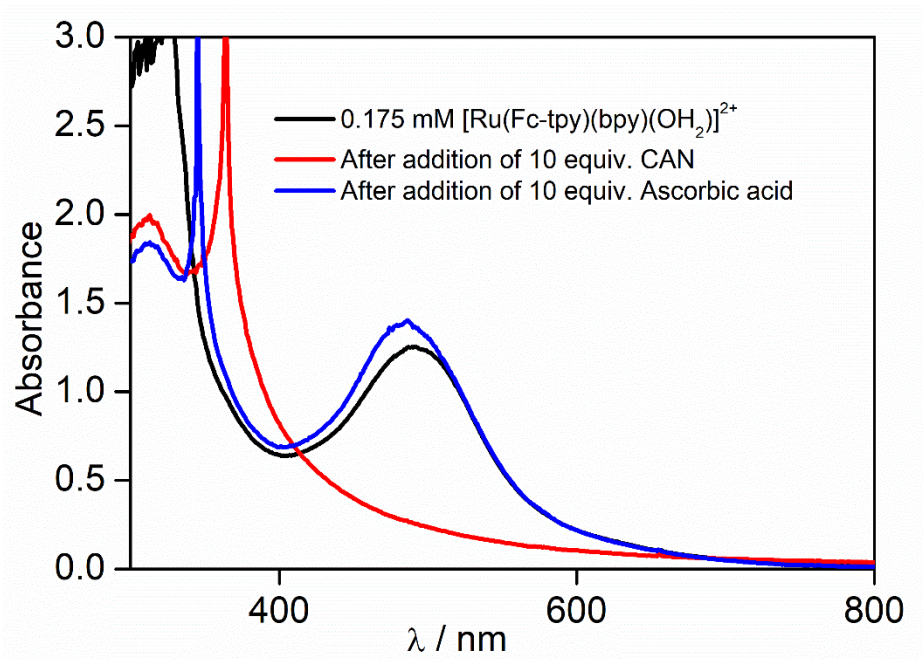

Figure A19. UV- Visible spectra of 0.175 mM of the **Ru-OH$_2$** complex (black) with addition of 10 equiv. of CAN (red) followed by addition of 10 equiv. of ascorbic acid (blue).

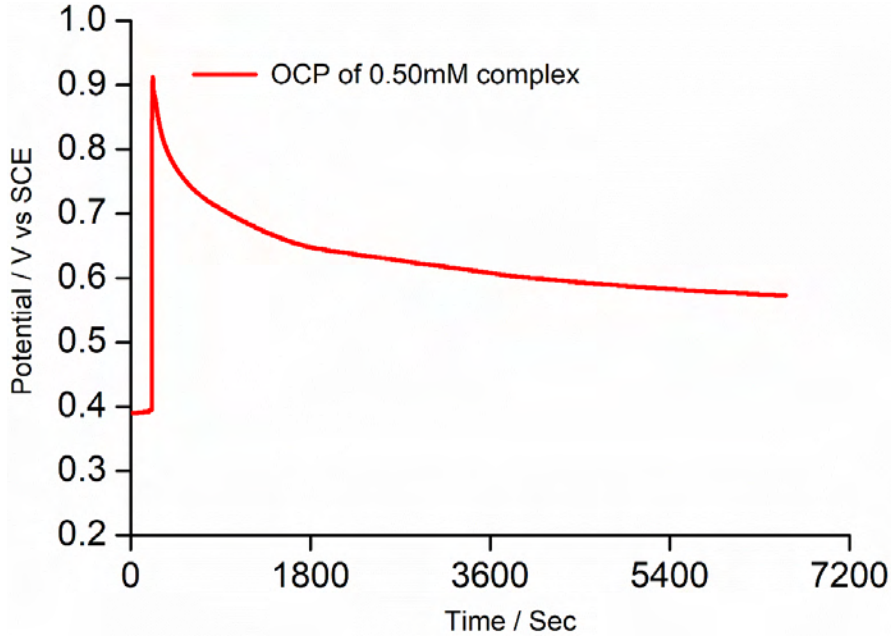

Figure A20. Open circuit potential vs time measurement of the 0.50mM complex in triflic acid at pH 1.0 by addition of 6 equivalent of CAN.

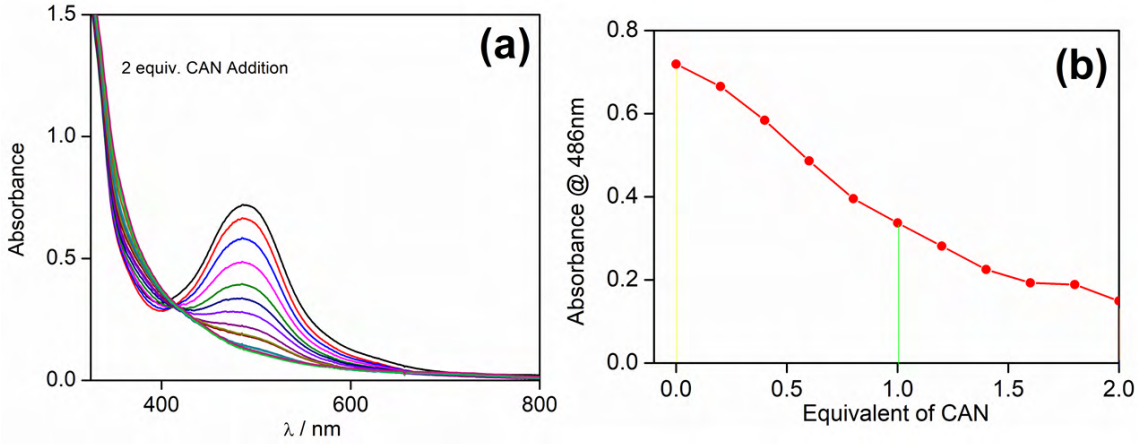

Figure A21. (a) Change in absorbance @486 nm by successive addition of CAN at pH 1.0 in 0.075 mM **Ru-OH$_2$**. **(b)** Decay in absorbance @486 nm by addition of CAN.

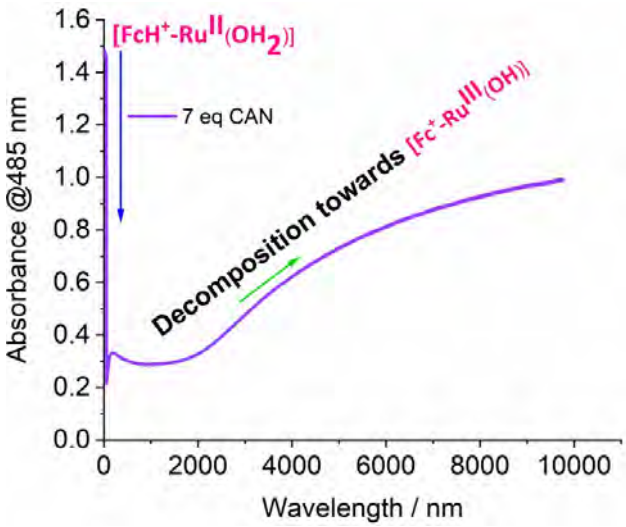

Figure A22. Absorbance@485 nm vs. Time plot of 0.150 mM of catalyst in presence of 7 equiv. of CAN at pH 1.0 triflic acid.

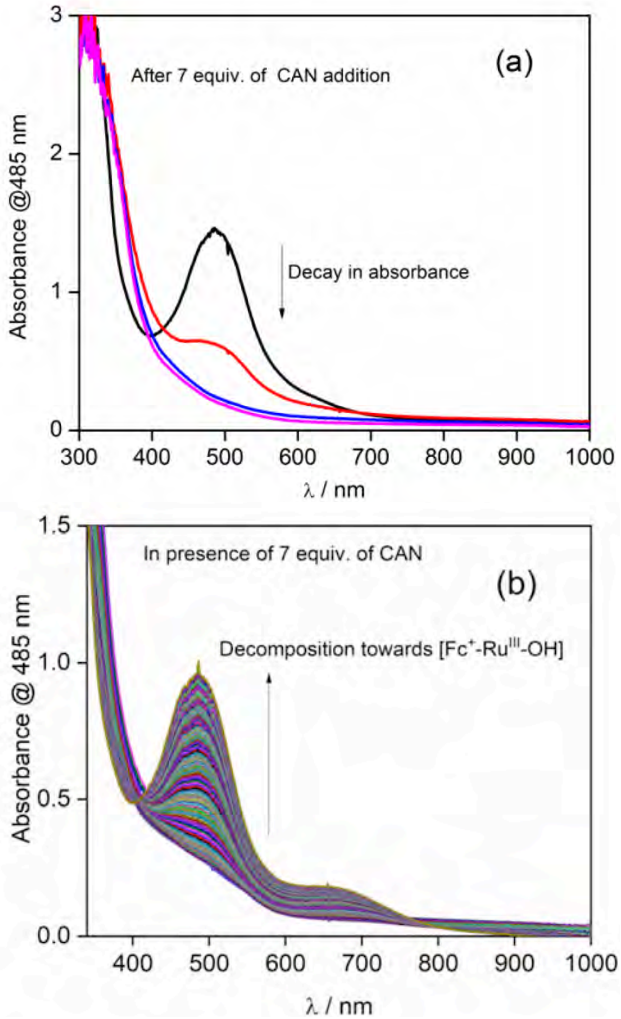

Figure A23. Change in Absorbance *vs.* Time plot of 0.150 mM of catalyst in presence of 7 equiv. of CAN at pH 1.0 triflic acid (a) instant decrease in absorbance (b) decomposition towards initial state

Table A1. Crystal data and structure refinement for [Ru(Fc-tpy)(bpy)(Cl)](PF_6).	
Identification code	1939912
Empirical formula	$C_{35}H_{27}ClF_6FeN_5PRu$
Formula weight	854.96
Temperature/K	298.0
Crystal system	triclinic
Space group	$P\bar{1}$
a/Å	10.3905(7)
b/Å	13.6630(9)
c/Å	14.4405(8)
α/°	76.772(5)
β/°	85.757(5)
γ/°	77.233(6)
Volume/Å^3	1945.7(2)
Z	2
ρ_{calc}g/cm^3	1.4592
μ/mm^{-1}	0.930
F(000)	855.1
Crystal size/mm^3	0.2 × 0.18 × 0.16
Radiation	Mo Kα (λ = 0.71073)
2Θ range for data collection/°	4.54 to 49
Index ranges	$-12 \leq h \leq 12$, $-15 \leq k \leq 15$, $0 \leq l \leq 16$
Reflections collected	6413
Independent reflections	6413 [R_{int} = 0.0000, R_{sigma} = 0.0819]
Data/restraints/parameters	6413/0/451
Goodness-of-fit on F^2	0.928
Final R indexes [I>=2σ (I)]	R_1 = 0.0649, wR_2 = 0.1637
Final R indexes [all data]	R_1 = 0.0984, wR_2 = 0.1794
Largest diff. peak/hole / e Å^{-3}	0.93/-0.68

Table A2. Selected Bond Lengths for [Ru(Fc-tpy)(bpy)(Cl)](PF$_6$).						
Atom	**Atom**	**Length/Å**		**Atom**	**Atom**	**Length/Å**
Ru1	Cl1	2.4234(17)		C20	C21	1.501(10)
Ru1	N3	2.082(5)		C20	C19	1.352(11)
Ru1	N4	2.080(5)		C21	C22	1.396(11)
Ru1	N2	1.971(5)		C30	C29	1.392(12)
Ru1	N1	2.070(5)		C30	Fe1	2.033(8)
Ru1	N5	2.052(5)		C1	C2	1.374(11)

Table A3. Selected Bond Angles for [Ru(Fc-tpy)(bpy)(Cl)](PF$_6$).								
Atom	**Atom**	**Atom**	**Angle/°**		**Atom**	**Atom**	**Atom**	**Angle/°**
N3	Ru1	Cl1	91.50(14)		Fe1	C28	C29	71.0(7)
N4	Ru1	Cl1	94.86(16)		C28	C29	C30	111.4(8)
N4	Ru1	N3	98.13(19)		Fe1	C29	C30	70.1(6)
N2	Ru1	Cl1	90.80(14)		Fe1	C29	C28	70.0(7)
N2	Ru1	N3	78.97(19)		C18	C19	C20	119.5(10)
N2	Ru1	N4	173.7(2)		C19	C18	C17	120.4(10)
N1	Ru1	Cl1	87.92(15)		C34	C33	Fe1	71.6(8)
N1	Ru1	N3	158.3(2)		C32	C33	Fe1	70.4(7)
N1	Ru1	N4	103.5(2)		C32	C33	C34	111.2(16)
N1	Ru1	N2	79.4(2)		C27	Fe1	C26	41.4(3)
N5	Ru1	Cl1	173.70(17)		C30	Fe1	C26	41.7(3)
N5	Ru1	N3	91.6(2)		C30	Fe1	C27	69.1(3)
N5	Ru1	N4	79.3(2)		C28	Fe1	C26	68.8(3)
N5	Ru1	N2	95.2(2)		C28	Fe1	C27	40.4(3)
N5	Ru1	N1	91.2(2)		C28	Fe1	C30	68.0(4)

Determination of pK$_a$ – Derivation of equation 3:

$HA \rightarrow H^+ + A^-$

$C_0 = [HA] + [A^-]$

$= [HA] + \frac{K_a\,[HA]}{[H^+]}$

$= [HA]\left(1 + \frac{K_a}{[H^+]}\right)$

$= [HA]\left(\frac{H^+ + K_a}{[H^+]}\right)$

$[HA] = C_0 \text{ x } \left(\frac{H^+}{[H^+] + K_a}\right)$

Absorbance (A) = $(\varepsilon_{HA} \text{ x } [HA] \text{ x } 1 \text{ cm}) + (\varepsilon_{A^-} \text{ x } [A^-] \text{ x } 1\text{cm})$

$= (\varepsilon_{HA} \text{ x } [HA] \text{ x } 1\text{cm}) + (\epsilon_{A^-} \text{ x } (C_0 - [HA]) \text{ x } 1\text{cm})$

$= (\varepsilon_{HA} \text{ x } [HA] \text{ x } 1\text{cm}) + (\varepsilon_{A^-} \text{ x } C_0 \text{ x } 1\text{cm}) - (\varepsilon_{A^-} \text{ x } [HA] \text{ x } 1\text{cm})$

$= \left(\varepsilon_{A^-} \text{ x } C_0 \text{ x } 1\text{cm}\right) + \left(\varepsilon_{HA} \text{ x } C_0 \left(\frac{[H^+]}{[H^+]+K_a}\right) \text{ x } 1\text{cm}\right)\left(\varepsilon_{A^-} \text{x } C_0 \left(\frac{[H^+]}{[H^+]+K_a}\right) \text{ x } 1\text{cm}\right)$

$= (\varepsilon_{A^-} \text{ x } C_0 \text{ x } 1\text{cm}) + \frac{[H^+]}{[H^+]+K_a}\{(\varepsilon_{HA} \text{ x } C_0 \text{ x } 1\text{cm}) - (\varepsilon_{A^-} \text{ x } C_0 \text{ x } 1\text{cm})\}$

$(\varepsilon \text{ x } C_0 \text{ x } 1\text{cm}) = (\varepsilon_{A^-} \text{ x } C_0 \text{ x } 1\text{cm}) + \frac{[H^+]}{[H^+]+K_a}\{(\varepsilon_{HA} \text{ x } C_0 \text{ x } 1\text{cm}) - (\varepsilon_{A^-} \text{ x } C_0 \text{ x } 1\text{cm})\}$

$\varepsilon = (\varepsilon_{A^-}) + \frac{[H^+]}{[H^+] + K_a}\{\varepsilon_{HA} - \varepsilon_{A^-}\}$

$= \frac{[H^+]\,\varepsilon_{A^-} + K_a\varepsilon_{A^-} + [H^+]\varepsilon_{HA} - [H^+]\varepsilon_{A^-}}{[H^+] + K_a}$

$= \frac{[H^+]\,\varepsilon_{HA} + K_a\varepsilon_{A^-}}{[H^+] + K_a}$

$= \frac{\varepsilon_{HA} + \frac{K_a\varepsilon_{A^-}}{[H^+]}}{1 + \frac{K_a}{[H^+]}} \qquad \therefore \varepsilon = \frac{\varepsilon_{HA} + \frac{K_a\varepsilon_{A^-}}{[H^+]}}{1 + \frac{K_a}{[H^+]}}$

Fitting equation:

$$y = M_2 + \frac{\{10^{-M_0}(M_3 - M_2)\}}{(10^{-M_1} + 10^{-M_0})}$$

Where y = A

$M_0 = \begin{pmatrix} \because pH = -\log[H^+] \\ \Rightarrow [H^+] = 10^{-.pH} \end{pmatrix}$

$M_1 = \begin{pmatrix} \because pK_a = -\log K_a \\ \Rightarrow K_a = 10^{-K_a} \end{pmatrix}$

$M_2 = (\varepsilon_{A^-} \text{ x } C_0 \text{ x } 1\text{cm}) = A_o$

$M_3 = (\varepsilon_{HA} \text{ x } C_0 \text{ x } 1\text{cm}) = A_\infty$

By putting all these values we get the following equation -

$$A = A_0 + K_a\left[\frac{A_\infty - A_0}{K_a + 10^{-pH}}\right]$$

CHAPTER 3

This chapter is published in

Vatsa, A. and Padhi, S. K.*, Eur. J. Inorg. Chem. 2021, 2021(34), 3499-3505.

Chapter 3

Catalytic Water Oxidation by a Ru^{II} Half Sandwich Complex

3.1 Introduction

Earlier Ru-based polypyridine complexes were extensively studied and synthesized as water oxidation catalysts (WOCs) for the oxidation of water into molecular oxygen by many researchers.[1-5] An elaborated literature survey on mononuclear Ru-polypyridyl complexes is discussed in Chapter 1. The catalytic water oxidation using few iridium-based half sandwich complexes is known.[6] The half-sandwich complexes have a simple molecular structure, and they are highly soluble in water. From the previous studies, it was observed that in the case of half-sandwich iridium complexes, there is the possibility of oxidation or degradation of ligand during the chemical water oxidation in the presence of ceric ammonium nitrate (CAN) as sacrificial oxidant, and may be IrO_2 could act as a catalyst for water oxidation as heterogeneous materials.[7-8] Yu and the group have synthesized a Ru/Rh azo conjugated complexes [η^5-Cp*Rh(L)(MeOH)] and [η^6-CyRu(L)(H_2O)] (where L = p-(2-hydroxy-1-naphthylazo)benzenesulfonic acid sodium salt). They have studied the electronic properties of the Ru / Rh complexes towards water oxidation.[9]

In this chapter, the synthesis, characterization of the half-sandwich [Ru(η^6-benzene)(hdm)]BF_4 [**Ru-hdm**] complex (**hdm = hydroxydi(pyridine-2-yl)methanolate**) and the catalytic activity towards the electrochemical and chemical water oxidation has been investigated. The **[Ru-hdm]** complex shows the formation of Ru(IV)=O and Ru(VI)=O based nanoparticles during the chemical water oxidation in the presence of CAN in simple deionized water, which may be due to ligand oxidation or degradation in harsh conditions. These nanoparticles deposited over the septum and in reaction mixtures were analyzed by different techniques such as DLS, FE-SEM EDX, HR-TEM, and X-ray photoelectron spectroscopy.

3.2. Experimental

3.2.1 Material and methods

3.2.1.1. Materials

All the reagents utilized in this work were of reagent grade. di(2-pyridyl) ketone and benzeneruthenium(II) chloride dimer were purchased from TCI chemicals and used without further purification. NaOH was purchased from Rankem and $AgPF_6$ and $NaBF_4$ from Sigma

Aldrich. All the solvents like acetone, diethyl ether, petroleum ether, dichloromethane was purchased from Merck and dried before use. Milli-Q- purified distilled water was used in all experiments.

3.2.1.2. Optical Spectra

UV-Visible spectroscopic experiments were performed with an Agilent Cary 8454 photodiode array UV-Visible spectrophotometer.

3.2.1.3. NMR Spectroscopy and Mass Spectrometry

Proton and ^{13}C NMR spectra were recorded on Bruker Ultrashield spectrometer at room temperature. High-resolution ESI mass spectrometry was recorded with Waters UPLC TQD and Bruker micrOTOF-Q II instruments.

3.2.1.4. Determination of pKa:

The determination of pKa was based on acid-base pH titration in an aqueous Britton-Robinson buffer within the pH range of 2.0-12.0. The pH of the buffer solution containing complex was adjusted by addition of KOH and spectra were recorded by using UV-Visible spectroscopy. The change in absorbance vs pH was plotted by fitting the value of absorbance at a particular wavelength to obtain the pKa value.

$$\boldsymbol{A} = \boldsymbol{A_0} + \mathbf{K_a}\left[\frac{\boldsymbol{A_\infty} - \boldsymbol{A_0}}{\mathbf{K_a} + \mathbf{10}^{-\boldsymbol{pH}}}\right]$$

3.2.1.5. Cyclic Voltammetry

Electrochemical measurements were conducted using CH instrument ALS/CHI model 1140C and 660D electrochemical analyzer. All the electrochemical experiments were carried out under an inert gas atmosphere at the scan rate of 100 mV/s at room temperature. Cyclic voltammetry and differential pulse voltammetry were performed with three-electrode cell systems consisting of a glassy carbon electrode as working, a platinum wire as an auxiliary, and a saturated calomel electrode as a reference electrode.

3.2.1.6. Controlled Potential Electrolysis

The controlled potential electrolysis (CPE) for the **[Ru-hdm]** complex was conducted in a customized H-type cell using glassy carbon as working electrode, platinum mesh as an

auxiliary electrode, and saturated calomel electrode (SCE) as a reference electrode for the quantification of the catalytic process in phosphate buffer at pH 6.6. The surface area of the glassy carbon electrode is 1.7 cm^2. The total volume of the working compartment is 55 mL, and the headspace volume of the working cell is 35 mL.

3.2.1.7. Gas Evolution

The evolution of gas was based on manometric results using 5 mL of double-jacketed reaction vessel containing 2 mL of the reaction mixture and having a headspace volume of 3 mL. The reference cell was filled with 2 mL of water, and 3 mL is headspace volume as of the working cell. The oxygen evolved during chemical water oxidation was converted into micromoles by using the ideal gas equation PV=*n*RT. The pressure of evolved gases was measured using a differential pressure manometer of TESTO 521 with a range of 0 to 100 hPa; 0.1 hPa accuracy was used. The O_2 evolution was tested in the absence and presence of the catalyst using CAN. The generated O_2 was quantified and detected using an oxygen FOXY sensor probe of NeoFox Ocean Optics with 80 ppm O_2 % resolution in gas and monitored by NeoFox Viewer using NeoFox phase fluorometer systems.

3.2.1.8. X-ray crystallographic analysis

A suitable crystal of **[Ru(hdm)(Bz)]BF_4.2H_2O** (**[Ru(hdm)]**) was selected and mounted on a SuperNova, Single source at offset/far, EosS2 diffractometer using Mo Kα radiation (λ = 0.71073 Å). The crystal was kept at 293(2) K during data collection. Using Olex2,[10] the structure was solved with the olex2.solve structure solution program using Charge Flipping [11] and refined with the XH [12] refinement package using Least Squares minimization. The crystal data, along with refinement parameters, are given in (Table B1). Selected bond lengths and bond angles are tabulated in (Table B2 and Table B3) respectively. The hydrogen atoms were included in the calculated positions, and O2 was refined isotopically using a riding model. The BF_4^- has distorted F atoms (F4 and F5) with each site occupancy of 0.5. Similarly, two oxygen atoms (O4 and O5) in the water molecules also have a site occupancy of 0.5.

3.2.1.9. X-ray photoelectron spectroscopy

The X-ray photoelectron spectroscopy studies were conducted on PHI 5000 versa probe III having monochromatic Al as source having argon ion gun, turnkey dual-beam neutralization,

compucentric Zalar^{TM} rotation, and advanced data reduction algorithms for depth profiling. The standard monochromatic argon ion gun is capable of generating 5 eV to 5 keV Ar ions.

3.2.1.10. High resolution transmission electron microscopy (HR-TEM)

The high-resolution transmission electron microscopy was studied on Thermo scientific Talos F200X G2 is a 200 kV HRTEM that delivers fast, precise, quantitative characterization of nanomaterials in multiple dimensions.

3.2.1.11. Field emission scanning electron microscopy (FE-SEM)

The field emission scanning electron microscopy studies were conducted on FE-SEM Supra 55 (Carl Zeiss, Germany) with airlock chambers. The attachments available with the FE-SEM are SREM, EDS (Oxford Liquid Nitrogen free SDD X MAX 50 EDS), ESBD (Oxford Integrated Advanced Aztec HKL EBSD with fore scatter detector system with four diodes for Nordlys Analysis), and Mono CL4 (Gatan, UK). The FE-SEM has a resolution of 0.8 nm at 15 kV, 1.6 nm at 1 kV, magnification of 12-1000000X, acceleration voltage within 100 V to 30 kV, gun-type Schottky field emission electron gun, maximum probe current 12 pA to 100 nA, and detectors: SE, In-lens, BSE, Retractable STEM Bright and dark field.

3.3. Synthesis

3.3.1. Synthesis. [Ru(η^6-benzene)(hdm)]BF_4 complex

[Ru(η^6-benzene)(hdm)]BF_4 complex. [Ru(η^6-benzene)Cl_2]$_2$ complex (100 mg, 0.199 mmol) was added to a solution containing di-2-pyridylketone (**dpk**) (73 mg, 0.399 mmol), NaOH (16 mg, 0.400 mmol) and $NaBF_4$ (43 mg, 0.3916 mmol) dissolved in 5 mL of water. The reddish orange coloured reaction mixture was stirred for 1 hr at room temperature until it converted to yellow suspension. The solid obtained was filtered and washed with cold H_2O and petroleum ether. Yield: 96% Calculated mass m/z: 381.01; Found: 380.9599 m/z. 400 MHz ^{1}H NMR (δ, (*J*, Hz), D_2O): 6.03 (6H, s), 7.01 (1H, s), 7.35 (2H, t, 12), 7.64 (2H, d, 12), 7.92 (2H, t, 16), 9.235 (2H, d, 4). 100 MHz ^{13}C NMR (δ, (*J*, Hz), D_2O): 84.23, 101.61, 121.06, 124.92, 140.45, 153.45 and 159.17. Six carbons of benzene moiety and ten carbons of pyridine moieties. Anal. Calcd for **[Ru(hdm)(η^6-benzene)]**$BF_4.2H_2O$, $C_{17}H_{19}BF_4N_2O_4Ru$: C, 40.58; H, 3.81; N, 5.57. Found: C, 40.63; H, 3.84; N, 5.61.

3.4 Results and Discussion

3.4.1. Synthesis

The [Ru-hdm] (hdm = hydroxydi(pyridine-2-yl)methanolate) was synthesized based on a similarly reported procedure.[13] The reaction scheme is depicted in Scheme 3.1A. The [Ru-hdm] complex was synthesized by dissolving one equivalent of dimer $[Ru(\eta^6\text{-benzene})Cl_2]_2$ with two equivalents of hdm ligand followed by the addition of 2 equivalents of NaOH and $NaBF_4$ in water. The reaction was stirred for 3 hours at room temperature, and the solid precipitate obtained was filtered and washed with cold H_2O and petroleum ether. In this case, the nucleophilic attack by OH^- to the carbonyl carbon center of di-2-pyridyl ketone (dpk) generates the geminal hydroxydi(pyridine-2-yl)methanolate (hdm) ligand (Scheme 3.1B).

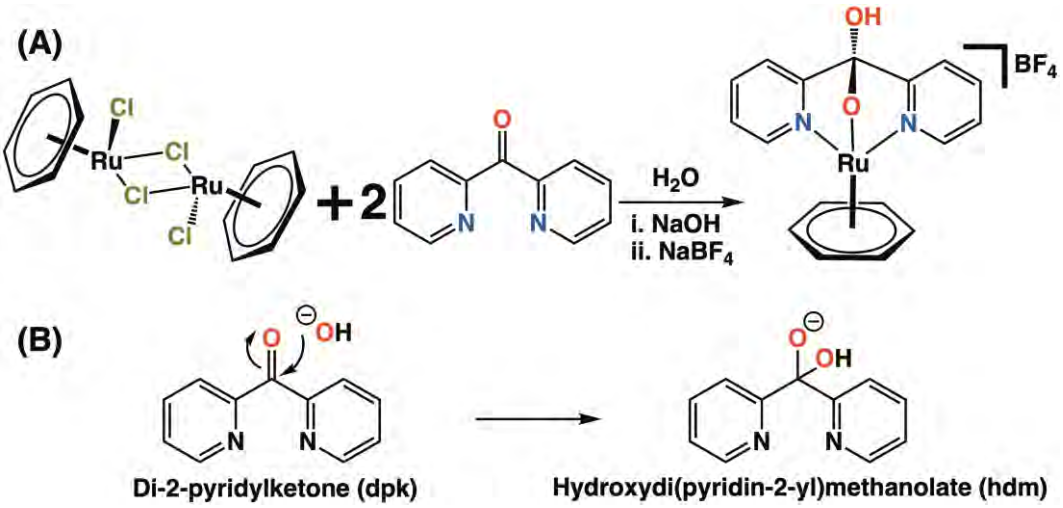

Scheme 3.1. Synthesis of **[Ru-hdm]** complex

3.4.2. Optical Spectra

The optical spectra of the complex **[Ru-hdm]** were studied in water. The complex exhibits three bands in the UV region at 260 nm, 273 nm, and 365 nm (Figure B1). The band at 260 nm (38461 cm^{-1}, 7269 M^{-1} cm^{-1}) attributed to forbidden $\pi \rightarrow \pi^*$ transition to a homonuclear excited state of benzene moiety, band at 273 nm (36630 cm^{-1}, 6819 M^{-1} cm^{-1}) and band at 365 nm (27777 cm^{-1}, 604 M^{-1} cm^{-1}) are attributed to $n \rightarrow \pi^*$ transitions.

3.4.3. NMR and Mass Spectra

The NMR spectra of the **[Ru-hdm]** were recorded in water. The ^1H NMR spectra of the **[Ru-hdm]** complex shows one singlet for six hydrogen of benzene moiety and two doublets for 2H, and two triplets for 2H each for two pyridine moieties of the **hdm** ligand (Figure B2). The ^1H-

^{1}H COSY NMR (Figure B3) shows the correlation among the neighboring protons. The spectra show that protons of benzene moiety 1-6 show correlation among them at chemical shift 5.98 ppm. In pyridine moiety, the H7 proton at 9.24 ppm shows a correlation only with proton H8 at 7.35 ppm. The H8 proton is correlated with two protons at H7 and H9 at 9.24 and 7.92 ppm. The proton H9 shows a correlation with proton H8 and H10 at 7.63 ppm. The H10 proton is only correlated with the H9 proton. The ^{13}C NMR for the **[Ru-hdm]** complex shows six carbons for benzene moiety and ten carbons for pyridine moieties of the **hdm** ligand (Figure B4). The mass spectra of the **[Ru-hdm]** were recorded in water, the calculated mass for the $[C_{17}H_{15}N_2O_2Ru]^+$ is m/z 381.01, and found mass is m/z 380.9599 (Figure B5).

3.4.4. Single crystal X-ray crystallography

The complex **[Ru(η^6-benzene)(hdm)](BF$_4$)** crystallizes in a monoclinic P2$_1$/c space group. The asymmetric unit consists of a mono-cationic **[Ru^{II}(η^6-benzene)(hdm)]$^+$** species and a BF_4^- anion. There are two water molecules present as solvents of crystallization. An ORTEP (Oak Ridge Thermal-Ellipsoid Plot) with 30% probability thermal ellipsoids for **[Ru(η^6-benzene)(hdm)]$^+$** is displayed in Figure 3.1.

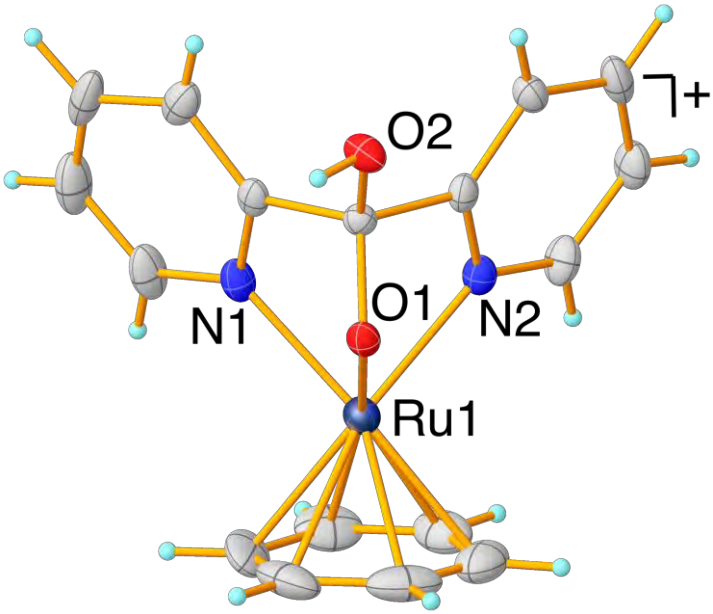

Figure 3.1. ORTEP (30% probability thermal ellipsoids) of **[Ru(η^6-benzene)(hdm)]$^+$** complex.

The crystallographic data and refinement parameters are provided in Table B1. Selected bond lengths and bond angles are given in Table B2 - Table B3 respectively. In this case, the **[Ru^{II}(η^6-benzene)(hdm)]$^+$** is a stable 18 e$^-$ coordination complex, wherein the benzene ligand

is attached to the Ru^{II}-metal center through a π-coordination with Hexa-hapticity. The arene ligand acts as a six e^- donor, which is equivalent to three coordinate bonds. A facially chelating tripodal **hdm** ligand occupies the other three coordinations. The **hdm** ligand coordinates to the Ru^{II}-metal center by two neutral pyridyl N-atoms and the apical position by the anionic alcoholate O^- atom. The Ru1–N1 and Ru1–N2 distances are longer than Ru1–O1 coordination. The ∠O1Ru1N1 and ∠O1Ru1N2 are significantly shorter than 90°.

3.4.5. Acid-Base Equilibria

The acid-base equilibria of the **[Ru-hdm]** complex were studied in Britton-Robinson buffer solution using UV-Visible spectroscopy and potentiometry within a pH range of 2.0 to 12.0 (Scheme 3.2A). The complex shows ligand to metal charge transfer band $n \rightarrow \pi^*$ at 365 nm wavelength. The UV-Visible spectra of **[Ru-hdm]** complex within pH range 2.0 to 5.5 show an increase in intensity at wavelength 260 nm, and a pKa of 4.2 was observed for the dechelated pyridine ring from Ru metal (Figure B6-B7). Further, a pKa at 6.7 was observed in UV-vis spectroscopy (Figure B8-B9) and potentiometry due to the protonation of the alcoholate O^- coordination to neutral OH coordination within pH span 5.0-8.0. As the pH increases from 7.0 to 12.0, observed an isosbestic point at 320 nm with a substantial increase in the absorbance at 340 nm. The isosbestic point at 320 nm was marked for the deprotonation of the aqua group coordinated with the **[Ru-hdm]** complex through a dechelated pyridine ring. The pKa was found to be 10.2 by fitting the plot of absorbance *vs.* pH at the wavelength 340 nm (Figure B10-B11).

The species mentioned in Scheme 3.2A has also been confirmed through ESI-mass spectroscopy (Scheme 3.2B). The observed mass of the species $[Ru(hdmH_2)(Bz)OH_2]^{3+}$ at pH 3.5 was 235.12 m/z (Scheme 3.2B, Mass (a)) and calculated for $[C_{17}H_{17}BF_4N_2O_2Ru]^{2+}$ 235.01 m/z. At pH 5.5, the observed mass of the species $[Ru(hdmH)(Bz)OH_2]^{3+}$ was 487.05 m/z (Scheme 3.2B, Mass (b)) and calculated for $[C_{17}H_{18}BF_4N_2O_3Ru]^+$ 487.03 m/z. The observed mass of the species $[Ru(hdm)(Bz)OH_2]^+$ at pH 8.0 was 381.02 m/z (Scheme 3.2B, Mass (c)) and calculated for $[C_{17}H_{15}N_2O_2Ru]^+$ 381.02 m/z. At pH 10.8, the observed mass of the species $[Ru(hdm)(Bz)OH]^{3+}$ was 436.99 m/z (Scheme 3.2B, Mass (d)) and calculated for $[C_{17}H_{16}N_2O_3RuK]^+$ 436.98 m/z.

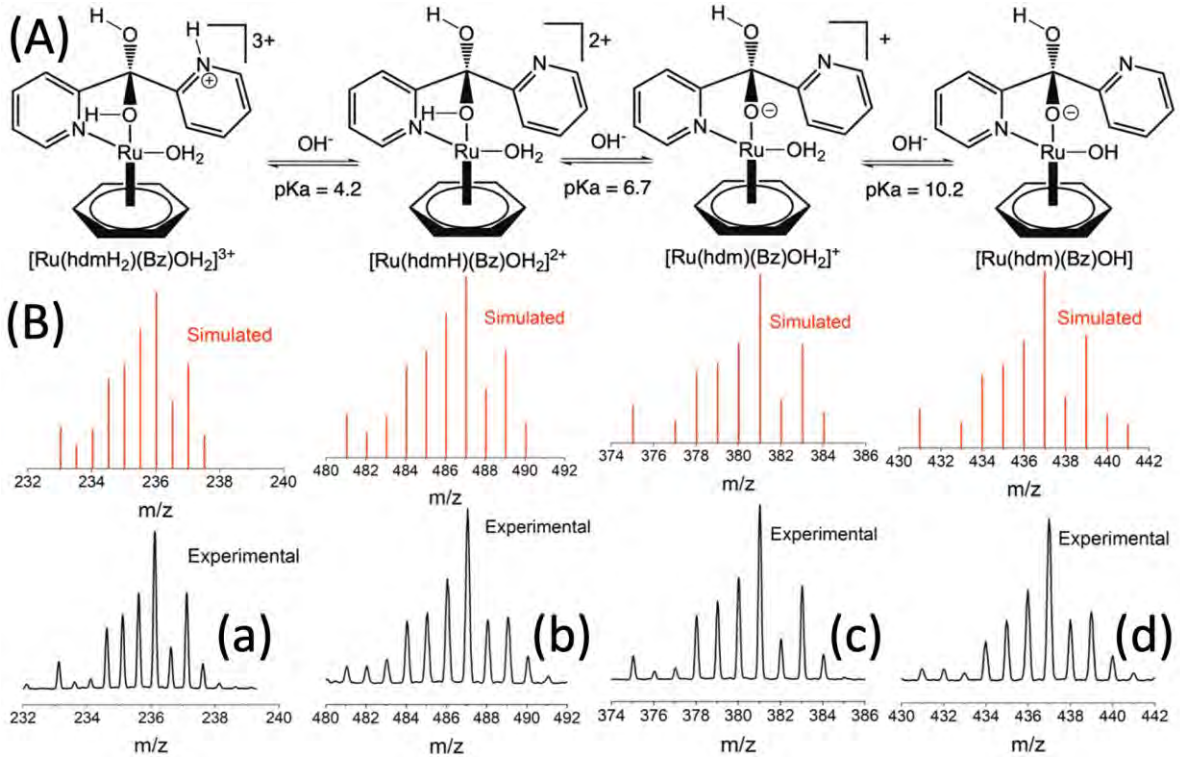

Scheme 3.2. Acid-base equilibria in **[Ru-hdm]** complex.

3.4.6. Electrochemistry

The electrochemistry of the **[Ru-hdm]** complex was studied in the water using 0.1 M of sodium tetrafluoroborate ($NaBF_4$) as a supporting electrolyte under an inert atmosphere. The complex exhibits two irreversible oxidation peaks and one quasi-reversible peak. The cyclic voltammogram (CV) and differential pulse voltammetry (DPV) of the 1.0 mM complex shows one quasi reversible peak for redox couple Ru^{II}/Ru^{III} at 0.74 V vs. SCE (E_{pa} = 0.76 V vs. SCE and E_{pc} = 0.71 V vs. SCE). The irreversible anodic peak at potential E_{pa} = 0.99 V vs. SCE corresponds to the Ru^{III}/Ru^{IV} redox couple (Figure B12). Another irreversible oxidation peak at 1.23 V vs. SCE is responsible for redox couple Ru^{IV}/Ru^{V}. The resting potential of the **[Ru(η^6-benzene)(hdm)]**$^+$ was found to be at 0.63 V vs. SCE in the water at neutral pH, which indicates that Ru is in a 2+ oxidation state (Figure 3.2).

3.4.7. Pourbaix Diagram

The aqueous electrochemistry of the complex was studied in the Britton Robinson buffer within a pH range of 2.0 to 12.0. The potentials from SWV of the complex at each pH were analyzed to construct the Pourbaix diagram (Figure 3.3).

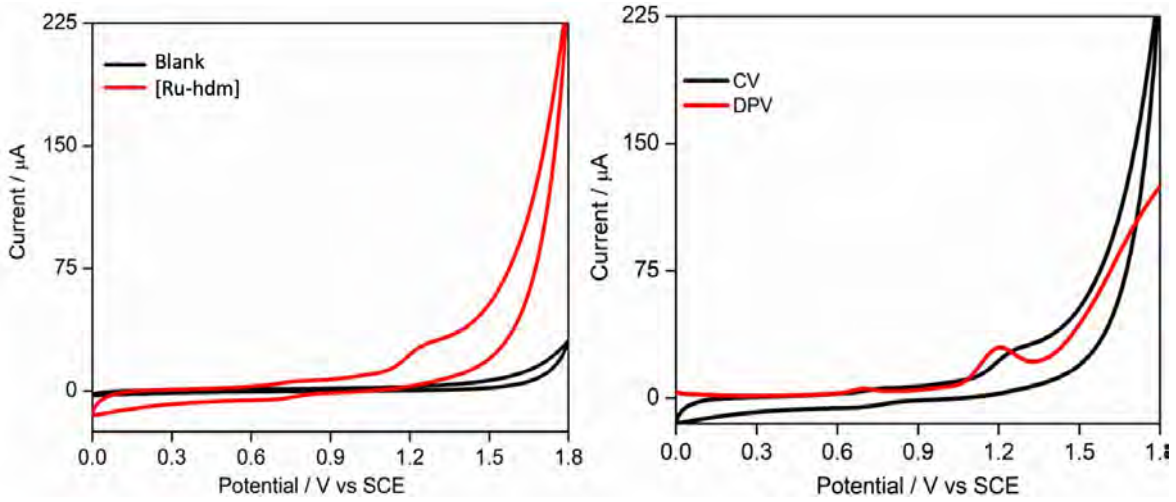

Figure 3.2. CV of 1.0 mM of **[Ru-hdm]** (red) and blank (black) in water using 0.1 M of $NaBF_4$ as supporting electrolyte (left) and CV and DPV of 1.0 mM **[Ru-hdm]** in water using 0.1 M $NaBF_4$ as supporting electrolyte(right).

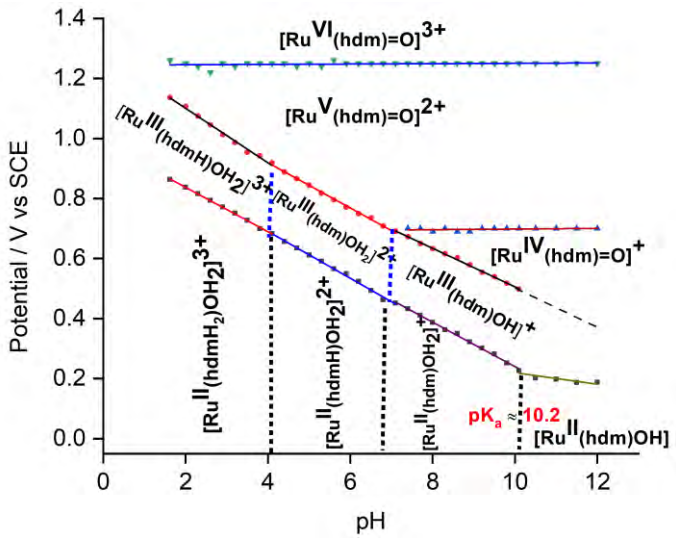

Figure 3.3. Pourbaix diagram of **[Ru-hdm]** complex in Britton-Robinson buffer.

At a highly acidic pH, one pyridine moiety gets dechelated from the **hdm** ligand, and a free pyridyl moiety is protonated in the acidic medium. The pyridine moiety gets protonated at a pKa value of 4.2. In the diagram, within pH 2.0 – 4.2, a slanted line for $1H^+/1e^-$ transfer from the $[Ru^{II}(hdmH_2)OH_2]^{3+} \rightleftarrows [Ru^{III}(hdmH)OH_2]^{3+}$ observed. In the pH region 4.2 – 6.7, $1e^-/1H^+$ transfer from $[Ru^{II}(hdmH)OH_2]^{2+} \rightleftarrows [Ru^{III}(hdm)OH_2]^{2+}$ with a slope of nearly 60 mV/ pH. A slope of 60 mV/ pH was also observed due to $1e^-/1H^+$ transfer from $[Ru^{II}(hdm)OH_2]^+ \rightleftarrows [Ru^{III}(hdm)OH]^+$ within the pH span 6.7 – 10.2. Beyond pH 10.2, the potential remains constant and indicates the $1e^-$ transfer from $[Ru^{II}(hdm)OH]$ to $[Ru^{III}(hdm)OH]^+$. The pKa for

$[Ru^{II}(hdm)OH_2]^+ \rightleftarrows [Ru^{II}(hdm)\text{-}OH]$ was found to be 10.2, which is in agreement with the UV-Visible spectra of the complex by varying the pH. In between the pH 2.0 – 4.2, $2e^-/3H^+$ transfer from $[Ru^{III}(hdmH)OH_2]^{4+} \rightleftarrows [Ru^{V}(hdm)=O]^{2+}$ with the slope of 90 mV/pH and within pH range 4.2 – 6.7, $2e^-/2H^+$ transfer from $[Ru^{III}(hdm)OH_2]^+ \rightleftarrows [Ru^{V}(hdm)=O]^{2+}$ with the slope of 60 mV/pH. Within pH span 6.7 to 12.0, a slope of 60 mV/pH was observed by $1e^-/1H^+$ transfer from $[Ru^{III}(hdm)OH]^+ \rightleftarrows [Ru^{IV}(hdm)=O]^+$. At potential 0.7 V vs. SCE and 1.23 V vs. SCE two horizontal lines were observed with zero slopes which correspond to $1e^-$ transfer from $[Ru^{IV}(hdm)=O]^+ \rightleftarrows [Ru^{V}(hdm)=O]^{2+}$ and $[Ru^{V}(hdm)=O]^{2+} \rightleftarrows [Ru^{VI}(hdm)=O]^{3+}$ respectively.

3.4.8. Electrochemical Catalysis

The electrochemical water oxidation was investigated in water with 1.0 mM of the **[Ru-hdm]** complex using a 0.1 M of sodium tetrafluoroborate ($NaBF_4$) supporting electrolyte. The cyclic voltammogram of the complex within a potential window of 0.0 to 1.8 V at the scan rate of 100 mV s^{-1} shows a strong catalytic current with an onset potential of 1.55 V vs. SCE in the water towards the anodic direction. The catalytic activity of the complex was studied by varying the concentration of the complex from 1.0 mM to 4.0 mM. It was observed that catalytic current shows a linear dependence on the catalyst concentration (Figure B13). The current rises with increasing the complex concentration shown in (Figure B14), for current density vs. catalyst concentration. The electrocatalytic water oxidation was not observed without catalyst in the blank CV in water. The electrochemical properties of the **[Ru-hdm]** complex were studied over a wide range of pH from 2.0 to 10.0 in the Britton Robinson buffer (Figure B15). The electrocatalytic water oxidation exhibits maximum current at pH 10.0, which is about 590 µA, and the onset potential also shifted towards a lower potential, i.e., 150 mV vs. SCE. The diffusion coefficient of the **[Ru-hdm]** complex was determined by considering the Ru^{II}/Ru^{III} redox couple in water using 0.1 M $NaBF_4$ as an electrolyte. The current intensity increases in both anodic and cathodic directions for the scan rates varied from 25 mV s^{-1} to 200 mV s^{-1}, wherein the charge transfer is lower as compared to the mass transfer because of the electron transport through surface absorbed species or freely diffusing redox species on the electrode (Figure B16). Therefore, the surface coverage was calculated by using the Randel-Sevcik equation (3.1).

$$\boldsymbol{i_p = \frac{n^2F^2}{4RT}\vartheta A\Gamma^\star} \qquad \textbf{(3.1)}$$

Herein, i_p = peak current, n = number of electrons, F = Faraday constant, A = area of the surface of the electrode 0.07 cm^2, ϑ = scan rate mV / sec, $\Gamma^\star$ = surface coverage of adsorbed species in

mol cm^{-2}, R = universal gas constant 8.314 J mol^{-1} K^{-1}, and T = temperature 298 K. The plot of i_p vs. ϑ was fitted linearly, and the slope was found to be 32.64 x 10^{-6} 4RT / n^2F^2 ϑ A was observed (Figure B17). The surface coverage was calculated to be 0.49 x 10^{-6} mol cm^{-2} using the Randle-Sevcik equation, which confirms that there is surface absorption on the electrode surface. The process is not completely homogeneous as no peak-to-peak separation shifting was observed with an increase in scan rate.

3.4.9. Controlled potential electrolysis (CPE)

The CPE of the **[Ru-hdm]** complex was carried out by taking 1.0 mM of the complex dissolved in 20 mL of phosphate buffer at pH 6.6 (Figure B18). The working cell was connected with an oxygen sensor to measure the volume of the evolved oxygen during electrolysis (Figure B19). After 1 hour of electrolysis at 1.8 V, 17.6 µmol of O_2 evolved, and a charge difference of 6.9 C was obtained concerning the blank experiment. The TOF of the reaction was calculated from equation (3.2).

$$TOF = \frac{\Delta c}{F n_1 t} \qquad \textbf{(3.2)}$$

Δc = charge difference generated from bulk electrolysis in the presence or absence of catalysts, F = Faraday constant, n_1 = number of moles of electrons required for the oxidation, and t = duration of electrolysis, 1 hour. The complex shows a TOF of 17.9 µmol of O_2 / hour, and the Faradaic efficiency was 98 %. The FE-SEM and EDX analyses were performed after the electrolysis to show the deposition of the catalyst on the electrode surface. The atomic weight % of C is 21.37 %, N is 4.13 %, O is 11.80 %, F is 54.07 %, Na is 13.64 % and Ru is 3.31 % (Figure B20).

3.4.10. Charge transfer resistance (R_{ct}) and TAFEL analysis

The Nyquist plot consisting of an imaginary impedance plot (Z_{im} / Ω cm^2) on the y-axis corresponding to the real plot (Z_{re} /Ω cm^2) on the x-axis has been studied for the **[Ru-hdm]** complex. The impedance of the 1.0 mM of the complex was performed by taking the higher frequency at 1 MHz and the lower frequency at 0.1 Hz. The amplitude for the analysis is at 5 mV RMS. The intrinsic resistance R_s was found to be 4.7 Ω cm^2. The surface area of the glassy carbon electrode is 0.07 cm^2. The charge transfer resistance (R_{ct}) analysis was carried out for the 1.0 mM of complex dissolved in water in the presence of $NaBF_4$ as a supporting electrolyte. The impedance analysis at 1.55 V for the water oxidation of the complex in the absence of CAN was conducted and the Nyquist plot obtained reveals the charge transfer resistance (R_{ct})

for the **[Ru-hdm]** complex is found to be 83.2 Ω cm^2 (Figure 3.4A). The impedance is fitted with the equivalent circuit diagram shown in supporting information (Figure B21). In this case, Warburg impedance [14] is observed, where the diffusion of electroactive species controls all the electrochemical reactions on the electrochemical surface.

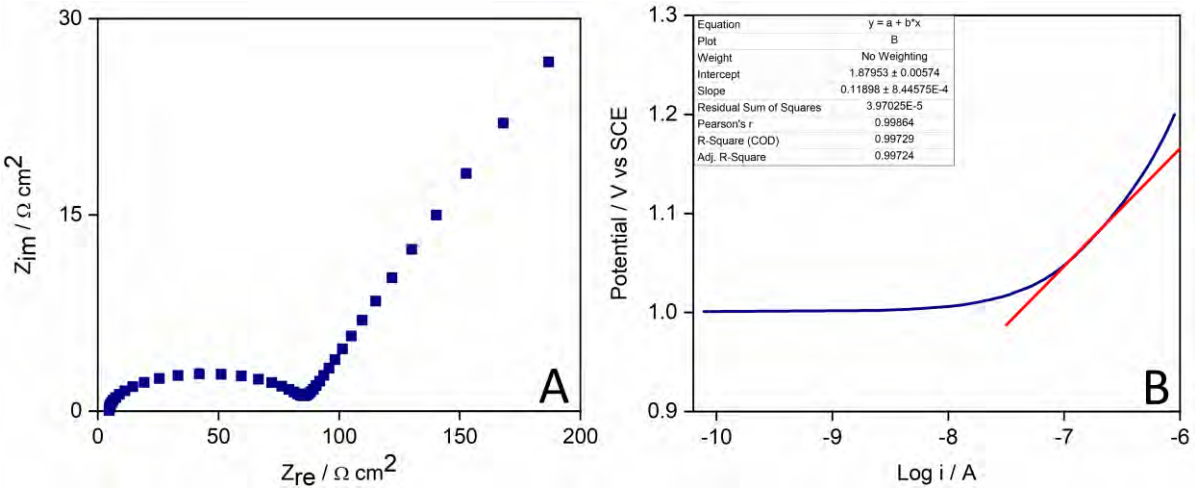

Figure 3.4. (A) The Nyquist plot of 1.0 mM of **[Ru-hdm]** in water using 0.1 M of $NaBF_4$ as supporting electrolyte. **(B)** Tafel plot of 1.0 mM **[Ru-hdm]** in water using 0.1 M of $NaBF_4$ as supporting electrolyte.

The Tafel plot (Figure 3.4B) has been analyzed for the 1.0 mM of the complex in water using $NaBF_4$ as a supporting electrolyte. The equilibrium potential for the complex is 1.00 V vs. SCE. The slope was found to be nearly 120 mV dec^{-1} by linear fitting at the anodic segment. The Tafel slope of 120 mV dec^{-1} indicates the step where surface species formed just before the rate-determining step showing the surface coverage of adsorbed species during electrolysis.[15]

3.4.11. Chemical Water Oxidation

The oxygen evolution through the complex was conducted chemically using ceric ammonium nitrate (CAN) as an oxidant in the water. A solution containing (1.5 mL) of complex dissolved water was added to the working cell, and 100 mM of CAN in 0.5 mL was injected through a rubber septum. The pressure generated due to gas evolution was monitored through a differential pressure manometer, and the gas was also quantified using an oxygen sensor. The chemical water oxidation for the **[Ru-hdm]** complex was performed with different buffers and oxidants. The rate of O_2 evolution is initially fast, but evolution stops within a minute; maybe there is the degradation of catalyst in highly acidic pH and the presence of a strong oxidizing agent. The oxygen evolution was also monitored at pH 3.6, using sodium periodate as an

oxidant in acetate buffer, but oxygen evolution was not observed. Surprisingly, the vigorous evolution of gas was observed in the simple deionized water using CAN as an oxidant. The evolution of gas started immediately after injecting CAN in a reaction mixture containing complex without any incubation time. The pH of the reaction mixture before the addition of CAN is 6.6, and after the addition of CAN, the pH of the reaction medium becomes highly acidic at pH 1.35. The overall chemical water oxidation reaction by CAN was represented as per equation (3.3).

$$\mathbf{2H_2O + 4Ce^{IV} \rightarrow O_2 + 4Ce^{III} + 4H^+} \qquad \mathbf{(3.3)}$$

For studying the kinetics of the catalytic water oxidation, different concentrations of complex varied from 1.0 mM to 4.0 mM with 100 mM of CAN as an oxidant (Figure B22), and different concentrations of CAN ranged from 25 mM to 100 mM with 1.0 mM of the complex (Figure 3.5(a)). From the kinetics plot, it was observed that the initial rate of reaction for complex follows the first-order kinetics where k_{obs} = 1.76 x 10^{-2} µmol s^{-1} (Figure B23). The kinetics plot for the CAN variation shows that the initial rate of reaction follows the first-order kinetics for the oxidant where k_{obs} = 1.3 x 10^{-3} µmol s^{-1} (Figure 3.5(b)). The reaction rate shows dependence on the concentration of the catalyst and CAN; as the concentration increases, the rate of reaction increases and indicates the maximum volume of gas evolved is 29.00 µmol. The gas evolution also examined through an oxygen sensor with 4.0 mM **[Ru-hdm]** using 100 mM of CAN as an oxidant (Figure B24). The oxygen evolution during water oxidation was not observed in the absence of catalyst in the presence of 100 mM of CAN (Figure B25). During the chemical water oxidation reaction, CAN trigger the conversion of the homogeneous **[Ru-hdm]** into very fine nanoparticles, which are found to be ruthenium oxide (Ru^{VI}=O) or the mixture of Ru^{IV}=O and (Ru^{VI}=O) facilitating the evolution of oxygen (Figure B26). The size of the particles was examined through the differential light scattering (DLS) technique, the size of the particles dispersed in the reaction medium was found in the range of 57 – 97 nm, and the size of the particles deposited over the septum was found within the range of 90 – 206 nm (Figure B27). These particles are examined through EDX, FE-SEM, XPS, and HR-TEM analyses. It was already reported that Ru^{IV}=O nanoparticles are most active towards catalytic water oxidation.[16] The formation of nanoparticles during water oxidation in the presence of CAN was previously reported in Iridium complexes.[17]

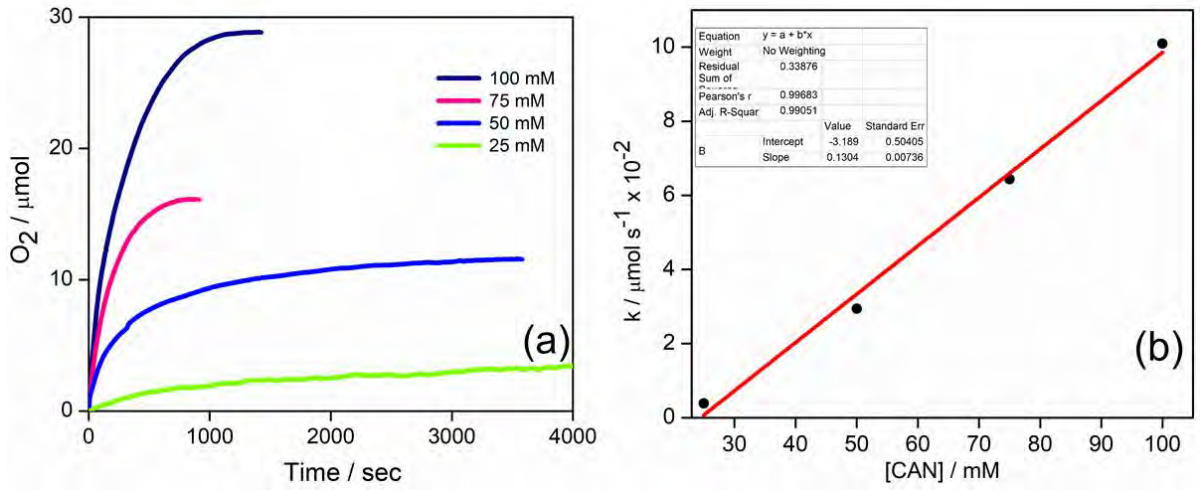

Figure 3.5: (a) O_2 evolution by **[Ru-hdm]** with various CAN concentration at 4.0 mM Complex. **(b)** Rate of O_2 evolution *vs.* CAN in water.

3.4.12. Morphological characterizations

During the chemical water oxidation, the black-colored insoluble particles form a coating over the surface of the septum after the addition of ceric ammonium nitrate as an oxidant. The deposition of black-colored insoluble particles was observed on the septum surface and dispersed within the reaction mixture. To analyze the particle, FE-SEM and EDX analyses were performed. The EDX of the particles in the region of 100 µm shown in the FE-SEM image revealing the composition of C, N, O, Ru, and Ce in the reaction mixture containing ceric ammonium nitrate and **[Ru-hdm]** in water. It was concluded that particles might be a composite of ruthenium oxide and carbon with cerium oxide as these elements have a high compound percentage compared to others. The contents of C are 19.21 %, O is 31.14 %, Ru is 32.37 %, and Ce is 9.90 % (Figure B28). This composite formation may be involved in enhancing the water oxidation activity of the **[Ru-hdm]** complex. High-resolution transmission electron microscopy (HR-TEM) was conducted for the particles forming coating over the surface of the septum on a copper grid to support the information obtained from the above techniques (Figure B29). According to EDX of the particles within the 500 nm region as shown in the HR-TEM image suggesting the formation of the nanoparticle.

3.4.13. X- Ray photoelectron spectroscopy

X-ray photoelectron spectroscopy (XPS) employed monochromatic Al, micro-focused (< 10 µm), scanning X-ray source to investigate the oxidation state of the ruthenium oxo species deposited on the surface of the rubber septum during the chemical water oxidation using CAN

as an oxidant. The particles were mounted on the surface of silicon wafers for analysis. This study reveals that the two peaks in the spectrum are associated with the core level of Ru $3d_{5/2}$ and C1s (Figure B30). The peak at a binding energy of 283.38 eV corresponds to Ru^{VI}=O, which confirms the +6 oxidation state of Ru and the peak at a binding energy of 286 eV ascribed to the core level of C1s.[18] In another spectrum, a peak at 530.7 eV was assigned to O1s linked with Ru, and the other peak at a binding energy of 533 eV attributed to O1s bonded with the C1s atom (Figure B31).[19] The X-ray electron spectroscopy (XPS) of the reaction mixture was taken, and it was found that there are three peaks; one peak corresponds to the core level of Ru $3d_{3/2}$ with a binding energy of 284.79 eV for anhydrous Ru^{IV}=O in which Ru is in +4 oxidation state. The peak at 282.3 eV corresponds to Ru $3d_{5/2}$ for Ru^{VI}=O, indicating the presence of Ru in a +6 oxidation state, and another peak at 286.7 eV corresponds to the core level of C1s (Figure 3.6). From the XPS analysis of both solid particles i.e., deposited over the septum and the reaction mixture, it was observed that Ru attained the +6-oxidation state at the end of the reaction forming the particle coating over the surface of the septum. During the chemical water oxidation reaction Ru sustaining in both +4 and +6 oxidation state confirmed through the XPS of the reaction mixture and after attaining +6 oxidation state reaction reaches its terminal point.

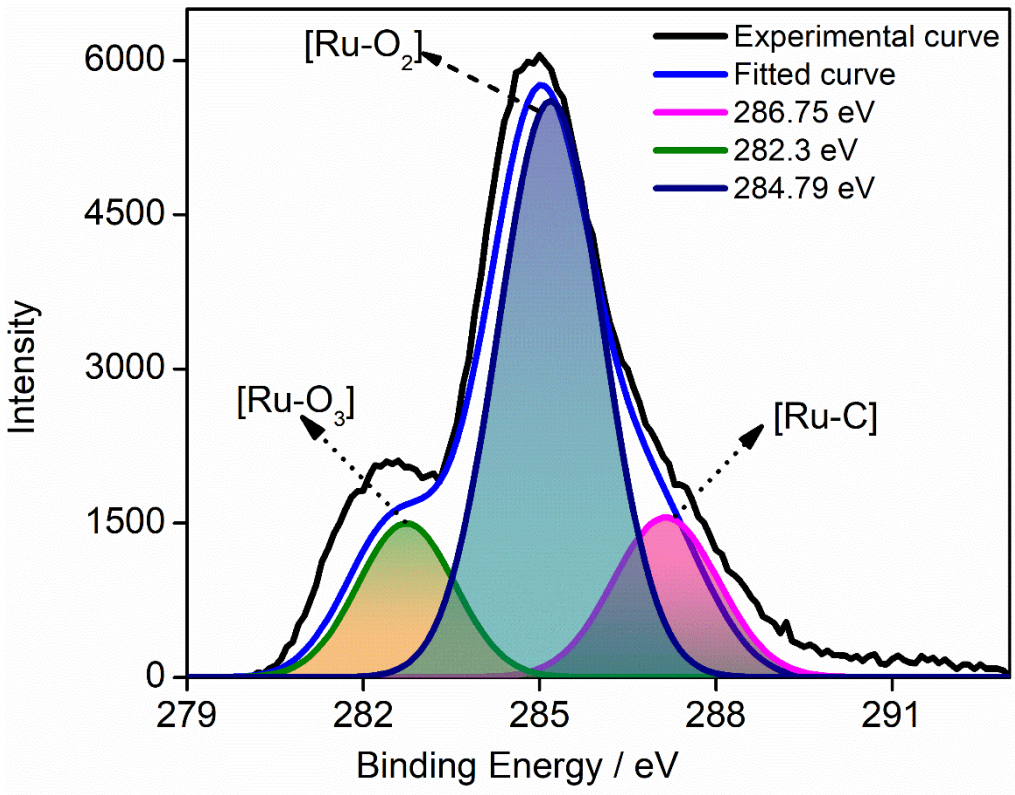

Figure 3.6. Fitted Ru(3d) XPS spectra for RuO_3 and RuO_2 in solution.

3.5 Summary

The complex **[Ru(η^6-benzene)(hdm)]BF_4 ([Ru-hdm])** has been synthesized and characterized by various spectroscopic techniques. Herein, we have successfully employed **[Ru-hdm]** as a catalyst for oxygen evolution reaction (OER). During the electrochemical investigation, the surface adsorption phenomenon was observed. The chemical water oxidation of the **[Ru-hdm]** complex was investigated at pH 6.6 using CAN as an oxidant. The experimental results reveal that the **[Ru-hdm]** catalyst having the **hdm** ligand, suffers decomposition under extreme harsh conditions of acidic pH, in the presence of an oxidant and doesn't exhibit O_2 evolution. The catalyst **[Ru-hdm]** performs electrochemical water oxidation at applied potential +1.8 V vs. SCE in pH 6.6 phosphate buffer with 98 % of Faradaic efficiency. The chemical water oxidation was studied by using CAN as an oxidant in deionized water as well as electrochemical water oxidation at different complex concentrations and different pH. The chemical water oxidation of **[Ru-hdm]** complex shows the formation of insoluble particles of [Ru^{VI}=O] and [Ru^{IV}=O] species in the reaction mixture and also a coating over the surface of the silicone rubber septum, which has been examined through FE-SEM, EDX, XPS, and HR-TEM analysis.

3.6. References

1. Bernet, L., Lalrempuia, R., Ghattas, W., Mueller-Bunz, H., Vigara, L., Llobet, A., Albrecht, M. Tunable single-site ruthenium catalysts for efficient water oxidation. *Chem. Commun.* **2011**, *47* (28), 8058–8060.
2. Matheu, R., Ertem, M. Z., Gimbert-Surinach, C., Sala, X., Llobet, A. Seven Coordinated Molecular Ruthenium−Water Oxidation Catalysts: A Coordination Chemistry Journey. *Chem. Rev.* **2019**, *119* (6), 3453-3471.
3. Sala, X.; Romero, I.; Rodriguez, M.; Escriche, L.; Llobet, A. Molecular Catalysts that Oxidize Water to Dioxygen, *Angew. Chem. Int. Ed.* **2009**, *48* (16), 2842-2852.
4. (a) Tong, L., Thummel, R. P. Mononuclear ruthenium polypyridine complexes that catalyze water oxidation. ***Chem. Sci.* 2016**, ***7* (11)**, 6591-6603.

   (b) Matheu, R., Ertem, M. Z., Gimbert-Suriñach, C., Sala, X., Llobet, A. Seven Coordinated Molecular Ruthenium−Water Oxidation Catalysts: A Coordination Chemistry Journey. *Chem. Rev.* **2019**, *119* (6), 3453-3471.

   (c) Kamdar, J. M., Grotjahn, D. B. An Overview of Significant Achievements in Ruthenium-Based Molecular Water Oxidation Catalysis. *Molecules*. **2019**, *24* (3), 494.

5. Zhang, Q., Guan, J. Mono-/Multinuclear Water Oxidation Catalysts. *ChemSusChem*. **2019**, *12* (15), 3209 – 3235.
6. Li, P., Liu, J. -B., Han, S., Deng, W., Yao, Z. -J. Half-sandwich Ir (III) and Rh (III) complexes as catalysts for water oxidation with double-site. *Appl Organometal Chem.* **2019**, *33* (9), 1-9.
7. Blakemore, J. D., Schley, N. D., Balcells, D., Hull, J. F., Olack, G. W., Incarvito, C. D., Eisenstein, O., Brudvig, G. W., Crabtree, R. H. Half-Sandwich Iridium Complexes for Homogeneous Water-Oxidation Catalysis. *J. Am. Chem. Soc.* **2010**, *132* (45), 16017–16029.
8. Savini, A., Belanzoni, P., Bellachioma, G., Zuccaccia, C., Zuccaccia, D., Macchioni, Al. Activity and degradation pathways of pentamethyl-cyclopentadienyl-iridium catalysts for water oxidation. *Green Chem*. **2011**, *13* (12), 3360-3374.
9. Yu, W.-B., He, Q.-Y., Shi, H.-T., Jia, J.-Y., Wei, X. Azo-conjugated half-sandwich Rh/Ru complexes for homogeneous water-oxidation catalysis. *Dalton Trans.* **2014**, *43* (17), 6561–6566.
10. Dolomanov, O.V., Bourhis, L.J., Gildea, R.J, Howard, J.A.K. & Puschmann, H. *OLEX2*: a complete structure solution, refinement and analysis program. *J. Appl. Cryst.* **2009**, *42*, 339-341.
11. Bourhis, L.J., Dolomanov, O.V., Gildea, R.J., Howard, J.A.K., Puschmann, H. The anatomy of a comprehensive constrained, restrained refinement program for the modern computing environment - Olex2 dissected. *Acta Cryst*. **2015**, *A71*, 59-75.
12. Sheldrick, G.M. *Acta Cryst*. **2008**, *A64*, 112-122.
13. Zuccaccia, D., Foresti, E., Pettirossi, S., Sabatino, P., Zuccaccia, C., Macchioni, A. From Ion Pairs to Ion Triples through a Hydrogen Bonding-Driven Aggregative Process. *Organometallics*. **2007**, *26* (25), 6099 - 6105.
14. Anantharaj, S., Noda, S. Appropriate Use of Electrochemical Impedance Spectroscopy in Water Splitting Electrocatalysis. *ChemElectroChem*., **2020**, *7* (10), 2297-2308.
15. Shinagawa, T., Garcia-Esparza, A. T., Takanabe, K. Insight on Tafel slopes from a microkinetic analysis of aqueous electrocatalysis for energy conversion. *Scientific reports*. **2015**, *5*, 1-21.
16. Naslund, L. -A., Sanchez-Sanchez, C. M., Ingason, A. S., Backstrom, J., Herrero, E., Rosen, J., Holmin, S. The Role of TiO_2 Doping on RuO_2-Coated Electrodes for the Water Oxidation Reaction. *J. Phys. Chem. C.* **2013**, *117* (12), 6126 − 6135.

17. Fukuzumi, S., Hong, D. Homogeneous versus Heterogeneous Catalysts in Water Oxidation', *Eur. J. Inorg. Chem.* **2014**, *2014* (4), 645-659.
18. Bianchi, C. L., Ragaini, V. An XPS study on ruthenium compounds and catalysts. *Materials & Chemistry and Physics.* **1991**, *29* (1-4), 297-306.
19. Morgan, D. J. Resolving ruthenium: XPS studies of common ruthenium materials. *Surf. Interface Anal*. **2015**, *47* (11), 1072–1079.

Appendix B

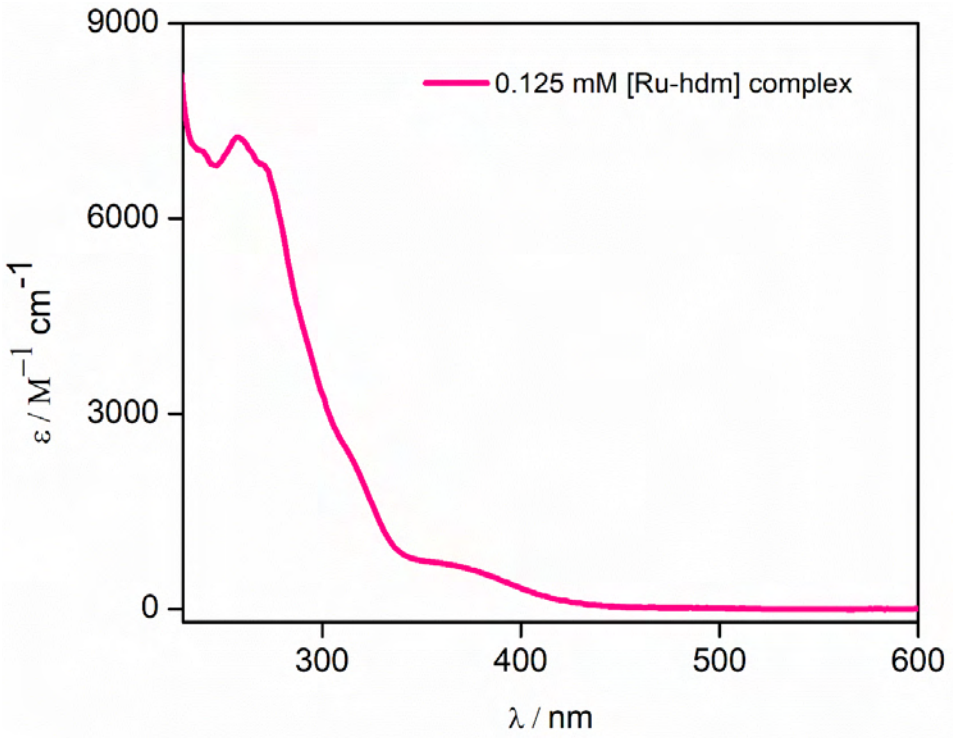

Figure B1. UV-Visible spectra of 0.125 mM **[Ru-hdm]** in water.

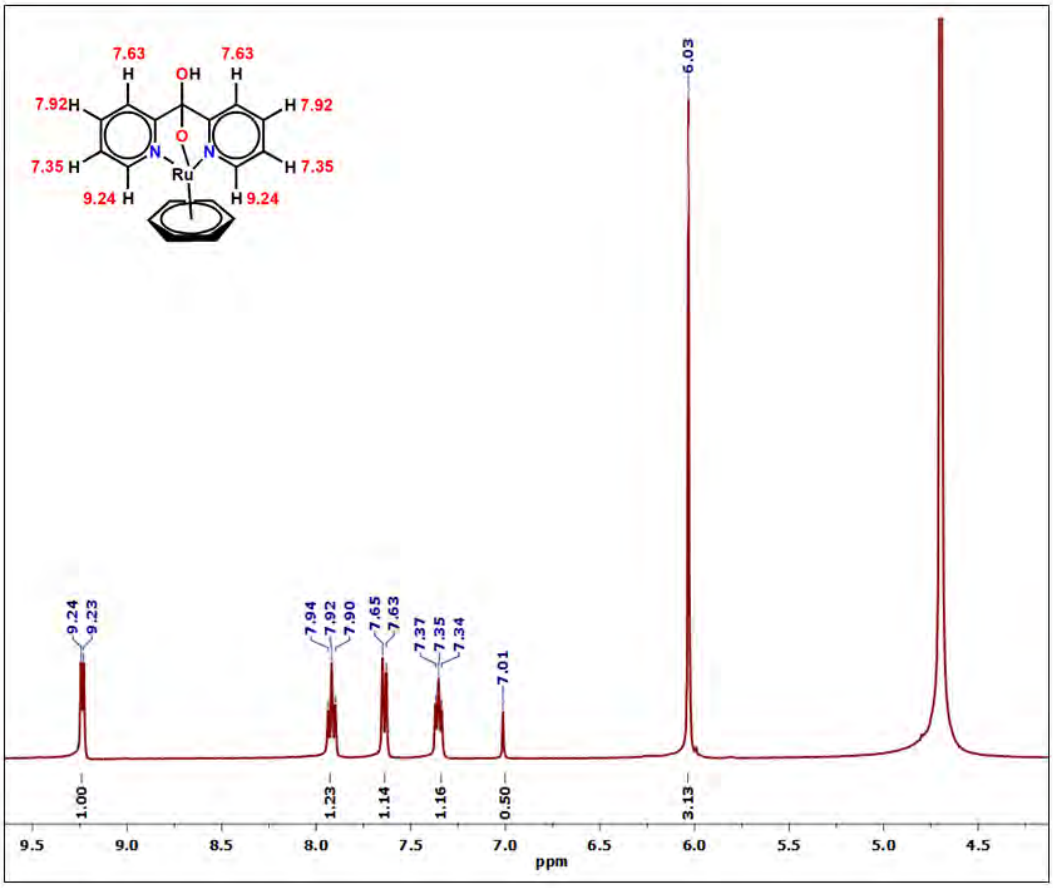

Figure B2. ^{1}H NMR of **[Ru-hdm]** in D_2O.

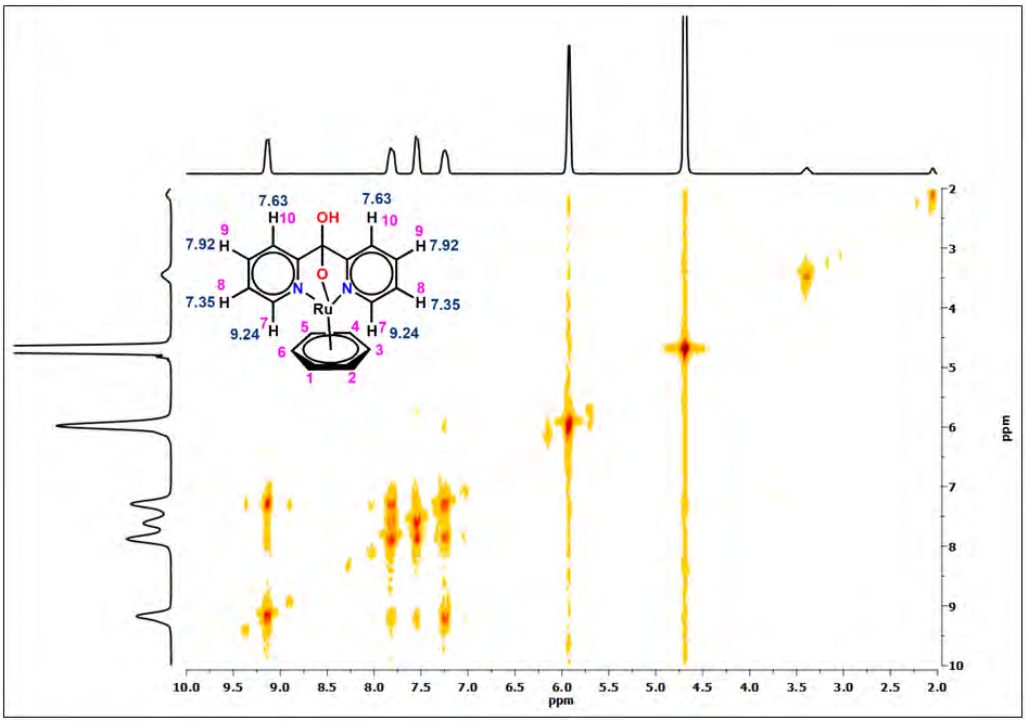

Figure B3. ^{1}H-^{1}H COSY NMR of **[Ru-hdm]** in D_2O.

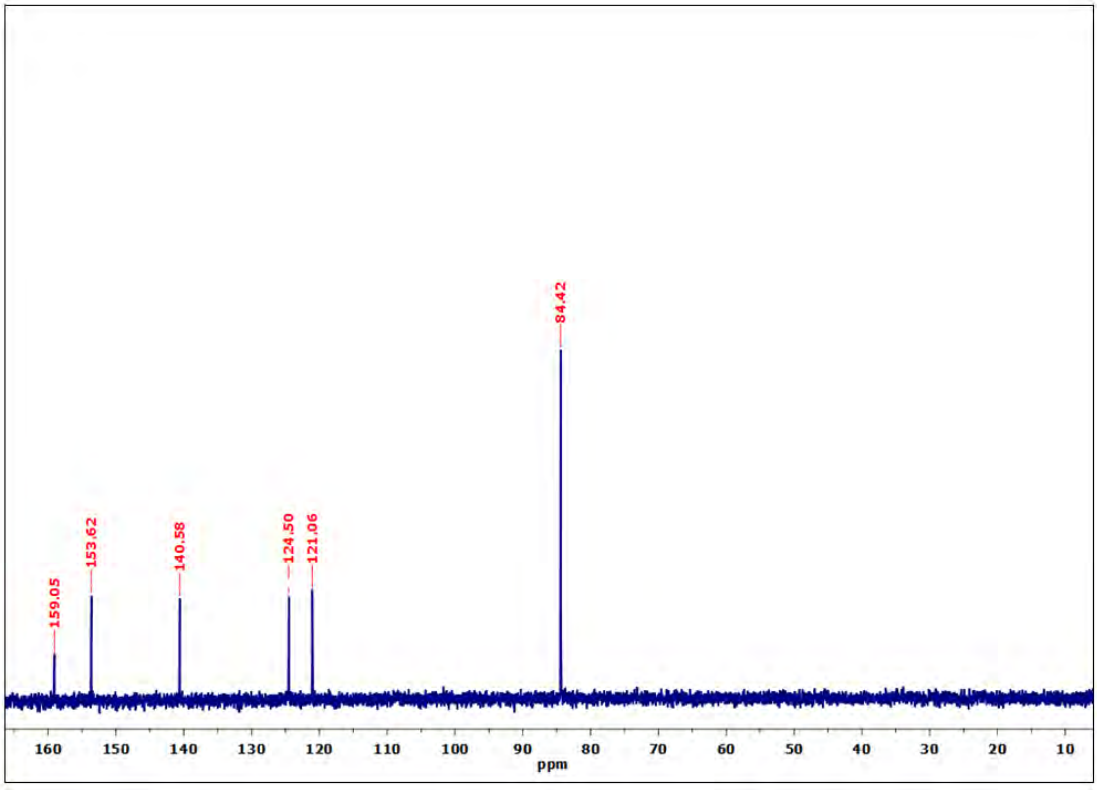

Figure B4. ^{13}C NMR of **[Ru-hdm]** in D_2O.

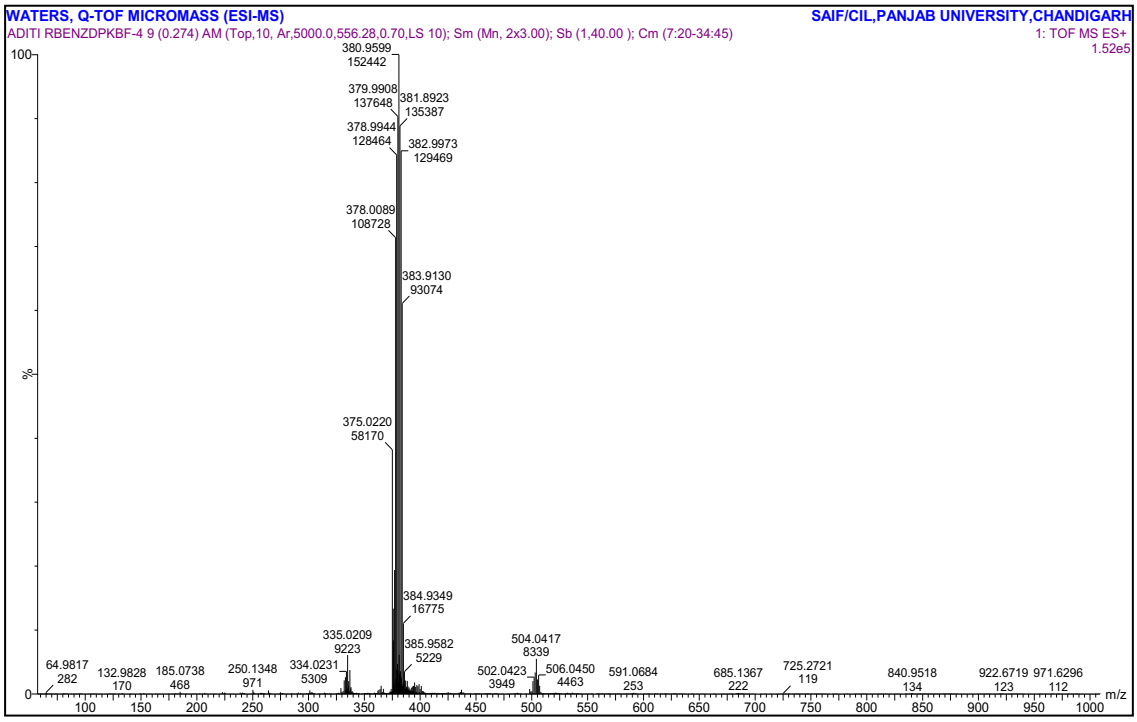

Figure B5. ESI-MS spectra of **[Ru-hdm]** in water.

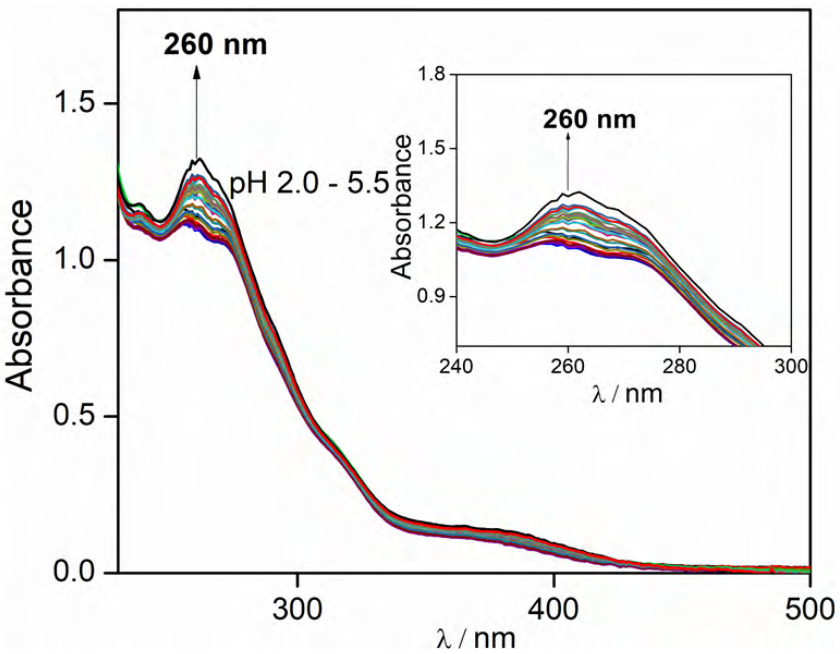

Figure B6. Change in UV-Visible spectra of **[Ru-hdm]** within the pH 2.0 -5.5.

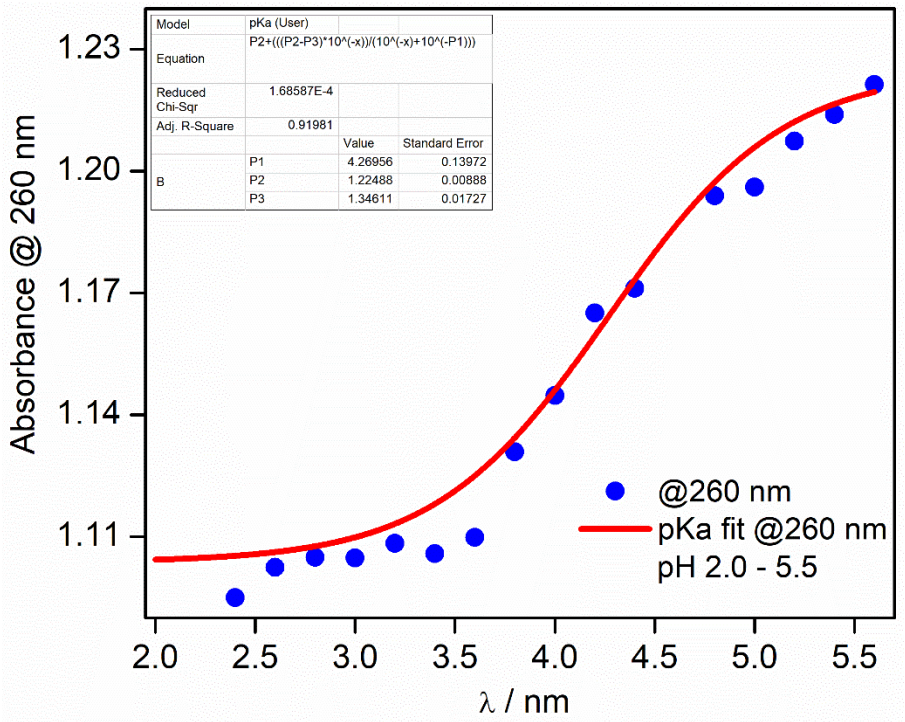

Figure B7. Absorbance vs. pH profile of **[Ru-hdm]** within the pH 2.0 – 5.5.

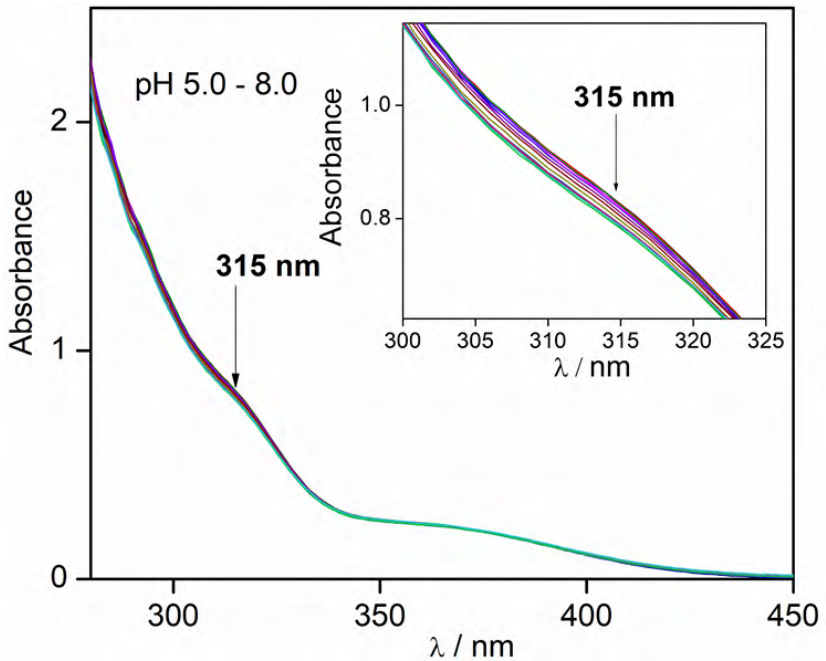

Figure B8. Change in UV-Visible spectra of **[Ru-hdm]** within the pH 5.0 - 8.0.

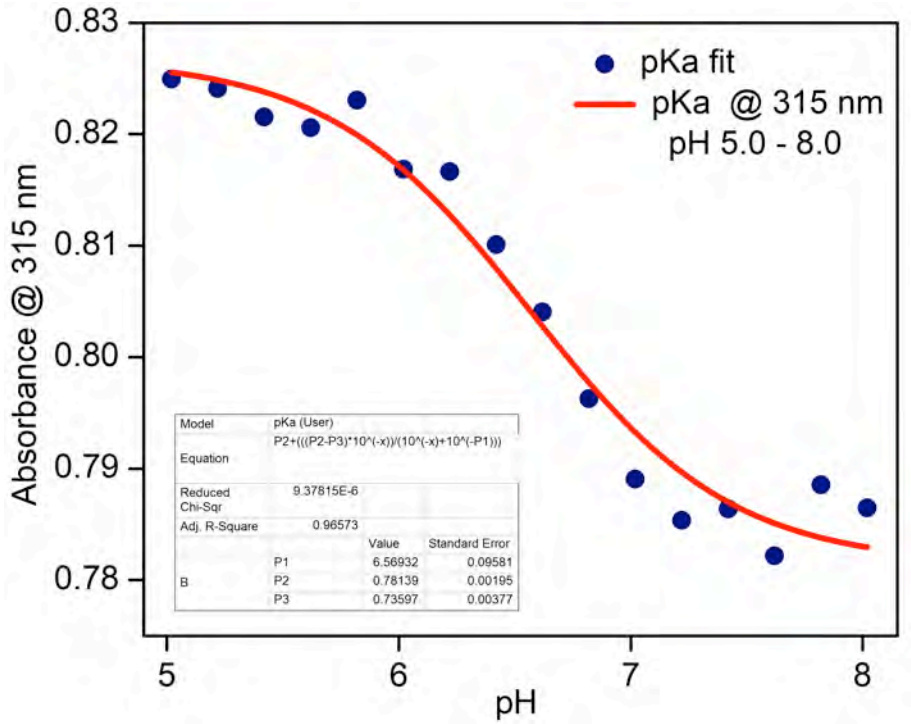

Figure B9. Absorbance vs. pH profile of **[Ru-hdm]** within the pH 5.0 - 8.0.

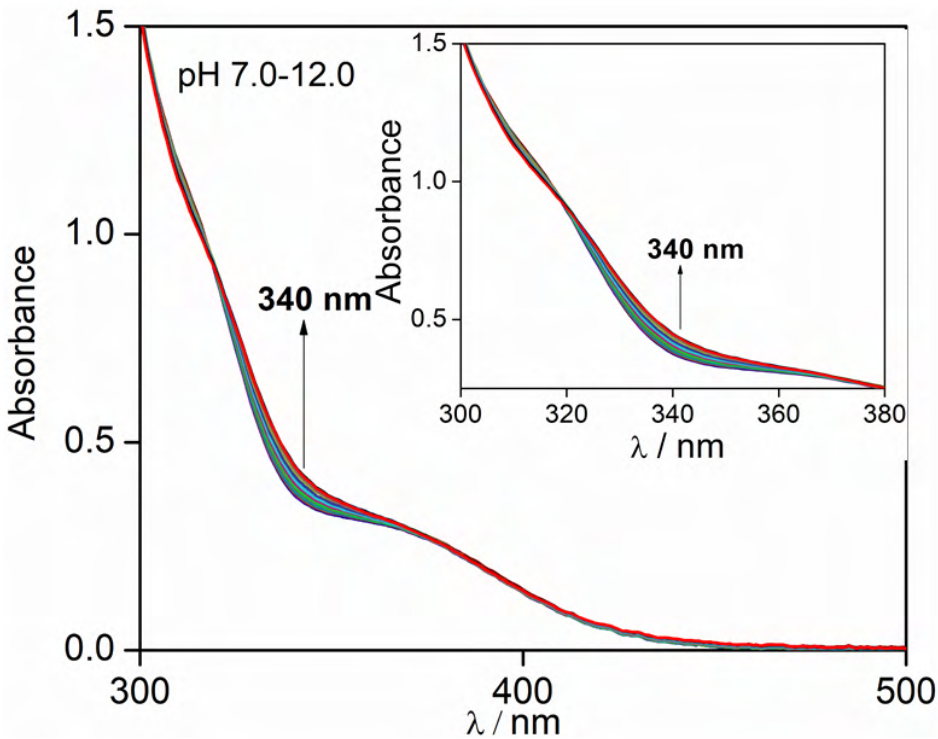

Figure B10. Change in UV-Visible spectra of **[Ru-hdm]** within the pH 7.0-12.0

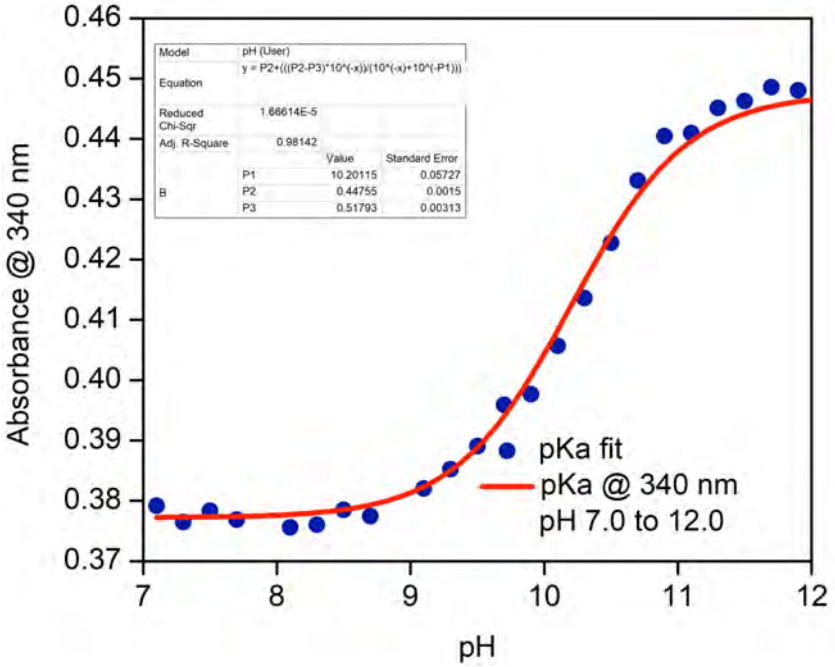

Figure B11. Absorbance vs. pH profile of **[Ru-hdm]** within the pH 7.0-12.0.

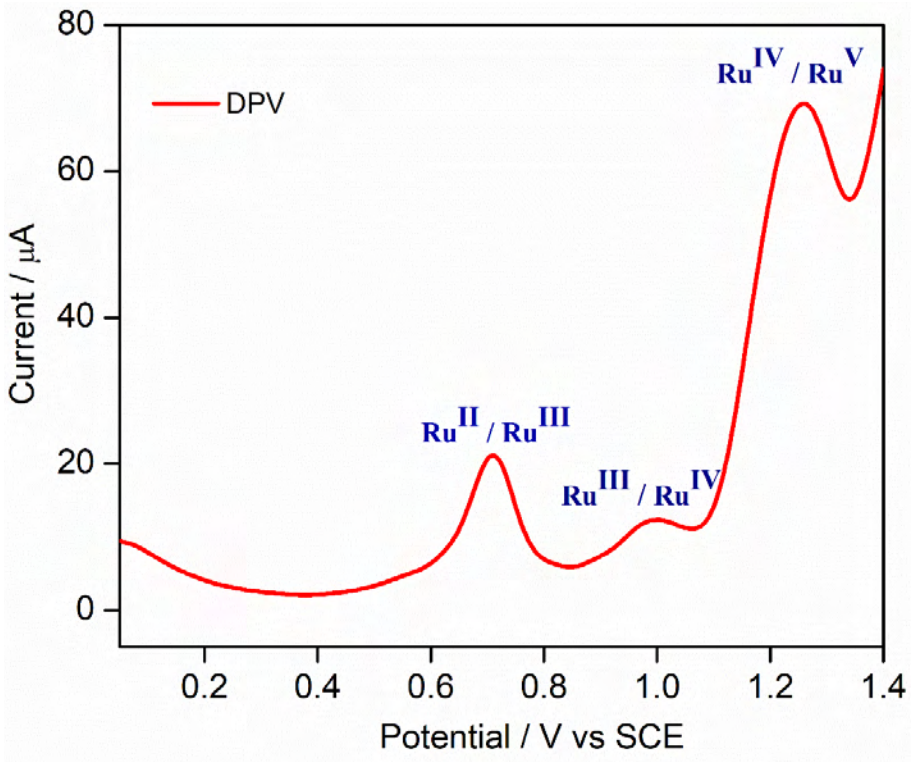

Figure B12. Differential pulse voltammetry of **[Ru-hdm]** complex in water using 0.1 M $NaBF_4$ as supporting electrolyte.

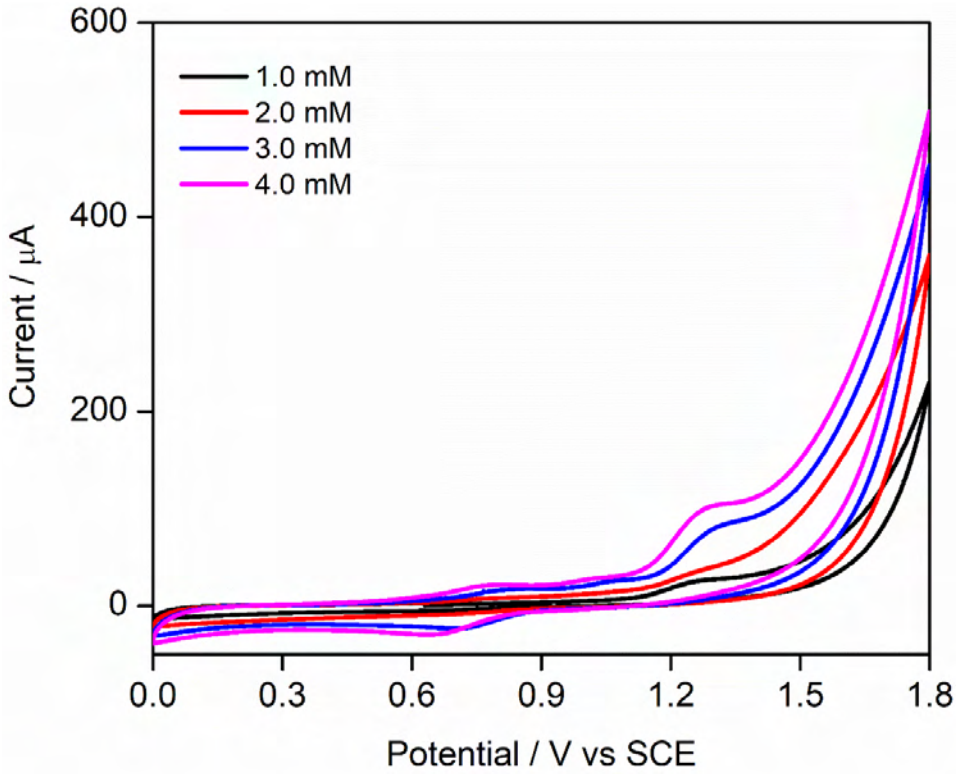

Figure B13. Cyclic voltammetry of **[Ru-hdm]** complex in different concentrations of the complex in the water using 0.1 M $NaBF_4$ as supporting electrolyte.

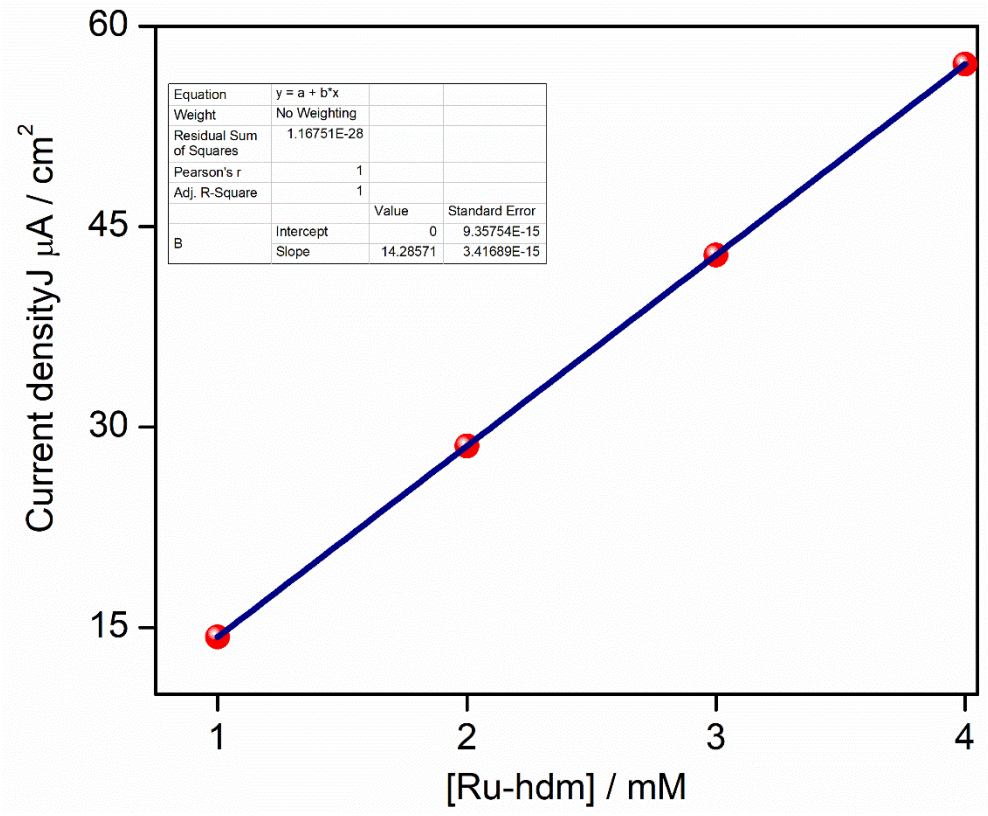

Figure B14. Plot for Current density vs. concentration of the catalyst **[Ru-hdm]**.

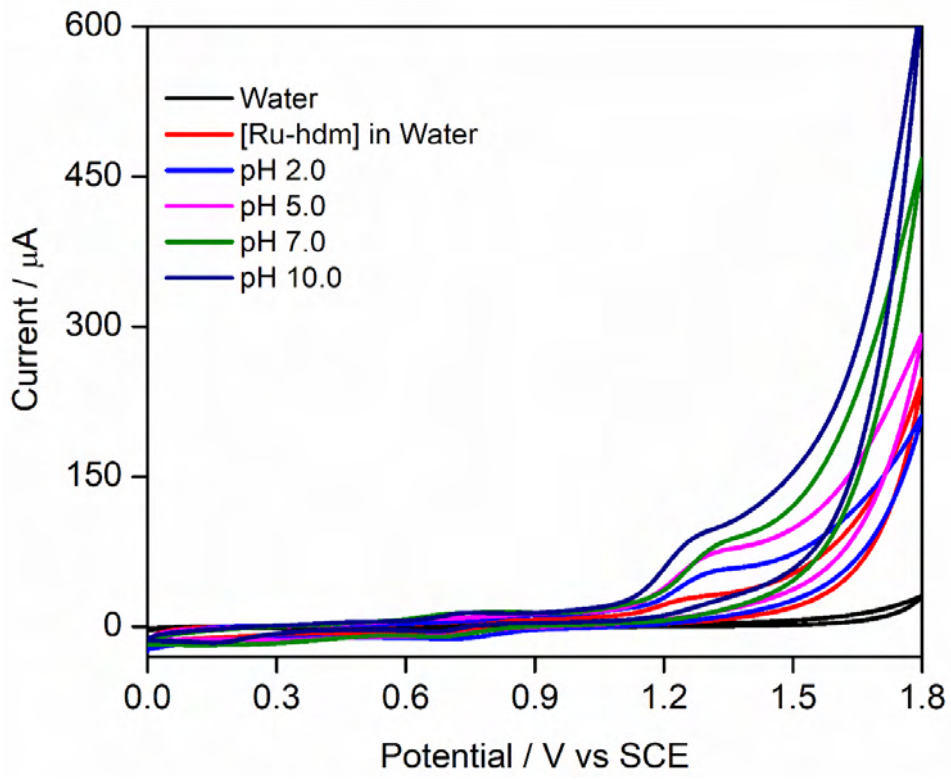

Figure B15. Cyclic voltammetry of **[Ru-hdm]** complex at different pH in Britton-Robinson buffer.

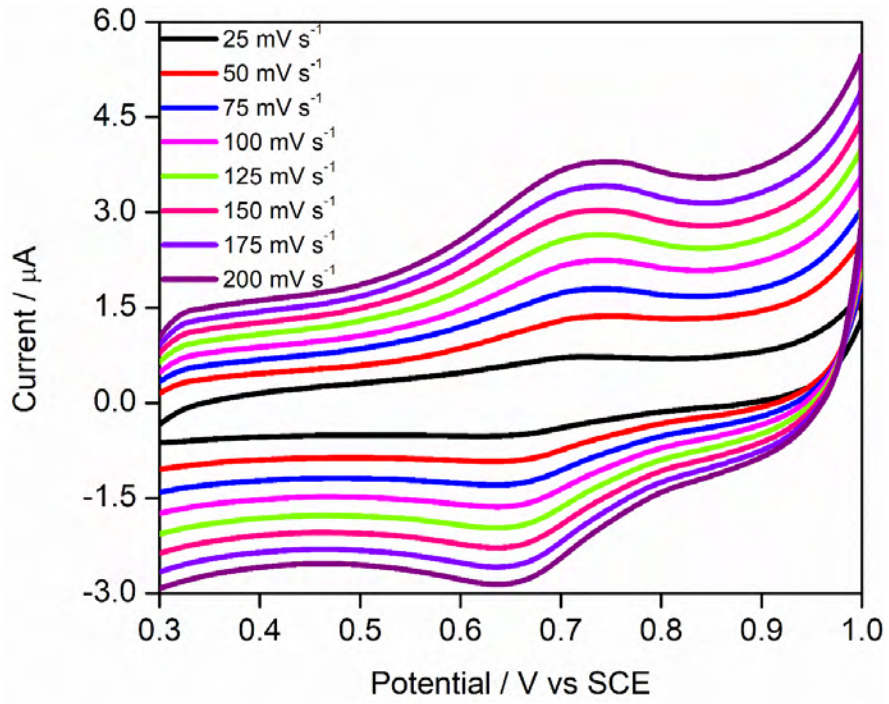

Figure B16. The plot of current vs. potential of the 1.0 mM of **[Ru-hdm]** complex with the variation of scan rate from 25 mV/s to 200 mV/s.

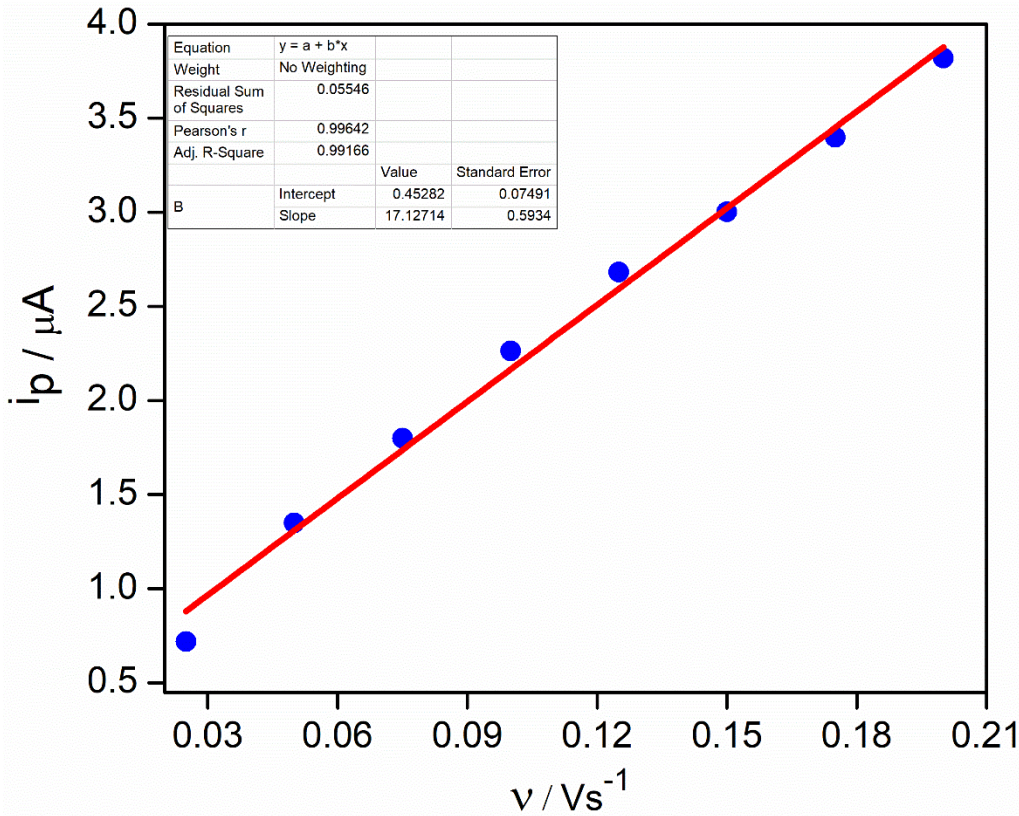

Figure B17. The plot of peak current (i_p) vs. scan rate ϑ.

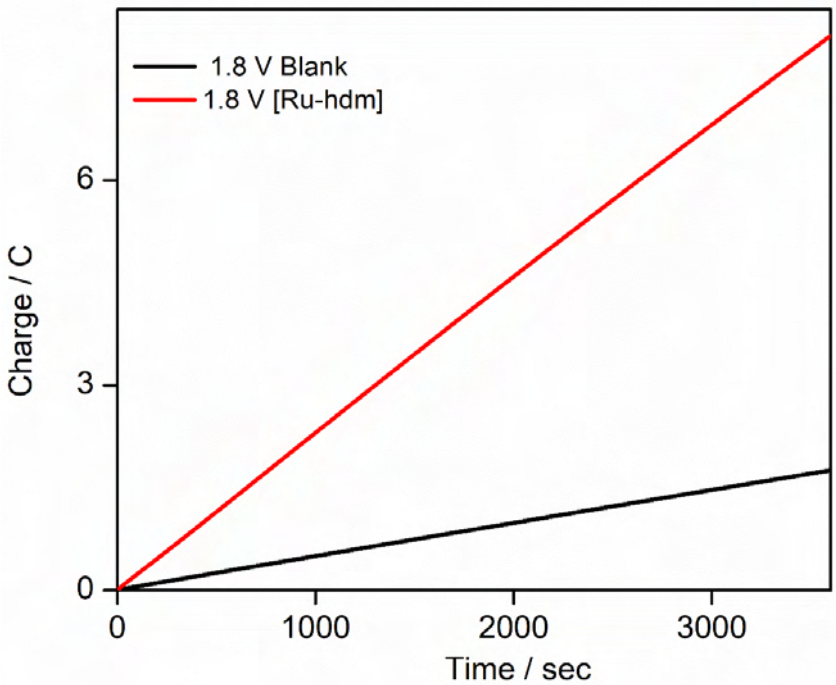

Figure B18. Bulk electrolysis of 1.0 mM of **[Ru-hdm]** in phosphate buffer at pH 6.6.

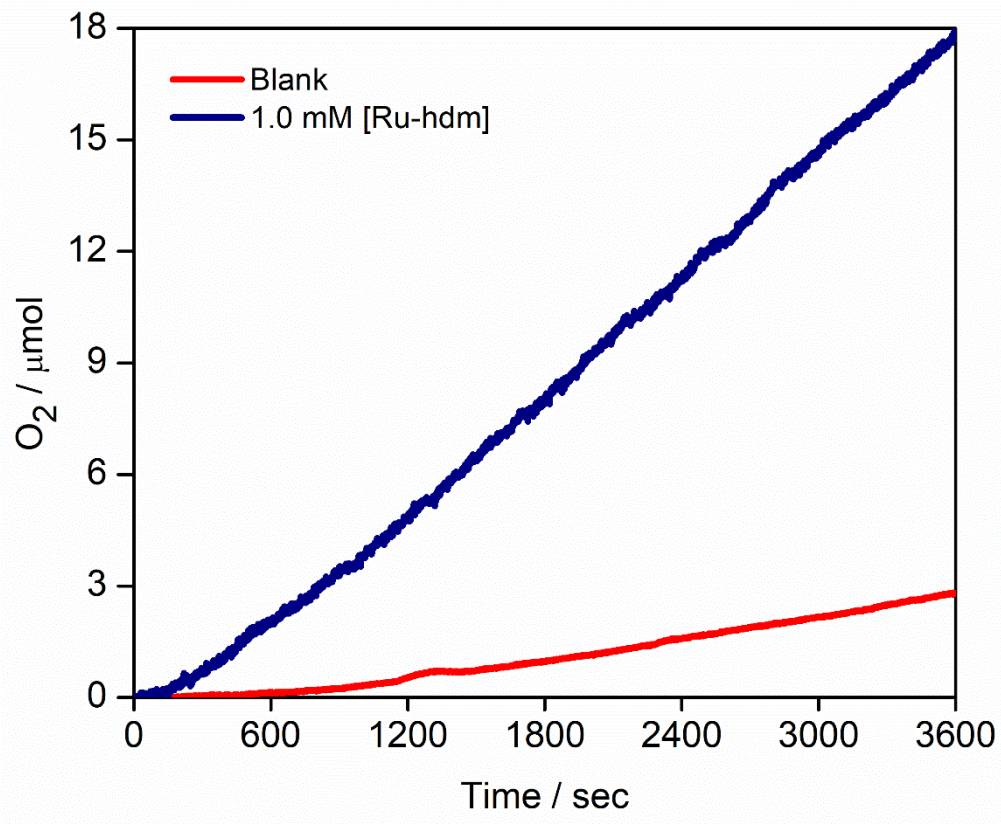

Figure B19. Oxygen evolution using O_2 sensor during bulk electrolysis at 1.8 V vs. SCE in phosphate buffer at pH 6.6 using 1.0 mM of **[Ru-hdm]** complex.

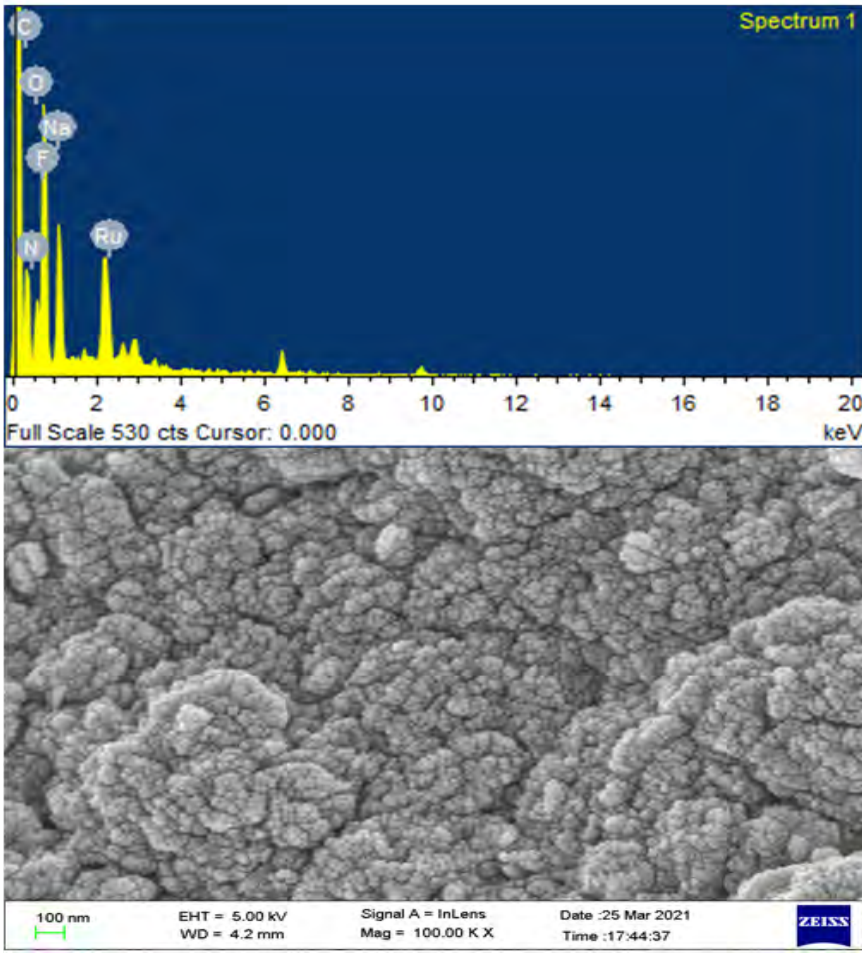

Figure B20. FE-SEM image and EDX analysis of the glassy carbon electrode after bulk electrolysis at 1.8 V vs. SCE in phosphate buffer at pH 6.6 using 1.0 mM of **[Ru-hdm]** complex.

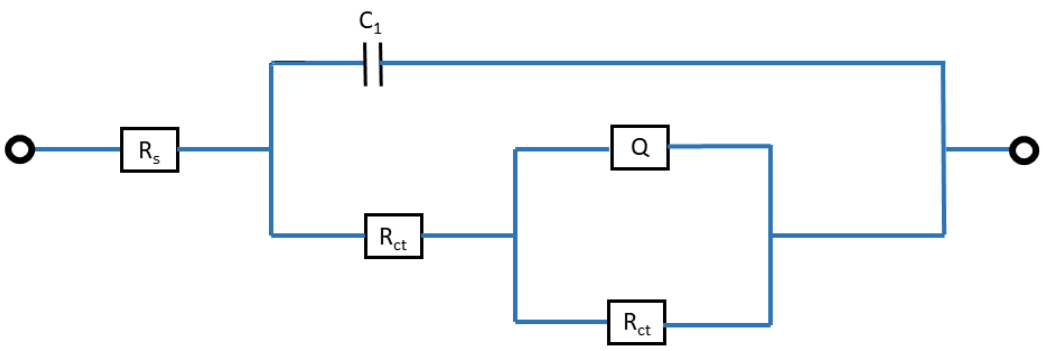

Figure B21. Equivalent circuit diagram for the fitting of impedance.

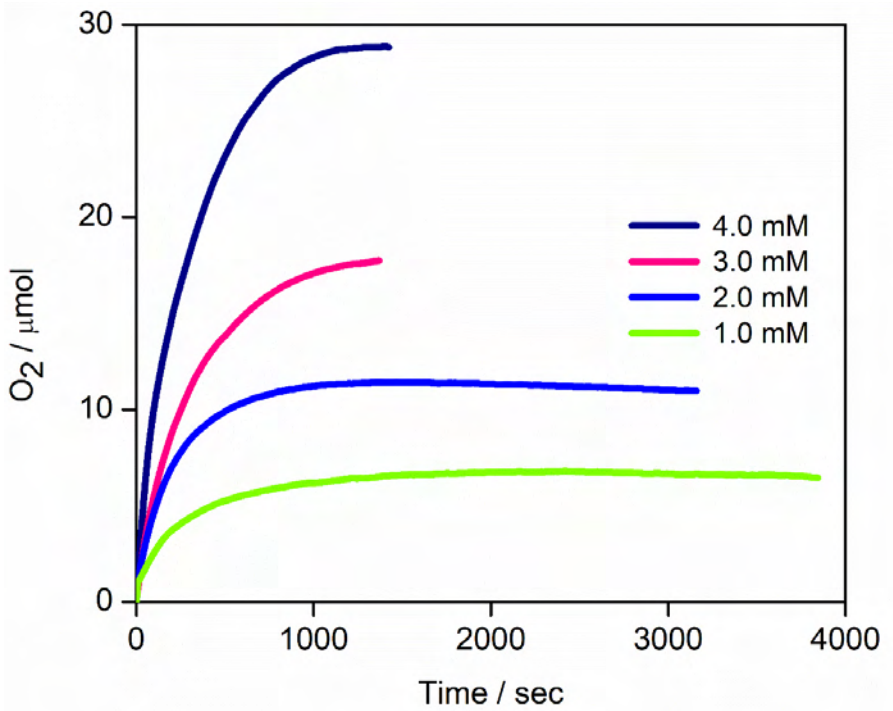

Figure B22. Variation of **[Ru-hdm]** complex concentration in the presence of 100mM of CAN in water.

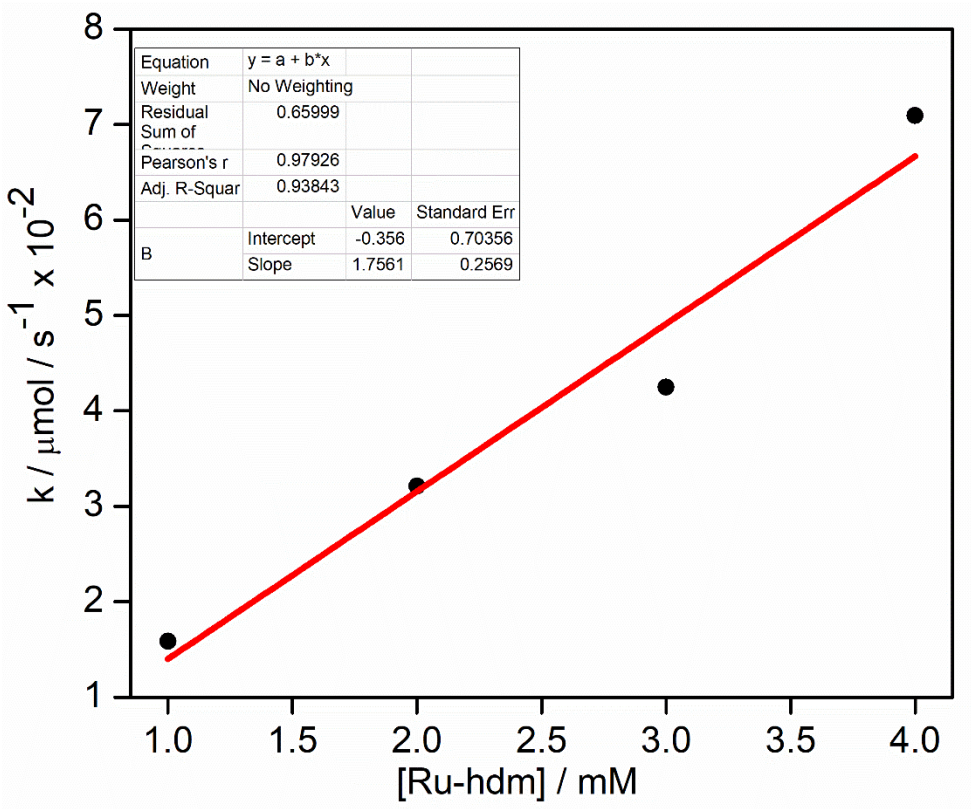

Figure B23. Rate of O_2 evolution *vs.* **[Ru-hdm]** Complex in water.

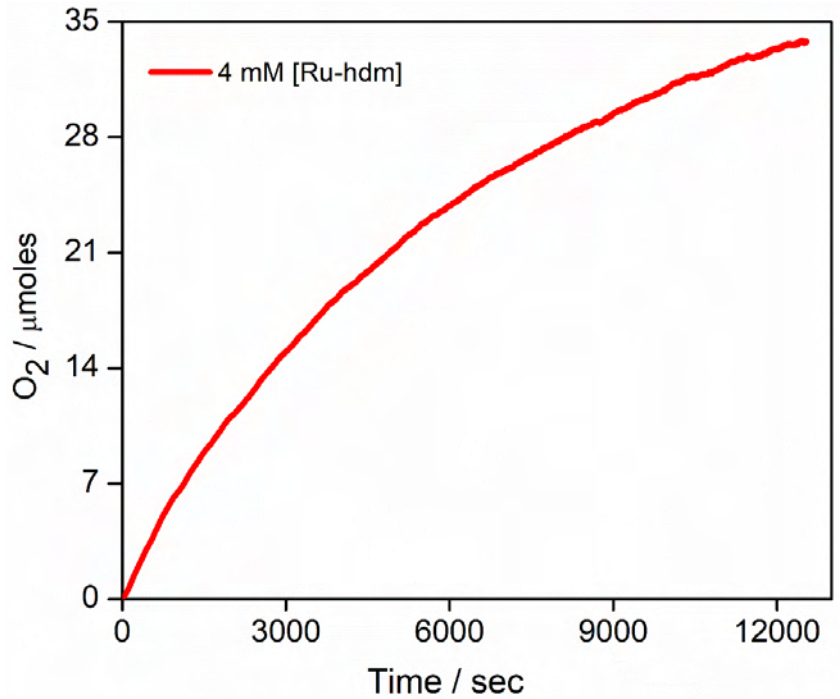

Figure B24. Oxygen sensor plot for 4.0 mM of **[Ru-hdm]** complex using 100 mM of CAN in water.

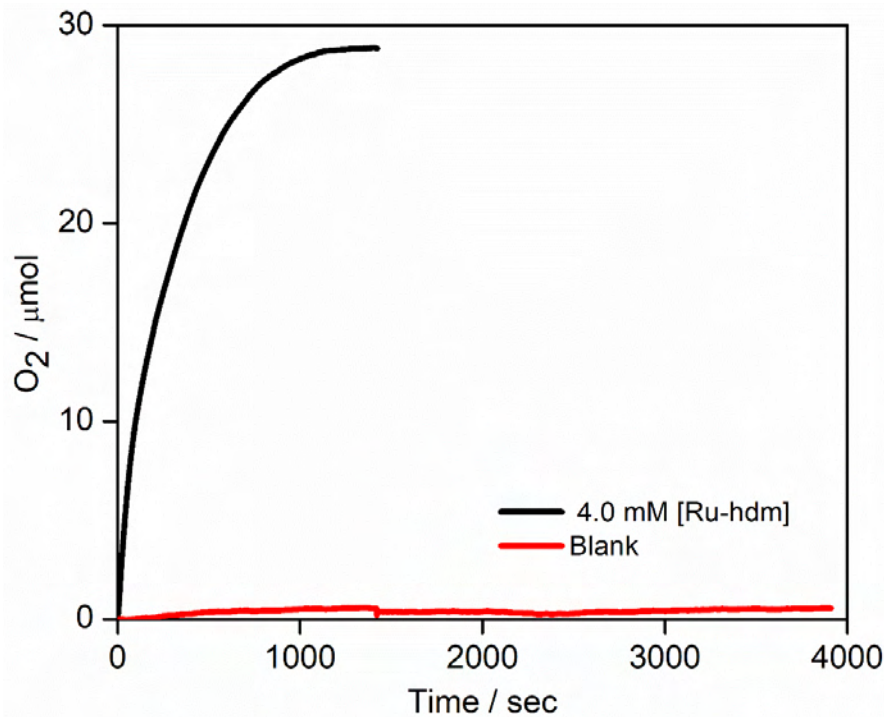

Figure B25. O_2 evolution in water in the presence of 100 mM of CAN (red) and 4.0 mM of catalyst (black).

Figure B26. Nanoparticle formation in the working compartment during catalytic chemical water oxidation with the addition of CAN into the complex solution in neutral water.

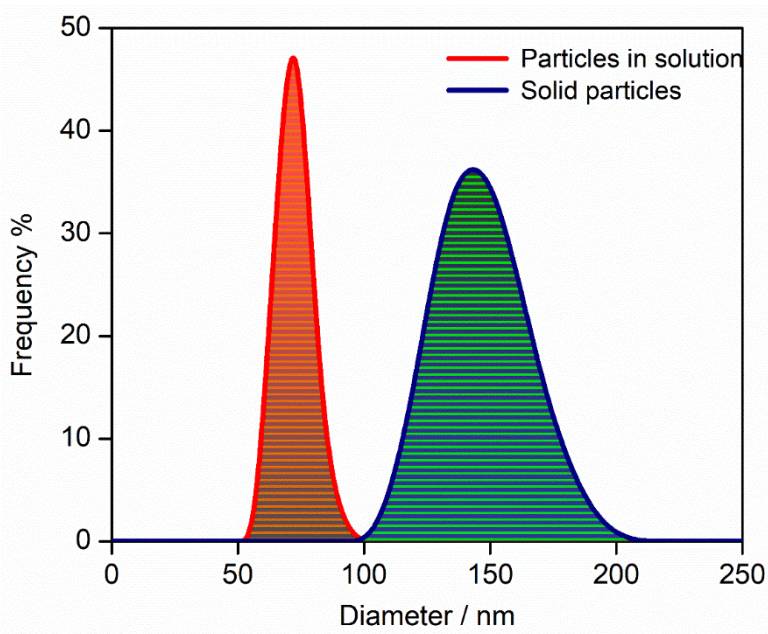

Figure B27. Differential light scattering (DLS) plot for solid particles and particles in solution.

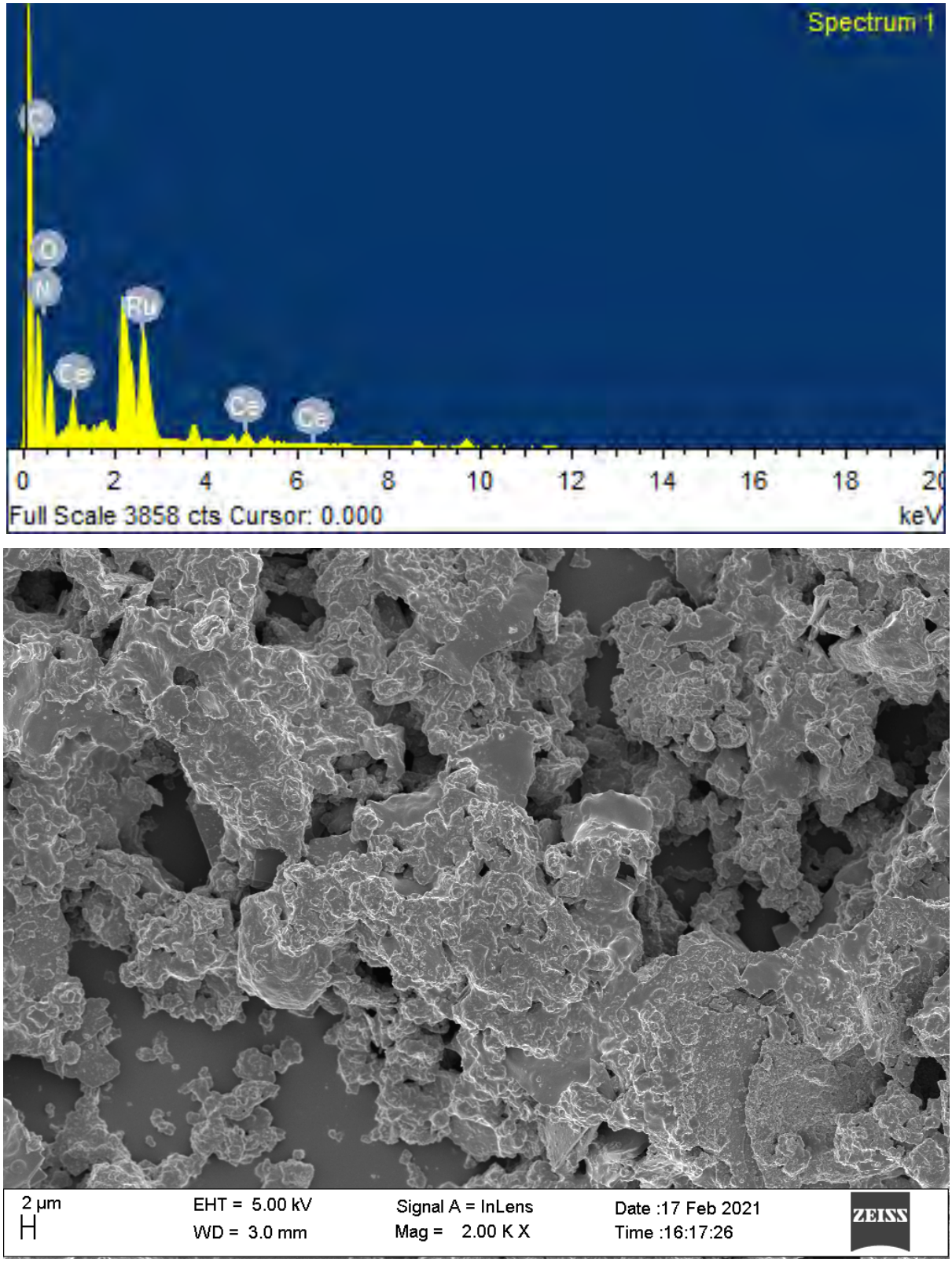

Figure B28. FE-SEM image and EDX analysis of the particles deposited over the septum during chemical water oxidation.

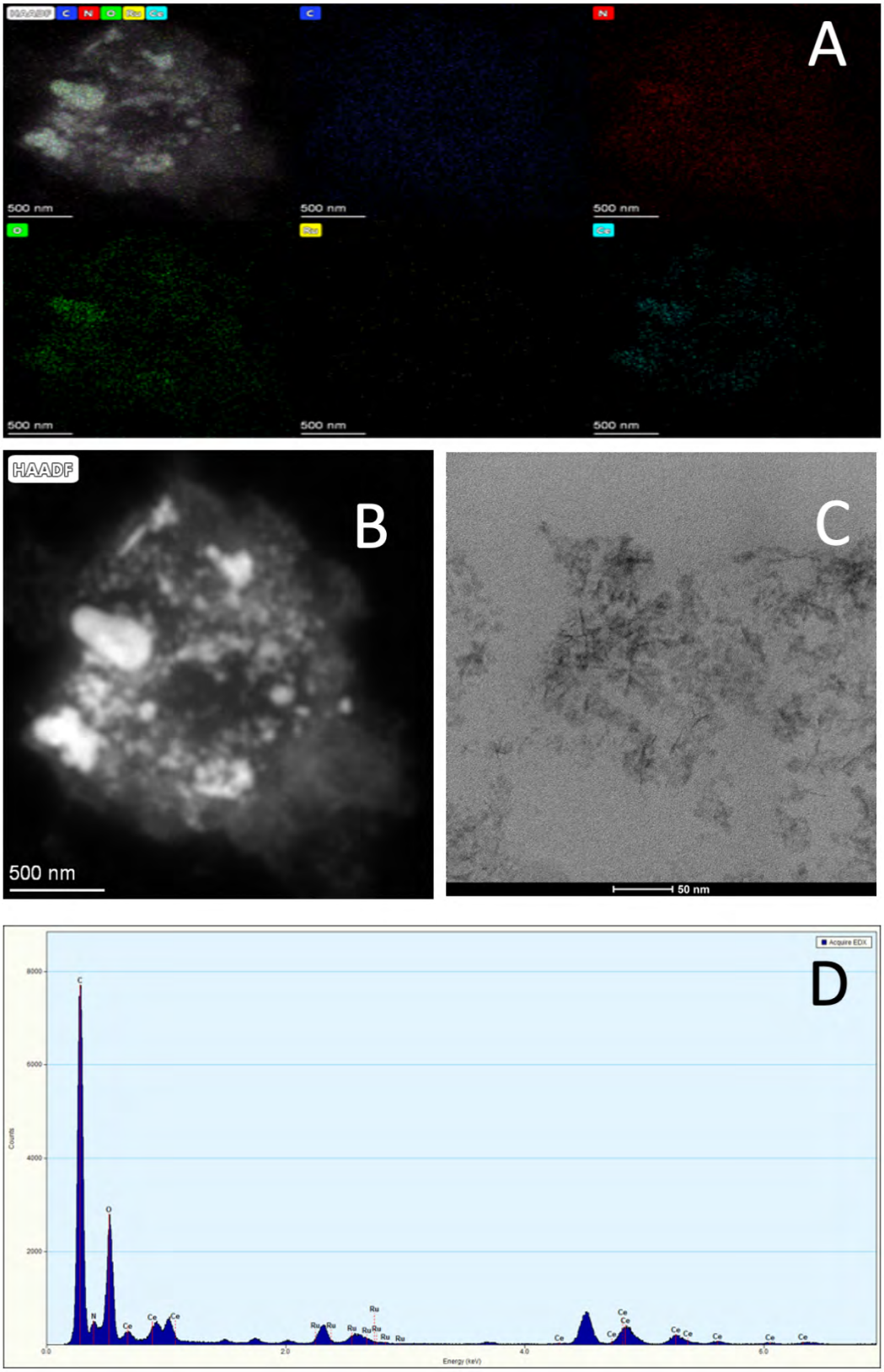

Figure B29. (A) Elemental mapping, (B-C) HR-TEM image, and (D) EDX analysis of the particles deposited over the septum.

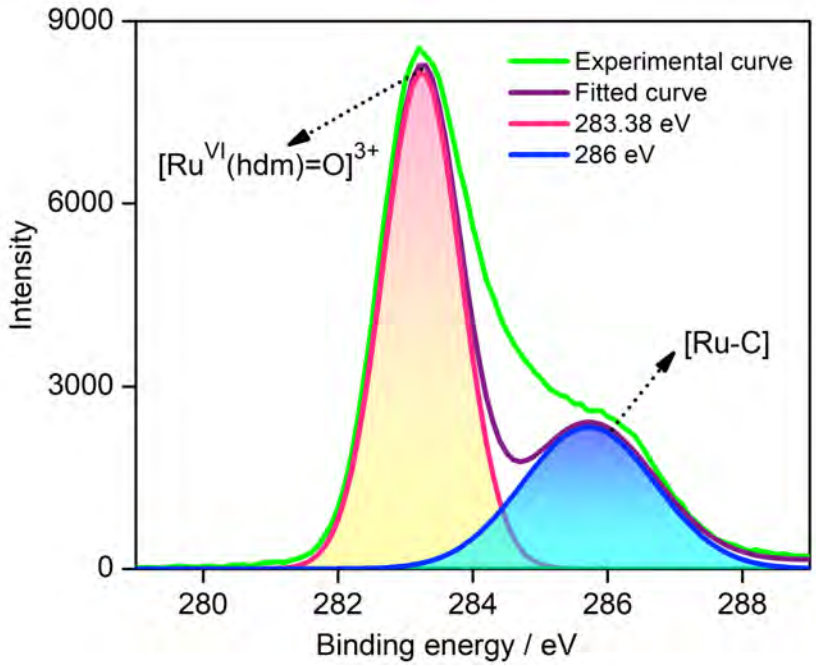

Figure B30. Fitted Ru(3d) spectra for Ru^{VI}=O of solid particle deposited over silicone septum.

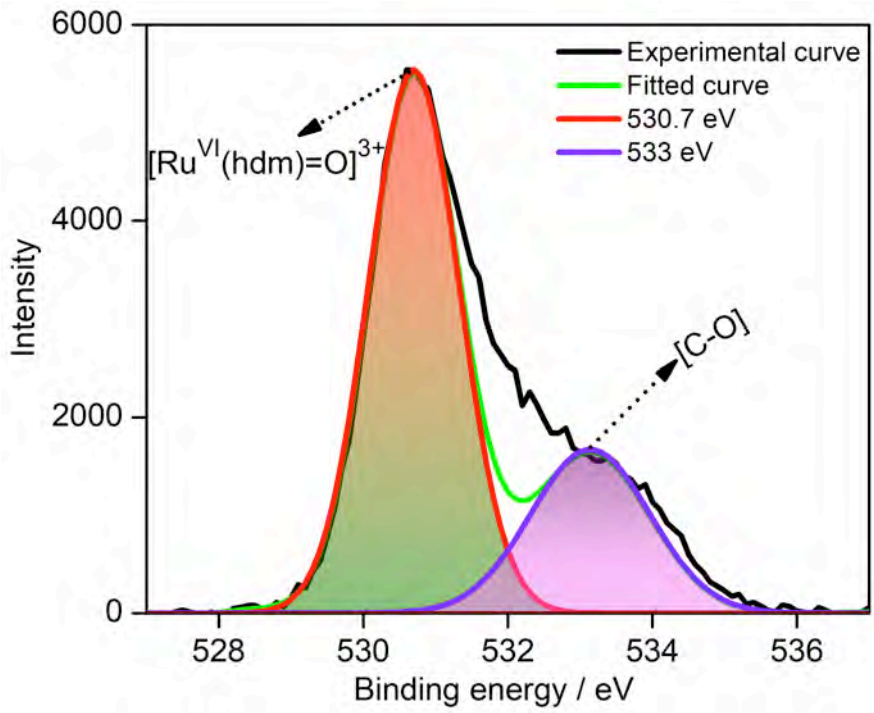

Figure B31. Fitted O(1s) spectra for Ru^{VI}=O of solid particles deposited over silicone septum.

Table B1. Crystal data and structure refinement for [Ru(hdm)(Bz)]BF_4.2H_2O.

CCDC Identification code	CCDC 2081415
Empirical formula	C17 H19 B F4 N2 O4 Ru
Formula weight	503.22
Temperature/K	293(2)
Crystal system	monoclinic
Space group	$P2_1/c$
a/Å	11.8988(11)
b/Å	16.8711(19)
c/Å	9.9405(11)
α/°	90.00
β/°	93.007(10)
γ/°	90.00
Volume/$Å^3$	1992.8(4)
Z	4
ρ_{calc}g/cm^3	1.677
μ/mm^{-1}	0.849
F(000)	1008.0
Crystal size/mm^3	0.26 × 0.23 × 0.21
Radiation	MoKα (λ = 0.71073)
2Θ range for data collection/°	5.74 to 53
Index ranges	$-14 \leq h \leq 14$, $-16 \leq k \leq 21$, $-12 \leq l \leq 12$
Reflections collected	9547
Independent reflections	4128 [R_{int} = 0.0582, R_{sigma} = 0.0731]
Data/restraints/parameters	4128/0/290
Goodness-of-fit on F^2	0.995
Final R indexes [I>=2σ (I)]	R_1 = 0.0495, wR_2 = 0.1048
Final R indexes [all data]	R_1 = 0.0751, wR_2 = 0.1201
Largest diff. peak/hole / e $Å^{-3}$	0.67/-0.87

Table B2. Selected Bond Lengths for [Ru(hdm)(Bz)]BF_4.2H_2O.

Atom	Atom	Length/Å
Ru1	O1	2.036(3)
Ru1	N1	2.117(4)
Ru1	N2	2.124(4)
Ru1	C13	2.147(7)
Ru1	C14	2.154(6)
Ru1	C12	2.184(6)
Ru1	C19	2.166(6)
Ru1	C15	2.163(6)
Ru1	C16	2.205(6)

Table B3. Selected Bond Lengths for $[Ru(hdm)(Bz)]BF_4.2H_2O$

Atom	Atom	Atom	Angle/°
O1	Ru1	N1	76.93(13)
O1	Ru1	N2	76.84(12)
O1	Ru1	C13	92.8(2)
O1	Ru1	C14	97.9(2)
O1	Ru1	C12	113.7(3)
O1	Ru1	C19	149.0(3)
O1	Ru1	C15	126.5(3)
O1	Ru1	C16	165.6(3)
N1	Ru1	N2	81.91(14)
N1	Ru1	C13	147.9(3)
N1	Ru1	C14	114.1(3)
N1	Ru1	C12	169.4(3)
N1	Ru1	C19	132.9(3)
N1	Ru1	C15	95.7(2)
N1	Ru1	C16	103.9(2)
N2	Ru1	C13	125.7(3)
N2	Ru1	C14	161.9(3)
N2	Ru1	C12	100.0(2)
N2	Ru1	C19	96.8(2)
N2	Ru1	C15	155.6(3)
N2	Ru1	C16	117.6(3)
C13	Ru1	C14	36.5(3)
C13	Ru1	C12	36.4(3)
C13	Ru1	C19	66.0(3)
C13	Ru1	C15	65.9(3)
C13	Ru1	C16	78.9(3)
C14	Ru1	C12	66.0(3)
C14	Ru1	C19	78.7(3)
C14	Ru1	C15	36.9(3)
C14	Ru1	C16	68.4(3)
C12	Ru1	C16	65.9(3)
C19	Ru1	C12	36.7(3)
C19	Ru1	C16	36.0(3)
C15	Ru1	C12	78.2(3)
C15	Ru1	C19	67.0(3)
C15	Ru1	C16	39.2(3)

CHAPTER 4

This chapter is published in

Vatsa, A. and Padhi, S. K.*, Chemistry Select, 2021, 6(35), 9447-9452.

Chapter 4

Dehydrogenation of Formic Acid by a Ru^{II} Half Sandwich Catalyst

4.1 Introduction

An enhancement in the exhaustion of fossil fuels and a rise in population is the major contributor headed for the emission of greenhouse gases and climatic changes. The worldwide energy fulfillment requires the breakthrough towards technologies dealing with renewable energy production which must be a clean, biodegradable, and sustainable form of energy.[1-2] Molecular hydrogen is one of the finest sources of fuel as it only produces water by its combustion during electrolysis. Formic acid is the most convenient material for the storage of hydrogen with 4.4 wt% of hydrogen content.[3] Dehydrogenation of the formic acid into hydrogen and carbon dioxide is the most promising reaction for H_2 generation under mild conditions.[4-5] The dehydrogenation reactions were catalyzed by using homogenous as well as heterogeneous catalysts. Coffey introduced the decomposition of formic acid by using phosphine-stabilized Ru, Ir, Pt complexes at a lower temperature.[6] Beller and group have reported the dehydrogenation of formic acid with precursor complexes such as [{$RuCl_2$(*p*-cymene)}$_2$] and [{$RuCl_2$(benzene)}$_2$] and [{RuI_2(*p*-cymene)}$_2$] by varying the concentration of formic acid–ammine adducts.[7] Fukuzumi and the group have synthesized the heterodinuclear iridium-ruthenium complex that catalyzes the dehydrogenation of formic acid in water. They have proposed that the kinetic isotopic effect (KIE) increases with an increase in pH and this complex shows the highest TON at pH 3.8.[8]

The dehydrogenation reaction of formic acid was investigated from lower to higher temperatures and also with a variety of concentrations of acid, base, and complex concentration. The kinetics of the H_2 generation was studied by using isotopic labeling of water and formic acid. The pH dependence of the formic acid was explored at different pH to find out its highest activity or reactivity at desired pH.[9-10]

The aforementioned results prompted us to study the catalytic activity of **[Ru-hdm]** towards dehydrogenation of formic acid in simple water using sodium formate (HCOONa) as a base. The effect of variable temperature, base, acid, and complex concentration, and kinetics of dehydrogenation has been investigated. The activity of the complex for dehydrogenation of formic acid has also been illustrated in different pH.

4.2. Experimental

4.2.1 Material and methods

4.2.1.1. Materials

All the reagents utilized in this work were of reagent grade. Di(2-pyridyl) ketone and Benzeneruthenium(II) chloride dimer were purchased from TCI chemicals and used without further purification. NaOH was purchased from Rankem and $AgPF_6$ and $NaBF_4$ from Sigma Aldrich. All the solvents like acetone, diethyl ether, petroleum ether, dichloromethane were purchased from Merck and dried before use. Milli-Q- purified distilled water was used in all experiments.

4.2.1.2. Optical Spectra

UV-Visible spectroscopic experiments were performed with an Agilent Cary 8454 photodiode array UV-Visible spectrophotometer.

4.2.1.3. NMR Spectroscopy and Mass Spectrometry

Proton NMR spectra were recorded on Bruker Ultrashield spectrometer at room temperature. High-resolution ESI mass spectrometry was recorded with Waters UPLC TQD and Bruker micrOTOF-Q II instruments.

4.2.1.4. Gas Evolution

The evolution of gas was based on manometric results by using 5 mL of double-jacketed reaction vessel containing 2 mL of the reaction mixture and having a headspace volume of 3 mL. The reference cell was filled with 2 mL of water and 3 mL is headspace volume as of the working cell. The H_2 and CO_2 evolved during dehydrogenation were converted into micromoles by using the ideal gas equation PV=nRT. The pressure of evolved gases was measured by using a differential pressure manometer of TESTO 521 with a range of 0 to 100 hPa, 0.1 hPa accuracy was used.

4.2.1.5. Gas chromatography mass spectrometer

The GC-MS of the gas sample was recorded on Thermo ISQ QD single quadruple mass analyser coupled with Trace 1300 GC equipped with HP-% column.

4.2.1.6. Gas chromatography analysis

The gas chromatography of the gas evolved during dehydrogenation reactions was recorded on MICHRO-9100 gas chromatograph on Netel (India) Limited.

4.3. Results and Discussion

4.3.1. Synthesis

The syntheses of the **[Ru-hdm]** (**hdm = hydroxydi(pyridine-2-yl)methanolate**)complex was discussed in Chapter 3.

4.3.2. Dehydrogenation reactions

The dehydrogenation of formic acid (FA) was investigated in the presence of base sodium formate (SF) and catalyst **[Ru-hdm]** using water as the solvent for the reaction. The reaction was carried out in a double jacketed round reaction vessel having **[Ru-hdm]** and base dissolved in water (Figure C1). To this solution, formic acid was injected through the rubber septum for initiating the gas evolution. The pressure evolved was observed through a differential pressure manometer. The catalyst towards dehydrogenation was studied by taking a different concentration of base, acid, catalyst and varying the temperature. These studies were essential for analyzing the rate constant for each set of reactions by kinetic plots concluded by linear fitting the initial reaction rate. The variation in concentrations of substrates and catalysts was important to determine the dependence of the rate of reaction on concentration to establish the order of reaction in each case at a fixed temperature of 55 °C. The catalyst shows an increase in gas evolution with time until the decomposition of formic acid by increasing the concentration of acid from 5 mmol to 20 mmol with 1.0 mM complex and 15 mmol base that indicates the first-order kinetics with acid concentration having rate constant k = 2.5 x 10^{-3} µmol s^{-1} (Figure 4.1(A) – 4.1 (B)).

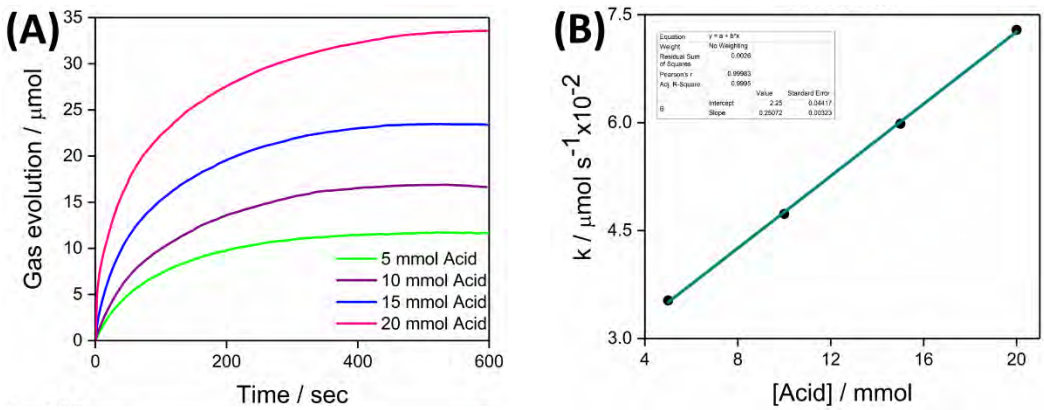

Figure 4.1. (A) Gas evolution by **[Ru-hdm]** with a variety of acid concentrations in the

presence of 1.0 mM of complex and 15 mmol of the base at 55 °C in water. **(B)** Rate of gas evolution *vs.* acid in water.

The TON is 5.87 and 16.90 at 5 mmol and 20 mmol of acid, respectively. The initial TOF for acid variation was found to be 0.114 s^{-1}. The base concentration varied from 1 mmol to 40 mmol with the catalyst at 1.0 mM, and acid concentration was constant at 10 mmol; it was observed that gas evolution rises with an increase in base concentration and attain maximum gas volume at 40 mmol. The TON is 3.85 for 1 mmol and a high TON of 15.64 for 40 mmol. The highest initial TOF of 0.11 s^{-1} was found for 40 mmol base and rate constant for base variation was found to be 1.5 x 10^{-3} µmol s^{-1} and follows the first-order kinetics showing dependence on base concentration for gas evolution (Figure C2 – C3). The complex concentration was varied from 0.50 mM to 1.0 mM with base 15 mmol and acid 10 mmol; the gas evolution starts increasing with time and becomes saturated on a decomposition of acid. The highest TON of 3.30 and the highest initial TOF of 0.09 s^{-1} was observed with a high concentration of complex of 1.50 mM. This reaction set also shows the dependence of the reaction rate on the concentration of complex with a rate constant of k = 4.27 x 10^{-2} µmol s^{-1} following the first-order kinetics (Figure C4 – C5). The dehydrogenation reaction is most favorable at high temperatures; therefore, the kinetics of decomposition of formic acid was also studied by varying the temperature from room temperature to high temperature. The temperature was changed from 25 °C to 70 °C by unvarying the concentration of base at 15 mmol, acid at 10 mmol, and catalyst at 1.0 mM, the rate constant for this reaction was found to be k = 4.7 x 10^{-4} µmol s^{-1} (Figure 4.2(A) – 4.2(B)).

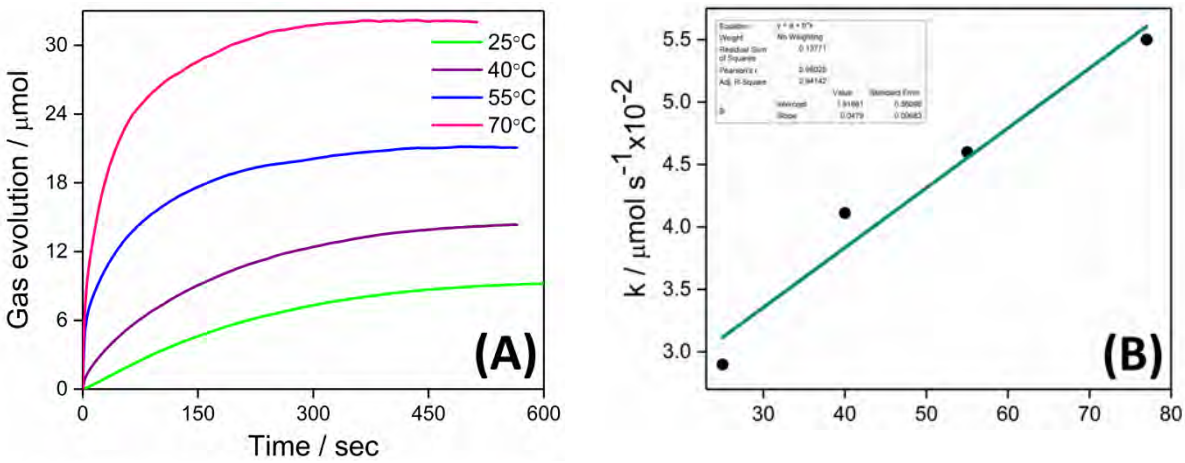

Figure 4.2. (A) Gas evolution by **[Ru-hdm]** with the variation of temperature in the presence of 1.0 mM of complex, 10 mmol of the base, and 15 mmol of acid in water. **(B)** Rate of gas evolution *vs.* temperature in water.

The highest TON of 16.24 and initial TOF of 0.13 s^{-1} at 70 °C and the lowest TON of 4.66 and initial TOF of 0.0165 s^{-1} at 25 °C were observed for this set of the reaction. The activity of the catalyst is much efficient with different concentrations of acid as compared to the base. The dehydrogenation reaction shows an increase in TON and TOF at a higher temperature than the room temperature. The total volume of gas is calculated based on the Ideal gas equation PV = *n*RT. The TON is calculated by equation no. of moles of gas evolved/no. of moles of catalyst utilized and TOF = TON/time. The TON, TOF, and volume of gas evolved in each reaction set were shown in Table 4.1. Blank experiment for dehydrogenation at 55 °C without catalyst using 10 mmol of formic acid and 15 mmol of sodium formate, evolved 3.0 µmol gas (Figure C6).

Table 4.1. Summary of experiments in different reaction conditions for dehydrogenation of formic acid.

Temperature / °C	Catalyst / [mM]	Acid / [mmol]	Base [mmol]	TON	Initial TOF / s^{-1}	The volume of Gas evolved / µmol
55	1.0	5	15	5.87	0.036	11.42
55	1.0	10	15	8.54	0.049	16.90
55	1.0	15	15	11.80	0.076	23.25
55	1.0	20	15	16.90	0.114	33.62
55	1.0	10	1	3.85	0.029	7.54
55	1.0	10	10	8.037	0.057	16.24
55	1.0	10	25	11.77	0.081	23.19
55	1.0	10	40	15.64	0.109	31.02
55	0.5	10	15	3.30	0.022	25.55
55	0.75	10	15	5.87	0.031	18.20
55	1.0	10	15	9.10	0.051	11.56
55	1.50	10	15	12.84	0.086	6.84
25	1.0	10	15	4.66	0.017	9.23
40	1.0	10	15	7.27	0.036	14.30
55	1.0	10	15	10.68	0.078	21.02
70	1.0	10	15	16.24	0.133	32.17

The evolution of hydrogen and carbon dioxide were also confirmed by GC-MS and gas chromatography techniques and it was observed that 3.6 x 10^{-5} moles of H_2, 3.88 x 10^{-5} moles of CO_2, and a very negligible amount of 0.0012 x 10^{-5} moles of CO (concentration of CO approx. 160 ppm) were evolved Figure C7 – C10). The concentration of H_2 and CO_2 is obtained in the ratio of 1:1. For the confirmation of the formation of [Ru-H], NMR was recorded at 90 °C in the presence of 10 mmol of the complex with the addition of 50 mmol of sodium formate. Still, the only signal at δ 8.25 ppm was observed for $HCOO^-$ and [Ru-H] species could not be identified through NMR. It is expected that the [Ru-H] species could be a transient species that got disappeared within a short period (Figure C11). The same results were observed with the

addition of 50 mmol formic acid and 50 mmol of sodium formate with 10 mmol catalysts at 90 °C in separate reactions (Figure C12).

4.2.3. Isotopic labelling kinetics of dehydrogenation reaction

The reaction mechanism was studied by kinetic isotopic effect using deuterated and non-deuterated water for dehydrogenation of the formic acid.[11-12] To find out the rate of the reaction decomposition of formic acid were performed with non-deuterated water and deuterium oxide with a high concentration of the catalyst in 20 mmol of acid and 40 mmol of the base at two different temperatures of 55 °C (Figure 4.3) and 70 °C (Figure C13). The kinetic isotopic effect is the ratio of rate constants of light water H_2O (k_H) for the rate constant of its heavier isotope D_2O (k_D). The rate constant k_H = 0.72 µmol s^{-1} for water and k_H = 0.24 µmol s^{-1} and the kinetic isotopic effect (KIE) k_H/k_D = 3.02 at 55 °C. At 70 °C, the rate constant for H_2O, k_H = 1.28 µmol s^{-1} and D_2O k_D = 0.27 µmol s^{-1} and its KIE value were found to be 4.69. At both temperatures, it was observed that the rate constant for H_2O is greater than its heavier isotope and the KIE ratio is greater than 1, which indicates that the reaction performed in heavy water had a slower reaction rate as compared to the reaction that occurred in water. Similarly, the TON and TOF values in non-deuterated water are higher than the deuterated water, as shown in Table 4.2.

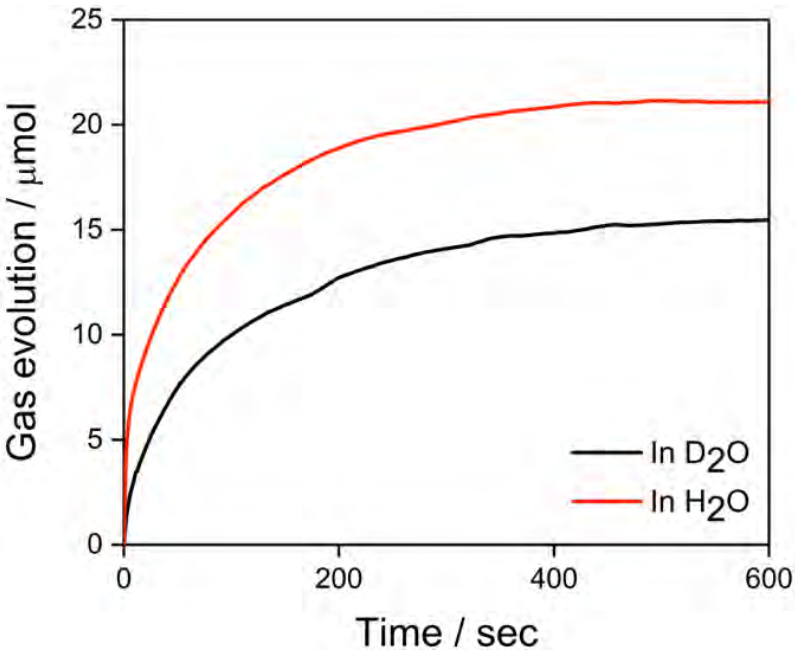

Figure 4.3. Gas evolution in H_2O and D_2O in 20 mmol of acid and 40 mmol of a base at 55°C in water

Table 4.2. TON, TOF, and volume of gas at different temperatures with deuterated and non-deuterated solvents.

Temperature / °C	Solvent	TON	Initial TOF / s^{-1}	The volume of gas evolved / µmol
55	H_2O	10.64	0.079	21.22
55	D_2O	7.70	0.050	15.71
70	H_2O	16.21	0.133	32.10
70	D_2O	11.71	0.087	23.44

4.2.4. Activation Parameters

The Arrhenius plot is the logarithm of the reaction rate constant *k* plotted for reciprocal of absolute temperature 1/T to calculate activation energy E_a using the equation (4.1).[13]

$$\boldsymbol{ln\, k = -\frac{E_a}{RT} + ln\, A} \qquad \textbf{(4.1)}$$

Where A = pre-exponential factor and R = gas constant. The initial rates of decomposition of formic acid at different temperatures varied from 298 K to 343 K and by plotting the log of initial rate vs. 1/T in the presence of 1.0 mM **[Ru-hdm]**, 10 mmol of formic acid, and 15 mmol of the base, the activation energy was estimated from the slope of the Arrhenius plot, i.e., E_a / R and measured to be 11.6 kJ/mol by taking R = 8.3145 J K^{-1} mol^{-1} and slope = -1395 (Figure 4.4(a)). Thermodynamical parameters like $\Delta H^{\ddagger}$ enthalpy, $\Delta S^{\ddagger}$ entropy, and $\Delta G^{\ddagger}$ free energy were calculated from the Eyring plot. The Eyring plot is the plot of the logarithm of *k*/T plotted against reciprocal absolute temperature 1/T, which is based on the Eyring – Polanyi equation (4.2).[14-15] Where, *k* = reaction rate constant, T = absolute temperature in K, R = gas constant, k_B = Boltzmann's constant, $\Delta H^{\ddagger}$ = enthalpy of activation and $\Delta S^{\ddagger}$ = entropy of activation. In the Eyring plot, slope = $\frac{-\Delta H^{\ddagger}}{R}$ and intercept = $\boldsymbol{ln\frac{k_B}{h} + \frac{\Delta S^{\ddagger}}{R}}$.

$$\boldsymbol{ln\frac{k}{T} = \frac{-\Delta H^{\ddagger}}{R} \cdot \frac{1}{T} + ln\frac{k_B}{h} + \frac{\Delta S^{\ddagger}}{R}} \qquad \textbf{(4.2)}$$

From the plot, the slope is found to be -1085, and the enthalpy $\Delta H^{\ddagger}$ is calculated to be 9024 J K^{-1} mol^{-1}. The intercept of the plot is -5.55, and the entropy of activation $\Delta S^{\ddagger}$ is estimated to be -243.7 J K^{-1} mol^{-1} (Figure 4.4(b)). As the value of $\Delta H^{\ddagger}$ and $\Delta S^{\ddagger}$ are known, Gibbs free energy can be calculated from the equation (4.3).

$$\Delta G^{\ddagger} = \Delta H^{\ddagger} - \boldsymbol{T}\Delta S^{\ddagger} \qquad \textbf{(4.3)}$$

By putting the value of $\Delta H^{\ddagger}$ and $\Delta S^{\ddagger}$ in the above equation, the $\Delta G^{\ddagger}$ is calculated to be 81.6 kJ at 298 K. The parameters are tabulated in Table 4.3.

Table 4.3. Calculations for Arrhenius plot and Eyring plot.

Temperature / °C	Temperature /K	$\frac{1}{T}$	$ln\ k$	$ln\frac{k}{T}$
25	298	0.00336	-3.5408	-9.2379
40	313	0.00319	-3.1912	-8.9380
55	328	0.00305	-3.0791	-8.8724
70	343	0.00292	-2.9004	-8.7384

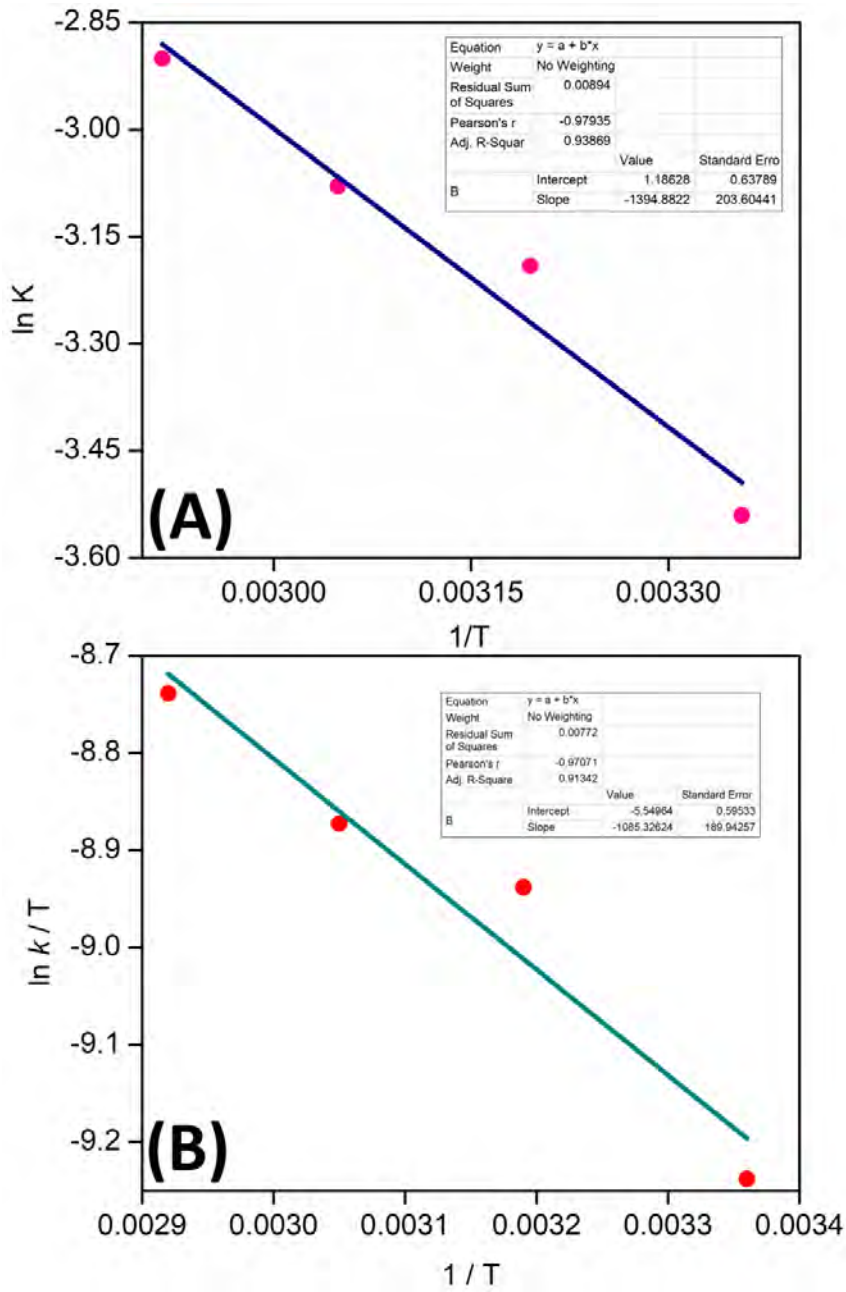

Figure 4.4 (A) Arrhenius plot for the complex [Ru-hdm] to estimate the activation energy. **(B)** Eyring plot for the complex [Ru-hdm] to estimate the $\Delta H^{\ddagger}$, $\Delta S^{\ddagger}$, and $\Delta G^{\ddagger}$.

4.2.5. pH variation for the decomposition of formic acid

The dehydrogenation reactions are pH-dependent and more favorable in water as solvent as water facilitates hydronium ions (H_3O^+) and metal hydride. The dehydrogenation reaction in the case of the **[Ru-hdm]** complex is efficient in deionized water as well as in a neutral pH. The dehydrogenation reactions were studied at different acidic, basic and neutral pH using phosphate buffer to confirm this. The decomposition of formic acid was performed in the presence of 1.0 mM **[Ru-hdm]**, 10 mmol of acid, and 15 mmol of the base at pH 2.0 to 11.0 (Figure C14, Table 4.4). The reaction rate is slow in highly acidic pH 2.0 but shows a slight increase in TOF at 4.0 pH. When the pH reaches pH 6.0, there is a remarkable rise in initial TOF of 0.08 s^{-1} and shows the highest initial TOF of 0.094 s^{-1} at neutral pH 7.0. After pH 7.0, in the basic medium initial TOF values start decreasing from 0.083 s^{-1} at pH 8.0 to 0.063 s^{-1} at pH 11.0. But the initial TOF values within pH 8.0 to 11.0 were higher than the initial TOF values at a highly acidic pH range within 2.0 to 6.0 (Figure 4.5). The reaction rate becomes slow in a highly acidic and highly basic medium than the neutral pH. This may be due to a lower rate of formation of H_3O^+ ions and metal hydride, which lowers the reaction rate and evolution of H_2 gas or maybe catalyst disintegrate at highly acidic or basic pH, and stable at slightly acidic, neutral, and slightly basic conditions. The plot of pH vs. initial TOF shows that the **[Ru-hdm]** achieved the highest TOF at pH 7.0.

Table 4.4. Decomposition of formic acid at different pH with 1.0 mM **[Ru-hdm]** in the presence of 10 mmol acid and 15 mmol bases.

pH	Initial TOF / s^{-1}	The volume of gas evolved / µmol
2.0	0.0402	7.92
4.0	0.0596	12.67
6.0	0.0803	20.98
7.0	0.0935	26.24
8.0	0.083	26.17
9.0	0.0792	23.79
11.0	0.0633	19.12

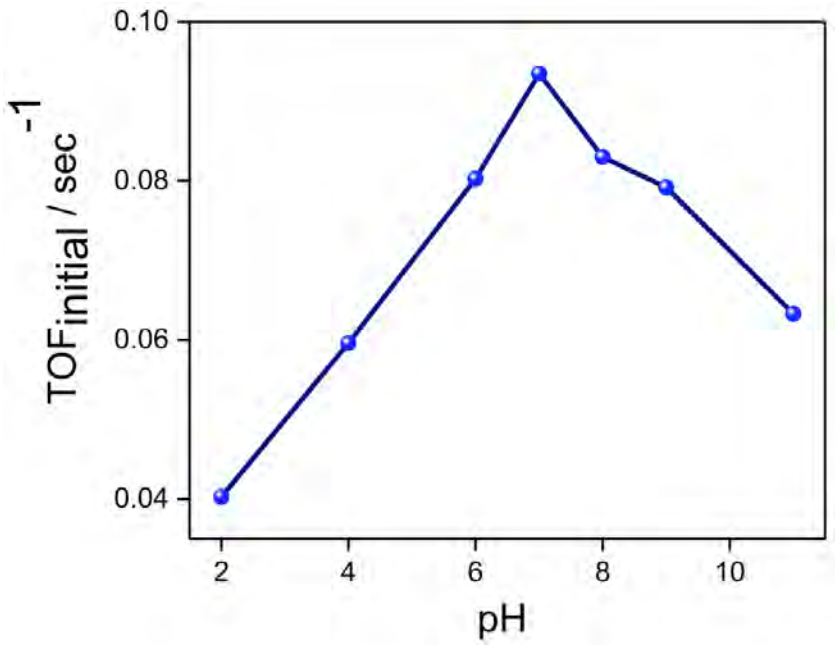

Figure 4.5. pH dependence of the initial TOF for the decomposition of formic acid with 1.0 mM complex, 10 mmol formic acid, and 15 mmol sodium formate in phosphate buffer.

4.2.6. Stability of the catalyst

The stability of the catalyst towards dehydrogenation was examined by the iterative addition of formic acid and sodium formate in a different set of reactions. Firstly, in the presence of 1.0 mM of complex and 25 mmol of sodium formate, 20 mmol of formic acid was added to the reaction vessel. to decompose the formic acid repetitively after completion of each cycle until the gas evolution stops monitored through differential pressure manometer. The catalyst shows its reproducibility up to seven cycles with a TON of 140 (Figure 4.6). Similarly, 25 mmol of sodium formate was added iteratively in the presence of 20 mmol of acid and 1.0 mM of catalyst. In this case, the catalyst is stable for up to six cycles with a TON of 130 (Figure C15). This suggests that catalyst is highly durable towards the dehydrogenation of formic acid. It remains stable during the reaction and shows the rise in gas evolution after every fresh injection of acid or base. The catalyst shows high stability and activity towards dehydrogenation. For evaluating the stability of the complex, UV-Visible studies have also been performed before and after the completion of dehydrogenation (Figure C16). No significant spectral changes were observed after the completion of the decomposition of formic acid. The absorbance at 365 nm is nearly the same as before the reaction that confirms the stability of the catalyst throughout the reaction.

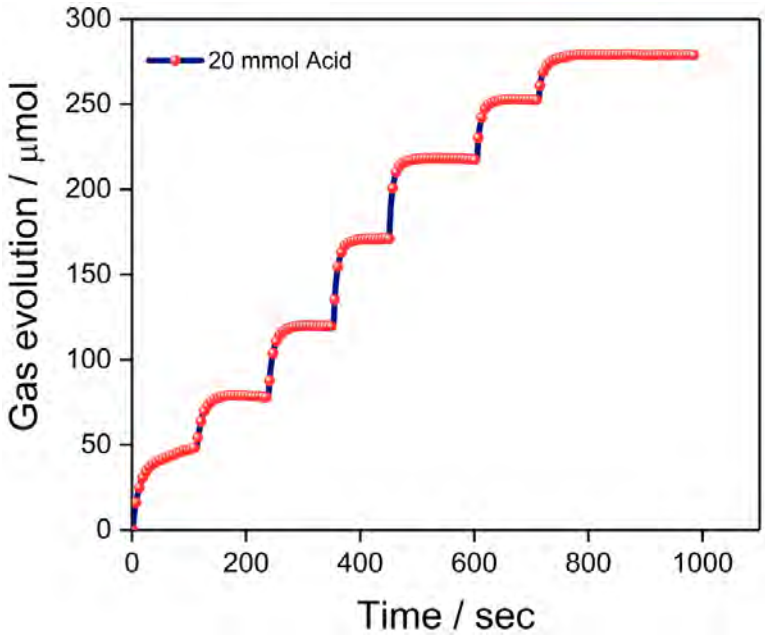

Figure 4.6. Catalytic cycles for the complex **[Ru-hdm]** with the iteration of 20 mmol of acid in the presence of 1.0 mM complex and 25 mmol bases in water.

4.2.7. Plausible Mechanism

A plausible mechanism for the catalytic cycle involved in the dehydrogenation of formic acid is presented in Scheme 4.1. Herein under the aqueous acidic conditions below pH 3.5, the dechelated pyridine ring and the alcoholate O^- gets protonated with the formation of $[Ru^{II}(hdmH_2)(OH_2)]^{3+}$ **[A]**.[16] In the presence of formate, $[Ru^{II}(hdmH_2)(OH_2)]^{3+}$ **[A]** loses the aqua coordination and forms a dative bond with formate ligand to generate $[Ru^{II}(hdmH_2)(OC(O)H)]^{2+}$ **[B]**. The ESI-mass of the complex $[Ru^{II}(hdmH_2)(OC(O)H)]^{2+}$ **[B]** was observed at 215.05 m/z and calculated for 215.02 m/z (Figure 4.7). The complex **[B]** undergoes decarboxylation with the formation of the transient [Ru-H] species $[Ru^{II}(hdmH_2)(H)]^{2+}$ **[C]**. The $[Ru^{II}(hdmH_2)(H)]^{2+}$ **[C]**, generates the transition state $[Ru^{II}(hdmH_2)(HH)]^{2+}$ **[D]**, might undergoes proton relay mechanism by the pyridnium moiety with the formation H⋯H bond. The transition state $[Ru^{II}(hdmH_2)(HH)]^{2+}$ **[D]** in the presence of H_3O^+, evolves H_2 and returns to $[Ru^{II}(hdmH_2)(OH_2)]^{3+}$ **[A]**.

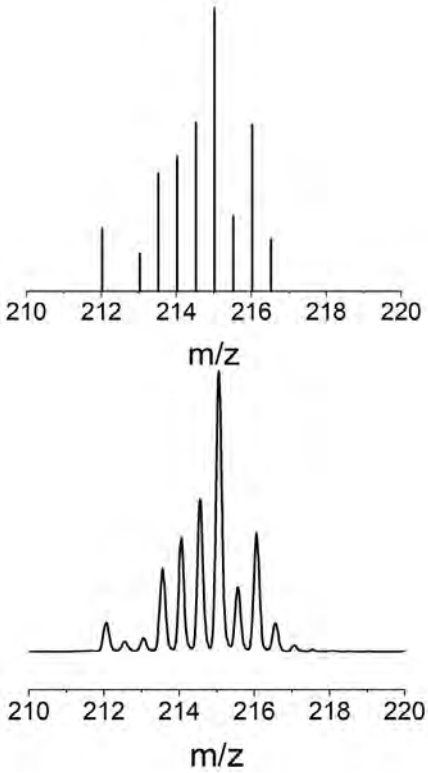

Figure 4.7. Mass spectrum of the complex in the presence of formic acid and formate [(Simulated; Top) and (Experimental; bottom)].

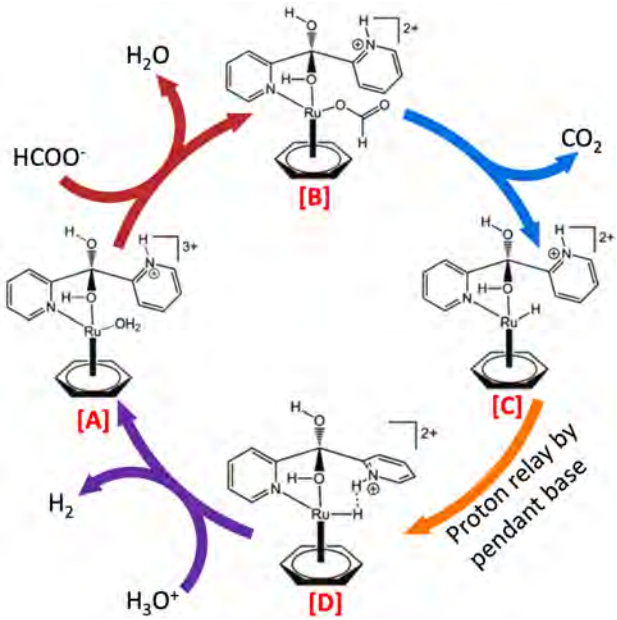

Scheme 4.1. Plausible catalytic cycle involved in the dehydrogenation of formic acid.

4.4. Summary

The complex **[Ru(η^6-benzene)(hdm)]BF$_4$ ([Ru-hdm])** has been employed for the dehydrogenation of formic acid using sodium formate as a base from low to high temperature,

with varying acid, base, and complex concentration. The increasing gas evolution was observed with increasing temperature, acid, and base amount as well. The activation energy was calculated from the Arrhenius plot, and enthalpy, entropy, and Gibbs free energy have been calculated from the Eyring plot for the dehydrogenation phenomenon. In this case, the activation energy required for dehydrogenation of formic acid was 11.6 kJ/mol, whereas the reaction is endergonic with the ΔG = 81.642 kJ at 298 K. The pH dependant dehydrogenation of formic acid reveals the efficient gas evolution at pH 7.0. The composition of gas was detected with FID and TCD detectors using Gas Chromatograph, wherein CO_2 and H_2 are present in 1:1 ratio.

4.5. References

1. Felderhoff, M., Weidenthaler, C., von Helmolt, R., Eberle, U. Hydrogen storage: the remaining scientific and technological challenges. *Phys. Chem. Chem. Phys.* **2007**, *9* (21), 2643 – 2653.
2. Suh, M. P., Park, H. J., Prasad, T. K., Lim, D.-W. Hydrogen Storage in Metal-Organic Frameworks. *Chem. Rev.*, **2012**, *112* (2), 782–835.
3. Mellmann, D., Sponholz, P., Junge, H., Beller, M. Formic acid as a hydrogen storage material – development of homogeneous catalysts for selective hydrogen release. *Chem. Soc. Rev*. **2016**, *45* (14), 3954-3988.
4. Singh, A. K., Singh, S., Kumar, A. Hydrogen Energy Future with Formic Acid: A Renewable Chemical Hydrogen Storage System', *Catal. Sci. Technol.***2016**, *6* (1), 12 - 40.
5. Celaje, J. J. A., Lu, Z., Kedzie, E. A., Terrile, N. J., Lo, J. N., Williams, T. J. A prolific catalyst for dehydrogenation of neat formic acid. *Nat. Commun.* **2016**, *7*, 1-6.
6. Coffey, R. S. The Decomposition of Formic Acid catalysed by Soluble Metal Complexes', *Chem. Commun*., **1967**, (18) , 923b-924.
7. Boddien, A., Loges, B., Junge, H., Beller, M. Hydrogen Generation at Ambient Conditions: Application in Fuel Cells. *ChemSusChem.* **2008**, *1* (8-9), 751 - 758.
8. Fukuzumi, S., Kobayashi, T., Suenobu, T. Unusually Large Tunneling Effect on Highly Efficient Generation of Hydrogen and Hydrogen Isotopes in pH-Selective Decomposition of Formic Acid Catalyzed by a Heterodinuclear Iridium-Ruthenium Complex in Water. *J. Am. Chem. Soc.* **2010**, *132* (5), 1496 – 1497.
9. Wang, W.-H., Xu, S., Manaka, Y., Suna, Y., Kambayashi, H., Muckerman, J. T., Fujita, E., Himeda, Y. Formic Acid Dehydrogenation with Bioinspired Iridium Complexes: A Kinetic

Isotope Effect Study and Mechanistic Insight. *ChemSusChem.* **2014**, *7* (7), 1976–1983.

10. Wang, W.-H., Ertem, M. Z., Xu, S., Onishi, N., Manaka, Y., Suna, Y., Kambayashi, H., Muckerman, J. T., Fujita, E., Himeda, Y. Highly Robust Hydrogen Generation by Bio-Inspired Ir Complexes for Dehydrogenation of Formic Acid in Water: Experimental and Theoretical Mechanistic Investigations at Different pH. *ACS Catal.* **2015**, *5* (9), 5496–5504.
11. Fukuzumi, S., Kobayashi, T., Suenobu T. Efficient Catalytic Decomposition of Formic Acid for the Selective Generation of H_2 and H/D Exchange with a Water-Soluble Rhodium Complex in Aqueous Solution. *ChemSusChem.* **2008**, *1* (10), 827 – 834.
12. Wang, W.-H., Hull, J. F., Muckerman, J. T., Fujita, E., Hirose, T., Himeda, Y. Highly Efficient D_2 Generation by Dehydrogenation of Formic Acid in D_2O through H^+/D^+ Exchange on Iridium Catalyst: Application to the Synthesis of Deuterated Compounds by Transfer Deuterogenation', *Chem. Eur. J.* **2012**, *18* (30), 9397–9404.
13. Boddien, A., Mellmann, D., Gartner, F., Jackstell, R., Junge, H., Dyson, P. J., Laurenczy, G., Ludwig, R., Beller, M. Efficient Dehydrogenation of Formic Acid Using an Iron Catalyst, *Science.* **2011**, *333* (6050), 1733−1736.
14. Eyring, H., Polanyi, M. On Simple Gas Reactions. *Z. Phys. Chem. B.* **1931**, *12* (11), 279.
15. Espenson, James, H. Chemical Kinetics and Reaction Mechanisms. *McGraw-Hill.* **1981** p. 117.
16. Vatsa, A., Padhi, S. K. Catalytic Water Oxidation by a Ru^{II} Half Sandwich Complex. *Eur. J. Inorg. Chem*. **2021,** *2021* (34), 3499-3505.

Appendix C

Figure C1. The presentation of the setup used for the dehydrogenation of formic acid.

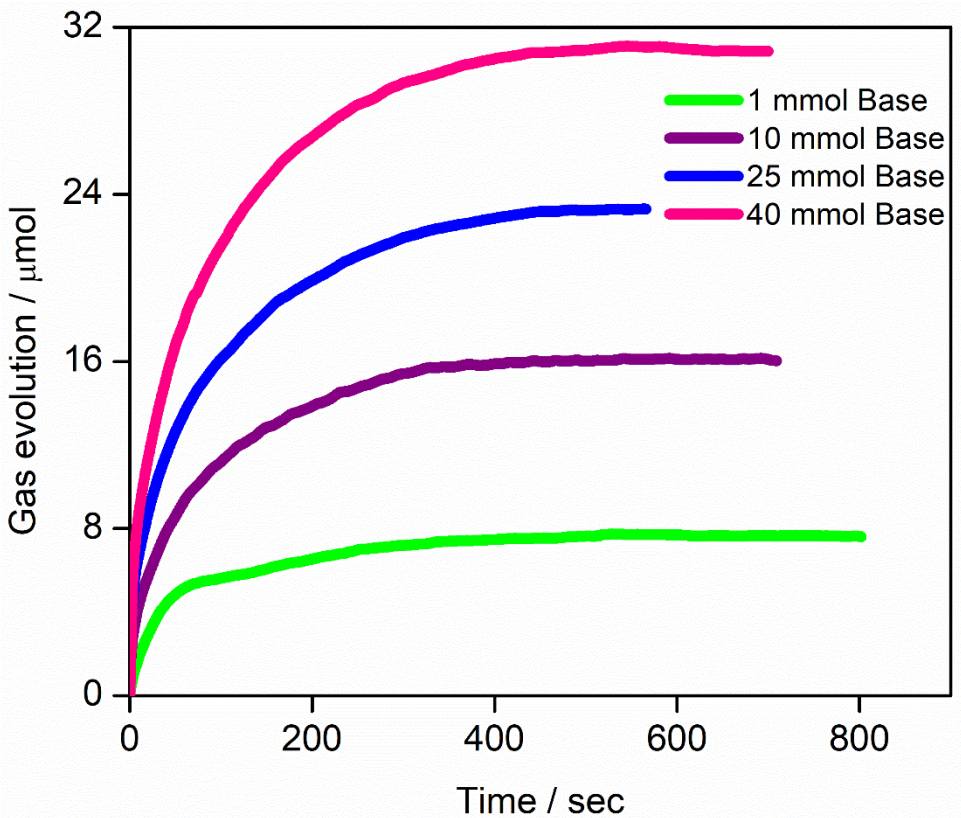

Figure C2. Gas evolution by **[Ru-hdm]** with a variation of base concentration in presence of 1.0 mM of complex and 10 mmol of acid at 55 °C in water.

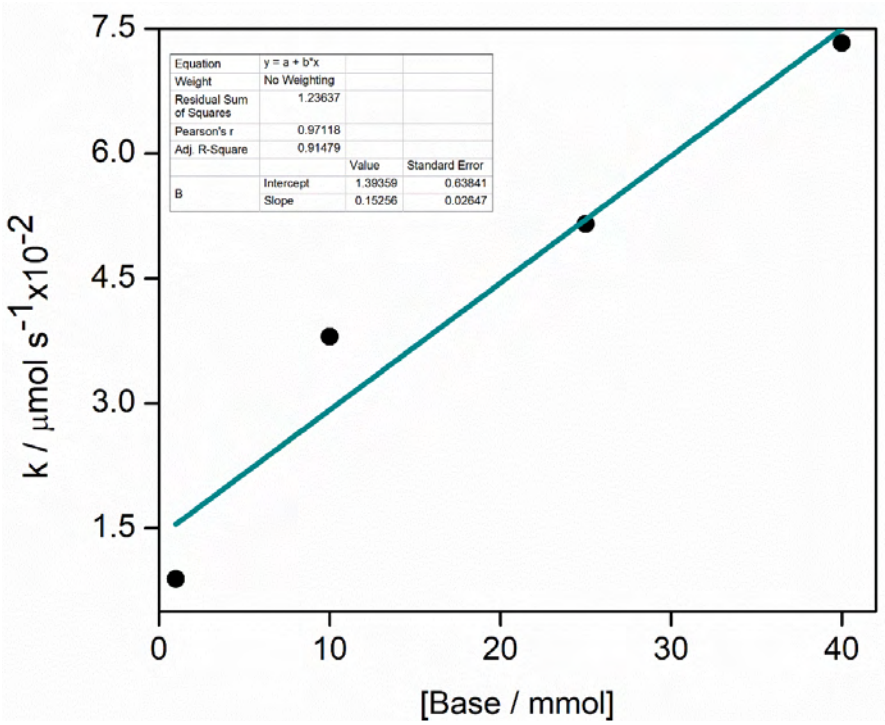

Figure C3. Rate of gas evolution *vs.* base in water.

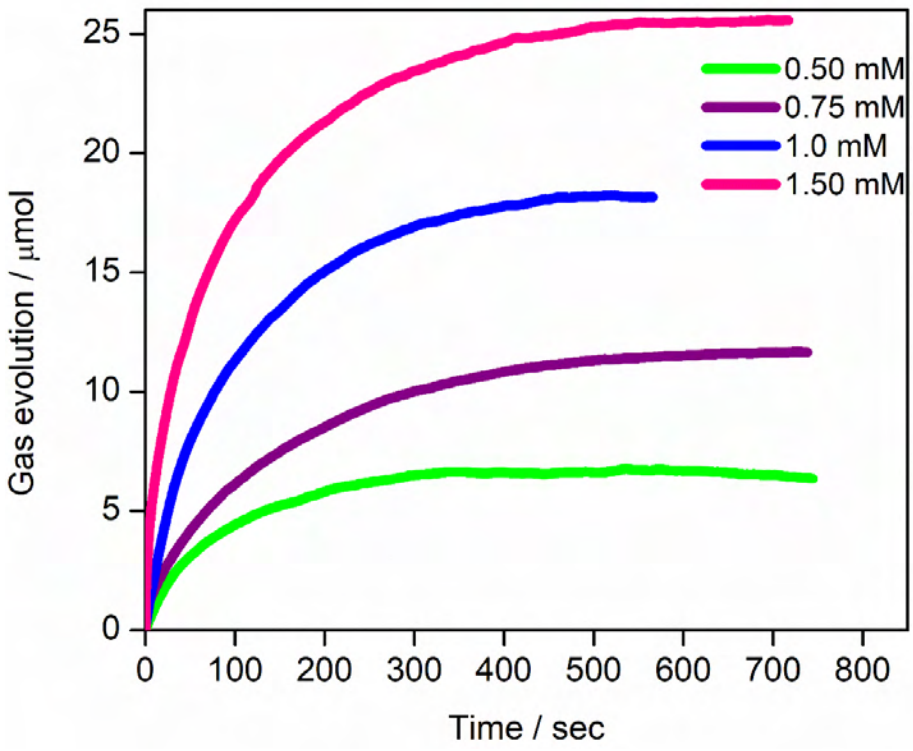

Figure C4. Gas evolution by **[Ru-hdm]** with a variation of complex concentration in presence of 10 mmol of acid and 15 mmol of the base at 55 °C in water.

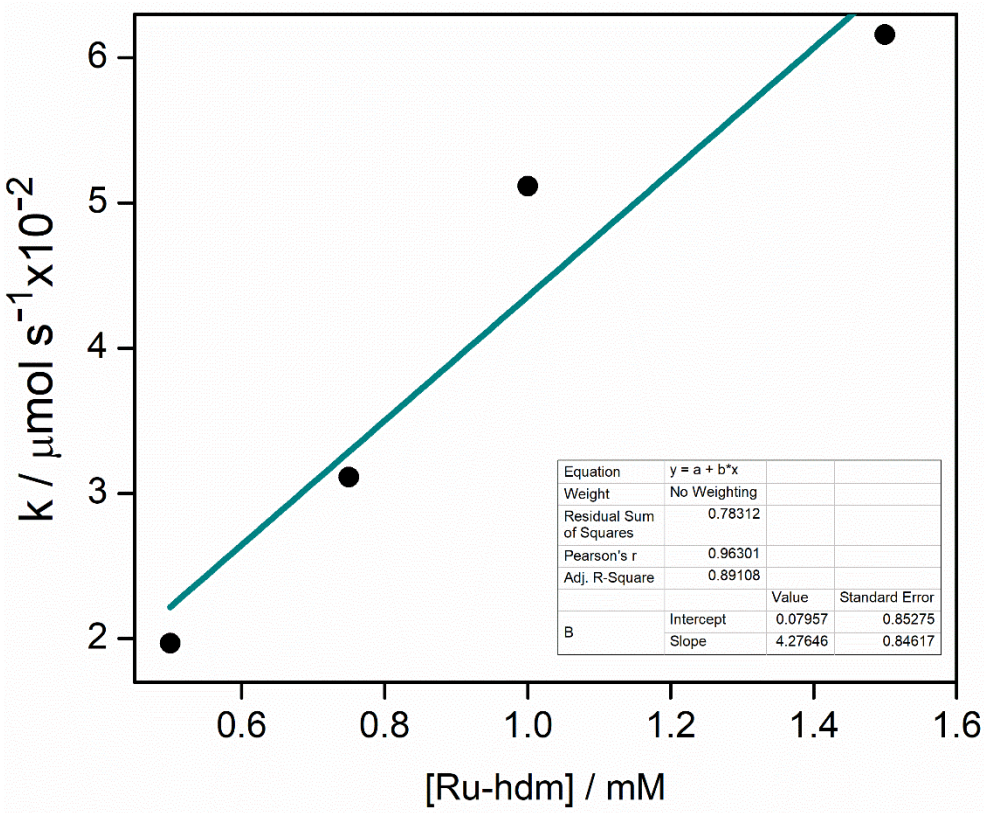

Figure C5. Rate of gas evolution *vs.* complex in water.

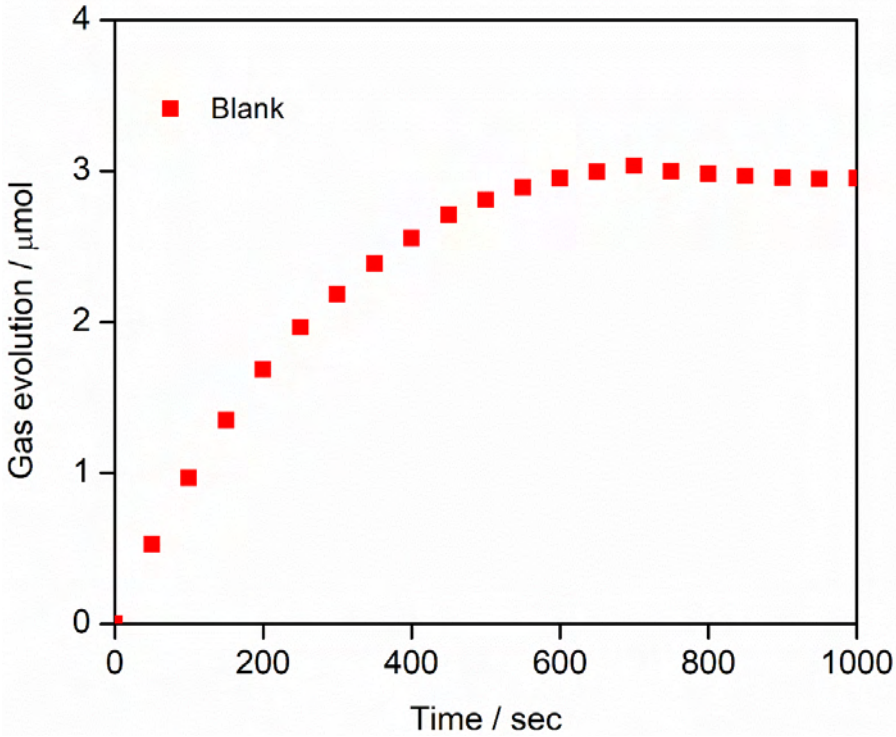

Figure C6. Blank experiment for dehydrogenation at 55 °C without catalyst using 10 mmol of formic acid and 15 mmol of sodium formate.

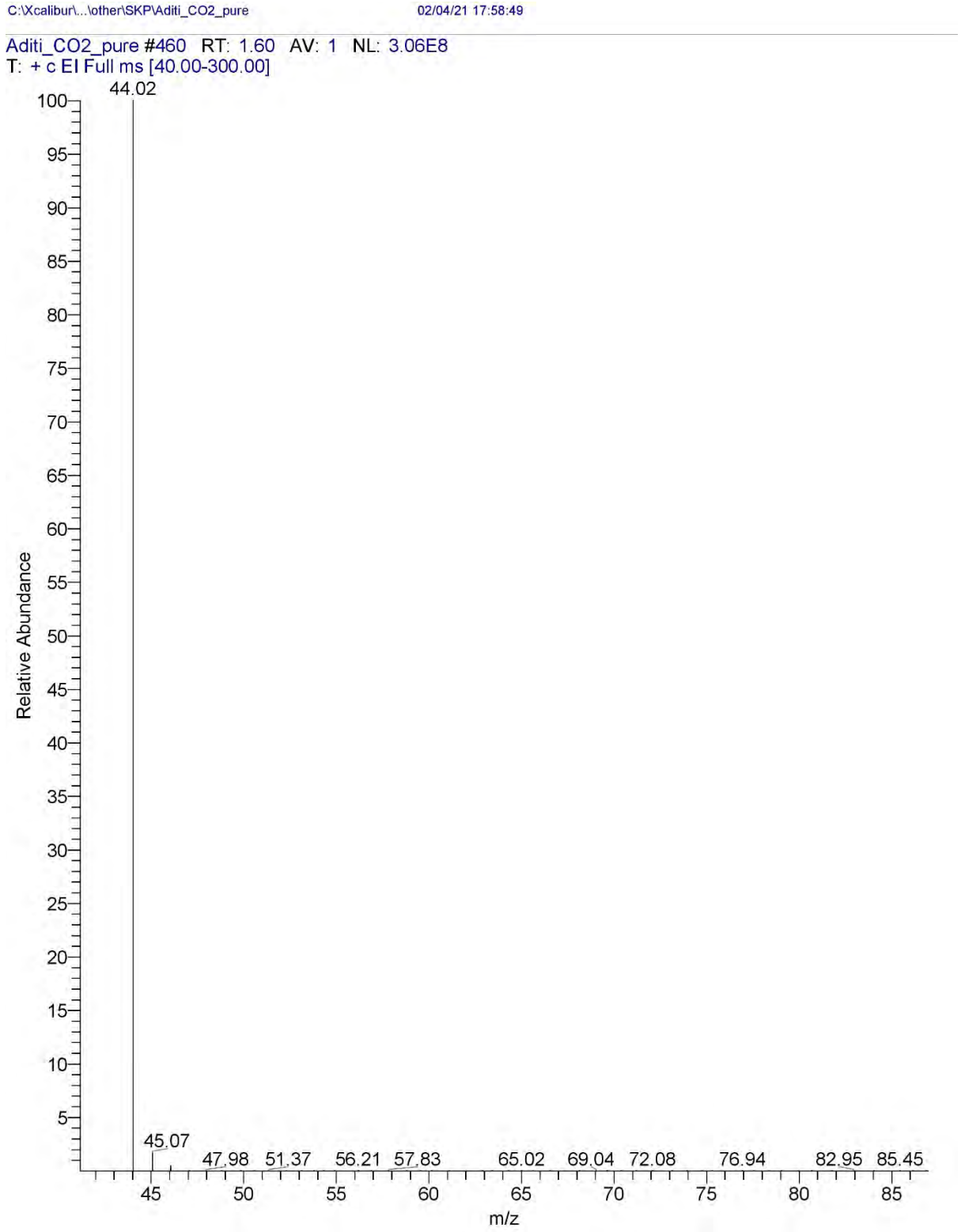

Figure C7. GC-MS of pure CO_2.

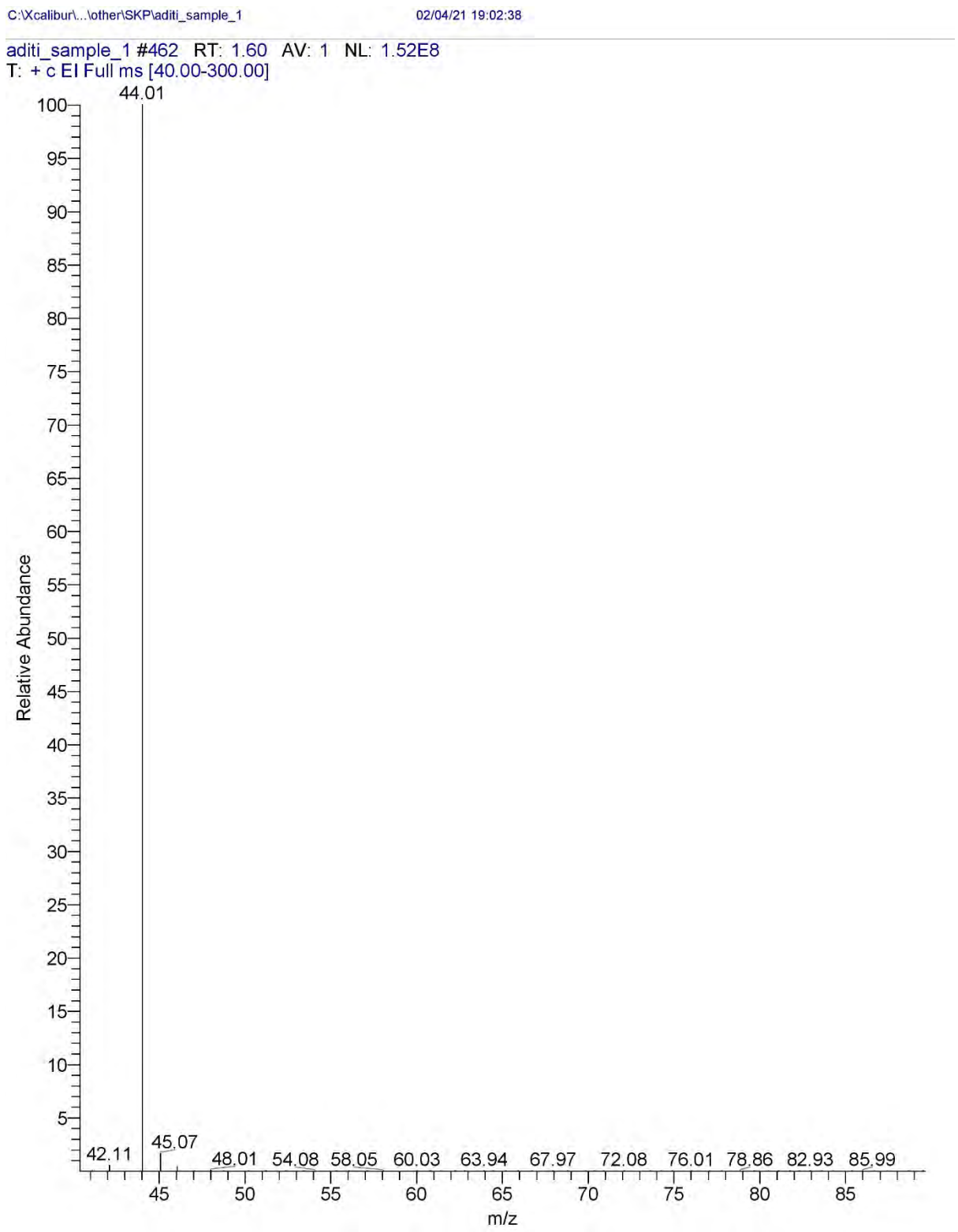

Figure C8. GC-MS of CO_2 from the dehydrogenation reaction.

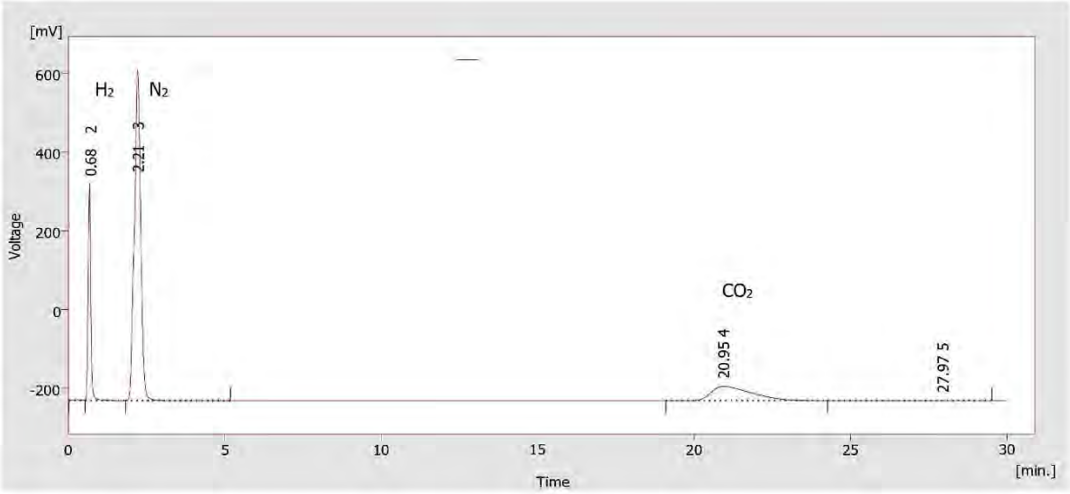

Chromatogram Info:

File Name	: D:\Manohar\2021\Aditi CHEM\TCD RDPK4 240221.PRM	File Created	: 2/24/2021 11:41:57 AM
Origin	: Acquired, Acquisition started 2/24/2021 11:11:57 AM	Acquired Date	: 2/24/2021 11:41:57 AM
Project	: C:\Clarity\Projects\Work 1.PRJ	By	: None

Result Table

	Reten. Time [min]	Area [mV.s]	Height [mV]	Area [%]	Height [%]
1	0.204	52.026	2.276	0.3	0.2
2	0.680	3234.444	550.027	17.5	38.5
3	2.215	11792.720	839.662	63.9	58.8
4	20.947	3290.682	36.342	17.8	2.5
5	27.975	94.527	0.491	0.5	0.0
	Total	18464.399	1428.798	100.0	100.0

Figure C9. Gas chromatography TCD file for the dehydrogenation using 1.0 mM **[Ru-hdm]** in presence of 10 mmol of formic acid and 15 mmol of sodium formate.

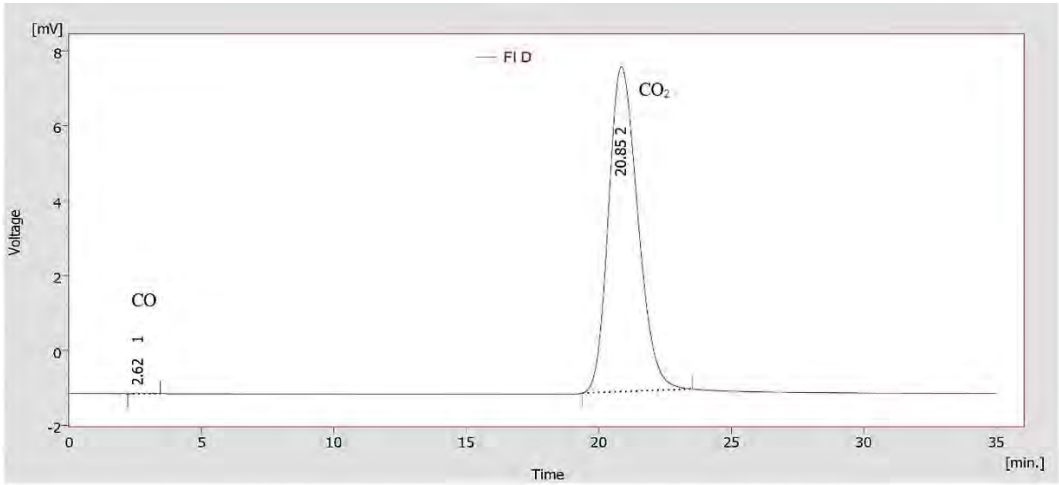

Result table

	Start Time [min]	End Time [min]	Start Value [mV]	End Value [mV]	Reten. Time [min]	Area [mV.s]	Height [mV]	Area [%]	Height [%]
1	2.219	3.452	-1.157	-1.149	2.620	0.761	0.022	0.1	0.3
2	19.376	23.524	-1.135	-1.027	20.845	667.937	8.681	99.9	99.7
					Total	668.698	8.703	100.0	100.0

Figure C10. Gas chromatography FID file for the dehydrogenation using 1.0 mM **[Ru-hdm]** complex in presence of 10 mmol of formic acid and 15 mmol of sodium formate.

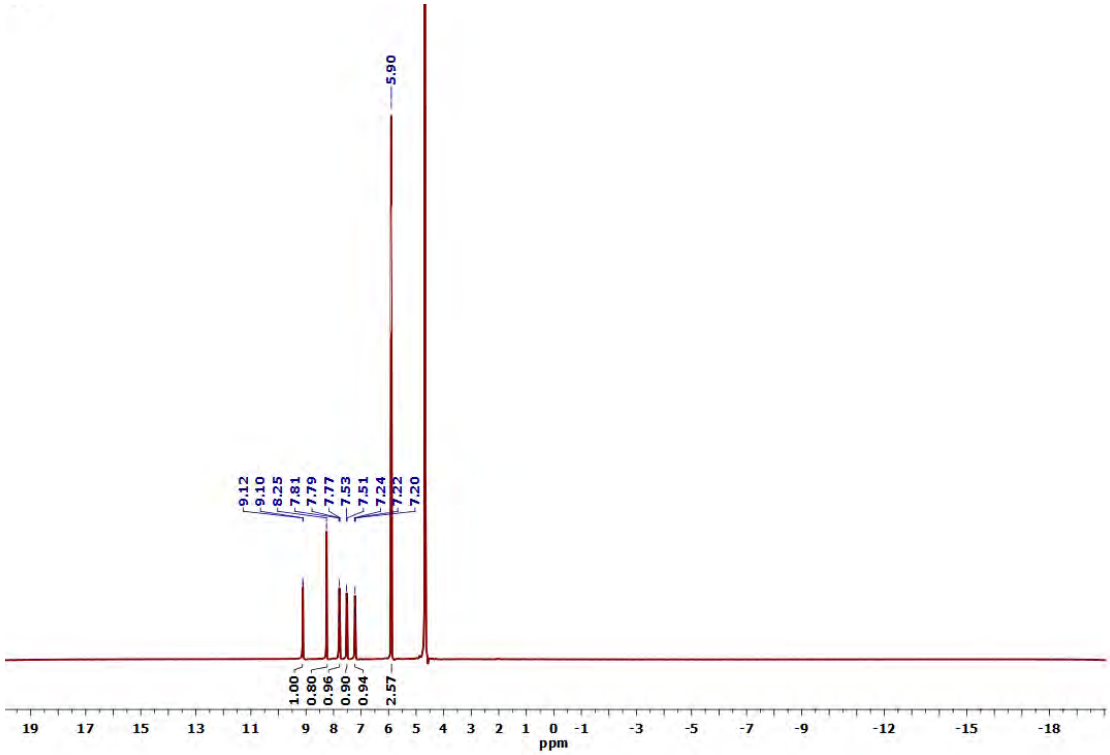

Figure C11. ^{1}H NMR of the [Ru-hdm] complex in D_2O in the presence of sodium formate.

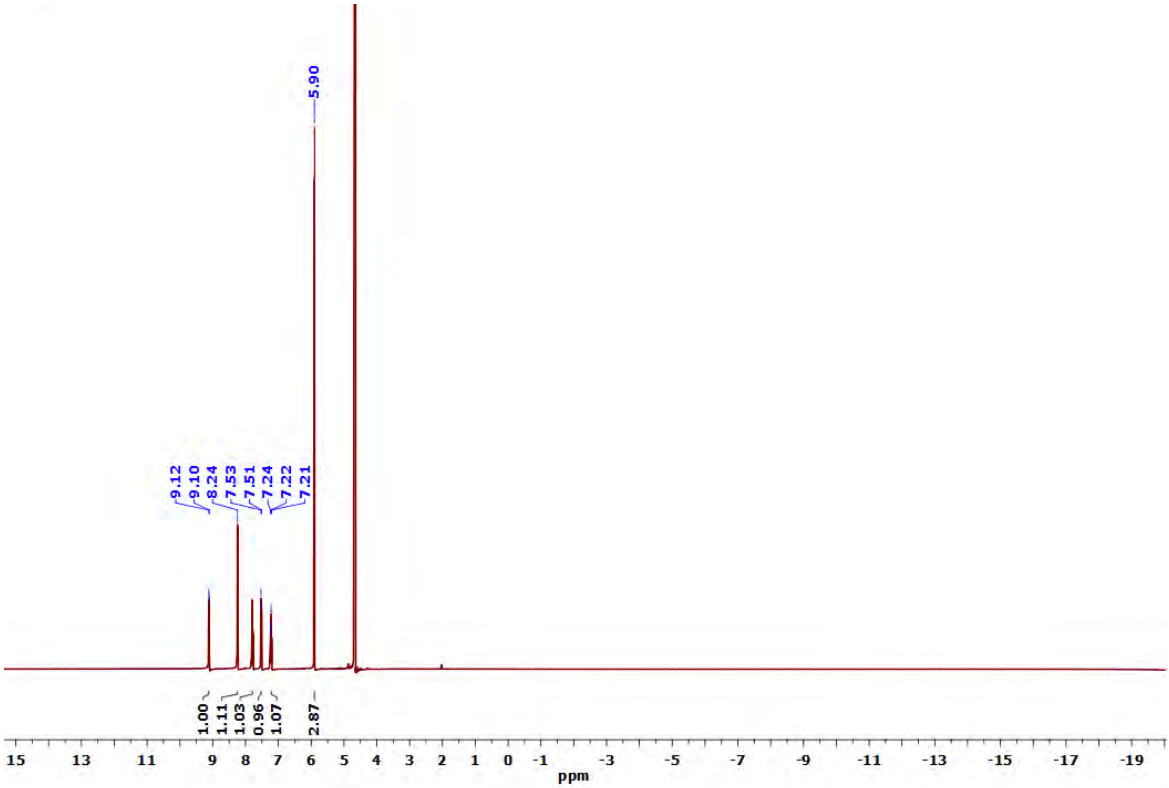

Figure C12. ^{1}H NMR of the **[Ru-hdm]** complex in D_2O in the presence of 50 mmol sodium formate and 50 mmol formic acid.

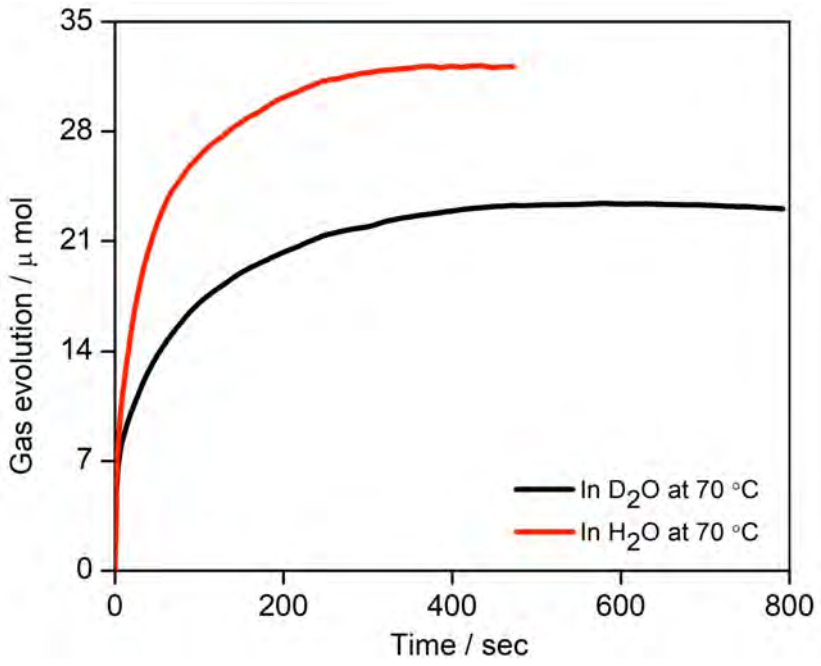

Figure C13. Gas evolution by **[Ru-hdm]** in H_2O and D_2O in presence of 20 mmol of acid and 40 mmol of the base at 70 °C in water.

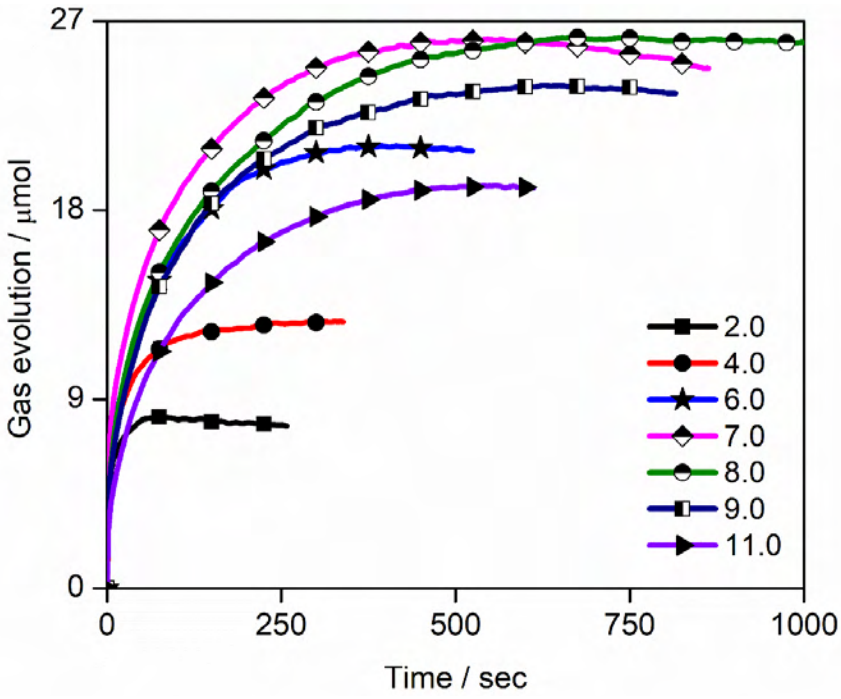

Figure C14. Gas evolution by **[Ru-hdm]** with the variation of pH in presence of 10 mmol of acid and 15 mmol of the base at 55 °C in water.

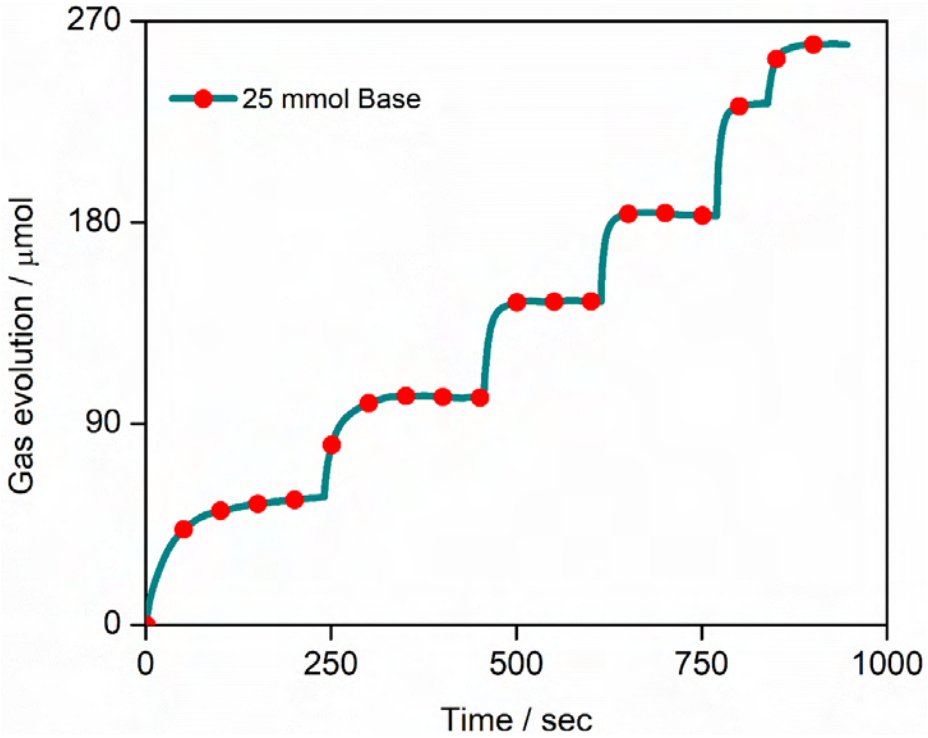

Figure C15. Catalytic cycles for the complex **[Ru-hdm]** with the iteration of 25 mmol of the base in the presence of 1.0 mM complex and 20 mmol acid in water.

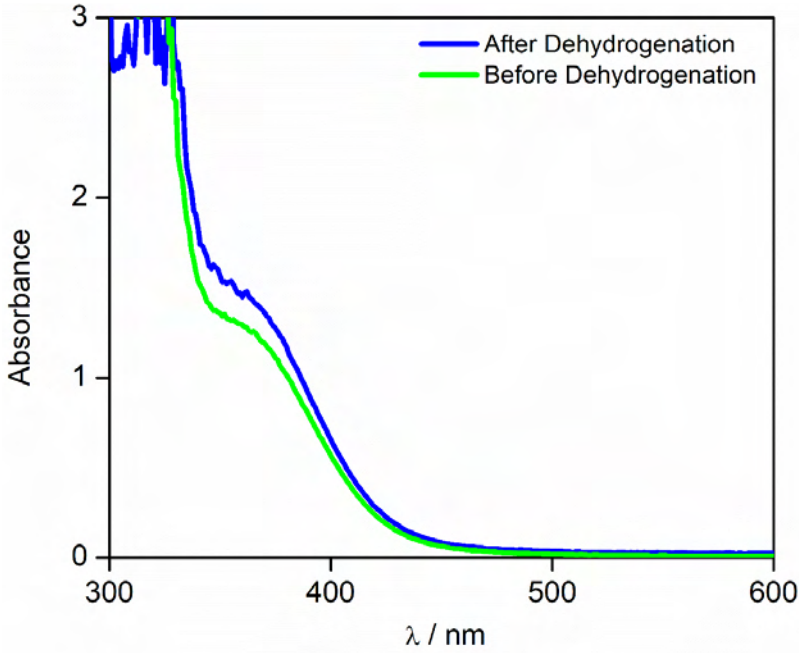

Figure C16. UV-Visible spectroscopy before and after dehydrogenation of formic acid using 10 mmol formic acid and 15 mmol sodium formate.

CHAPTER 5

This chapter is unpublished work

Vatsa, A. and Padhi, S. K.*, Manuscript under Preparation.

Chapter 5

Dehydrogenation of formic acid using mononuclear Ruthenium (II) $[Ru(2py\text{-}tpy)(dqn)Cl]^+$ complex

5.1 Introduction

Hydrogen as a fuel is one of the cleanest sources of storable energy carrier which produces water on its combustion. Due to the explosive nature of hydrogen, it becomes difficult to store or transport hydrogen as fuel.[1-2] The dehydrogenation of formic acid is one of the most sustainable processes for producing H_2 gas.[3]. Hence the Formic acid is the simplest form of a carboxylic acid having 53 g/L or 4.4 % w/w of hydrogen content, and it is liquid at ambient temperature. [4]

After developing the first homogenous catalyst for dehydrogenation reaction by Coffey[30], dehydrogenation reactions have been studied extensively by various groups.[5] Beller and groups have been employed the Ru metal salts like $RuCl_3.xH_2O$ and catalyst precursor-like $[\{RuCl_2(p\text{-cymene})\}_2]$, $[\{RuCl_2(benzene)\}_2]$, etc. for the decomposition of formic acid using different types of amine adducts and with different phosphine ligands. The complex $[\{RuCl_2(benzene)\}_2]$ complex with dppe ligand (dppe = 1,2-bis(diphenylphosphino)ethane) has shown the highest activity towards the decomposition of formic acid with a TON of 1376 in comparison with other phosphine ligands used.[6] Huang and coworkers have reported the decomposition of formic acid by utilizing Ru *p*-cymene complex coordinated with 2,2′-biimidazoline ligand. The complex shows a TOF of 12000 h^{-1} and TON of 350000 using HCOOH/HCOONa in a 1:2 ratio at 90 °C in an aqueous solution.[7] Sasson *et al.* have been studied the dehydrogenation of formic acid using $[\{RuCl_2(p\text{-cymene})\}_2]$/DPPM (DPPM = Bis(diphenylphosphino)methane) catalyst at 40 °C having TON >530 and TOF >600 h^{-1} [22]. Lei and group have synthesized the $[(\eta^6\text{-arene})RuCl(k^2\text{-N,N-dmobpy})]^+$ complex to study the dehydrogenation of formic acid in aqueous media and demonstrates the dependence of pH on dehydrogenation reaction.[8]

Herein the synthesis and characterization of $[Ru(2py\text{-}tpy)(dqn)Cl]^{2+}$ (where dqn = 2,3-di(pyridine-2-yl)quinoxaline) and its activity dehydrogenation of formic acid using sodium formate as base in different acid, base, and complex concentration as well as its activity from low to high temperature have also been studied.

5.2. Experimental

5.2.1. Materials and methods

5.2.1.1. Materials

All the chemicals used in this work were of reagent grade. $RuCl_3.xH_2O$, $AgPF_6$ and pyridil were purchased from Sigma Aldrich. O-phenylene diamine from Loba chemicals and used without further purifications. NaOH was purchased from Merck. The solvents like acetone, diethyl, petroleum, dichloromethane, methanol, and ethanol were purchased from Merck and dried before use. In all the experiments, Milli-Q- purified distilled water was used.

5.2.1.2. Optical Spectra

All the UV-Visible spectroscopic experiments and analysis were performed with an Agilent Cary 8454 photodiode array UV-Visible spectrophotometer.

5.2.1.3. NMR Spectroscopy and Mass Spectrometry

Proton and ^{13}C NMR spectra were recorded on Bruker Ultrashield spectrometer at room temperature. High-resolution ESI mass spectrometry was recorded with Waters UPLC TQD and Bruker micrOTOF-Q II instruments.

5.2.1.4. Cyclic Voltammetry

Electrochemical measurements were conducted using the CH instrument ALS/CHI model 1140C and 660D electrochemical analyzer. All the electrochemical experiments were carried out under an inert gas atmosphere at the scan rate of 100 mV/s at room temperature. Cyclic voltammetry and differential pulse voltammetry were performed with three-electrode cell systems consisting of a glassy carbon electrode as working, a platinum wire as an auxiliary, and a saturated calomel electrode as a reference electrode.

5.2.1.5. Gas Evolution

The evolution of gas was based on manometric results by using 5 mL of double-jacketed reaction vessel containing 2 mL of the reaction mixture and having a headspace volume of 3 mL. The reference cell was filled with 2 mL of water and 3 mL is headspace volume as of the working cell. The gas evolved was converted into micromoles by using the ideal gas equation PV= nRT. The pressure of evolved gas was measured using a differential pressure manometer of TESTO 521 with a range of 0 to 100 hPa, 0.1 hPa accuracy was used.

5.2.1.6. X-ray crystallographic analysis

All the suitable single crystal of [Ru(2py-tpyH)(dqn)Cl]$(PF_6)_2$ were mounted on a Rigaku SuperNova G8910B EosS2 single-crystal X-ray diffractometer using Mo Kα radiation (λ = 0.71073 Å). An EosS2 CCD detector was used for the collection of Frames, and the data collected by the instrument were processed by using CrysAlis^{Pro} software. The data was collected at 293 K and solved through Olex2 software utilizing the Charge Flipping solution program. In this case, one of the phosphorous is situated in a special position.

5.3. Synthesis

5.3.1. Synthesis of 2,3-di(pyridin-2-yl) quinoxaline (dqn) ligand

2,2'-pyridil (1.0g, 4.7 mmol) was dissolved in 60 mL of ethanol followed by the addition of one equivalent of O-phenylenediamine (0.509g, 4.7 mmol). The reaction mixture was refluxed overnight at 80 °C. After the completion of the reaction, the solvent was removed under vacuum, and the solid product obtained was further purified using DCM and hexane. The ligand was further purified by column chromatography in $CHCl_3$ / MeOH (95:5) using neutral alumina. Yield 74 % (1.0 g, 3.5 mmol). 400 MHz ^{1}H NMR (δ, (*J*, Hz), $CDCl_3$): 7.25-7.28 (1H, m), 7.82-7.86 (2H, m), 7.98 (1H, d, 8), 8.24-8.27 (1H, q), 8.40-8.41 (1H, m). 100 MHz ^{13}C NMR (δ, (*J*, Hz), $CDCl_3$): 122.95, 124.24, 130.47, 136.62, 141.11, 148.58, 152.41, and 157.35.

5.3.2. Synthesis of [Ru(2py-tpy)(dqn)Cl](PF_6)

One equivalent of Ru(2py-tpy)Cl_3 (350 mg, 0.68 mmol) and 2.5 equivalents of $AgPF_6$ (452 mg, 1.78 mmol) was dissolved in 30 ml of ethanol, and it was refluxed for one hour at 80°C. After one hour, the AgCl precipitated during the reaction was filtered through celite and complex collected after evaporating the filtrate was dissolved in a minimum amount of ethanol and one equivalent of 2,3-di(pyridin-2-yl) quinoxaline (194 mg, 0.68 mmol) was added and the reaction was refluxed for overnight. The solvent of the reaction mixture obtained was removed under a vacuum. The product isolated was purified by column chromatography using alumina in $CHCl_3$ / MeOH (90:10) mixture. Yield 24 % (165 mg, 0.161 mmol) Calculated mass for $[C_{38}H_{26}N_8RuCl]^+$ m/z = 731.10 obtained mass m/z = 731.06. 400 MHz ^{1}H NMR (δ, (*J*, Hz),DMSO D_6): 6.92 (1H, d, 8), 7.39-7.45 (2H, m), 7.49-7.53 (2H, m), 7.66-7.77 (5H, m), 7.98-8.00 (2H, m), 8.05-8.09 (3H, m), 8.20-8.24 (3H, m), 8.68 (1H, d, 8), 8.775 (1H, d, 4), 8.94 (3H, t, 8), 9.51 (2H, s) and 10.14 (1H, d, 8).

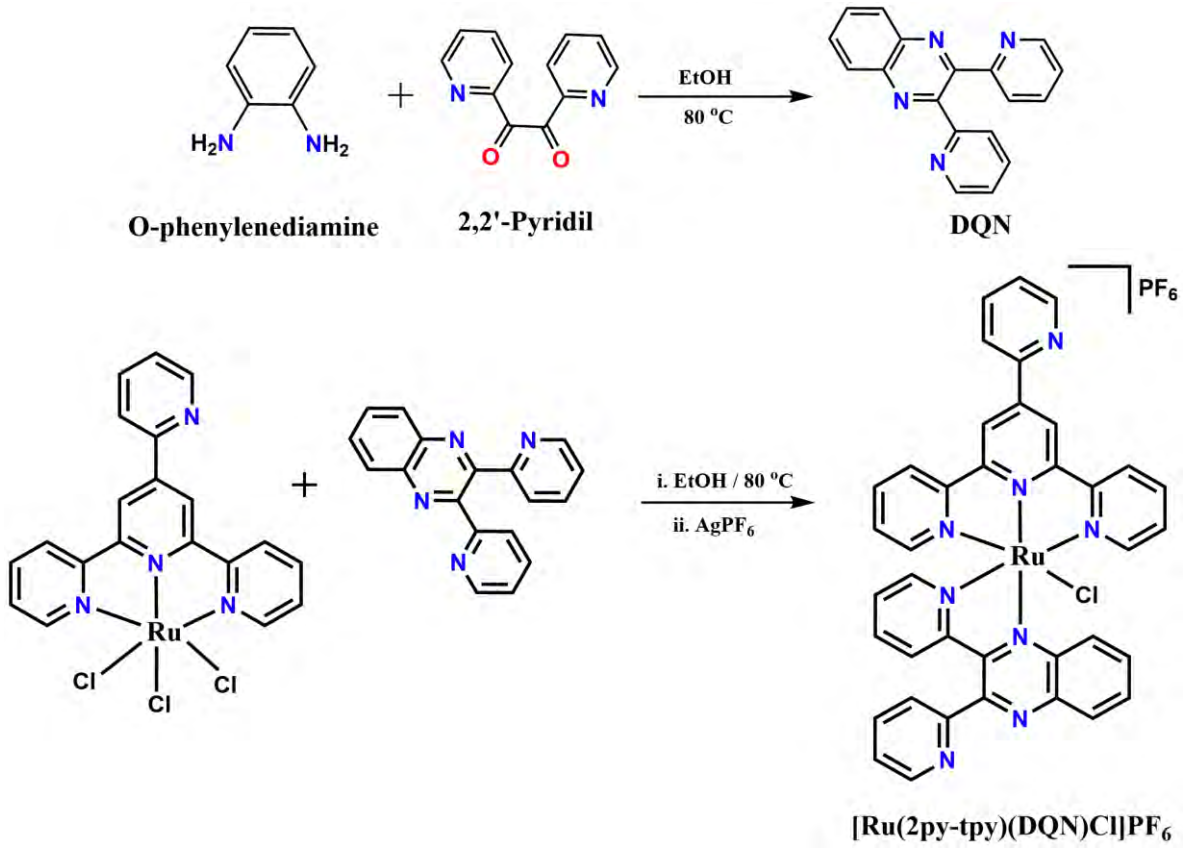

Scheme 5.1. Syntheses of the **dqn** ligand and **[Ru(dqn)]** complex.

5.4 Results and Discussion

5.4.1. Synthesis

The ligand 2,3-di(pyridin-2-yl) quinoxaline was synthesized according to the reported procedure.[9] The reaction scheme of **dqn** ligand and **[Ru(dqn)]** are depicted in Scheme 5.1. The **[Ru(dqn)]** was synthesized by dissolving one equivalent of Ru(2py-tpy)Cl_3 and 2.5 equivalents of $AgPF_6$ in ethanol and refluxed at 80 °C. After forming AgCl precipitate, the reaction mixture was filtered using celite, and the filtrate obtained was evaporated under vacuum. The filtrate and one equivalent of **dqn** ligand were dissolved in the minimum amount of the ethanol and refluxed at 80 °C overnight. The single crystals of [Ru(2py-tpyH)(dqn)Cl] $(PF_6)_2$, suitable for X-ray crystallography, were grown in MeOH and isolated after two days.

5.4.2. Optical and NMR spectra

The optical spectra of the complex **[Ru-dqn]** have been studied in methanol. The complex exhibits two bands in the visible region at 453 nm and 560 nm. The band at 460 nm (22075 cm^{-1}, 4685 M^{-1} cm^{-1}) attributed to MLCT band, and broad shoulder band appeared at 560 nm

(17857 cm^{-1}, 10376 M^{-1} cm^{-1}) for **[Ru-dqn]** complex (Figure D1). The NMR spectra of the **[Ru(dqn)]** were recorded in DMSO-d_6. The ^1H NMR spectra of the **[Ru(dqn)]** complex shows total of 26 hydrogens. The 14 hydrogens correspond to **2py-tpy** moiety, and 12 hydrogens attributed to **dqn** ligand. The mass spectra of the **[Ru(dqn)]** were recorded in MeOH, the calculated mass for the $[C_{38}H_{26}N_8RuCl]^+$ is m/z 731.01, and found mass is m/z 731.06 (Figure D2-Figure D5).

5.4.3. X-ray crystal structure

The single-crystal X-ray structure of the complex **[Ru(dqn)]** was determined through a Rigaku SuperNova G8910B EosS2 single-crystal X-ray diffractometer. The asymmetric unit consists of a di-cationic species $[Ru(2py\text{-}tpyH)(dqn)Cl]^{2+}$, and two anionic $(PF_6)^-$ molecules. In case of $[Ru(2py\text{-}tpyH)(dqn)Cl]^{2+}$, the non-coordinating N-atom of **2py-tpy** ligand is in protonated form. The overall structure at the Ru-center is distorted octahedral, wherein the N3-coordination of 2py-tpy ligand occupies one side of the meridional plane and the other side of the meridional plane is engaged by the N_2-coordination of **dqn** ligand and a chloride ion. A perspective view of the crystal structure of the di-cationic species $[Ru(2py\text{-}tpyH)(dqn)Cl]^{2+}$ is displayed in Figure 5.1. The square plane is generated by N1, N2, N3, and N5 coordination, and N6 and Cl1 occupy the apical positions. In the square plane, Ru1-N2 bond distance (1.970 Å) is the shortest among the rest of the bonds and is expected due to the efficient overlap of the t_{2g} orbitals of Ru^{2+} with the π^* orbitals of the central pyridine ring of **2py-tpy** ligand. Among the apical coordination, the Ru1-Cl1 is the longer bond distance than Ru1-N6. The bite-angles generated by the **2py-tpy** and **dqn ligands** at the Ru-center span 79.3 – 77.6 °. The angles ∠N1Ru1N3, ∠N2Ru1N5 and ∠N6Ru1Cl1 are respectively 158.8 °, 177.4 ° and 170.2 °, which reveals that ∠N2Ru1N5 is closer to linearity whereas the other two angles deviate from linearity.

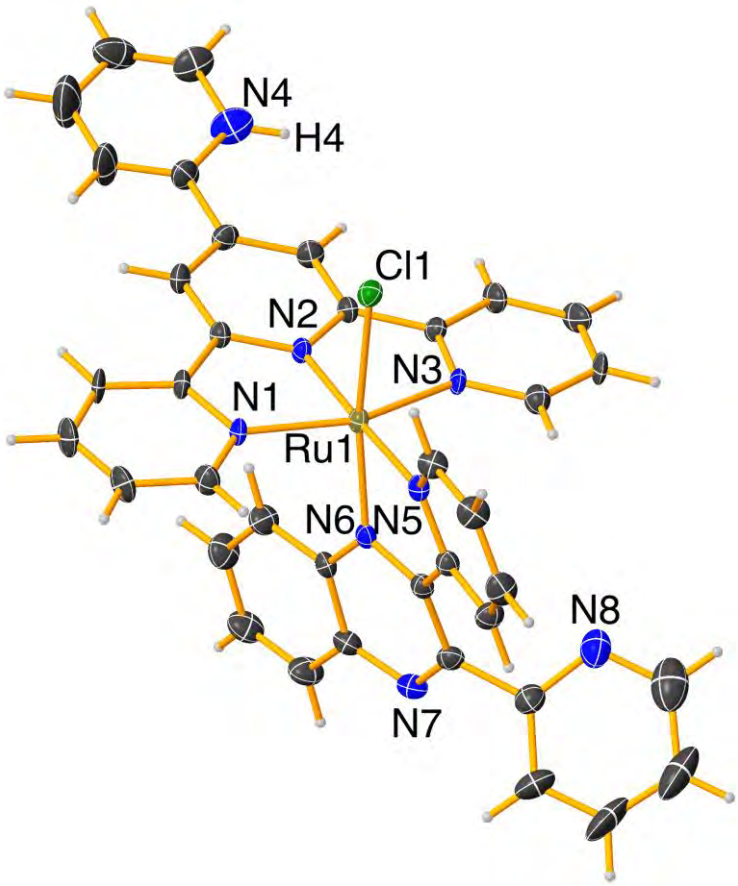

Figure 5.1. ORTEP of $[Ru(2py\text{-}tpyH)(dqn)Cl]^{2+}$.

5.4.4. Electrochemistry in organic medium

The electrochemical studies of **[Ru(dqn)]** and the ligands **2py-tpy** and **dqn** has been conducted in acetonitrile using 0.1 M $^{n}Bu_4NClO_4$ (TBAP) as supporting electrolyte, under inert atmosphere at the scan rate of 100 mV s^{-1}. The cyclic voltammogarm of ligand 2py-tpy ligand shows one reduction peak at $E_{1/2}$ = -1.77 V vs SCE (E_{pa} = -1.59 V vs SCE and E_{pc} = -1.96 V vs SCE) for the reduction of the (Figure D6(a)). The ligand DQN show one reduction peak at $E_{1/2}$ = -1.53 V vs SCE (E_{pa} = -1.48 V vs SCE and E_{pc} = -1.58 V vs SCE) (Figure D6 (b)). The cyclic voltammogram of the complex **[Ru(dqn)]** shows one irreversible oxidation peak at $E_{1/2}$ = 0.94 V vs SCE (E_{pa} = 0.97 V vs SCE and E_{pc} = 0.91 V vs SCE) for Ru^{III}/Ru^{II}. The reduction peak in cathodic direction at $E_{1/2}$ = -0.88 V vs SCE (E_{pa} = -0.84 V vs SCE and E_{pc} = -0.92 V vs SCE) corresponds to the radical anion of the **dqn** ligand. Another reduction peak at $E_{1/2}$ = -1.29 V vs SCE (E_{pa} = -1.26 V vs SCE and E_{pc} = -1.32 V vs SCE attributed to the radical anion of the terpyridine moiety (Figure 5.2).

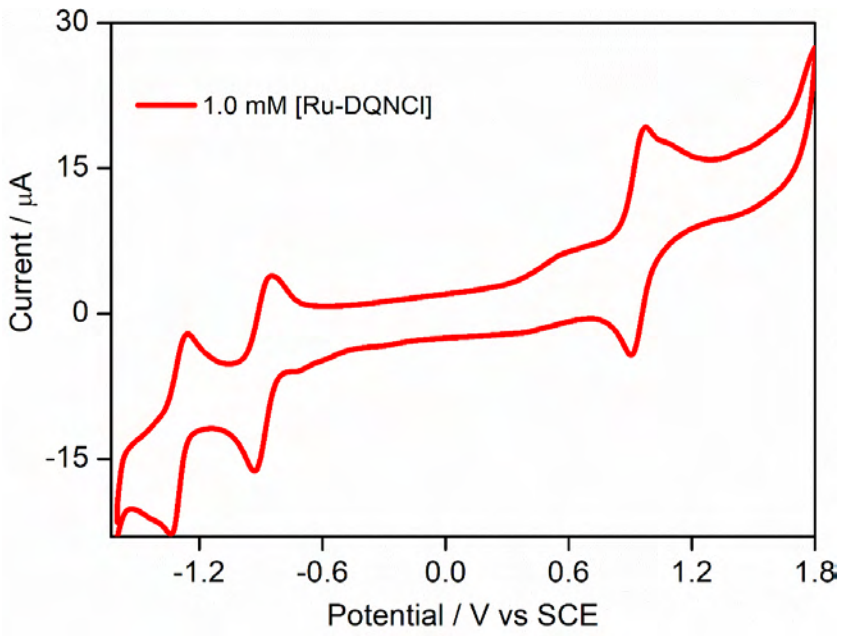

Figure 5.2. CV of 1.0 mM of **[Ru(dqn)]** in DMF using 0.1 M $^{n}Bu_4NClO_4$ (TBAP) as supporting electrolyte.

5.4.5. Acid-base equilibria

The acid-base equilibria of the complex were studied in the Britton-Robinson Buffer within a pH range of 2.0 to 7.0 through UV-Visible spectroscopy (Scheme 5.2). Within the pH range of 2.5 to 5.0, an increase in band intensity was observed at 247 nm, and by fitting the absorbance *vs.* pH, a pKa of 3.12 was observed for the protonation of the pyridine moiety of the DQN ligand (Figure D7-D8). A substantial decrease in band intensity at 228 nm was observed with a pKa of 4.91 within the pH range of 4.5 to 7.0 for the protonation of the free nitrogen of the pyridine ring in the terpyridine **2py-tpy** ligand (Figure D9-D10).

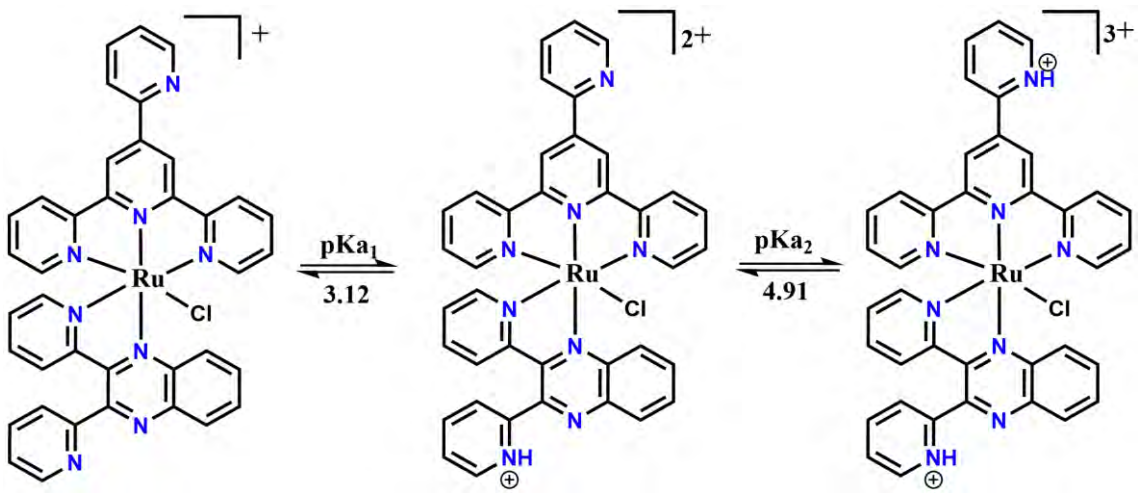

Scheme 5.2. The acid-base equilibria in **[Ru(dqn)]** complex.

5.4.6. Dehydrogenation of formic acid

The catalyst **[Ru(dqn)]** also shows catalytic activity towards dehydrogenation effectively. The decomposition of formic acid into hydrogen and carbon dioxide is studied using water as a solvent in sodium formate as a base and **[Ru(dqn)]** as the catalyst. The dehydrogenation reactions were conducted in a double jacketed reaction vessel containing catalyst dissolved in water with sodium formate as a base. The formic acid was injected through a rubber septum. The dehydrogenation reactions were studied in four different sets by varying the concentration of acid, base, catalyst, and temperature to study the kinetics of dehydrogenation reaction for the evolution of hydrogen and carbon dioxide gas. The substrate and catalyst concentrations were varied to find out the dependence of the rate of reaction on the concentration of acid, base, and catalyst by linear fitting the initial rate of reaction at a fixed temperature of 55 °C. The acid concentration was varied from 5 mmol to 20 mmol by using 15 mmol of base and 1.0 mM of catalyst at 55 °C (Figure 5.3(a)-Figure 5.3(b)). The reaction rate increases with an increase in the concentration of acid and follows first-order kinetics with acid concentration having a rate constant k = 0.16 x 10^{-2} µmol s^{-1}. The TON at 5 mmol acid concentration is 6.9 with an initial TOF 0.05 s^{-1} which is the lowest and highest TON of 15, and an initial TOF of 0.114 s^{-1} is observed with 15 mmol of acid concentration. The maximum volume of gas evolved is 30 µmol. The base concentration was varied from 1 mmol to 40 mmol using 10 mmol of acid and 1.0 mM of catalyst at 55 °C (Figure D11-Figure D12). As the base concentration increases, the rate of reaction increases thus follows the first-order kinetics with base concentration with a rate constant of k = 0.19 x 10^{-2} µmol s^{-1}. The TON of 3.53 and initial TOF of 0.03 s^{-1} were observed for the lowest base concentration of 1 mmol and TON of 10.5, and initial TOF of 0.12 s^{-1} were observed for the highest base concentration of 40 mmol with maximum gas evolution of 33 µmol was observed at 40 mmol of the base. The complex concentration was varied from 0.25 mM to 1.0 mM by keeping the acid concentration at 10 mmol and the base at 15 mmol at a fixed temperature of 55 °C (Figure D13-Figure D14). The reaction rate increases with an increase in concentration catalyst following the first-order kinetics with complex concentration having a rate constant of k = 6.07 x 10^{-2} µmol s^{-1}. The maximum TON of 15 and TOF of 0.12 s^{-1} was observed for 1.0 mM of the complex concentration with maximum gas evolution of 30 µmol.

Table 5.1. Summary of experiments in different reaction conditions for dehydrogenation of formic acid

Temperature [°C]	Catalyst [mM]	Acid [mmol]	Base [mmol]	TON	Initial TOF [s^{-1}]	The volume of Gas evolved / µmol
55	1.0	5	15	6.9	0.05	14
55	1.0	10	15	8.7	0.06	17
55	1.0	15	15	11.0	0.08	22
55	1.0	20	15	15.0	0.114	30
55	1.0	10	1	3.53	0.03	7
55	1.0	10	10	5.82	0.04	12
55	1.0	10	25	9.6	0.07	19
55	1.0	10	40	16.5	0.12	33
55	0.25	10	15	7.4	0.045	15
55	0.50	10	15	9.7	0.06	19
55	0.75	10	15	11.34	0.083	23
55	1.0	10	15	15.0	0.12	30
25	1.0	10	15	4.5	0.014	9
40	1.0	10	15	9.0	0.05	18
55	1.0	10	15	11.4	0.08	23
70	1.0	10	15	15.1	0.12	30

The effect of temperature on dehydrogenation reaction was studied by varying the temperature from 25 °C to 70 °C by taking the concentration of acid 10 mmol, base 15 mmol, and 1.0 mM of catalyst (Figure 5.3(c)-Figure 5.3(d)). With the increase in temperature, the rate of reaction increases and follows the first-order kinetics with temperature having a rate constant of k = 0.30 x 10^{-2} µmol s^{-1}. The volume of 30 µmol gas evolved is maximum at 70 °C with a TON of 15.1 and an initial TOF of 0.12 s^{-1}. The minimum TON and initial TOF of 4.5 and 0.014 s^{-1} were observed for the lowest temperature of 25 °C. Among all the sets of reactions, the maximum TON of 16.5, initial TOF of 0.12 $s^{-1,}$ and volume of gas evolved is 33 µmol in the presence of 10 mmol of acid, 40 mmol of the base, and 1.0 mM of the complex at 55 °C. The rate of reaction, as well as the volume of gas evolved, is higher at high temperatures as compared to room temperature. Hydrogen and carbon dioxide evolution was also confirmed through gas chromatography, and 2.6 x 10^{-6} moles of H_2 and 3.6 x 10^{-5} moles of CO_2 were evolved (Figure D15-Figure D16).

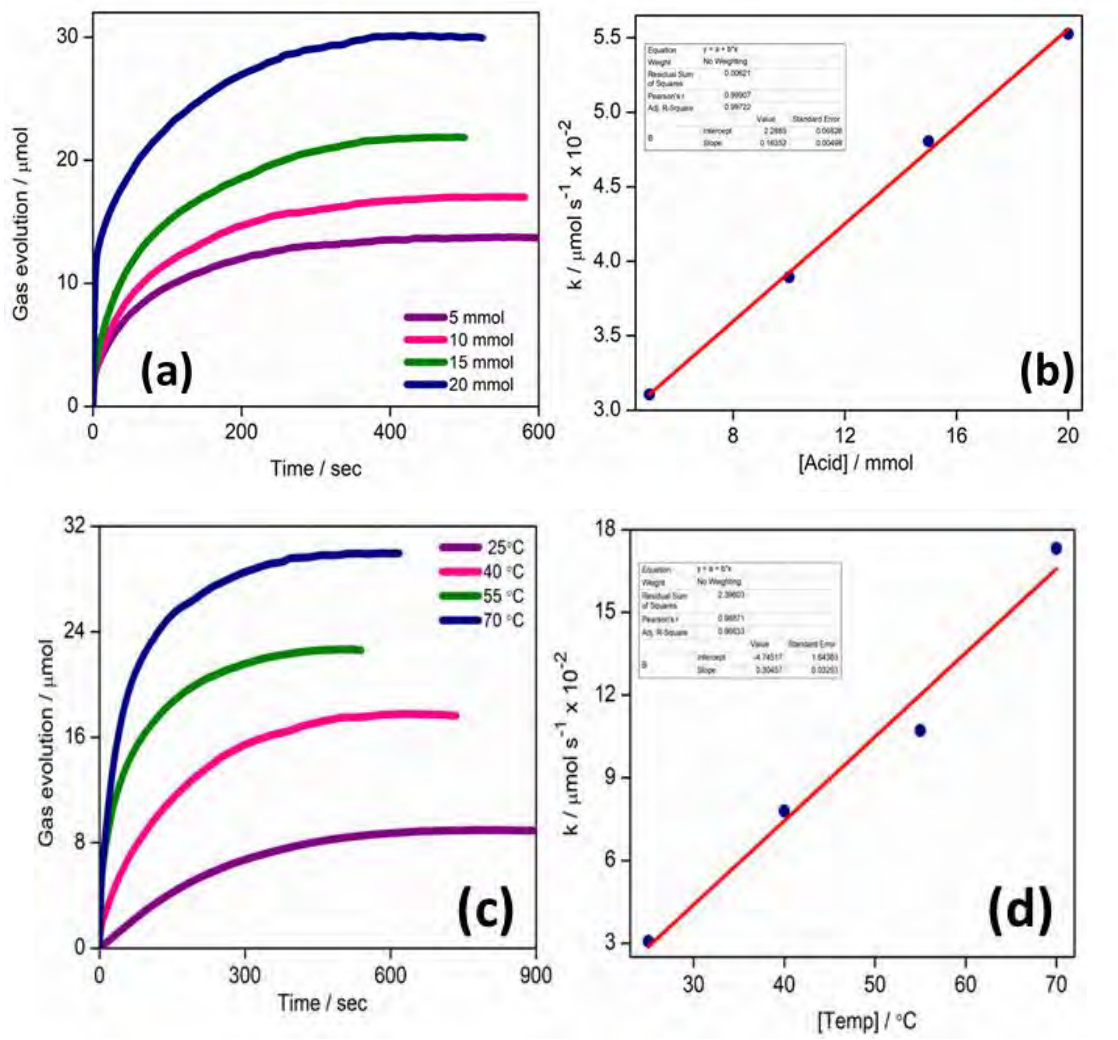

Figure 5.3. (a) Gas evolution by **[Ru(dqn)]** with a variety of acid concentration in the presence of 1.0 mM of complex and 15 mmol of the base at 55 °C in water. **(b)** Rate of gas evolution *vs.* acid in water. **(c)** Gas evolution by **[Ru(dqn)]** with temperature variation in the presence of 1.0 mM of complex, 10 mmol of the base, and 15 mmol of acid in water. **(d)** Rate of gas evolution *vs.* temperature in water.

5.4.7. Thermodynamical Analysis.

The activation energy E_a is estimated from the Arrhenius plot, which is the logarithm of reaction rate constant *k* plotted in reference to reciprocal of temperature 1/T by employing the equation 5.1.

$$\boldsymbol{ln\, k = -\frac{E_a}{RT} + ln\, A} \qquad \textbf{(5.1)}$$

Where A = pre-exponential factor and R = gas constant. [11-12] The decomposition of formic acid was studied at four different temperatures by varying the temperature from 298 K to 343

K by using 1.0 mM **[Ru(dqn)]** with 10 mmol of acid and 15 mmol of sodium formate as base to determine the initial rate of decomposition of formic acid. The activation energy E_a is calculated from the slope of Arrhenius plot $-\frac{E_a}{R}$ with intercept *ln A*. The slope from the plot = -3782.82 and R = 8.3145 J K^{-1} mol^{-1}; by putting these values activation energy was found to be 31.45 kJ / mol (Figure 5.4).

Table 5.2. Calculations for Arrhenius plot

Temperature °C	Temperature K	$\frac{1}{T}$	k	$ln\ k$
25	298	0.00336	0.03063	-3.4857
40	313	0.00319	0.07794	-2.5518
55	328	0.00305	0.10711	-2.2339
70	343	0.00292	0.17319	-1.7533

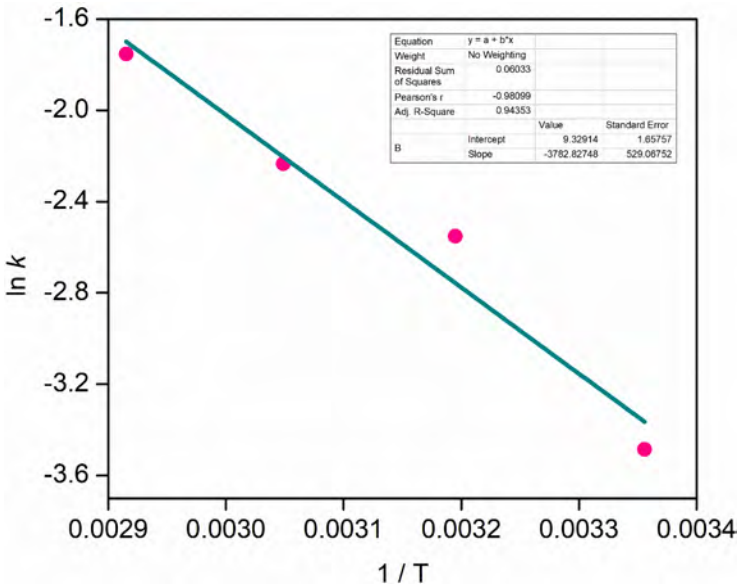

Figure 5.4. Arrhenius plot for the complex **[Ru(dqn)]** to estimate the activation energy.

From the Eyring plot, thermodynamical parameters like $\Delta H^{\ddagger}$ = enthalpy of activation and $\Delta S^{\ddagger}$ = entropy of activation, and $\Delta G^{\ddagger}$ free energy were calculated. The Eyring plot can be described as the logarithm of *k*/T plotted for reciprocal of temperature 1/T derived from the following equation (5.2).[13-14]

$$ln\frac{k}{T} = \frac{-\Delta H^{\ddagger}}{R} \cdot \frac{1}{T} + ln\frac{k_B}{h} + \frac{\Delta S^{\ddagger}}{R} \quad \textbf{(5.2)}$$

Where, k = reaction rate constant, T = absolute temperature in K, R = gas constant, k_B = Boltzmann's constant. The enthalpy $\Delta H^{\ddagger}$ was calculated to be 29131 J K^{-1} mol^{-1} from the slope

of the plot = $\frac{-\Delta H^{\ddagger}}{R}$, where R = 8.3145 J K^{-1} mol^{-1} and slope = -3503.75. The intercept of Eyring plot is = $ln\frac{k_B}{h} + \frac{\Delta S^{\ddagger}}{R}$ and $\Delta S^{\ddagger}$ entropy was calculated to be -175 J K^{-1} mol^{-1} where intercept from the plot is = 2.68. After obtaining the values of $\Delta H^{\ddagger}$ and $\Delta S^{\ddagger}$, $\Delta G^{\ddagger}$ Gibbs free energy can be calculated from the following equation (5.3).

$$\Delta G^{\ddagger} = \Delta H^{\ddagger} - T\Delta S^{\ddagger} \qquad \textbf{(5.3)}$$

By putting the value of $\Delta H^{\ddagger}$ = 29131 J K^{-1} mol^{-1}, $\Delta S^{\ddagger}$ = -175 J K^{-1} mol^{-1} and T = 298 K in the above equation the $\Delta G^{\ddagger}$ was estimated to be 81.33 kJ (Figure 5.5).

Table 5.3. Calculations for Eyring plot

Temperature °C	Temperature K	$\frac{1}{T}$	k	$\frac{k}{T}$	$ln\frac{k}{T}$
25	298	0.00336	0.0306	102 x 10^{-6}	-9.190
40	313	0.00319	0.0779	249 x 10^{-6}	-8.298
55	328	0.00305	0.1071	326 x 10^{-6}	-8.028
70	343	0.00292	0.1732	504 x 10^{-6}	-7.592

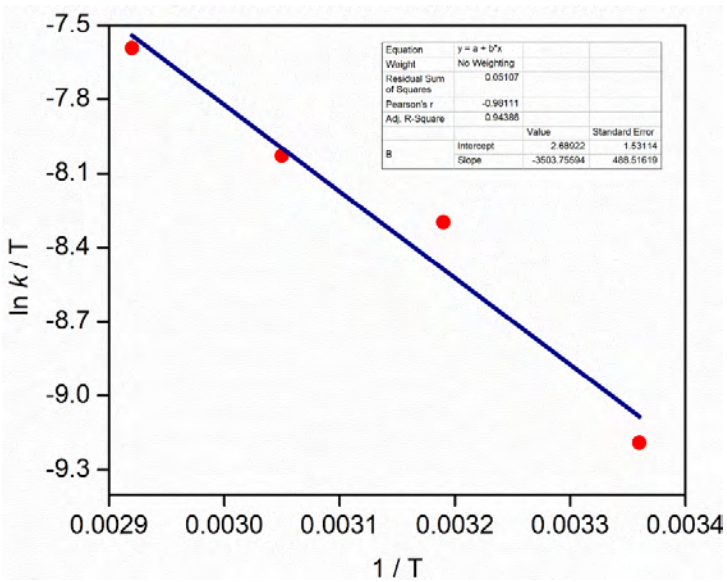

Figure 5.5. Eyring plot for the complex **[Ru(dqn)]** to estimate the $\Delta H^{\ddagger}$, $\Delta S^{\ddagger}$, and $\Delta G^{\ddagger}$.

5.4.8. pH variation for the decomposition of formic acid

The dehydrogenation reaction shows dependence on the pH that influences the rate of evolution of H_2 gas from the formic acid. The dehydrogenation reactions were performed in the aqueous medium at different pH, and the catalytic behavior of the complex varies in acidic, neutral, and

basic pH. The dehydrogenation reactions are most preferably performed in water as a solvent because it assists the formation of hydronium ions (H_3O^+) and metal hydride in accelerating the reaction. The **[Ru(dqn)]** complex shows an efficient dehydrogenation of the formic acid in deionized water and at neutral pH. The dependence of the **[Ru(dqn)]** on the pH for the dehydrogenation reactions was studied in phosphate buffer within a pH range of 2.0 to 11.0 in the presence of 10 mmol of formic acid, 15 mmol of sodium formate, and 1.0 mM of the complex at 55 °C (Figure 5.6). The reaction rate was slow in a highly acidic pH of 2.0, and the TOF increased very slightly at pH 4.0 and at pH 6.0. The highest initial TOF of 0.0279 s^{-1} was observed at neutral pH 7.0. The TOF is nearly identical for the dehydrogenation reaction at pH 6.0 and at pH 8.0. The initial TOF decreases to a minimum at highly basic pH 9.0 and 11.0. In the highly acidic pH due to the the formation of unreactive metal hydroxides, formic acid's dehydrogenation is terminated as the formation of metal hydride and release of H_2 gets terminated. The **[Ru(dqn)]** complex shows dehydrogenation of the formic acid efficiently at neutral pH 7.0 and in deionized water.

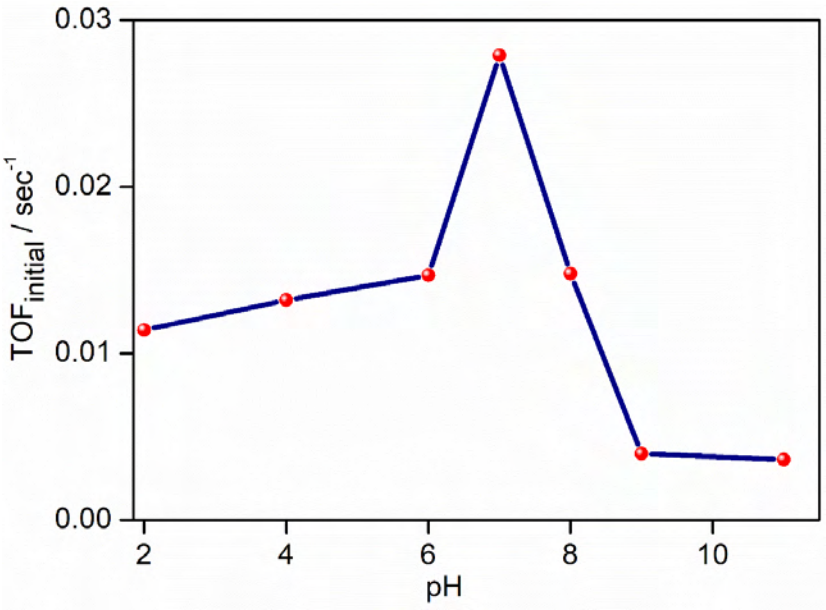

Figure 5.6. pH dependence of the initial TOF for the decomposition of formic acid with 1.0 mM complex, 10 mmol formic acid, and 15 mmol sodium formate in phosphate buffer at 55 °C.

5.4.9. Stability of the catalyst

The stability of the complex towards the decomposition of formic acid was studied by iterative addition of formic acid and sodium formate in a separate set of reactions. The reproducibility of the complex was investigated by repetitive addition of 20 mmol of formic acid after the

completion of every cycle monitored by differential pressure manometer in the reaction vessel containing 25 mmol of sodium formate and 1.0 mM of **[Ru(dqn)]** at 55 °C. The complex shows catalytic stability up to 5 cycles with a TON of 62 (Figure D17). In the other set of reactions, 25 mmol of the base was added iteratively in the presence of 20 mmol of formic acid and 1.0 mM of the complex in the reaction vessel at 55 °C after the completion of each cycle. The catalyst shows reproducibility up to 6 cycles for base variation with a TON of 66 (Figure 5.7). This indicates that catalyst is reliable during the dehydrogenation of formic acid as it shows gas evolution after every fresh injection of formic acid or sodium formate. The catalyst is highly stable and efficient during the dehydrogenation reaction.

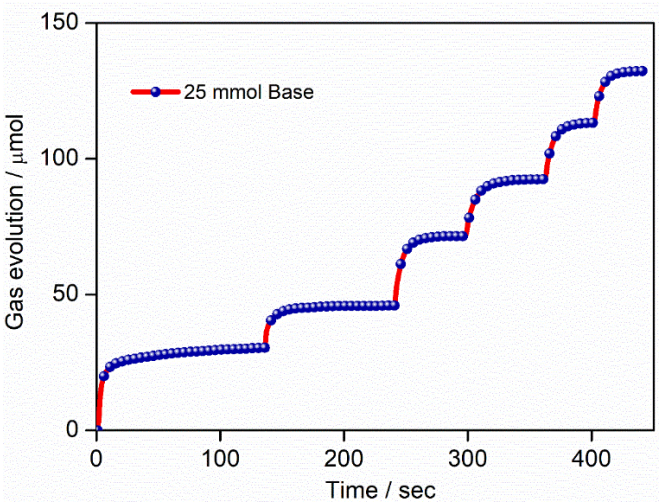

Figure 5.7. Catalytic cycles for the complex **[Ru(dqn)]** with the iteration of 20 mmol of acid in the presence of 1.0 mM complex and 25 mmol base in water at 55 °C.

5.5 Plausible Mechanism

A mechanism has been proposed in Scheme 5.3 based on experimental results obtained during the dehydrogenation of HCOOH by complex **[Ru(dqn)]**. Herein, the chloride complex **[A]** undergoes the formation of the aqua-complex **[B]** in an aqueous solution. In HCOOH and HCOONa, the aqua-complex **[B]** generates the formate complex **[C]**. The ESI-mass spectra (Figure D18) calculated for $[Ru(2py\text{-}tpy)(DQN)OOCH]+2HCOONa]^+$ (m/z 878.1133), and found to be (m/z = 878.0984). The formate complex **[C]** undergoes rearrangement to generate the Ru-H complex **[D]** with the release of CO_2 (After several trials, the NMR peak for Ru-H species couldn't be observed). In an acidic aqueous solution, the Ru-H complex **[D]** evolves H_2 and returns to the aqua complex **[B].**

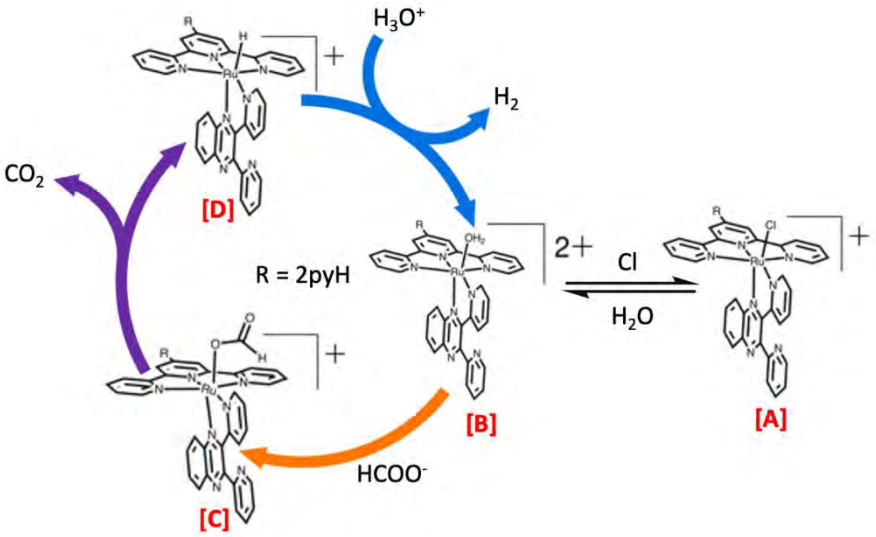

Scheme 5.3. A plausible mechanism for the catalytic cycle for dehydrogenation of HCOOH by **[Ru(dqn)]**.

5.6 Summary

The **[Ru(2py-tpy)(dqn)Cl](PF$_6$) ([Ru(dqn)])** complex was synthesized and characterized with various spectroscopic techniques. The complex **[Ru(dqn)]** was employed for catalyzing the dehydrogenation of formic acid using sodium formate as the base in deionized water. The dehydrogenation of formic acid was studied at different concentrations of acid, base, and complex and from lower to a higher temperatures to determine the kinetics of the reaction. The dehydrogenation of formic acid was also performed at different pH values from 2.0 to 11.0. The dehydrogenation of formic acid at different temperatures reveals that activation energy required for the dehydrogenation of formic acid was 31.45 kJ / mol, and ΔG was estimated to be 81.33 kJ. The composition of gas was detected from the TCD and FID detectors of the Gas Chromatograph. The catalytic stability of the complex towards dehydrogenation was examined by the iterative addition of formic acid and sodium formate in different sets of reactions.

5.7 References

1. Felderhoff, M.; Weidenthaler, C.; Helmolt, R. V.; Eberle, U.; Hydrogen storage: the remaining scientific and technological challenges. *Phys. Chem. Chem. Phys.* **2007**, *9* (21), 2643 – 2653.
2. Suh, M. P., Park, H. J.; Prasad, T. K.; Lim, D.-W. Hydrogen Storage in Metal_Organic Frameworks. *Chem. Rev.* **2012**, *112* (2), 782–835.

3. Mellmann, D.; Sponholz, P.; Junge, H.; Beller, M.; Formic acid as a hydrogen storage material – development of homogeneous catalysts for selective hydrogen release. *Chem. Soc. Rev*. **2016**, *45* (14), 3954-3988.
4. Singh, A. K.; Singh, S.; Kumar, A. Hydrogen Energy Future with Formic Acid: A Renewable Chemical Hydrogen Storage System. *Catal. Sci. Technol.* **2016**, *6* (1), 12 - 40.
5. Coffey, R. S. The Decomposition of Formic Acid catalysed by Soluble Metal Complexes. *Chem. Commun*. **1967**, *18*, 923b-924.
6. Boddien, A.; Loges, B.; Junge, H.; Beller, M.; Hydrogen Generation at Ambient Conditions: Application in Fuel Cells. *ChemSusChem.* **2008**, *1* (8-9), 751 - 758.
7. Guan, C.; Zhang, D.-D.; Pan, Y.; Iguchi, M.; Ajitha, M. J.; Hu, J.; Li, H.; Yao, C.; Huang, M.-H.; Min, S.; Zheng, J.; Himeda, Y.; Kawanami, H.; Huang, K.-W. Dehydrogenation of Formic Acid Catalyzed by a Ruthenium Complex with an N,N′-Diimine Ligand. *Inorg. Chem.* **2017**, *56* (1) 438 - 445.
8. Treigerman, Z.; Sasson, Y.; Further Observations on the Mechanism of Formic Acid Decomposition by Homogeneous Ruthenium Catalyst. *ChemistrySelect*, **2017**, *2* (21), 5816 - 5823.
9. Luo, C.; Li, L.; Yue, X.; Li, P.; Zhang, L.; Yang, Z.; Pu, M.; Cao, Z.; Lei, M. pH-Dependent transfer hydrogenation or dihydrogen release catalyzed by a [(η^6-arene)RuCl(k^2-N,N-dmobpy)]$^+$ complex: a DFT mechanistic understanding. *RSC Adv.* **2020**, *10* (18), 10411–10419.
10. Elchishcheva, N. V. ; Shklyaev, Y. V.; Vnutskikh, Z. A.; Chekryshkin, Y. S.; Odegova, T. F.; Synthesis And Antimicrobial Activity of Quaternized Heterocyclic Systems Based on A-Pyridoin And 2,2_-Pyridyl. *Pharmaceutical Chemistry Journal*, **2012**, *46* (6), 23-26.
11. Boddien, A.; Mellmann, D.; Gartner, F.; Jackstell, R.; Junge, H.; Dyson, P. J.; Laurenczy, G.; Ludwig, R.; Beller, M.; Efficient Dehydrogenation of Formic Acid Using an Iron Catalyst. *Science*. **2011**, *333* (6050), 1733−1736.
12. Fukuzumi, S.; Kobayashi, T.; Suenobu, T.; Unusually Large Tunneling Effect on Highly Efficient Generation of Hydrogen and Hydrogen Isotopes in pH-Selective Decomposition of Formic Acid Catalyzed by a Heterodinuclear Iridium-Ruthenium Complex in Water. *J. Am. Chem. Soc.* **2010**, *132* (5), 1496 – 1497.
13. Eyring, H.; Polanyi, M.; On Simple Gas Reactions. *Z. Phys. Chem. B.* **1931**, *12*, 279.
14. Espenson, James, H. Chemical Kinetics and Reaction Mechanisms. *McGraw-Hill*. **1981**, p. 117.

Appendix D

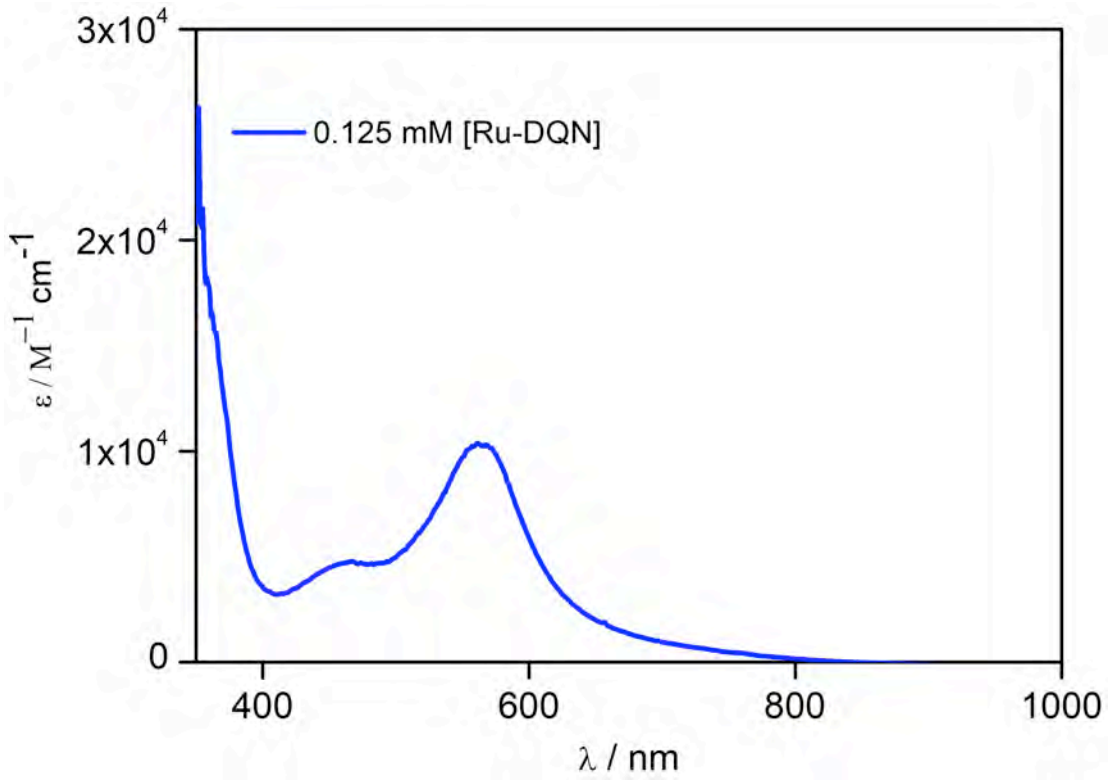

Figure D1. UV-Visible spectra of **[RuDQNCl]** in MeOH.

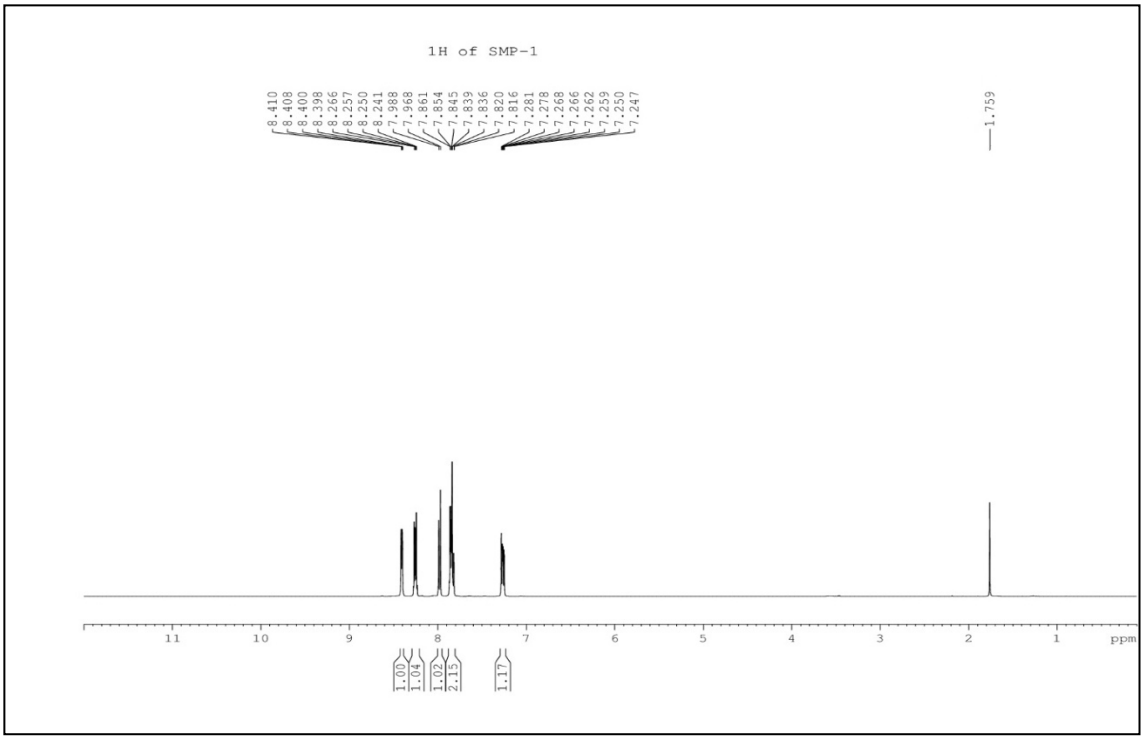

Figure D2. ^{1}H NMR Spectra of the dqn ligand in $CDCl_3$

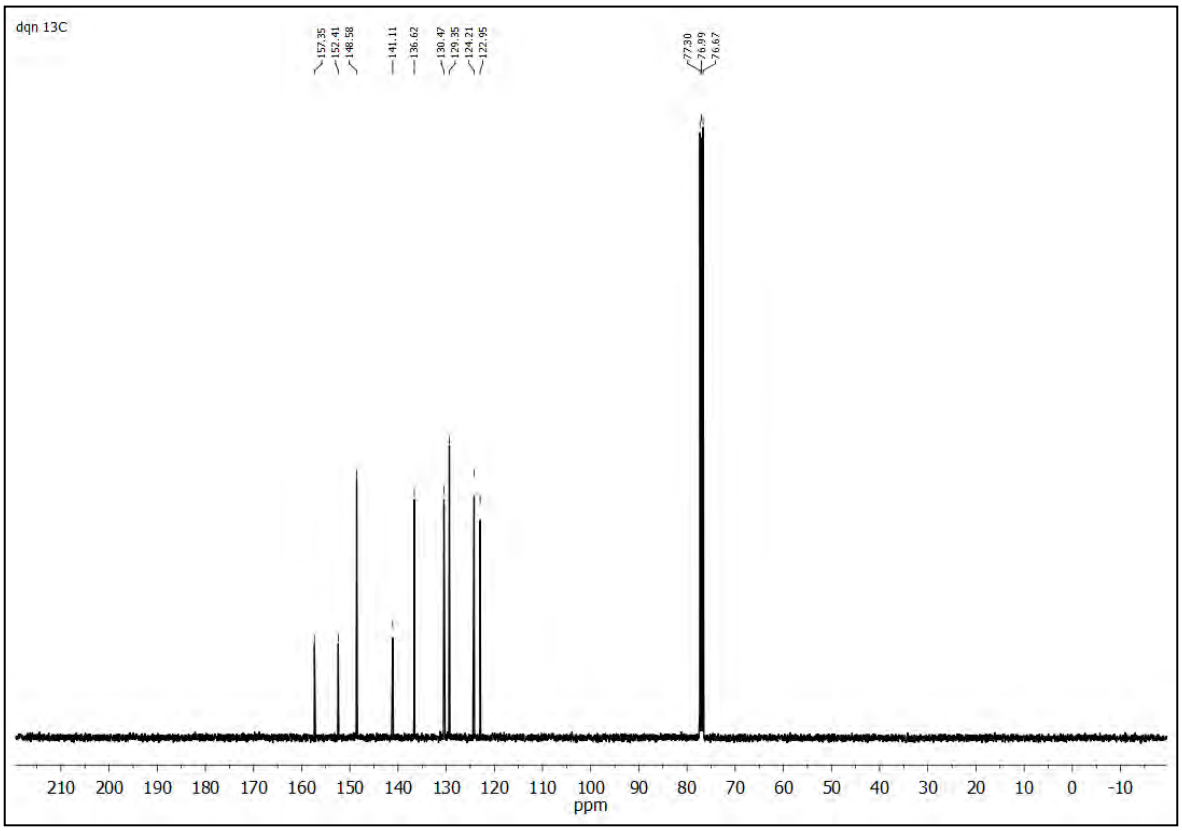

Figure D3. ^{13}C NMR Spectra of the dqn ligand in $CDCl_3$.

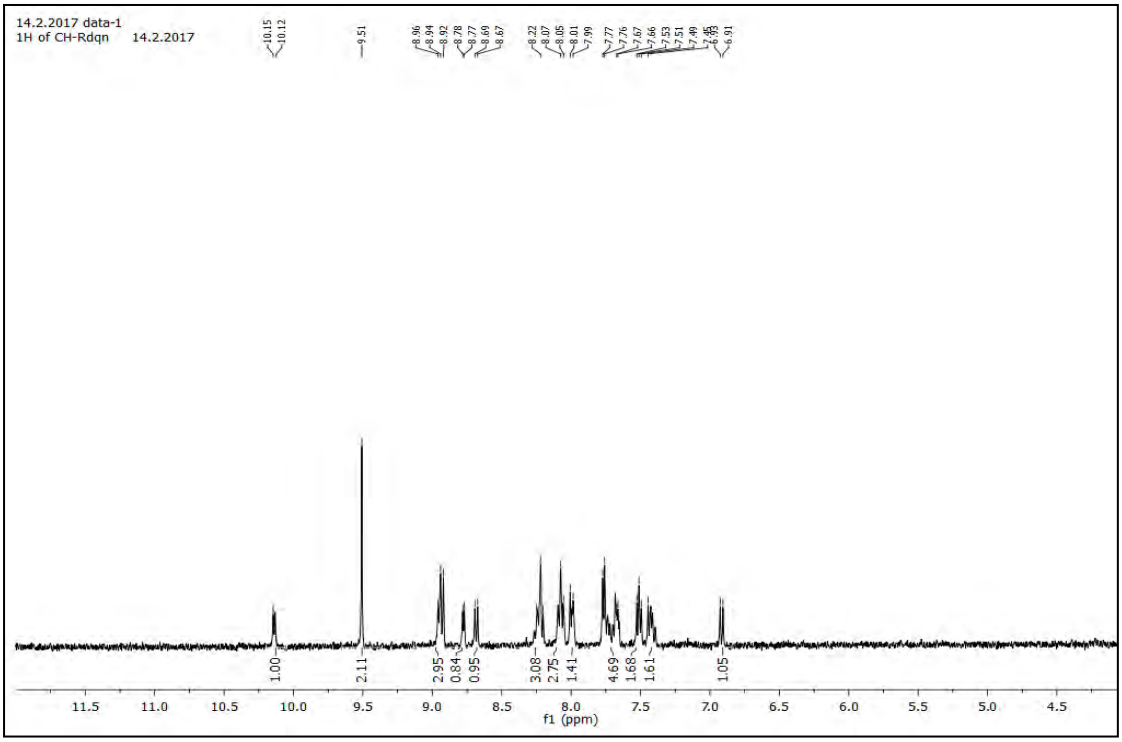

Figure D4. ^{1}H NMR Spectra of the [Ru (2py-tpy) (dqn) Cl] complex in DMSO-d_6.

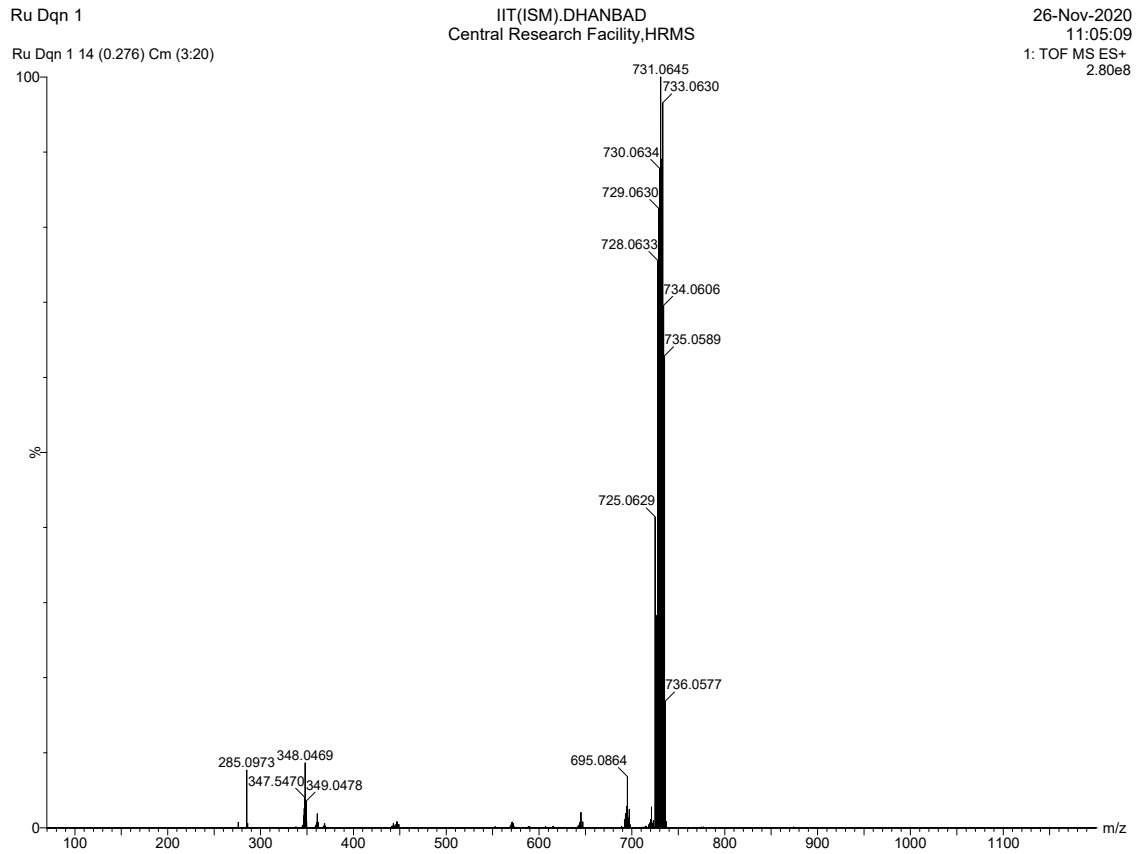

Figure D5. Mass Spectra for [Ru (2py-tpy)(dqn)Cl]$^{+}$ complex.

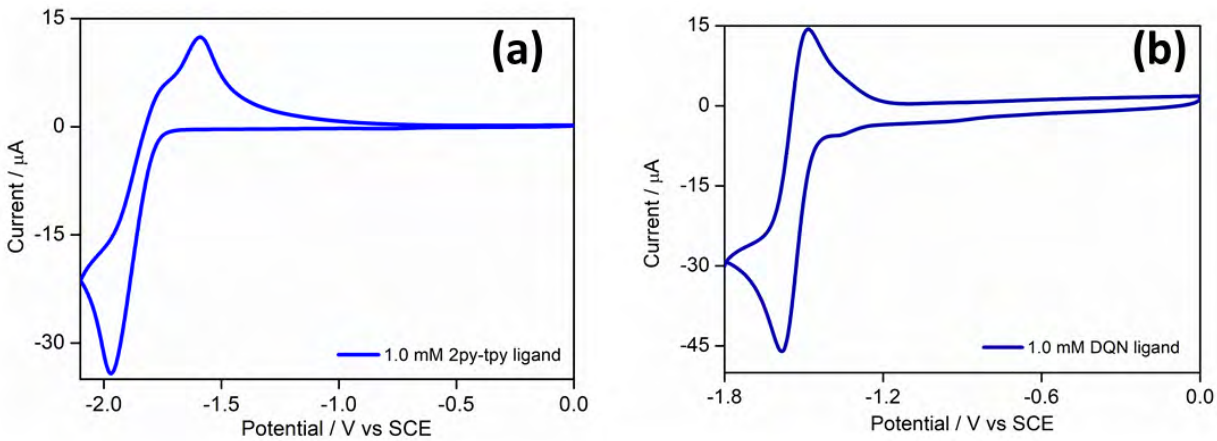

Figure D6 (a). The CV of the 2py-tpy ligand and (b) The CV of the DQN ligand in acetonitrile using 0.1 M $^{n}Bu_4NClO_4$ (TBAP) as supporting electrolyte, under inert atmosphere at the scan rate of 100 mV s^{-1}.

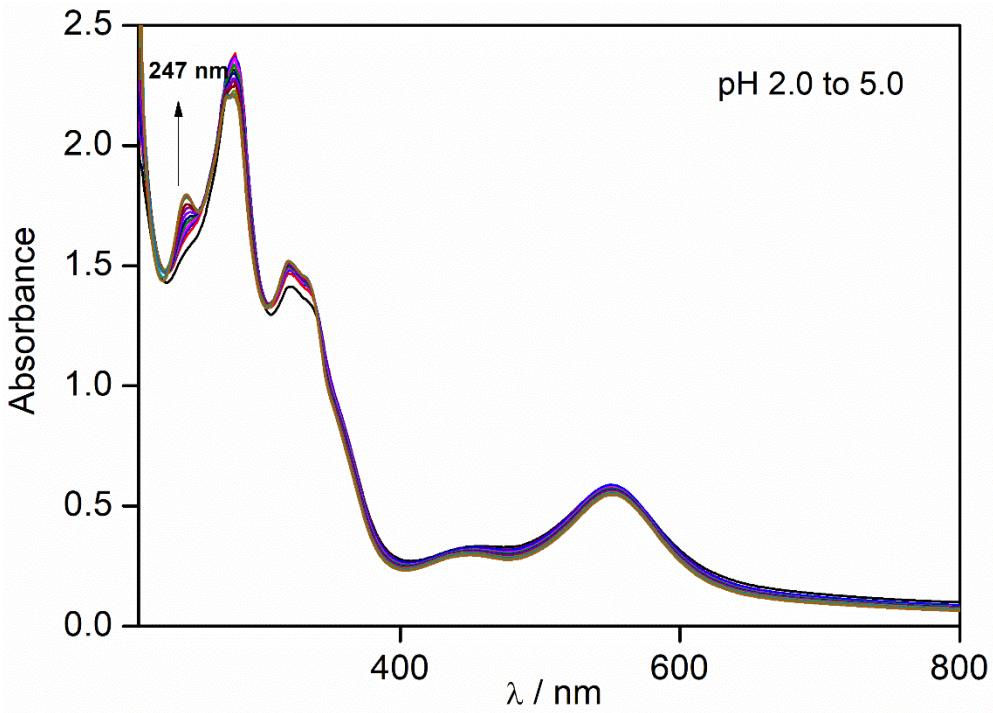

Figure D7. Change in UV-Visible spectra of [Ru-DQN] in Britton–Robinson buffer from pH 2.0 to 5.0.

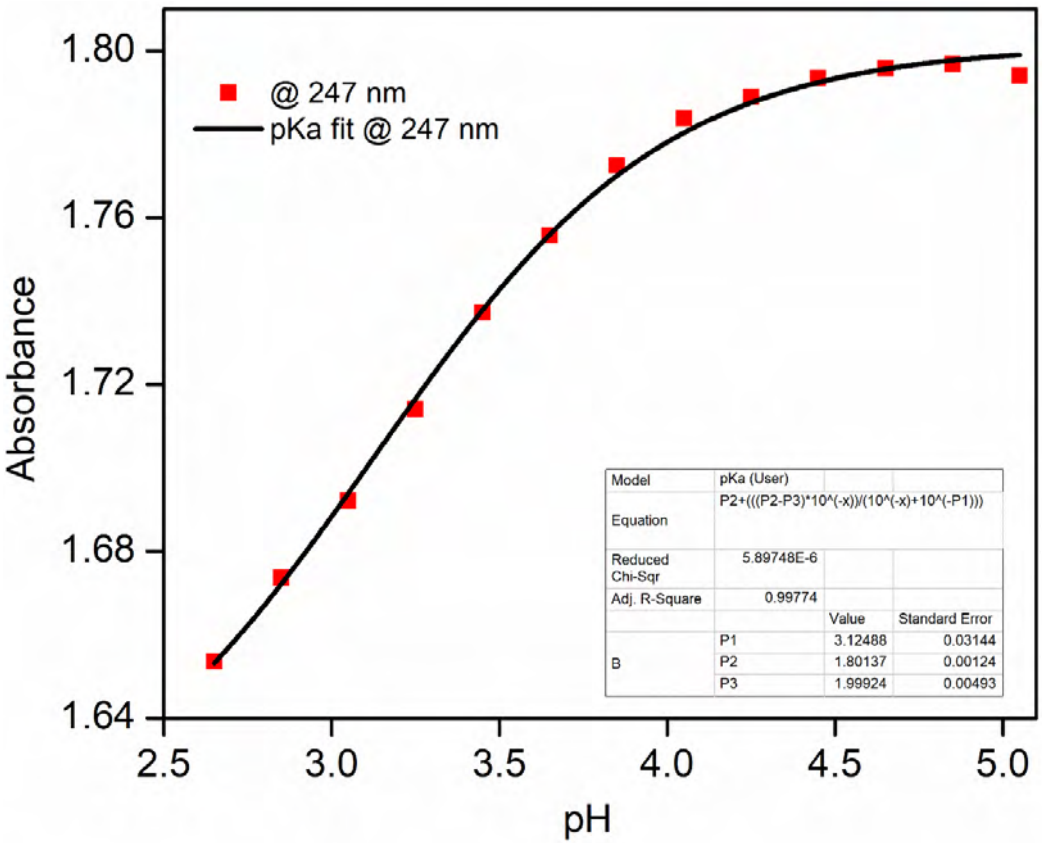

Figure D8. Absorbance vs. pH profile of **[Ru-DQN]** within the pH 2.0-5.0.

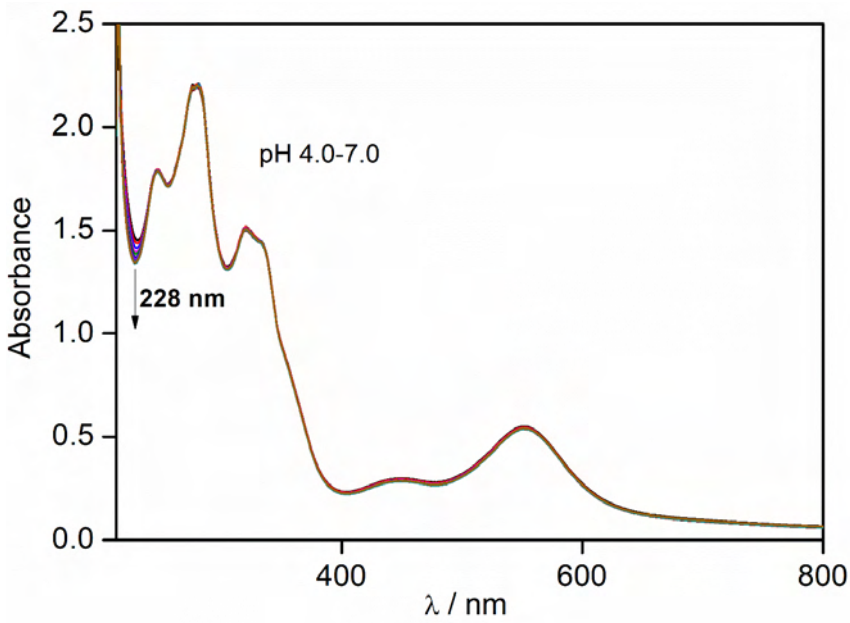

Figure D9. Change in UV-Visible spectra of [Ru-DQN] in Britton–Robinson buffer from pH 4.0 to 7.0.

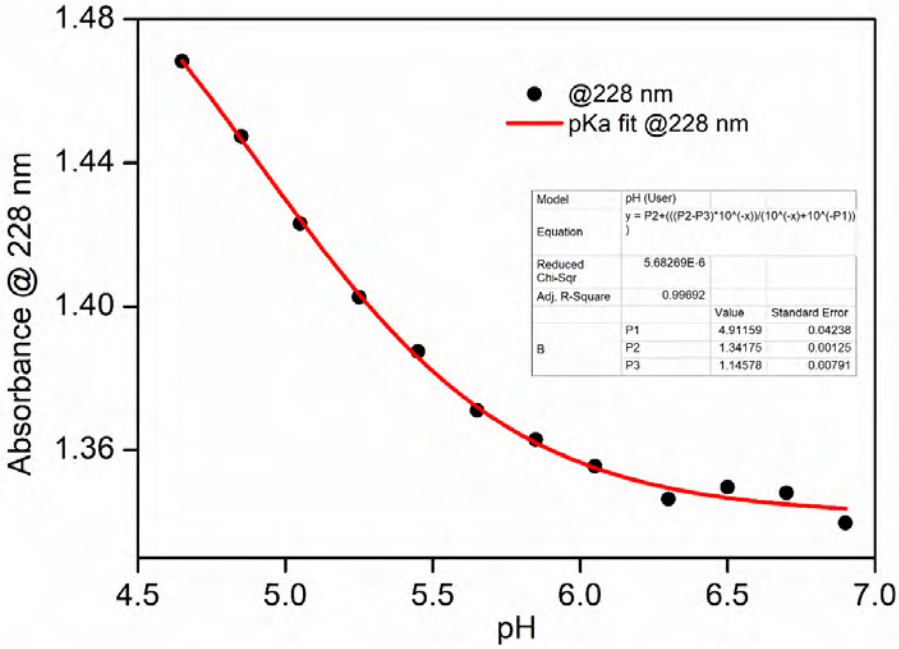

Figure D10. Absorbance vs. pH profile of **[Ru-DQN]** within the pH 4.0-7.0.

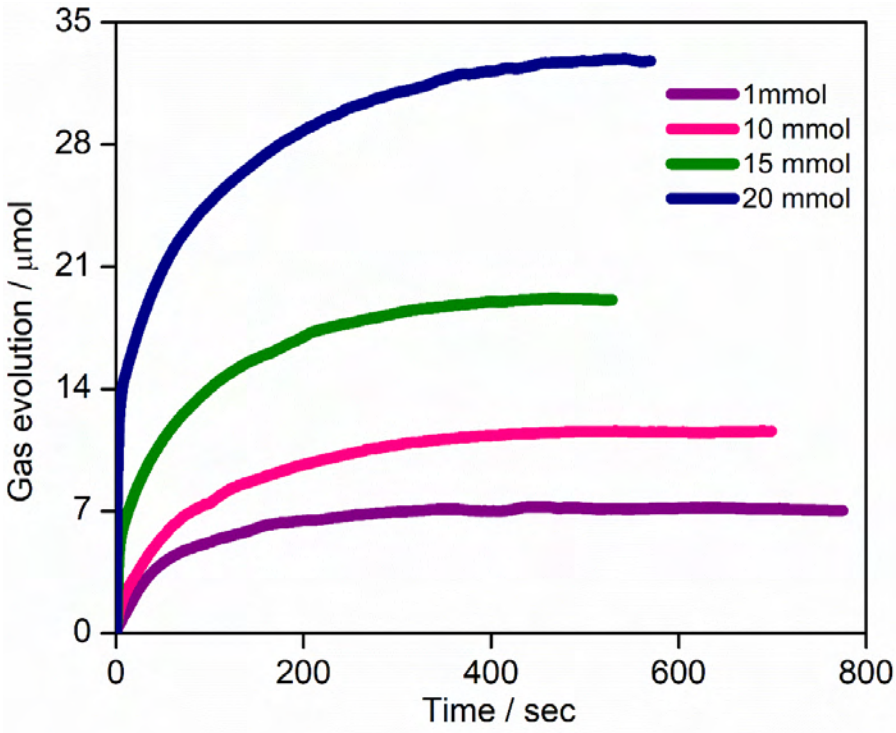

Figure D11. Gas evolution by **[RuDQNCl]** with a variation of base concentration in presence of 1.0 mM of complex and 10 mmol of acid at 55 °C in water.

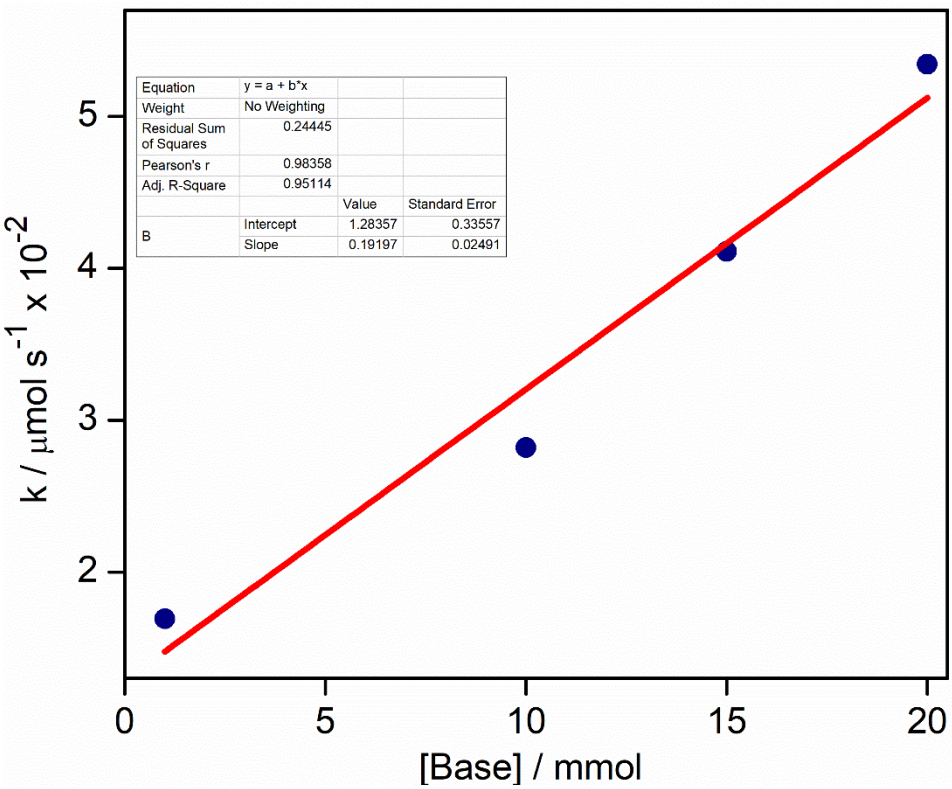

Figure D12. Rate of gas evolution *vs.* [base] in water.

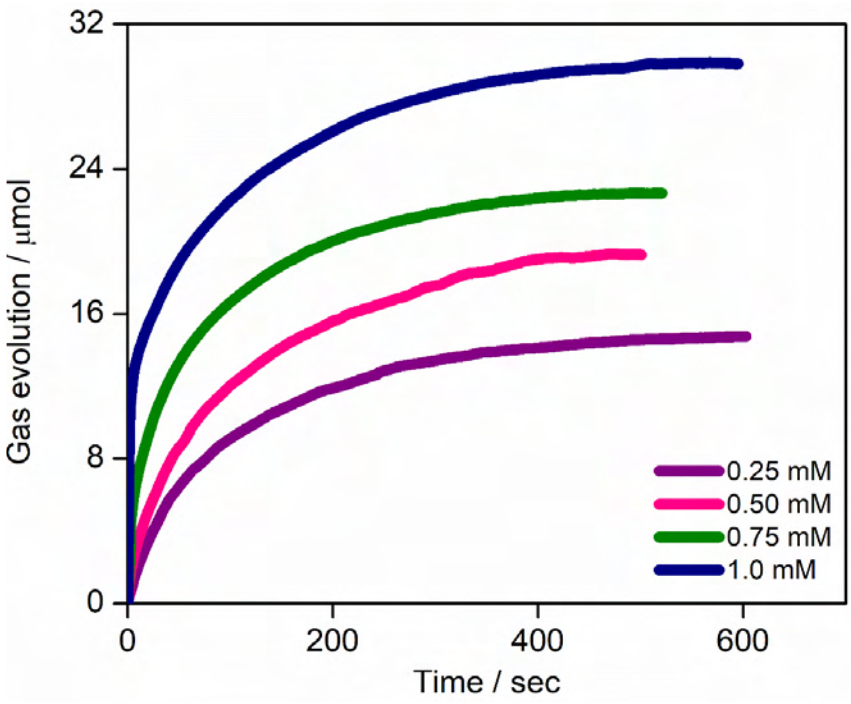

Figure D13. Gas evolution by **[Ru(dqn)]** with a variation of complex concentration in presence of 10 mmol of acid and 15 mmol of the base at 55 °C in water.

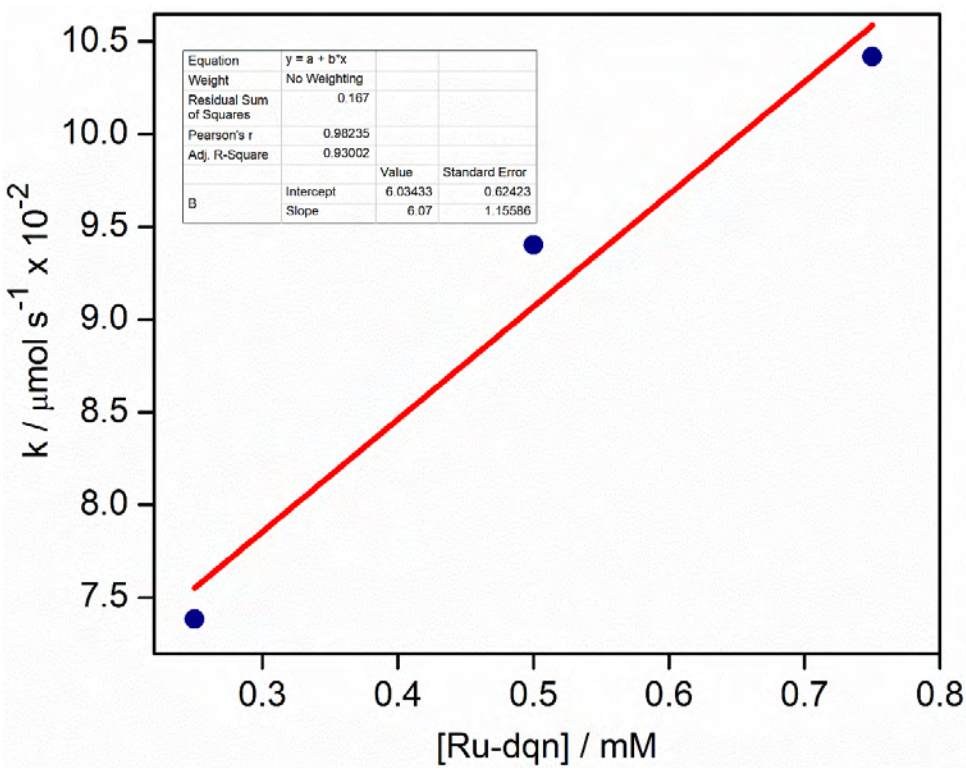

Figure D14. Rate of gas evolution *vs.* [complex] in water.

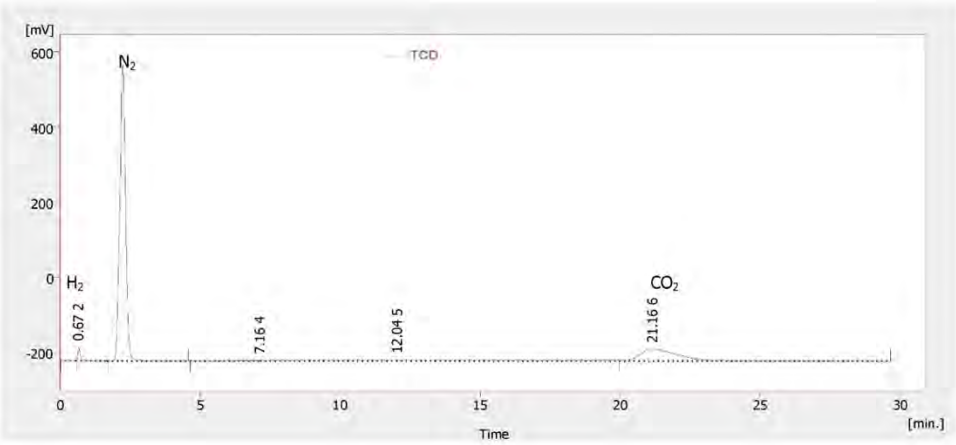

Sample Info:

Sample ID	: Run TCD	Amount	0
Sample	: Run TCD for NC-100 2	ISTD Amount	0
Inj. Volume [mL]	: 0.5	Dilution	1

Result Table

	Reten. Time [min]	Area [mV.s]	Height [mV]	Area [%]	Height [%]
1	0.205	47.951	2.028	0.3	0.2
2	0.669	232.066	34.803	1.4	4.0
3	2.243	11172.346	790.787	68.4	91.6
4	7.156	59.992	1.018	0.4	0.1
5	12.036	1681.687	2.873	10.3	0.3
6	21.163	3137.373	31.557	19.2	3.7
	Total	16331.415	863.066	100.0	100.0

Figure D15. Gas chromatography TCD file for the dehydrogenation using 1.0 mM **[Ru(dqn)]** in presence of 10 mmol of formic acid and 15 mmol of sodium formate at 90 °C.

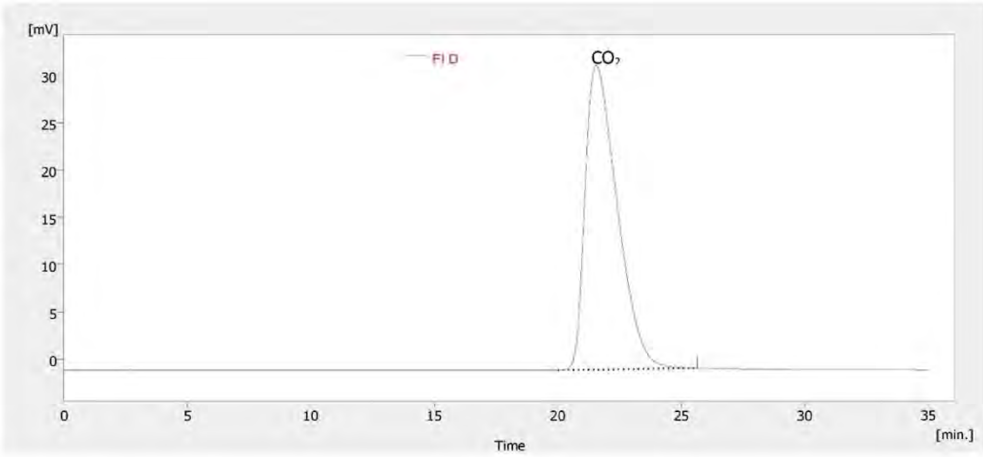

Sample Info:

Sample ID	: Run 1 FID	Amount	0
Sample	: Run FID for NC-100 2	ISTD Amount	0
Inj. Volume [mL]	: 0.1	Dilution	1

Result Table

	Reten. Time [min]	Area [mV.s]	Height [mV]	Area [%]	Height [%]
1	21.552	2917.107	32.209	100.0	100.0
	Total	2917.107	32.209	100.0	100.0

Figure D16. Gas chromatography FID file for the dehydrogenation using 1.0 mM **[Ru(dqn)]** complex in presence of 10 mmol of formic acid and 15 mmol of sodium formate at 90 °C.

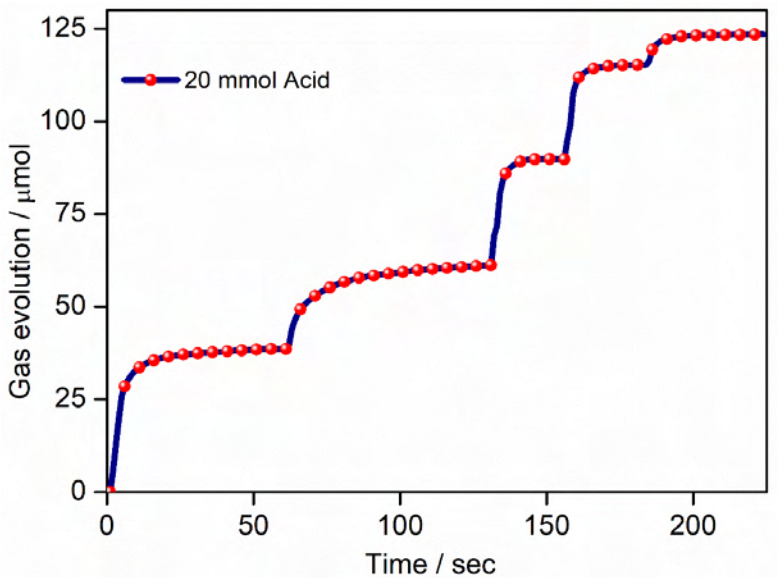

Figure D17. Catalytic cycles for the complex **[Ru(dqn)]** with the iteration of 25 mmol of base in the presence of 1.0 mM complex and 20 mmol formic acid in water at 70 °C.

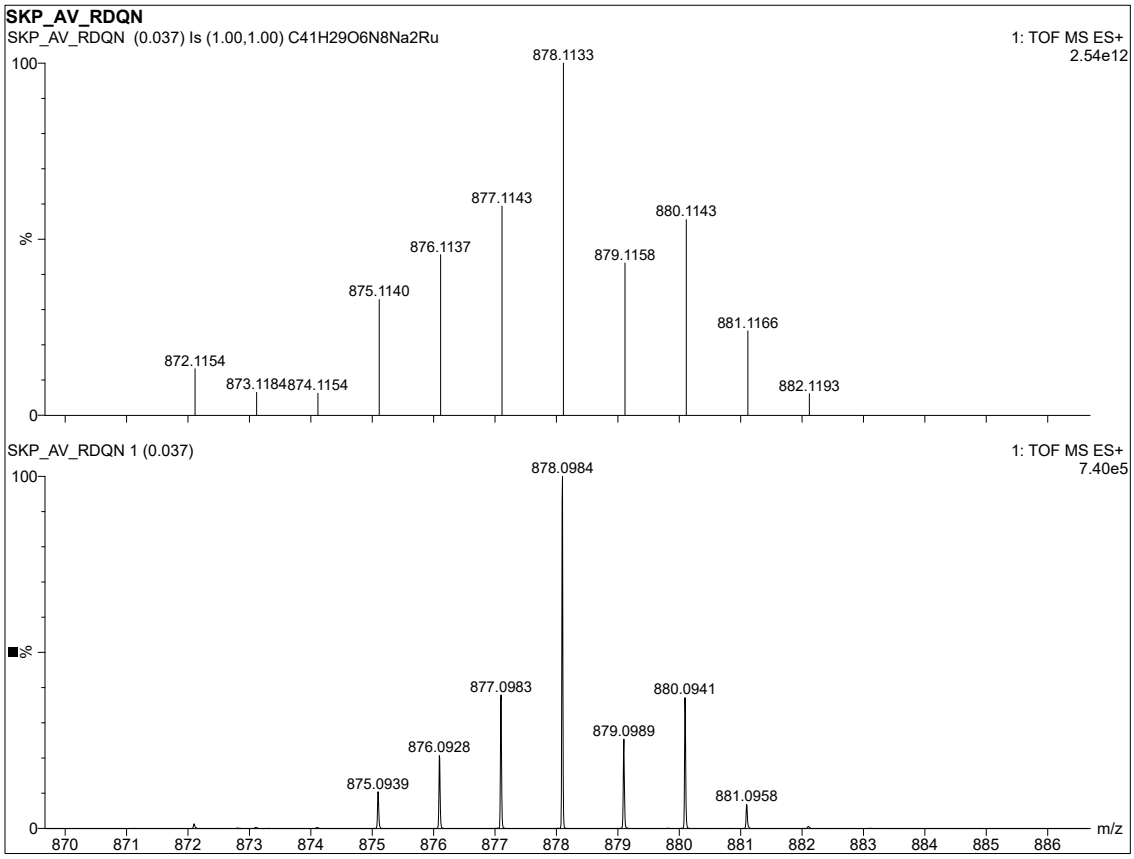

Figure D18. ESI-mass spectra of complex **[Ru(2py-tpy)(DQN)Cl]** with the addition of HCOOH and HCOONa; Calcd. for [Ru(2py-tpy)(DQN)OOCH]+ 2HCOONa]$^{+}$ (m/z 878.1133), Found (m/z = 878.0984).

Table D1. Crystal data and structure refinement for [Ru(dqn)].

Identification code	2112866
Empirical formula	$C_{76}Cl_2F_{18}N_{16}P_3Ru_2H_{54}$
Formula weight	1899.31
Temperature/K	293.2
Crystal system	triclinic
Space group	P-1
a/Å	8.817(7)
b/Å	14.911(11)
c/Å	15.718(14)
α/°	83.06(3)
β/°	73.897(18)
γ/°	74.80(3)
Volume/Å^3	1913(3)
Z	1
ρ_{calc}g/cm^3	1.6483
μ/mm^{-1}	0.628
F(000)	949.7
Radiation	Mo Kα (λ = 0.71073)
2Θ range for data collection/°	11.6 to 49
Index ranges	$-11 \leq h \leq 11$, $-17 \leq k \leq 14$, $-21 \leq l \leq 21$
Reflections collected	11516
Independent reflections	4676 [R_{int} = 0.0490, R_{sigma} = 0.0760]
Data/restraints/parameters	4676/11/524
Goodness-of-fit on F^2	1.071
Final R indexes [I>=2σ (I)]	R_1 = 0.0569, wR_2 = 0.1466
Final R indexes [all data]	R_1 = 0.0753, wR_2 = 0.1629

Table D2. Selected bond lengths for [Ru(dqn)].

Atom	Atom	Length/Å
Ru1	Cl1	2.403(2)
Ru1	N1	2.049(6)
Ru1	N2	1.970(6)
Ru1	N3	2.069(6)
Ru1	N5	2.046(6)
Ru1	N6	2.075(5)

Table D3. Selected Bond Angles for [Ru(dqn)].

Atom	Atom	Atom	Angle/°
N1	Ru1	Cl1	89.63(14)
N2	Ru1	Cl1	84.06(14)
N2	Ru1	N1	79.4(2)
N3	Ru1	Cl1	88.19(13)
N3	Ru1	N1	158.8(3)
N3	Ru1	N2	79.3(3)
N5	Ru1	Cl1	93.39(14)
N5	Ru1	N1	100.9(2)
N5	Ru1	N2	177.44(19)
N5	Ru1	N3	100.3(3)
N6	Ru1	Cl1	170.17(18)
N6	Ru1	N1	95.9(2)
N6	Ru1	N2	104.9(2)
N6	Ru1	N3	89.49(19)
N6	Ru1	N5	77.6(2)

CHAPTER 6

This chapter published in

Vatsa, A. and Padhi, S. K.*, Manuscript under Preparation.

Chapter 6

Dehydrogenation of Formic Acid by Half Sandwich [Ru(η^6-benzene)(L)Cl]$^+$ catalysts: L = 8-Hyroxyquinoline and 8-Hydroxy-2-methyl quinoline

6.1 Introduction

The current climatic conditions face many fluctuations due to the rise in emissions of fossil fuels and other energy sources. These complications in the environment can be minimized by utilizing a clean source of energy. [1] Hydrogen as fuel originated from renewable sources is one of the most convenient energy carriers. Formic acid is the most promising low boiling liquid for storage and acts as a liquid organic hydrogen carrier (LOHCs). Formic acid contains 53g of H_2/Litre.[2-3] Dehydrogenation of formic acid generated hydrogen and carbon dioxide using catalyst under mild conditions. The carbon dioxide produced can be recycled back through the hydrogenation of CO_2. [4-5] For this purpose, developing an effective catalyst for selective generation of H_2 is essential. Huang and group have synthesized a ruthenium complex with *N, N′*-diimine ligand for the decomposition of formic acid. This complex shows a high TON of 350000 and TOF of 12000 h^{-1}. [6] Lei and group studied the dehydrogenation of formic acid in aqueous medium by a [(η^6-arene)RuCl(κ^2-N,N-dmobpy)]$^+$ (where dmobpy = 4,4'-dimethoxy-2,2'-bipyridine). [7] Singh and group have reported a water-soluble [(η6-arene)Ru(κ^2-L)]$^{n+}$ coordinated with pyridine–based ligands for the dehydrogenation of the formic acid in water. This complex shows a TOF of 1548 h^{-1} and the highest TON of 6050. [8] Beller and group have synthesized a ruthenium pincer type complexes Ru(H)(Cl)(CO)(HN{$CH_2CH_2P(iPr)_2$}$_2$) and Ru(H)(Cl)(CO)(CH_3N{$CH_2CH_2P(iPr)_2$}$_2$) and this complex shows highest catalytic activity for the dehydrogenation of formic acid at pH 4.5. [9] Laurenczy and Gonsalvi and group have reported a catalyst $RuCl_3 \cdot 3H_2O$ with monoaryl-biaryl or alkyl-biaryl phosphines and aryl diphosphines bearing sulfonated groups for catalyzing the dehydrogenation of formic acid with the highest TON. [10]

Herein, the synthesis and characterization of [Ru(η^6-benzene)(L)Cl]$^+$ (In complex **1,** L = 2-Methyl 8-hydroxy quinoline and in complex **2**, L = 8-hydroxy quinoline) and its activity towards dehydrogenation of formic acid in the presence of sodium formate as a base are depicted. The catalysis was examined in different acid, base, and complex concentrations and low to high-temperature variations. The decomposition of formic acid was also investigated at different pH.

6.2. Experimental

6.2.1 Material and methods

6.2.1.1. Materials

All the chemicals used in this work were of reagent grade. The benzeneruthenium(II) chloride dimer was purchased from TCI chemicals; 8-Hydroxy-2-methyl quinoline and 8-hydroxy quinolone were purchased from Alfa Aesar used without further purifications. $AgPF_6$ and $NaBF_4$ are purchased from Sigma Aldrich, and NaOH was purchased from Merck. The solvents like acetone, diethyl, petroleum, dichloromethane, methanol, and ethanol were purchased from Merck and dried before use. In all the experiments, Milli-Q- purified distilled water was used.

6.2.1.2. Optical Spectra

All the UV-Visible spectroscopic experiments and analyses were performed with an Agilent Cary 8454 photodiode array UV-Visible spectrophotometer.

6.2.1.3. NMR Spectroscopy and Mass Spectrometry

Proton and ^{13}C NMR spectra were recorded on Bruker Ultrashield spectrometer at room temperature. High-resolution ESI mass spectrometry was recorded with Waters UPLC TQD and Bruker micrOTOF-Q II instruments.

6.2.1.4. Gas Evolution

The evolution of gas was based on manometric results by using 5 mL of double-jacketed reaction vessel containing 2 mL of the reaction mixture and having a headspace volume of 3 mL. The reference cell was filled with 2 mL of water, and 3 mL is headspace volume as of the working cell. The oxygen evolved was converted into micromoles by using the ideal gas equation PV=nRT. The pressure of evolved O_2 was measured using a differential pressure manometer of TESTO 521 with a range of 0 to 100 hPa, 0.1 hPa accuracy was used. The O_2 evolution was tested in the absence and presence of the catalyst using CAN and sodium periodate as an oxidant. The generated O_2 was quantified and detected using an oxygen FOXY sensor probe of NeoFox Ocean Optics with 80 ppm O_2 % resolution in gas and monitored by NeoFox Viewer using NeoFox phase fluorometer systems.

6.2.1.5. X-ray crystallographic analysis

All the suitable single crystals of [Ru(η^6-benzene) (L)Cl] were mounted on a Rigaku SuperNova G8910B EosS2 single-crystal X-ray diffractometer using Mo Kα radiation (λ = 0.71073 Å). The crystal data were collected at 293(2) K. Using Olex2,[11] the structure was solved with the olex2.solve structure solution program using Charge Flipping [12].

6.2.1.6. Gas chromatography analysis

The gas chromatography of the gas evolved during dehydrogenation reactions was recorded on MICHRO-9100 gas chromatograph on Netel (India) Limited.

6.3. Synthesis

6.3.1. Synthesis of [Ru(η^6-benzene)(L)] complex

[Ru(η^6-benzene)Cl_2]$_2$ (100 mg, 0.200 mmol) was dissolved in MeOH / $CHCl_3$ (4:1) solvent mixture and ligands L (L= 2M8hq = 8-Hydroxy-2-methyl quinoline (63 mg, 0.396 mmole) and 8hq = 8-hydroxy quinoline (60 mg, 0.410 mmol) were added to a reaction mixture. The mixture was further stirred for 1.5 hours at 40-45 °C. The solution was filtered with a sintered funnel of fine porosity, and the solvent was evaporated under a vacuum. The solid orange-yellow complex thus obtained was re-precipitated from acetone or MeOH by adding ether/hexane.

[Ru(η^6-benzene) (2M8hq)Cl] **(1)**: Yield: 93 % Calculated mass m/z: 337.48; Found: 338.9599 m/z. 400 MHz ^{1}H NMR (δ, (*J*, Hz), DMSO D_6): 3.172 (3H, s), 5.91 (6H, s), 6.37(1H, s), 6.67-6.76(1H, dd), 7.165 (1H, t, 10), 7.49 (1H, d, 8), 8.11(1H, d, 8). 100 MHz ^{13}C NMR (δ, (*J*, Hz), DMSO D_6): 28.69, 83.69, 110.27, 113.76, 124.35, 128.59, 128.80, 138.04, 144.51, 159.77, and 169.10.

[Ru(η^6-benzene) (8hq)Cl] **(2)**: Yield: 95 % Calculated mass m/z: 323.01; Found: 323.99 m/z. 400 MHz ^{1}H NMR (δ, (*J*, Hz),DMSO D_6): 5.97 (6H, s), 6.70 (1H, t, 10), 6.83 (1H, d, 8), 7.25 (1H,t, 8), 7.49-7.52 (1H, q), 8.25(1H, d, 8), 9.33 (1H, d, 4). 100 MHz ^{13}C NMR (δ, (*J*, Hz), DMSO D_6): 85.22, 124.19, 126.55, 128.49, 128.67, 129.26, 139.26, 140.64, 146.04, and 157.19.

6.4. Results and Discussion

6.4.1. Synthesis

The [Ru(η^6-benzene)(2M8hq)Cl] and [Ru(η^6-benzene)(2M8hq)Cl] complexes were

synthesized (Scheme 6.1) by the reaction of one equivalent of $[Ru(\eta^6\text{-benzene})Cl_2]_2$ dimer complex with two equivalents of 8-Hydroxy-2-methyl quinoline (2M8hq) and 8-hydroxy quinoline (8hq) respectively in 4:1 solvent mixture of MeOH: $CHCl_3$. The reaction was stirred for 1.5 hours at 40-45 °C. The solution was filtered and evaporated under a vacuum. The reddish orange-colored solid obtained was purified from acetone with the addition of ether/hexane. The orange-colored crystals suitable for single-crystal X-ray crystallography were grown in MeOH and isolated after three days.

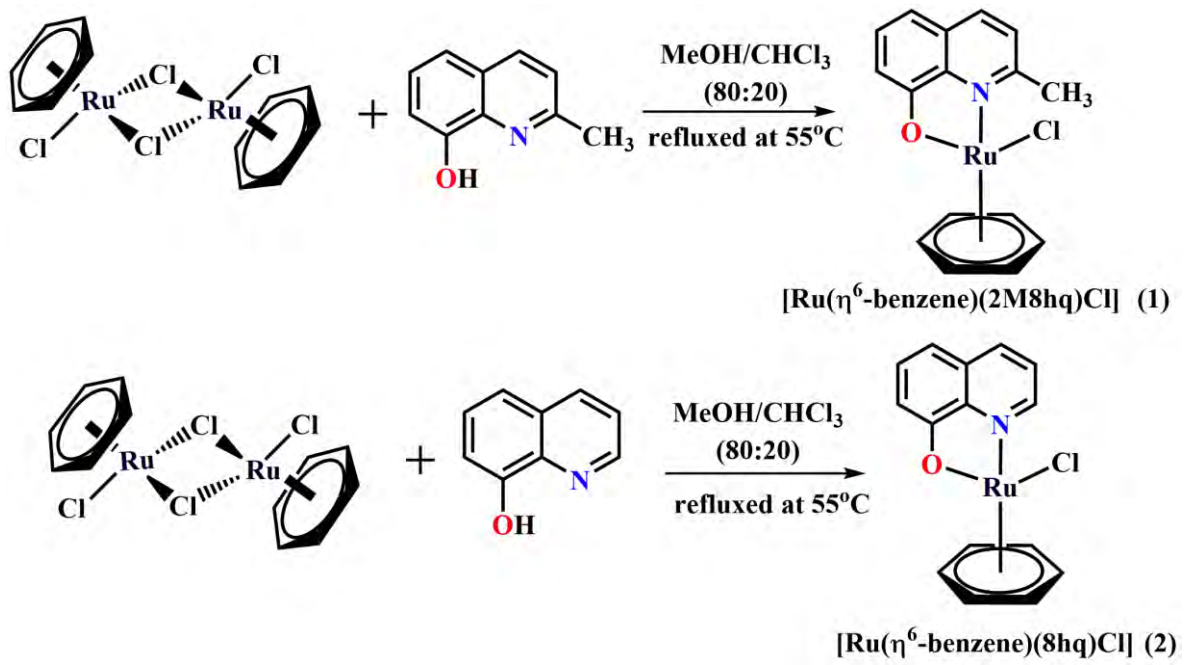

Scheme 6.1 Syntheses of complexes **1** and **2**

6.4.2. Optical Spectra

The optical spectra of complex **1** were studied in the methanol (Figure E1-E2). The complex shows three bands in the UV region at 240 nm, 272 nm, 370 nm, and one band in the visible range at 460 nm. The bands at 240 nm (41666 cm^{-1}, 14963 M^{-1} cm^{-1}) and 272 nm (36764 cm^{-1}, 19360 M^{-1} cm^{-1}) attributed to the $\pi \rightarrow \pi^*$ transition. The band at 370 nm shows $n \rightarrow \pi^*$ transition. The UV-Visible spectra of complex **2** were studied in the MeOH. This complex shows four bands in the UV region at 240 nm, 256 nm, 272 nm, and 395 nm. The band at 240 nm attributed to $\pi \rightarrow \pi^*$ transition and band at 256 nm attributed to forbidden $\pi \rightarrow \pi^*$ transition to a homonuclear excited state of benzene moiety. The bands at 272 nm and 395 nm are attributed to $n \rightarrow \pi^*$ transitions. The band at 460 nm corresponds to MLCT transition.

6.4.3. NMR and Mass Spectra

The NMR spectra of complexes **1** and **2** were performed in DMSO-d_6 (Figure E3-E4). The ^{1}H NMR of complex **1** shows one singlet for six hydrogens of benzene moiety at 5.91 ppm and one singlet for methyl group at 3.172 ppm. One triplet, two doublets, and one doublet of doublets were observed for the quinoline moiety. The ^{13}C NMR of the complex shows one carbon at 28.69 ppm for a methyl group, six carbons for benzene moiety, and 9 carbons of the quinoline moiety. The ^{1}H NMR of complex **2** shows one singlet for six hydrogens of benzene moiety at 5.97 ppm. The complex shows three doublets, two triplets, and one quartet for the hydrogens of quinoline moiety. The ^{13}C NMR shows 6 carbons for benzene moiety and 9 carbons for quinoline moiety (Figure E5-E6). The mass spectra of both complexes **1** and **2** were recorded in MeOH. The calculated and observed mass for complex **1** are $[C_{16}H_{14}NORuCl]^+$ $[[Ru(\eta^6\text{-benzene})(2M8hq)Cl]\text{-}Cl]^+$ m/z 337.48 and m/z 338.0 respectively. The calculated and observed mass for complex **2** are $[C_{15}H_{12}NORuCl]^+$ $[[Ru(\eta^6\text{-benzene})(8hq)Cl]\text{-}Cl]^+$ m/z 323.46 and m/z 323.99 respectively (Figure E7-E8).

6.4.4. X-ray crystal structure

The single-crystal X-ray structure for $[Ru(\eta^6\text{-benzene})(L)Cl]$ (L = 8-Hydroxy-2-methyl quinoline or 8-Hydroxy quinoline) was determined by Rigaku SuperNova G8910B EosS2 single-crystal X-ray diffractometer. The perspective views of the neutral complexes **1** and **2** are displayed in Figure 6.1. The crystallographic data and the refinement parameters are provided in Tables E1 to E6. Complex **1** crystallizes in a triclinic P-1 space group, whereas complex **2** belongs to a monoclinic P21/c space group. The asymmetric unit of **1** consists of a neutral $[Ru(\eta^6\text{-benzene})(2M8hq)Cl]$ molecule. In this case, the Ru-center has three π-coordinations by benzene ring, two σ-coordinations by 2M8hq ligand, and another σ-coordination by a chloride ion. Overall a six-coordinations are there at the Ru-center. The π-coordinations by the benzene ring spans from 2.161 to 2.213 Å. Out of the two σ-coordinations by 2M8hq ligand, Ru-O (2.052 Å) is shorter than the Ru-N (2.142 Å). The σ-coordination by the chloride ion, i.e., Ru-Cl (2.416 Å), is the longest among all the coordinations. The bite angle generated by ∠N-Ru-O is 79.55°. In complex **2** the asymmetric unit consists of a neutral molecule of $[Ru(\eta^6\text{-benzene})(8hq)Cl]$. In $[Ru(\eta^6\text{-benzene})(8hq)Cl]$, the coordination pattern is almost very similar to that of $[Ru(\eta^6\text{-benzene})(2M8hq)Cl]$. The π-coordinations by the benzene ring at the Ru-center in complex **2** spans from 2.140 to 2.175 Å. Out of the two σ-coordinations by 8hq ligand, Ru-O (2.048 Å) is shorter than the Ru-N (2.097 Å). Alike complex **1**, the σ-

coordination by the chloride ion, i.e., Ru-Cl (2.428 Å), is the longest one among all the coordinations. The bite angle generated by ∠N-Ru-O in complex **2** by 8hq ligand is 78.60°.

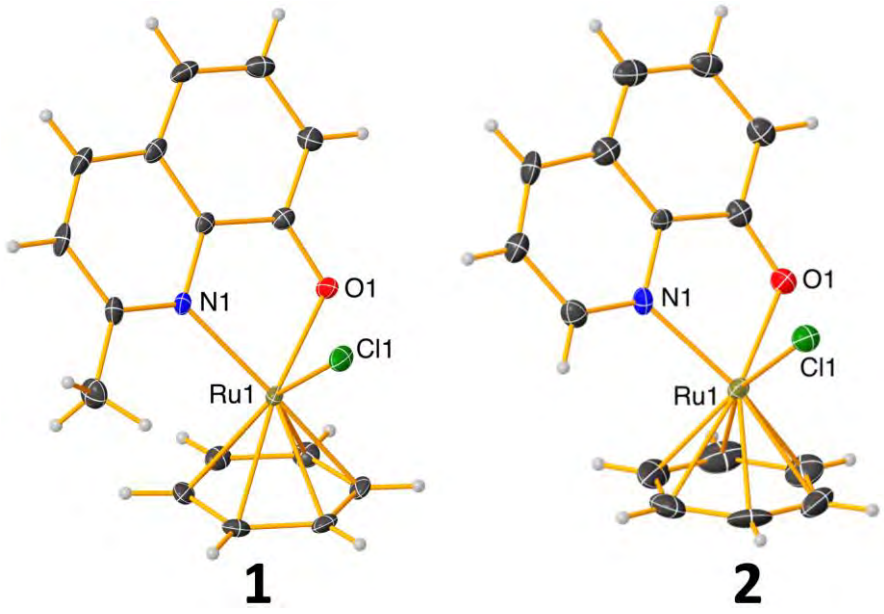

Figure 6.1. ORTEP of complexes **1** and **2**.

6.4.5. Dehydrogenation reactions

The dehydrogenation of the formic acid catalyzed by complexes **1** and **2** were studied in deionized water using sodium formate as the base. The reaction was conducted in the double-jacketed reaction vessel using a rubber septum through which acid was injected into the reaction mixture. The evolution of H_2 gas and CO_2 gas was monitored through a differential pressure manometer. The kinetics of the reaction was investigated by varying the concentration of the acid, base, complex, and at different temperatures. For complex **1**, the acid concentration ranged from 10 mmol to 25 mmol in the presence of a 1.0 mM catalyst and 15 mmol of sodium formate as the base at 70 °C (Figure E9). In the case of acid variation, the reaction rate is independent of the concentration of the acid. The volume of gas increases with an increase in the concentration of the acid at the same rate. Complex **1** shows the highest TON of 54 for 25 mmol of acid and the lowest TON of 25 for 10 mmol of acid. The concentration of base was varied from 1 mmol to 25 mmol using 1.0 mM of the catalyst with 10 mmol of acid at 70 °C (Figure 6.2 (a) - 6.2(b)). The lowest TOF of 0.108 s^{-1} was observed for the 1 mmol base and the highest TOF of 0.166 s^{-1} for 25 mmol of the base. The catalyst shows an increase in gas evolution when the base concentration increases from 1 mmol to 25 mmol until the decomposition of the formic acid that indicates the rate of reaction follows the first-order

kinetics having rate constant k = 0.20 x 10^{-2} µmol s^{-1}. In another set of reactions, complex concentration was varied from 0.25 mM to 1.0 mM, keeping the acid and base constant at 10 mmol and 15 mmol respectively at 70 °C (Figure E10). The highest TON of 24 for 1.0 mM of catalyst and the lowest of 12 was observed for 0.25 mM of the catalyst. As the concentration of complex increases from 0.25 mM to 1.0 mM, the reaction rate increases, thus indicating the first-order kinetics with a rate constant k = 8.56 x 10^{-2} µmol s^{-1}. To study the effect of temperature on the reaction rate, the dehydrogenation of formic acid was examined at different temperatures. The temperature of the reaction was varied from 25 °C to 70 °C in the presence of 10 mmol of formic acid, 15 mmol of sodium formate, and 1.0 mM of the complex (Figure 6.2(c) – 6.2(d)). The evolution of gas increases with an increase in the temperature, with the highest TOF of 0.147 s^{-1}. This shows that the catalyst follows the first-order rate kinetics with temperature variation with the rate constant k = 0.21 x 10^{-2} µmol s^{-1}.

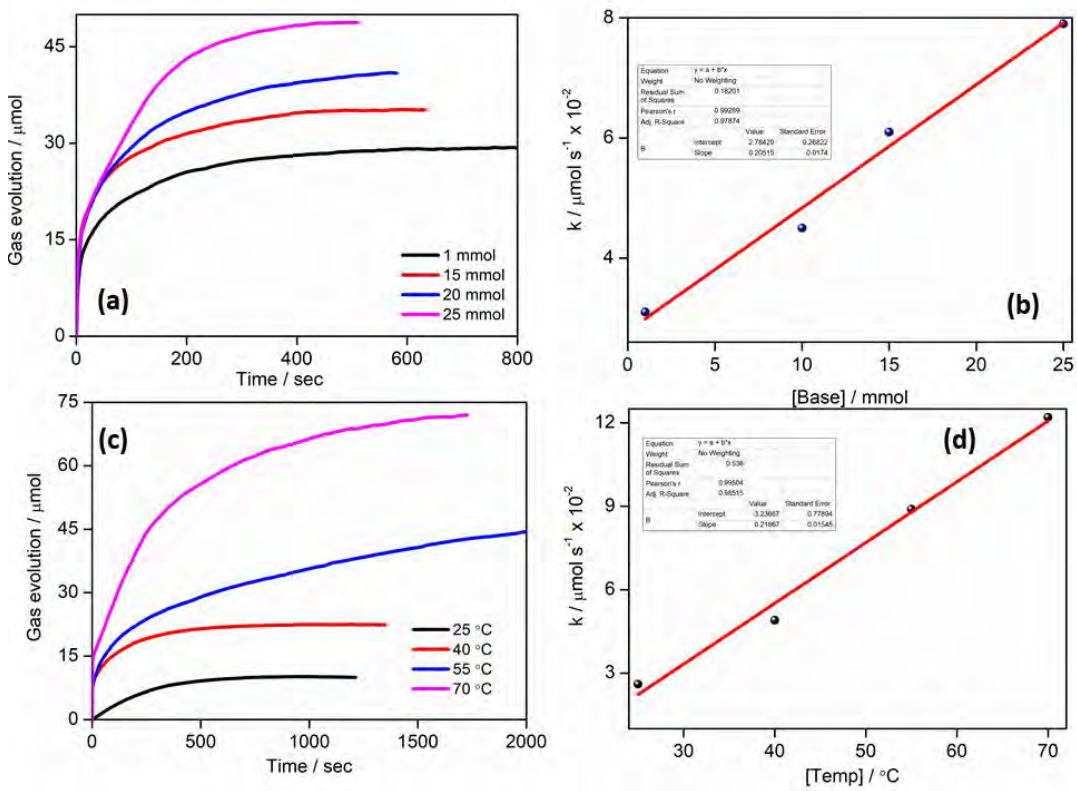

Figure 6.2. (a) Gas evolution by complex 1 with various base concentrations in the presence of 1.0 mM of complex and 10 mmol of the acid at 70 °C in water. (b) Rate of gas evolution *vs.* base in water. (c) Gas evolution by complex 1 with the variation of temperature in the presence of 1.0 mM of complex, 15 mmol of the base, and 10 mmol of acid in water. (d) Rate of gas evolution *vs.* temperature in water.

Table 6.1. Summary of experiments in different reaction conditions for dehydrogenation of formic acid for complex **1**

Temperature / °C	Catalyst / [mM]	Acid / [mmol]	Base [mmol]	TON	Initial TOF / s^{-1}	The volume of Gas evolved / µmol
70	1.0	10	15	25	0.137	49
70	1.0	15	15	33	0.114	66
70	1.0	20	15	42	0.152	82
70	1.0	25	15	54	0.184	108
70	1.0	10	1	15	0.108	29
70	1.0	10	10	18	0.14	35
70	1.0	10	15	20	0.16	41
70	1.0	10	20	24	0.17	49
70	0.25	10	15	12	0.08	24
70	0.50	10	15	17	0.10	34
70	0.75	10	15	20	0.115	40
70	1.0	10	15	24	0.145	49
25	1.0	10	15	5	0.015	10
40	1.0	10	15	12	0.072	22
55	1.0	10	15	22	0.092	44
70	1.0	10	15	35	0.147	72

Similarly, for complex **2** the reaction kinetics for catalyzing the dehydrogenation of formic acid was studied by varying the concentration of the acid, base, and complex and changing the temperature from lower to higher. The acid concentration was varied from 10 mmol to 25 mmol at 70 °C in the presence of 1.0 mM of the complex by keeping the concentration of base constant at 15 mmol in deionized water (Figure 6.3(a)-6.3(b)). The highest TOF of 0.172 s^{-1} was observed for the 25 mmol of acid and the lowest TOF of 0.05 s^{-1} for 10 mmol of acid. The gas evolution increases with an increase in the acid concentration, and the rate of reaction follows the first-order kinetics having a rate constant k = 0.81 x 10^{-2} µmol s^{-1}. In the next set of reactions, the base concentration was varied from 1 mmol to 25 mmol by keeping the concentration of acid constant at 10 mmol in the presence of 1.0 mM of the complex at 70 °C (Figure E11). The catalyst shows the highest reaction rate, with a 25 mmol base having a TOF of 0.172 s^{-1}. The rate of reaction for base variation increases with the increase in the base concentration. It follows the first-order reaction kinetics by showing the dependence on the concentration of the base having rate constant k = 0.37 x 10^{-2} µmol s^{-1}. The dependence of the rate of reaction on the concentration of the complex was studied by varying the concentration of the complex from 0.25 mM to 1.0 mM by keeping the concentration of base and acid

constant at 15 mmol and 10 mmol respectively at 70 °C (Figure 6.3(c)-6.3(d)). The lowest TON of 8 was observed for the 0.25 mM complex and the highest of 24 for the 1.0 mM complex. The rate of reaction increases by increasing the concentration of the catalyst and follows the first order with rate constant k = 9.62 x 10^{-2} µmol s^{-1}. The complex shows a rise in the reaction rate by varying the temperature from 40 °C to 85 °C in the presence of 1.0 mM complex using 10 mmol of acid and 15 mmol of base (Figure E12). The reaction rate depends on the temperature following the first-order kinetics having a rate constant k = 0.21 x 10^{-2} µmol s^{-1}. The gas evolved was also quantified from the gas chromatography analysis (Figure E13-E16).

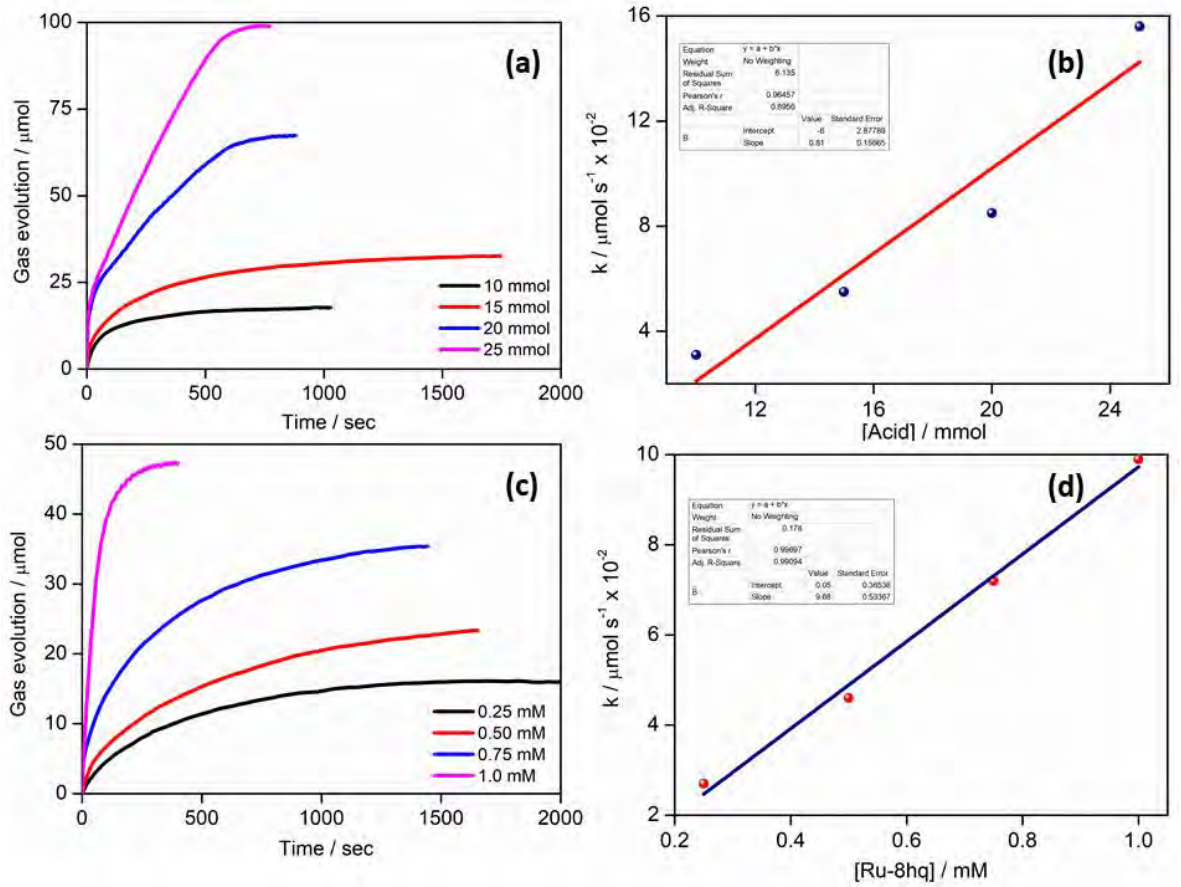

Figure 6.3. (a) Gas evolution by complex **2** with a variety of acid concentrations in the presence of 1.0 mM of complex and 15 mmol of the base at 70 °C in water. **(b)** Rate of gas evolution *vs.* acid in water. **(c)** Gas evolution by complex **2** with the variation of complex concentration in the presence of 15 mmol of the base and 10 mmol of acid in water. **(d)** Rate of gas evolution *vs.* complex concentration in water.

Table 6.2. Summary of experiments in different reaction conditions for dehydrogenation of formic acid for complex **2**

Temperature / °C	Catalyst / [mM]	Acid / [mmol]	Base [mmol]	TON	Initial TOF / s^{-1}	The volume of Gas evolved / µmol
70	1.0	10	15	9	0.05	18
70	1.0	15	15	16	0.078	32
70	1.0	20	15	34	0.144	63
70	1.0	25	15	49	0.172	99
70	1.0	10	1	16	0.058	31
70	1.0	10	10	22	0.117	44
70	1.0	10	15	25	0.132	49
70	1.0	10	20	35	0.172	71
70	0.25	10	15	8	0.023	16
70	0.50	10	15	12	0.032	23
70	0.75	10	15	18	0.071	35
70	1.0	10	15	24	0.194	46
25	1.0	10	15	6	0.037	13
40	1.0	10	15	14	0.109	27
55	1.0	10	15	24	0.140	48
70	1.0	10	15	29	0.245	58

6.4.6. Activation Parameters

The activation energy for the dehydrogenation of formic acid was calculated from the Arrhenius plot, which comprises the logarithm of the reaction rate constant *k* plotted for reciprocal of absolute temperature 1/T to calculate activation energy E_a using the equation (6.1).

$$\boldsymbol{ln\, k = -\frac{E_a}{RT} + ln\, A} \qquad \textbf{(6.1)}$$

Where A = pre-exponential factor and R = gas constant. [13] For the complex **1**, the initial rates of dehydrogenation of formic acid obtained from different temperatures varied from 298 K to 343 K and the log of initial rate vs. 1/T plot in the presence of 1.0 mM **1**,10 mmol of formic acid, and 15 mmol of the base, the activation energy was calculated from the slope of the Arrhenius plot, i.e., E_a / R and estimated to be 29.81 kJ/mol by taking R = 8.3145 J K^{-1} mol^{-1} and slope = -3585.31. In complex **2**, the temperature was varied from 313 K to 358 K, and the activation energy was found to be 29.83 kJ/mol with a slope of -3588.20. The Eyring plot is

the plot of the logarithm of k/T plotted against reciprocal absolute temperature 1/T for determining the thermodynamical parameters like $\Delta H^{\ddagger}$ enthalpy, $\Delta S^{\ddagger}$ entropy, and $\Delta G^{\ddagger}$ free energy. [14] The Eyring plot is based on the Eyring – Polanyi equation (6.2). Where, k = reaction rate constant, T = absolute temperature in K, R = gas constant, k_B = Boltzmann's constant, $\Delta H^{\ddagger}$ = enthalpy of activation and $\Delta S^{\ddagger}$ = entropy of activation. In the Eyring plot, slope $=\frac{-\Delta H^{\ddagger}}{R}$ and intercept = $ln\frac{k_B}{h} + \frac{\Delta S^{\ddagger}}{R}$.

$$ln\frac{k}{T} = \frac{-\Delta H^{\ddagger}}{R} . \frac{1}{T} + ln\frac{k_B}{h} + \frac{\Delta S^{\ddagger}}{R} \qquad \textbf{(6.2)}$$

For complexes **1** and **2,** the slope is respectively found to be -3282.42 and -3271.66; the enthalpy $\Delta H^{\ddagger}$ is calculated to be 27291.58 J K^{-1} mol^{-1} for **1** and 27202.11 for **2**. The entropy of activation $\Delta S^{\ddagger}$ is estimated to be -184.76 J K^{-1} mol^{-1} having intercept = 1.536 for the complex **1,** and $\Delta S^{\ddagger}$ is calculated to be -187.11 J K^{-1} mol^{-1} with an intercept of 1.254. From the values of $\Delta H^{\ddagger}$ and $\Delta S^{\ddagger}$, Gibbs free energy can be calculated from the equation (6.3).

$$\Delta G^{\ddagger} = \Delta H^{\ddagger} - T\Delta S^{\ddagger} \qquad \textbf{(6.3)}$$

By putting the value of $\Delta H^{\ddagger}$ and $\Delta S^{\ddagger}$ in the above equation, the $\Delta G^{\ddagger}$ is calculated to be 90 kJ for complex **1** and 82.96 kJ for complex **2** at 298 K (Figure 6.4(a) – 6.4(b)). The parameters are tabulated in Tables 6.3 and 6.4.

Table 6.3. Calculations for Arrhenius plot and Eyring plot for complex **1**

Temperature / °C	Temperature /K	$\frac{1}{T}$	$ln\ k$	$ln\frac{k}{T}$
25	298	0.00336	-3.699	-9.408
40	313	0.00319	-3.240	-8.987
55	328	0.00305	-2.852	-8.650
70	343	0.00292	-2.064	-7.904

Table 6.4. Calculations for Arrhenius plot and Eyring plot for complex **2**

Temperature / °C	Temperature /K	$\frac{1}{T}$	$ln\ k$	$ln\frac{k}{T}$
40	313	0.00319	-3.4561	-9.2379
55	328	0.00304	-2.9132	-8.9380
70	343	0.00291	-2.2990	-8.8724
85	358	0.00279	-2.07688	-8.7384

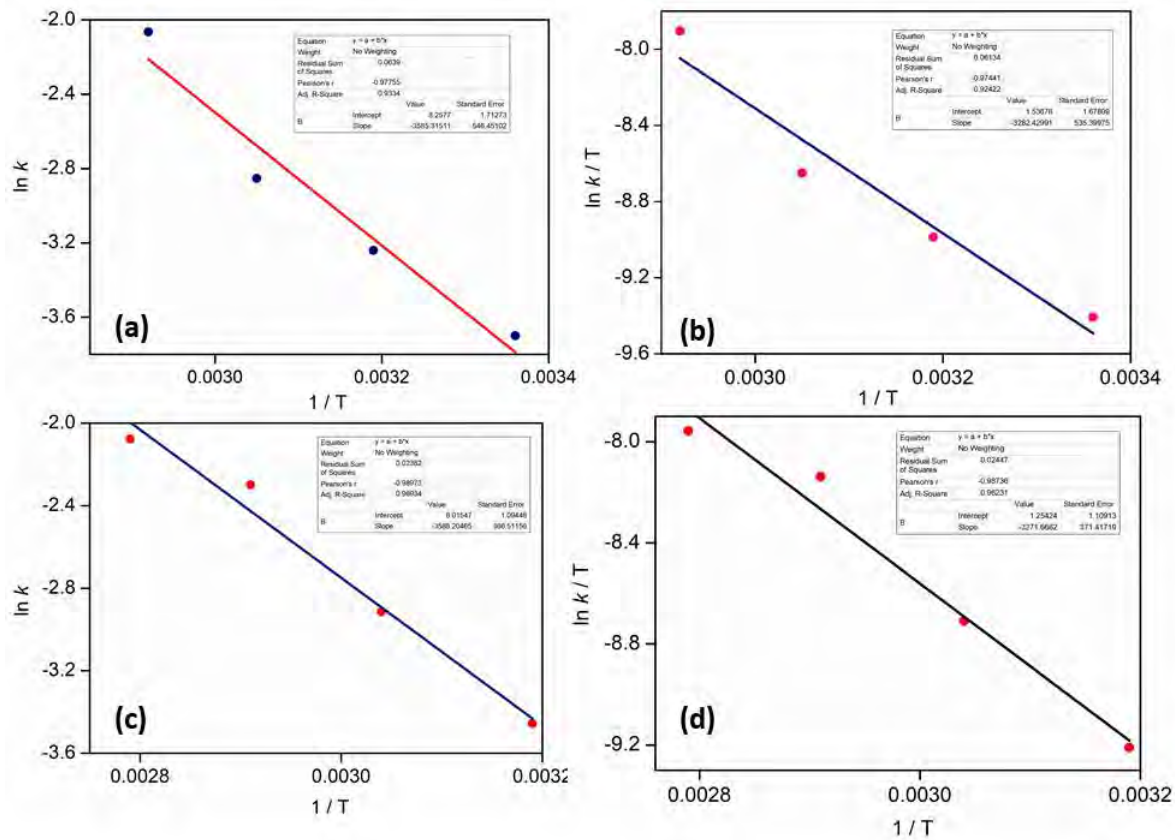

Figure 6.4. (a) Arrhenius plot for complex **1** to estimate the activation energy **(b)** Eyring plot for complex **1** to estimate the $\Delta H^{\ddagger}$, $\Delta S^{\ddagger}$, and $\Delta G^{\ddagger}$. **(c)** Arrhenius plot for complex **2** to calculate the activation energy (d) Eyring plot for complex **2** to estimate the $\Delta H^{\ddagger}$, $\Delta S^{\ddagger}$, and $\Delta G^{\ddagger}$.

6.4.7. pH variation for the decomposition of formic acid

The dehydrogenation reactions depend on the pH of the solution for the evolution of hydrogen gas efficiently. The dehydrogenation of formic acid was preferably performed in the water as solvent as it triggers the formation of hydronium ions (H_3O^+) and metal hydride. [15-16] To confirm the dependence of the rate of dehydrogenation reaction on the pH, the dehydrogenation reactions were performed in different pH from pH 2.0 to 11.0 in the presence of 1.0 mM of catalyst **1** and **2** using 15 mmol of sodium formate as a base with 10 mmol of acid at 70 °C and 85 °C respectively in phosphate buffer. Complex **1** shows an increase in TOF from pH 2.0 to 7.0, and the TOF value decreases in the basic medium and becomes very small at highly basic pH. The TOF increases from 0.02 s^{-1} at pH 2.0 to 0.033 s^{-1} at pH 6.0. The TOF highest TOF of 0.057 s^{-1} was observed for the pH 7.0. The TOF decreases to 0.032 s^{-1} at pH 8.0 and becomes 0.011 s^{-1} at highly basic pH 11.0. This shows that the complex efficiently catalyzes the dehydrogenation of formic acid at neutral pH and in deionized water. In the case of complex

2, the dehydrogenation of formic acid was not favorable at a highly acidic and highly basic medium with a very low reaction rate. The highest TOF of 0.1758 s^{-1} was observed at pH 7.0, and the TOF value decreases towards the basic pH with TOF of 0.016 s^{-1} at pH 11.0 (Figure 6.5(a)-(b)). For both the complexes, neutral pH 7.0 is most suitable for efficiently catalyzing the dehydrogenation of the formic acid. In the highly acidic, the complex may be decomposed and doesn't show catalytic activity. The formation of metal hydroxide under highly basic pH reduces the formation of metal hydride and hydronium ions which causes a decrease in the rate of the reaction.

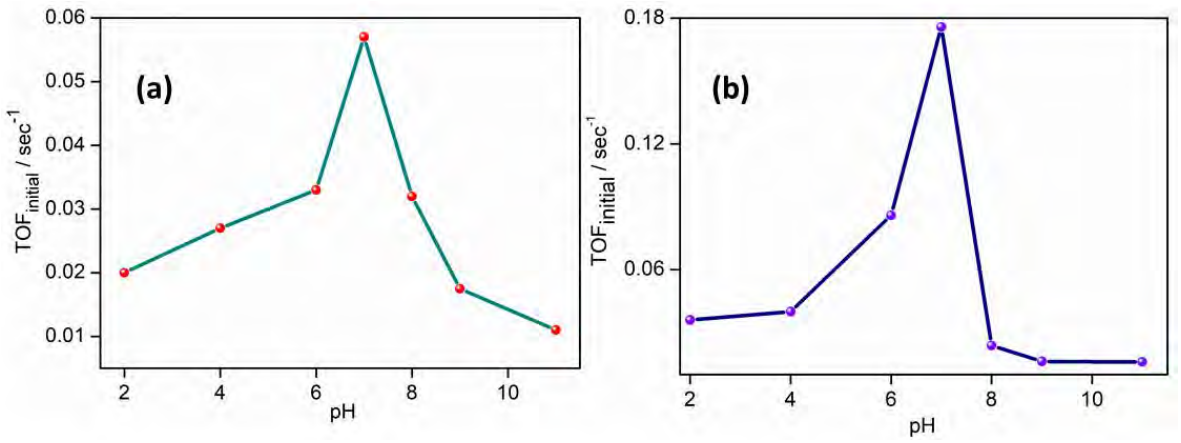

Figure 6.5. (a) pH dependence of the initial TOF for the decomposition of formic acid with 1.0 mM **1**, 10 mmol formic acids, and 15 mmol sodium formate in phosphate buffer at 70 °C **(b)** pH dependence of the initial TOF for the decomposition of formic acid with 1.0 mM **2**, 10 mmol formic acids, and 15 mmol sodium formate in phosphate buffer at 85 °

6.4.8. Stability of the catalyst

The stability of the catalysts **1** and **2** for the dehydrogenation of the formic acid was determined by the iterative addition of the 20 mmol of acid and 25 mmol of the base in separate reactions in the presence of 1.0 mM of the catalyst concentration in deionized water at 70 °C. For complex **1**, the dehydrogenation of formic acid was studied at 70 °C, in the presence of 1.0 mM of complex, 25 mmol of sodium formate as a base, and 20 mmol of acid added iteratively after the completion of each cycle (Figure 6.6). Complex **1** shows reproducibility up to 4 cycles with a TON of 98. Similarly, in another set of reactions, 25 mmol of the base was added iteratively when the response completes in the presence of 20 mmol of formic acid using 1.0 mM of the complex in deionized water at 70 °C. Complex **1** shows stability up to four cycles with a TON of 48 (Figure E17).

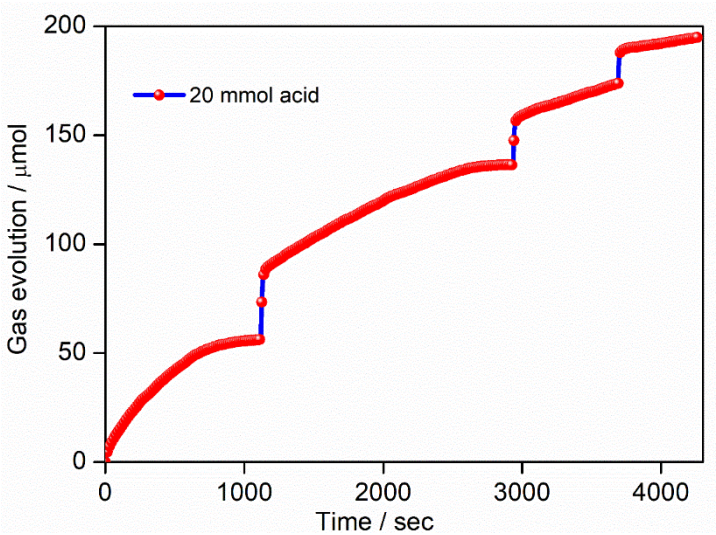

Figure 6.6. Catalytic cycles for **1** with the iteration of 20 mmol of acid in the presence of 1.0 mM complex and 25 mmol bases in deionized water at 70 °C.

In another experiment, the stability of the complex **2** towards the dehydrogenation of formic acid was studied firstly by repetitive addition of 20 mmol of formic acid and then with 25 mmol of sodium formate. In the first set of reactions, 20 mmol of acid are added sequentially until the reaction completes. The complex shows stability up to 4 cycles with a TON of 66 (Figure 6.7). In a similar condition, the 25 mmol of the base was added repetitively after completion of each cycle in the presence of 20 mmol of formic acid and 1.0 mM of the complex. The catalyst shows stability up to 4 cycles with a TON of 43 (Figure E18).

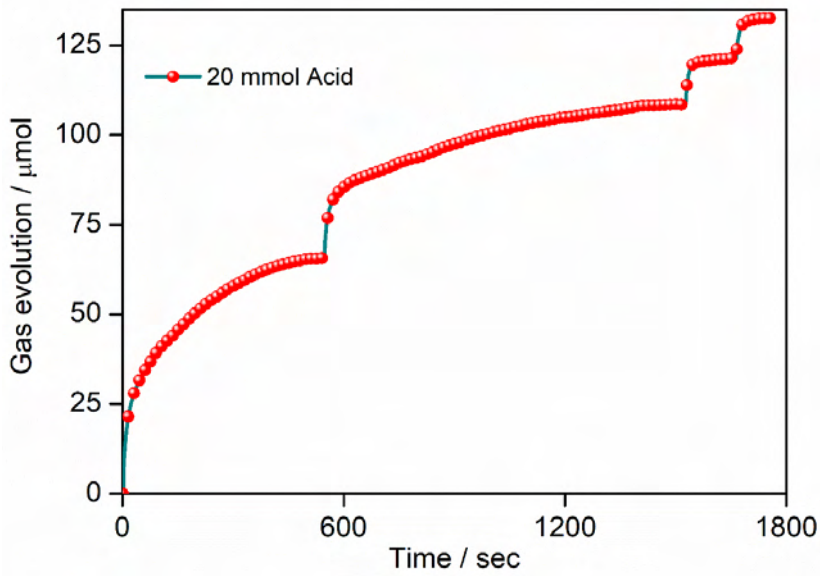

Figure 6.7. Catalytic cycles for **2** with the iteration of 20 mmol of acid in the presence of 1.0 mM complex and 25 mmol bases in water at 70 °C.

6.5 Plausible Mechanism

The plausible mechanism (Scheme 6.2) for the dehydrogenation of HCOOH has been predicted considering the experimental results. Complexes **1** and **2** contain a labile σ-coordinated chloride ion (**[A]**), which in the presence of H_2O generates the corresponding aqua-complex (**[B]**). The ESI-mass spectra (Figures E19-E20) of the complexes **1** and **2** in the presence of HCOOH and HCOONa in an aqueous solution reveal the formation of the coordinated formate complex **[C]**. The ESI-mass spectra of complex **1** with the addition of HCOOH and HCOONa; calculated for [Ru(η^6-benzene)(2M8hq)OOCH]+ HCOONa] + H^+ (m/z 452.005), and found at (m/z = 451.9497). In the case of complex **2** with the addition of HCOOH and HCOONa, the ESI-mass spectra calculated for [Ru(η^6-benzene)(8hq)OOCH] + Na^+ (m/z 391.9841), and found at (m/z = 391.9792).The formate complex undergoes a rearrangement reaction to generate the Ru-H complex (**[D]**), with the release of CO_2. The NMR spectra of the Ru-H species (**[D]**) (Figures E21-E22) in complexes **1** and **2** confirm the formation of hydride species, wherein the ^{1}H NMR of Ru-H peak was observed at -7.11 ppm for **1** and -7.14 ppm for **2** in D_2O. In the presence of the acidic aqueous condition, the Ru-H complex (**[D]**) releases H_2 and reverts to aqua-complex (**[B]**).

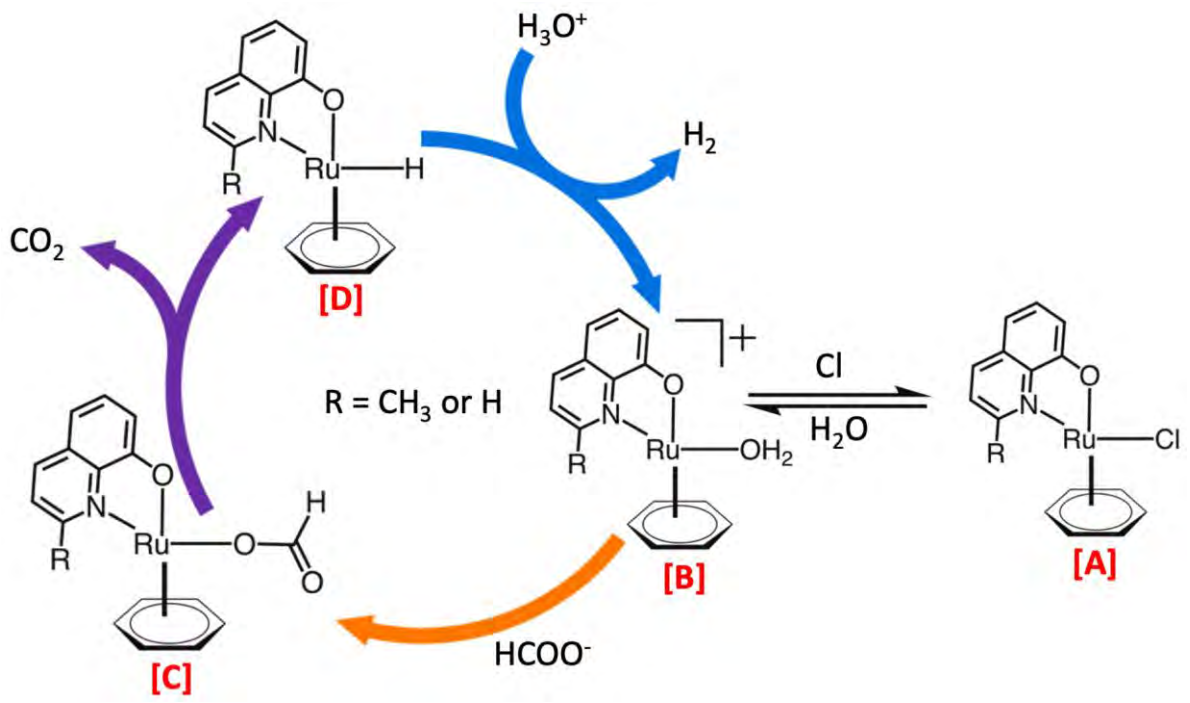

Scheme 6.2. A plausible mechanism for the catalytic cycles for complexes **1** and **2**.

6.6 Summary

The two complexes $[Ru(\eta^6\text{-benzene})(L)Cl]^+$ (In complex **1,** L = 2-Methyl 8-hydroxy quinoline and in complex **2**, L **=** 8-hydroxy quinoline) were synthesized and characterized by different spectroscopic techniques. These complexes were utilized for the dehydrogenation of formic acid in sodium formate as a base in deionized water. The catalytic activity towards dehydrogenation of formic acid was compared between complexes **1** and **2**. For studying the kinetics of the dehydrogenation reaction, the reactions were performed with various concentrations of acid, base, and complex and by varying the temperature. The dehydrogenation of formic acid was also studied at different pH from highly acidic to highly basic medium. The dehydrogenation of formic acid at different temperatures reveals that the activation energy required for formic acid's dehydrogenation was 29.81 kJ / mol. $\Delta G^{\ddagger}$ was estimated to be 90 kJ for complex **1,** and activation energy E_a required for the dehydrogenation of formic acid was 29.83 kJ / mol, and $\Delta G^{\ddagger}$ was found to be 83 kJ for complex **2**. The composition of gas was examined from the TCD and FID detectors of the Gas Chromatograph. The catalytic stability of the complex towards dehydrogenation was examined by the repetitive addition of formic acid and sodium formate in a different set of reactions.

6.7 References

1. Solomona, S.; Plattnerb, G.-K.; Knuttic, R.; Friedlingstein, P. Irreversible climate change due to carbon dioxide emissions, *Proc. Natl. Acad. Sci. U.S.A.* **2009**, *106* (6), 1704-1709.
2. Felderhoff, M.; Weidenthaler, C.; Helmolt, R. V.; Eberle, U.; Hydrogen storage: the remaining scientific and technological challenges. *Phys. Chem. Chem. Phys.* **2007**, *9* (21), 2643 – 2653.
3. Moriarty, P.; Honnery, D. A hydrogen standard for future energy accounting? *Int. J. Hydrogen Energy*. **2010**, *35* (22) 12374-12380.
4. Suh, M. P., Park, H. J.; Prasad, T. K.; Lim, D.-W. Hydrogen Storage in Metal_Organic Frameworks. *Chem. Rev.* **2012**, *112* (2), 782–835.
5. Guo, J.; Li, X.; Yao, H.; Yin, C.; Zhong, D.; Wang, Y.; QI, T.; Liu, G.; Shen, L.; Zhou, Q.; Peng, Z. Formic acid as a potential on-board hydrogen storage method development of homogeneous noble-metalcatalysts for the dehydrogenation reactions. *ChemSusChem*. **2021**, *14* (13) 2655-2681.
6. Guan, C.; Zhang, D.-D.; Pan, Y.; Iguchi, M.; Ajitha, M. J.; Hu, J.; Li, H.; Yao, C.; Huang, M.-H.; Min, S.; Zheng, J.; Himeda, Y.; Kawanami, H.; Huang, K.-W. Dehydrogenation of Formic Acid Catalyzed by a Ruthenium Complex with an N,N′-Diimine Ligand. *Inorg. Chem.* **2017**, *56* (1) 438 - 445.
7. Luo, C.; Li, L.; Yue, X.; Li, P.; Zhang, L.; Yang, Z.; Pu, M.; Cao, Z.; Lei, M. pH-Dependent transfer hydrogenation or dihydrogen release catalyzed by a [(η^6-arene)RuCl(k^2-N,N-dmobpy)]$^+$ complex: a DFT mechanistic understanding. *RSC Adv.* **2020** *10* (18), 10411–10419.
8. Patra, S.; Singh, S. K. Hydrogen Production from Formic Acid and Formaldehyde over Ruthenium Catalysts in Water. *Inorg. Chem*. **2020**, *59* (7), 4234−4243.
9. Agapova, A.; Alberico, E.; Kammer, A.; Junge, H.; Beller, M. Catalytic Dehydrogenation of Formic Acid with Ruthenium-PNP-Pincer Complexes: Comparing N-Methylated and NH-Ligands. *ChemCatChem*. **2019**, *11* (7), 1910 - 1914.
10. Guerriero, A.; Bricout, H.; Sordakis, K.; Peruzzini, M.; Monflier, E.; Hapiot, F.; Laurenczy, G.; Gonsalvi, L. Hydrogen production by selective dehydrogenation of HCOOH catalyzed by Ru-Biaryl Sulfonated Phosphines in aqueous solution. *ACS Catalysis*, **2014** *4* (9), 3002-3012.
11. Boddien, A.; Mellmann, D.; Gartner, F.; Jackstell, R.; Junge, H.; Dyson, P. J.; Laurenczy, G.; Ludwig, R.; Beller, M.; Efficient Dehydrogenation of Formic Acid Using an Iron

Catalyst. *Science*. **2011**, *333* (6050), 1733−1736.

12. Eyring, H.; Polanyi, M.; On Simple Gas Reactions. *Z. Phys. Chem. B.* **1931**, 12, 279.
13. Wang, W.-H.; Ertem, M. Z.; Xu, S.; Onishi, N.; Manaka, Y.; Suna, Y.; Kambayashi, H.; Muckerman, J. T.; Fujita, E.; Himeda, Y. Highly Robust Hydrogen Generation by Bio-Inspired Ir Complexes for Dehydrogenation of Formic Acid in Water: Experimental and Theoretical Mechanistic Investigations at Different pH. *ACS Catal*. **2015** *5* (9), 5496–5504.
14. Onishi, N.; Ertem, M. Z.; Xu, S.; Tsurusaki, A.; Manaka, Y.; Muckerman, J. T. ; Fujita, E.; Himeda, Y. Direction to practical production of hydrogen by formic acid dehydrogenation with Cp*Ir complexes bearing imidazoline ligands. *Catal. Sci. Technol.* **2016**, *6* (4), 988-992.

Appendix E

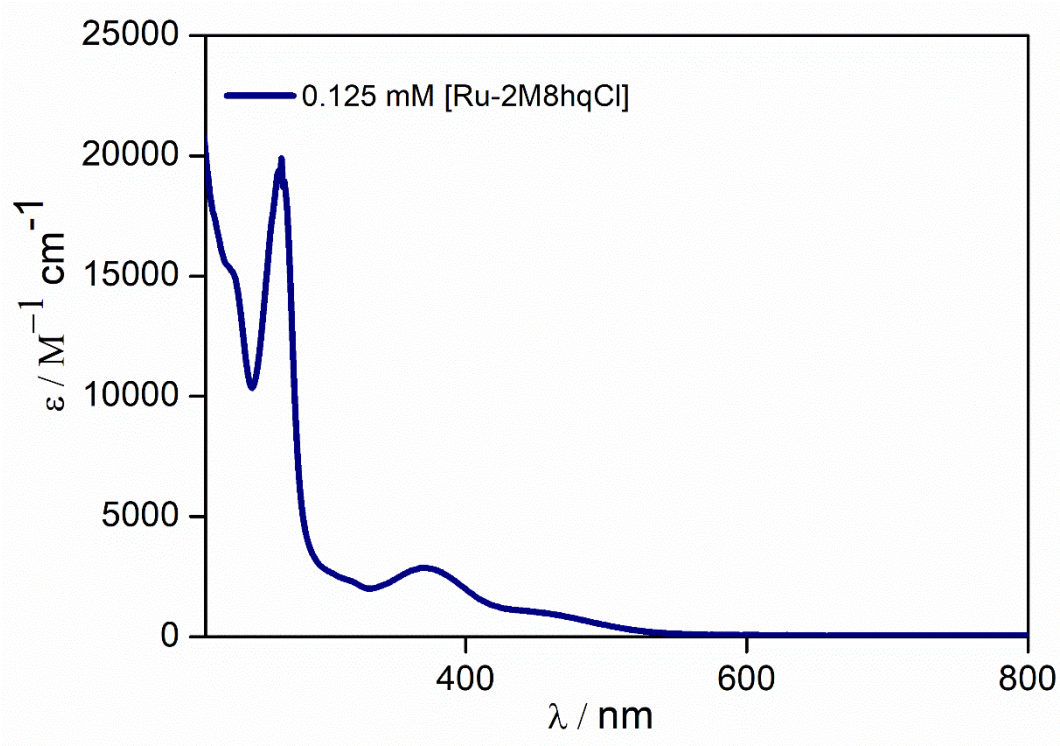

Figure E1. UV-Visible spectra of complex **1**.

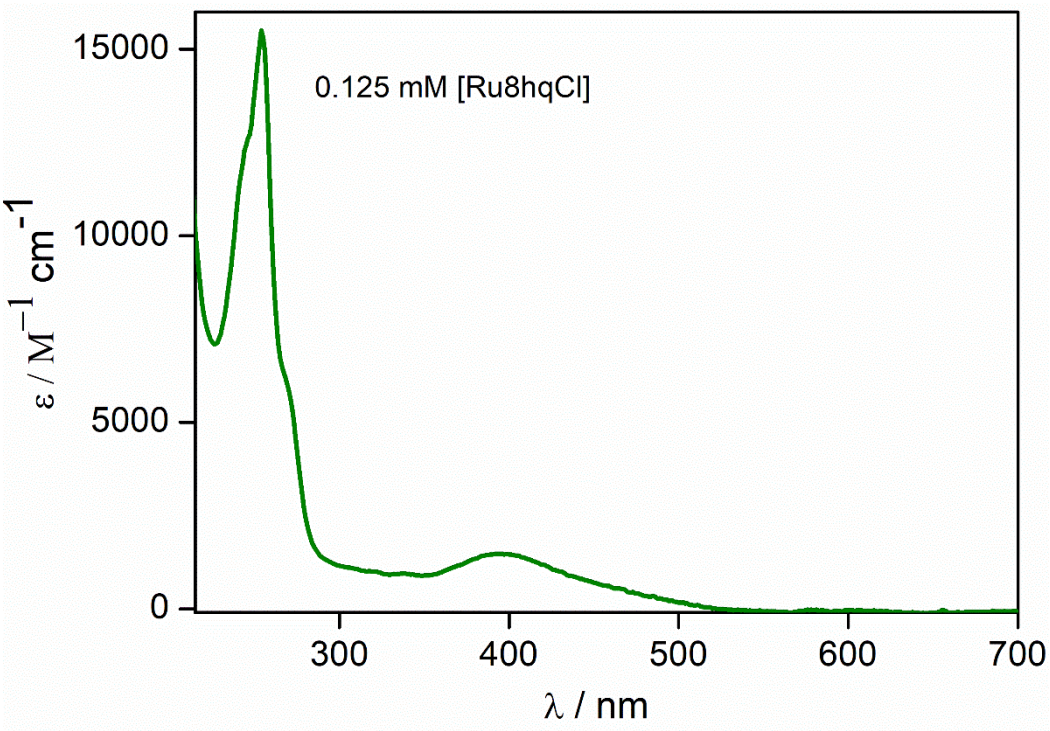

Figure E2. UV-Visible spectra of complex **2**.

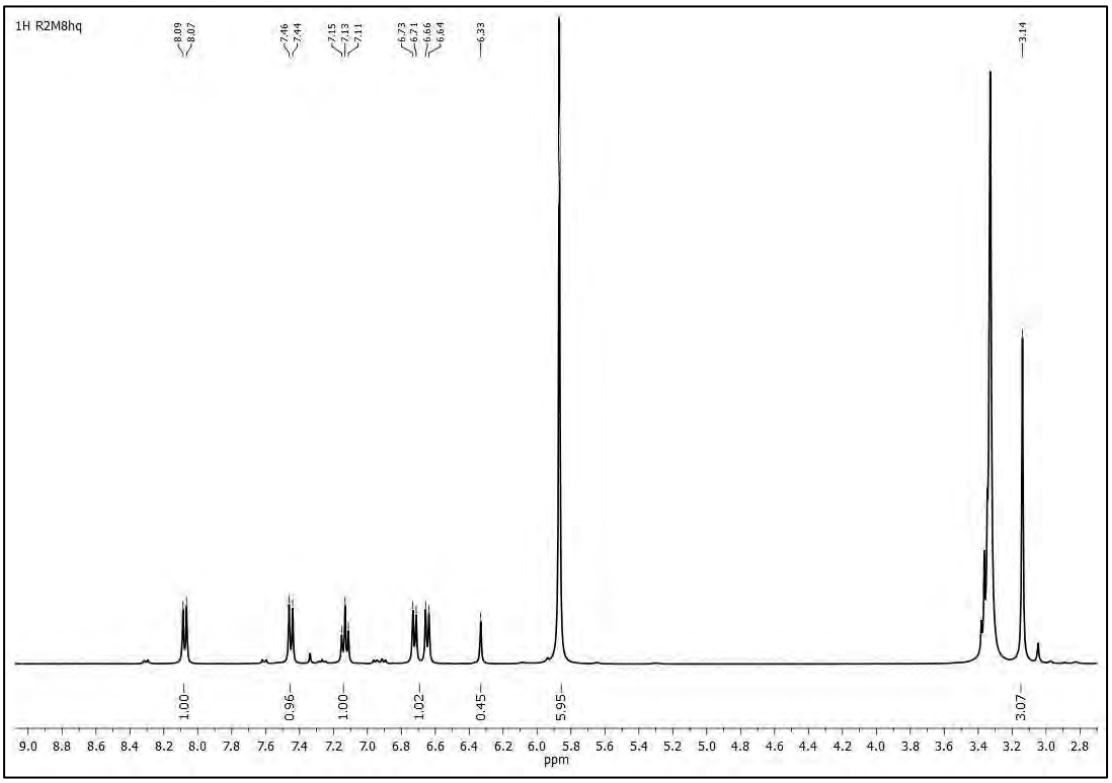

Figure E3. ^{1}H NMR of complex **1** in DMSO-d_6

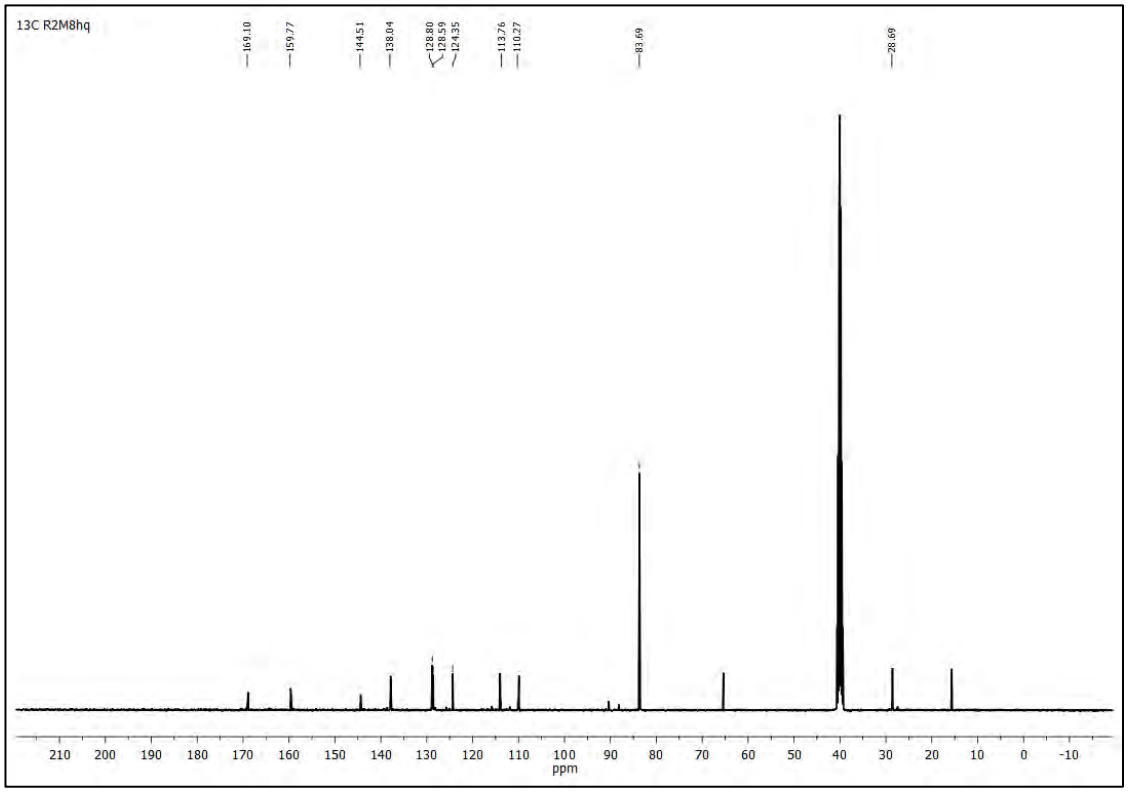

Figure E4. ^{13}C NMR of complex **1** in DMSO-d_6

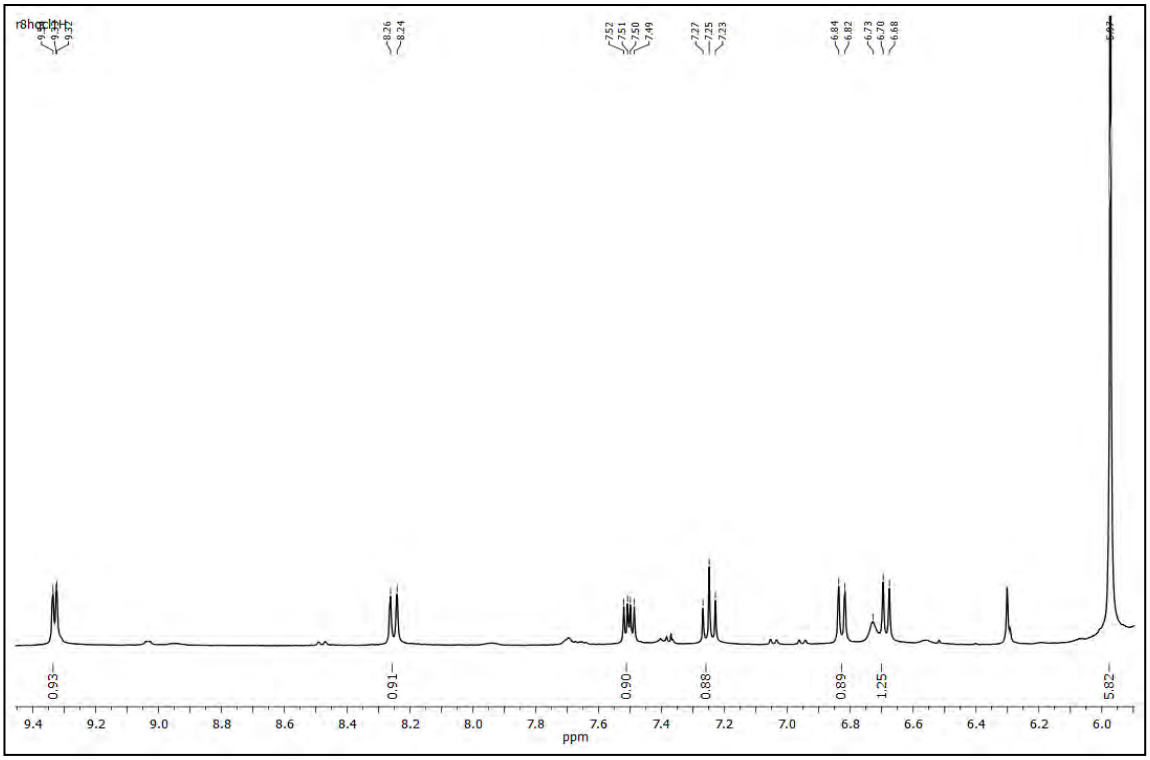

Figure E5. ^{1}H NMR Spectra of the Complex 2 in DMSO-d_6

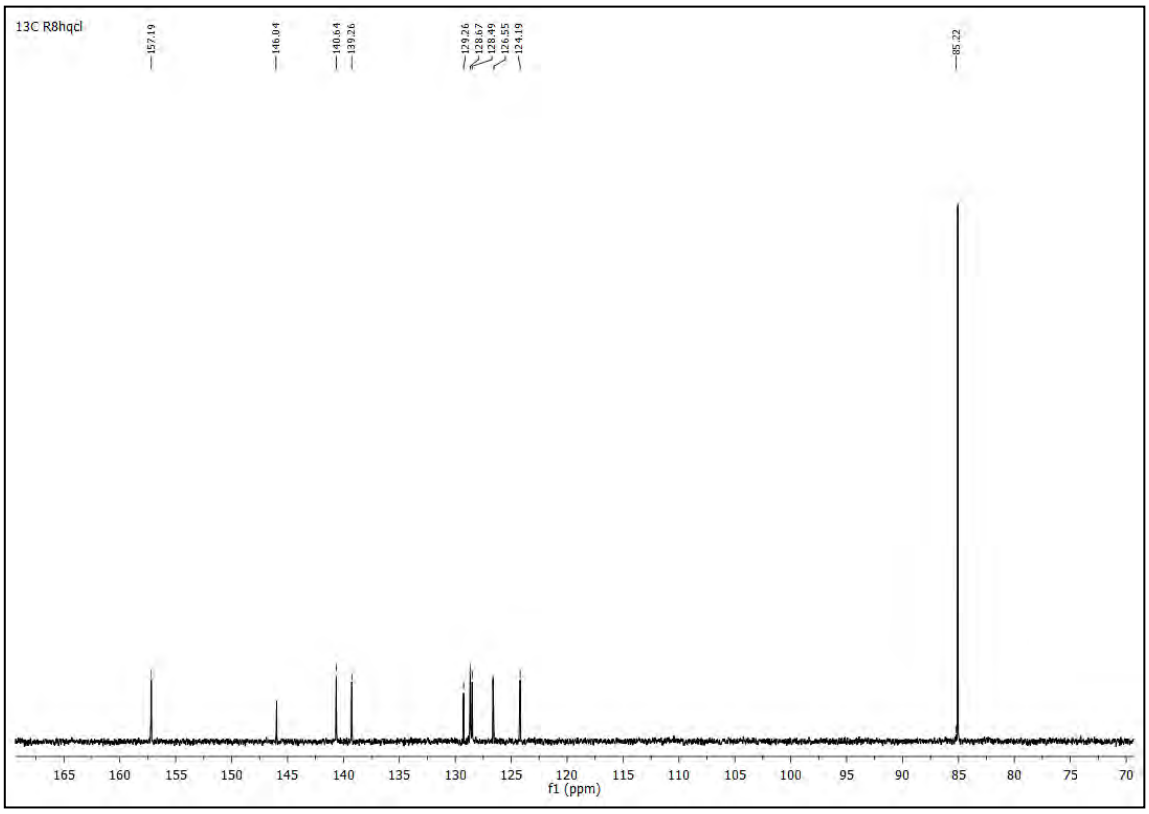

Figure E6. ^{13}C NMR Spectra of the Complex 2 in DMSO-d_6.

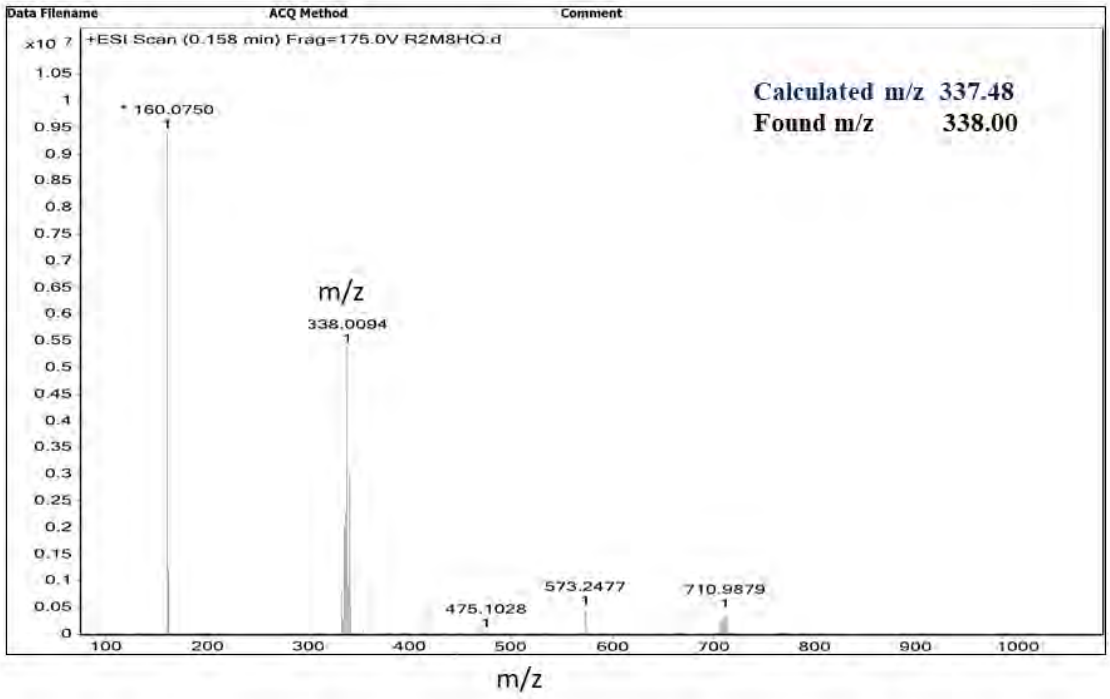

Figure E7. Mass Spectra of the Complex **1**.

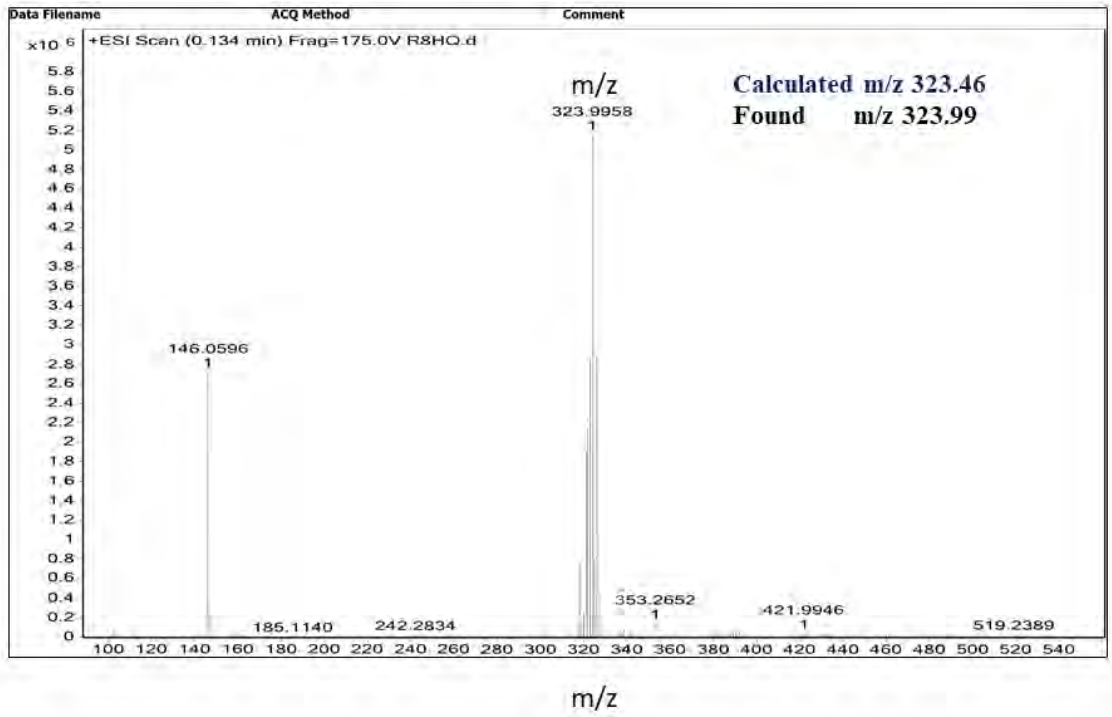

Figure E8. Mass Spectra of the Complex **2**.

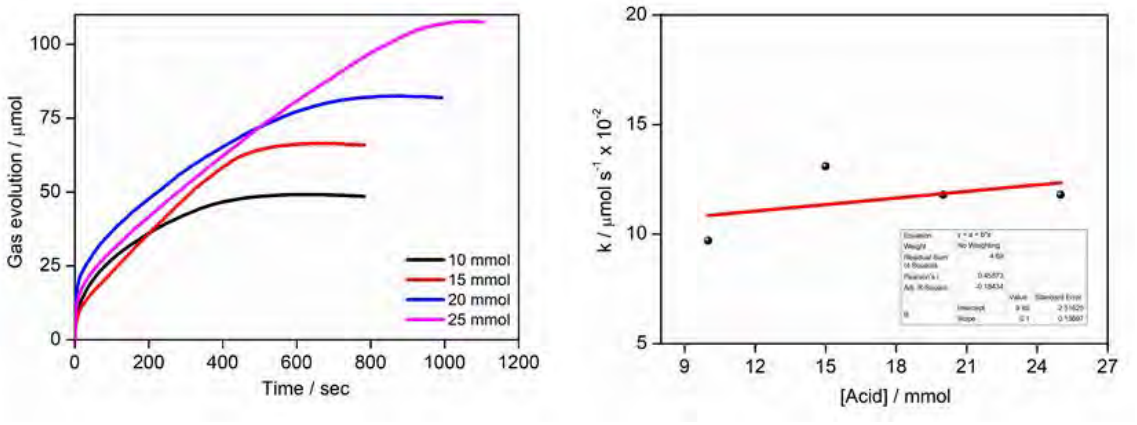

Figure E9. Gas evolution by complex **1** with a variation of acid concentration in presence of 1.0 mM of complex and 15 mmol of base at 70 °C in water. **(b)** Rate of gas evolution *vs.* acid in water.

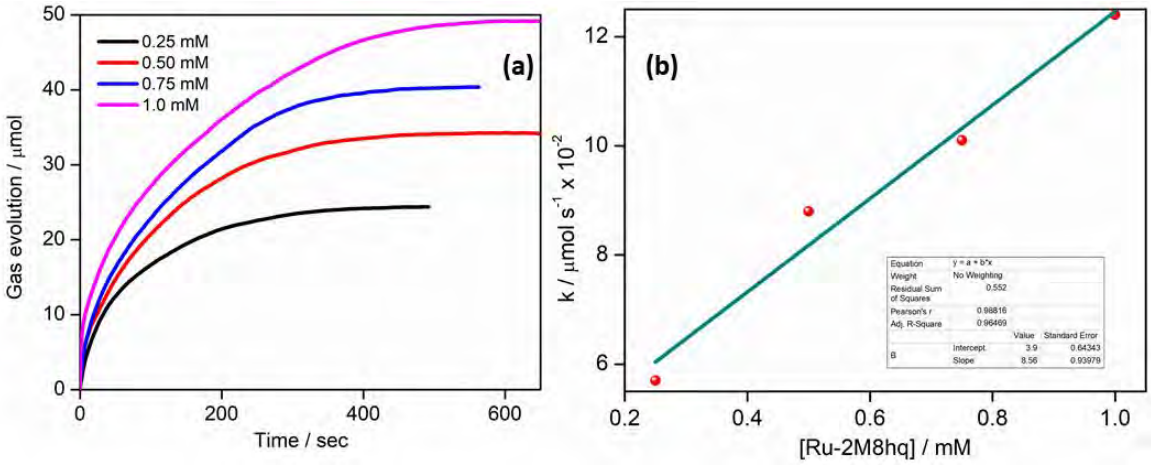

Figure E10. Gas evolution by complex **1** with a variety of complex concentration in the presence of 10 mmol of acid and 15 mmol of the base at 70 °C in water. **(b)** Rate of gas evolution *vs.* complex in water.

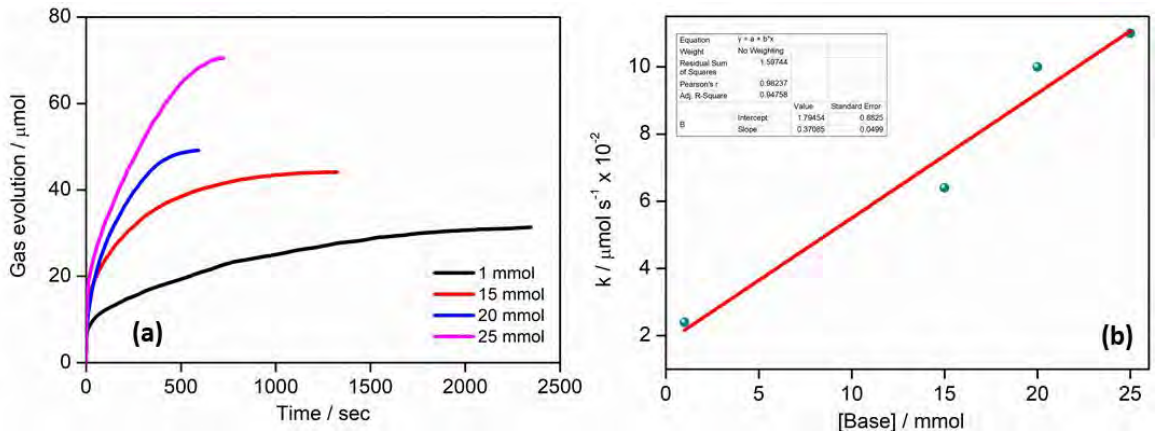

Figure E11. Gas evolution by complex **2** with a variety of base concentration in the presence of 10 mmol of acid and 1.0 mM of the complex at 70 °C in water. **(b)** Rate of gas evolution *vs.* base in water.

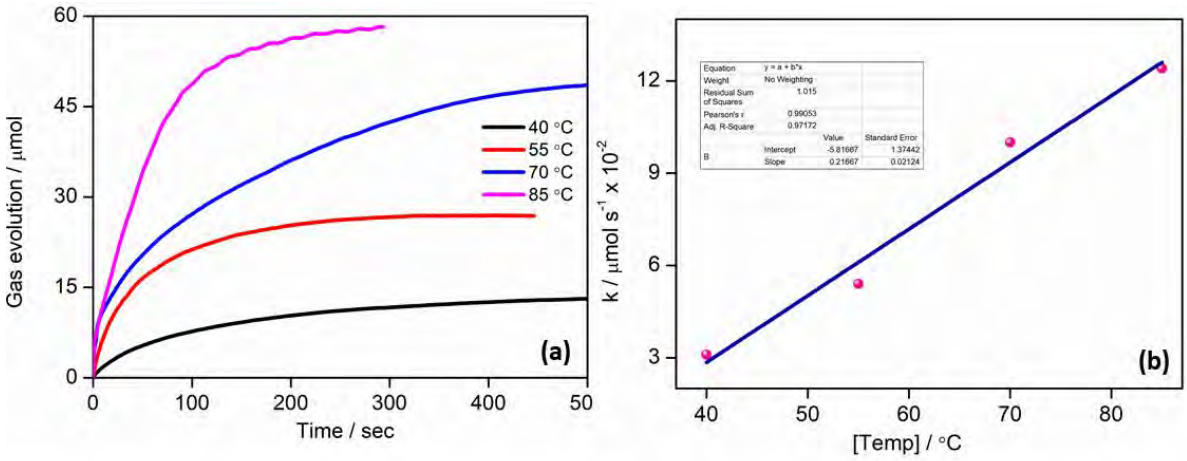

Figure E12. (a) Gas evolution by complex **2** with the variation of temperature in the presence of 1.0 mM of complex, 15 mmol of the base, and 10 mmol of acid in water. **(d)** Rate of gas evolution *vs.* temperature in water.

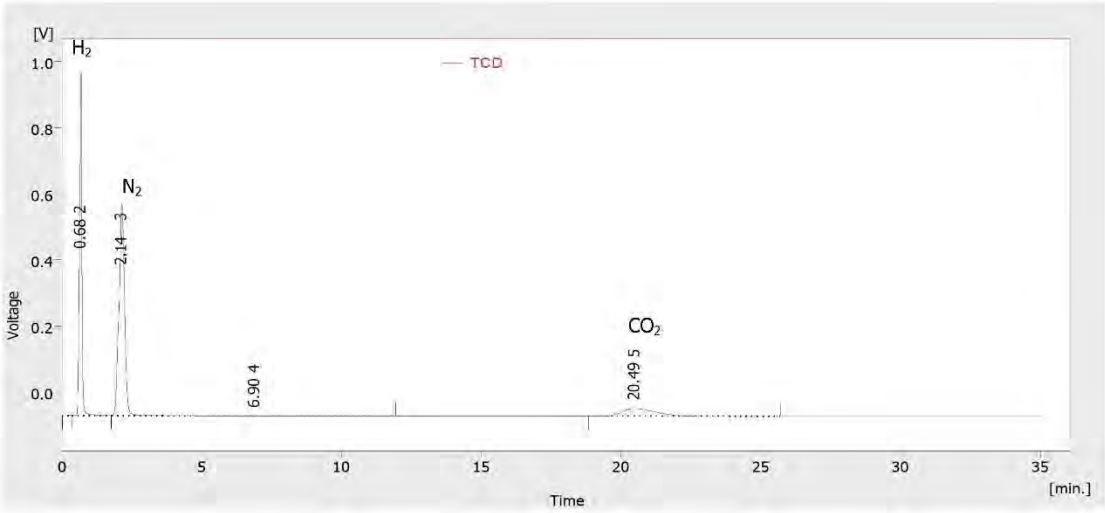

Result Table

	Reten. Time [min]	Area [mV.s]	Height [mV]	Area [%]	Height [%]
1	0.211	29.362	2.271	0.2	0.1
2	0.681	6144.158	1036.200	35.8	60.8
3	2.143	8927.545	642.069	52.0	37.7
4	6.901	86.601	0.495	0.5	0.0
5	20.493	1990.351	23.591	11.6	1.4
	Total	17178.018	1704.626	100.0	100.0

Figure E13. Gas chromatography TCD file for the dehydrogenation using 1.0 mM complex **1** in presence of 10 mmol of formic acid and 15 mmol of sodium formate at 90 °C.

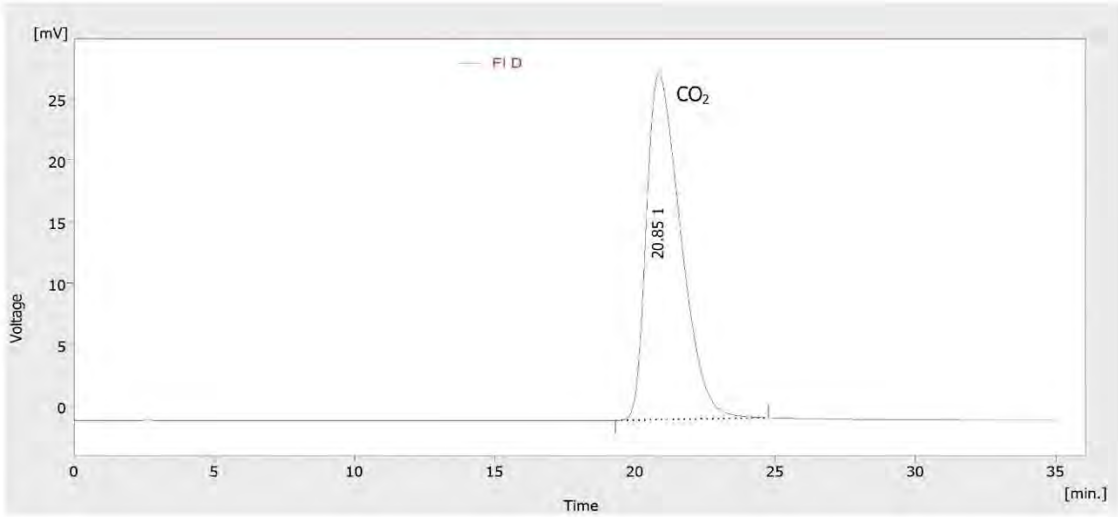

Result Table

	Reten. Time [min]	Area [mV.s]	Height [mV]	Area [%]	Height [%]
1	20.853	2396.361	28.152	100.0	100.0
	Total	2396.361	28.152	100.0	100.0

Figure E14. Gas chromatography FID file for the dehydrogenation using 1.0 mM complex **1** in presence of 10 mmol of formic acid and 15 mmol of sodium formate at 90 °C.

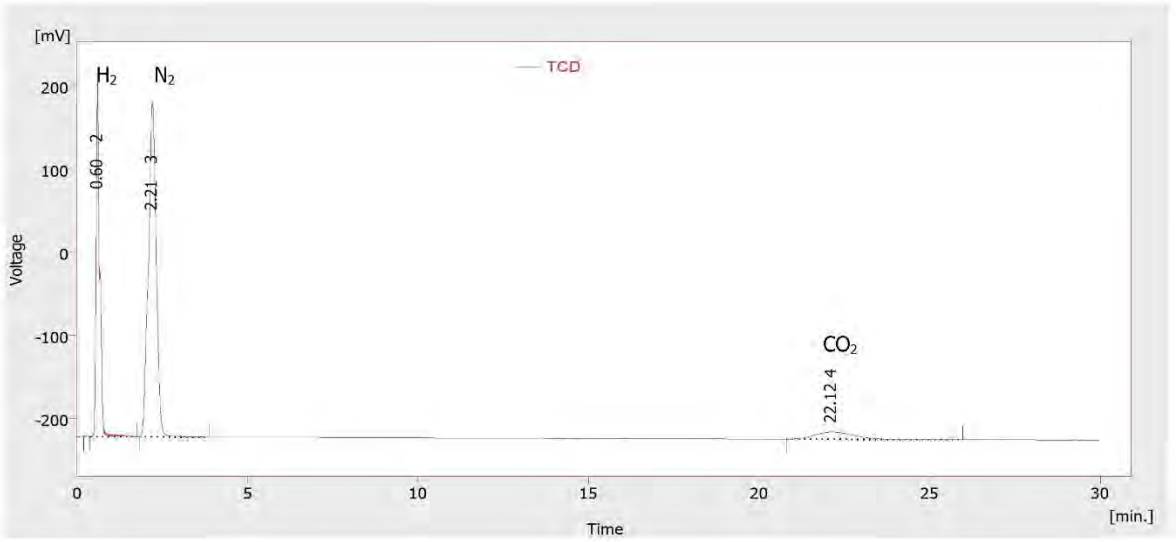

Result Table

	Reten. Time [min]	Area [mV.s]	Height [mV]	Area [%]	Height [%]
1	0.217	8.874	0.903	0.1	0.1
2	0.604	3042.580	431.812	29.8	51.1
3	2.207	6415.499	402.663	62.8	47.7
4	22.124	742.375	9.021	7.3	1.1
	Total	10209.329	844.399	100.0	100.0

Figure E15. Gas chromatography TCD file for the dehydrogenation using 1.0 mM complex **2** in presence of 10 mmol of formic acid and 15 mmol of sodium formate at 90 °C.

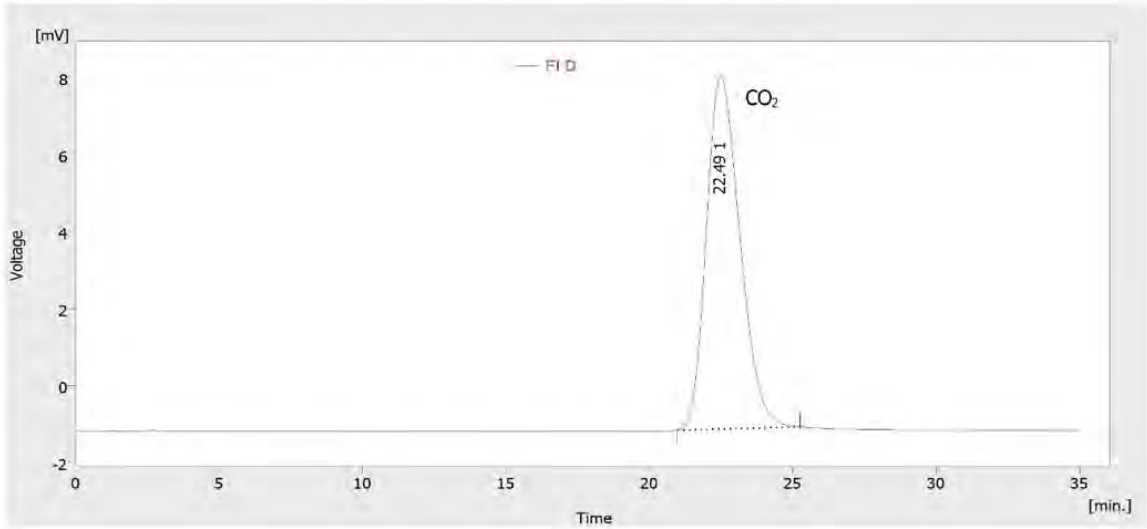

Result Table

	Reten. Time [min]	Area [mV.s]	Height [mV]	Area [%]	Height [%]
1	22.488	744.757	9.157	100.0	100.0
	Total	744.757	9.157	100.0	100.0

Figure E16. Gas chromatography FID file for the dehydrogenation using 1.0 mM complex **2** in presence of 10 mmol of formic acid and 15 mmol of sodium formate at 90 °C.

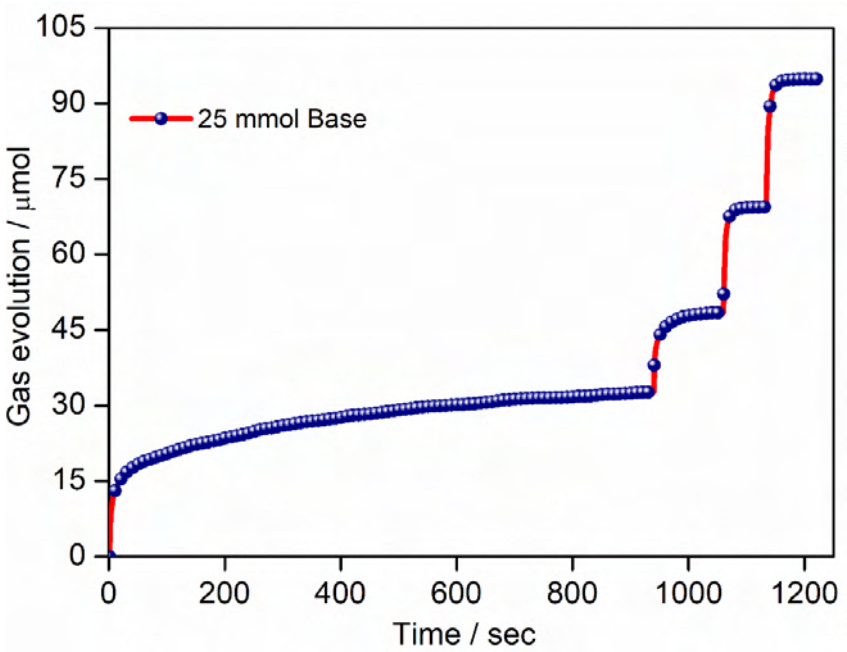

Figure E17. Catalytic cycles for the complex **1** with the iteration of 25 mmol of base in the presence of 1.0 mM complex and 20 mmol acid in deionized water at 70 °C

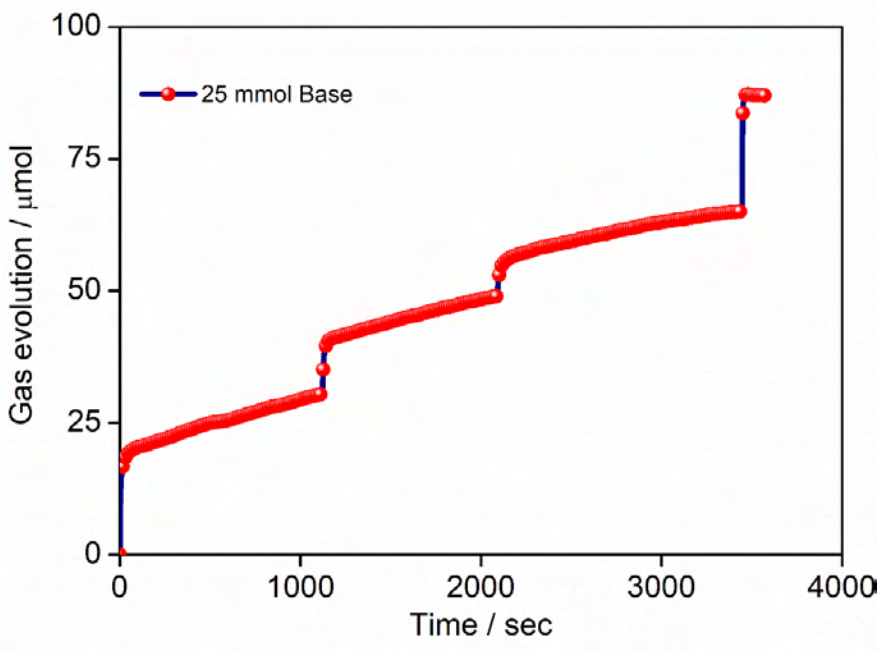

Figure E18. Catalytic cycles for the complex **2** with the iteration of 25 mmol of base in the presence of 1.0 mM complex and 20 mmol acid in deionized water at 70 °C.

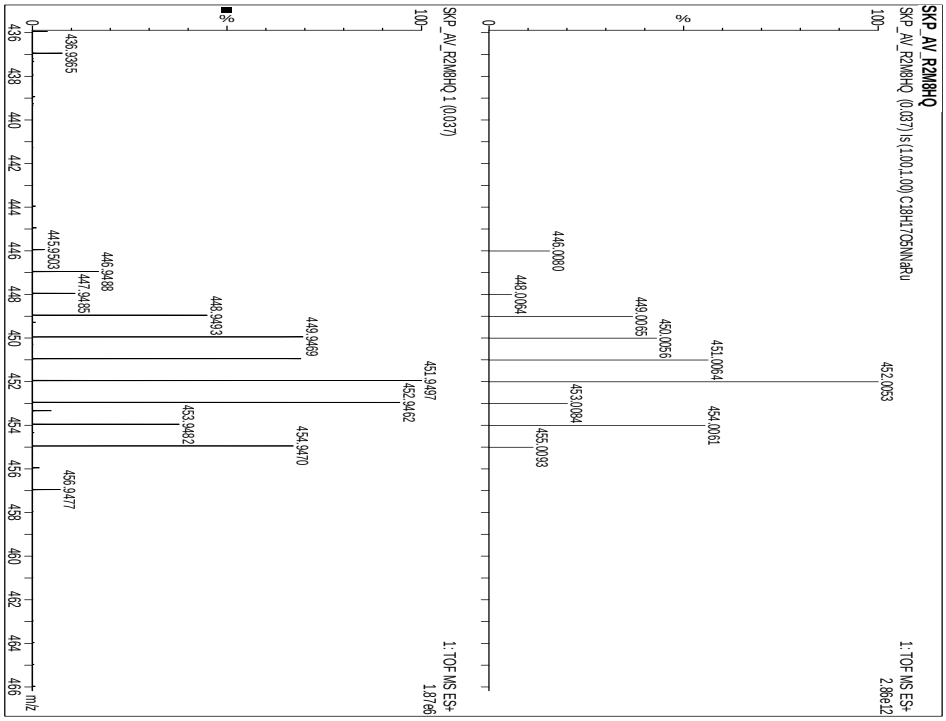

Figure E19. ESI-mass spectra of complex **1** with the addition of HCOOH and HCOONa; Calcd. for [Ru(η^6-benzene)(2M8hq)OOCH]+ HCOONa] + H^+ (m/z 452.005), Found (m/z = 451.9497).

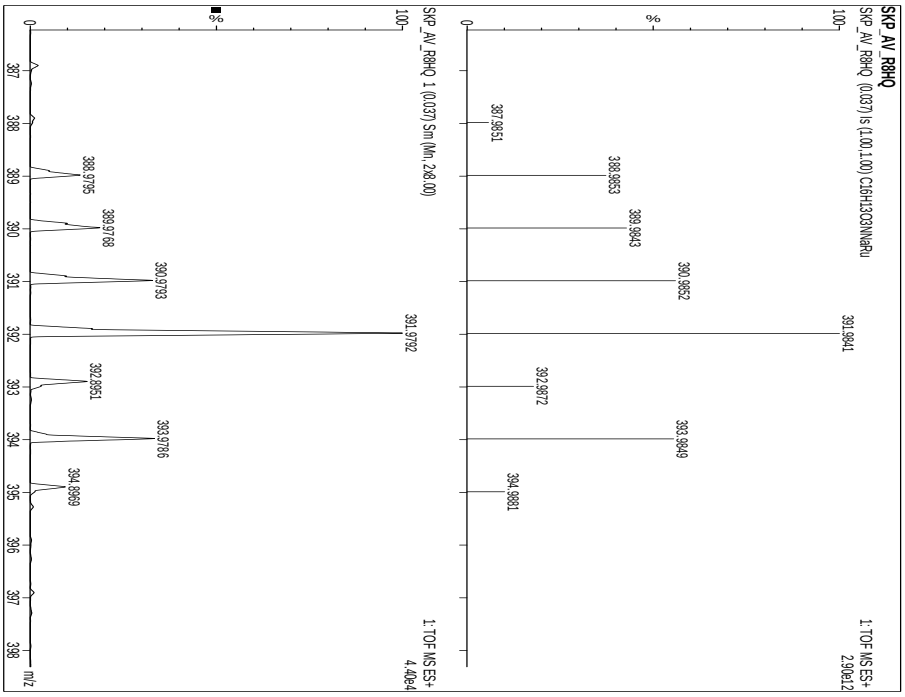

Figure E20. ESI-mass spectra of complex **2** with the addition of HCOOH and HCOONa for Calcd. for [Ru(η^6-benzene)(8hq)OOCH] + Na^+ (m/z 391.9841), Found (m/z = 391.9792).

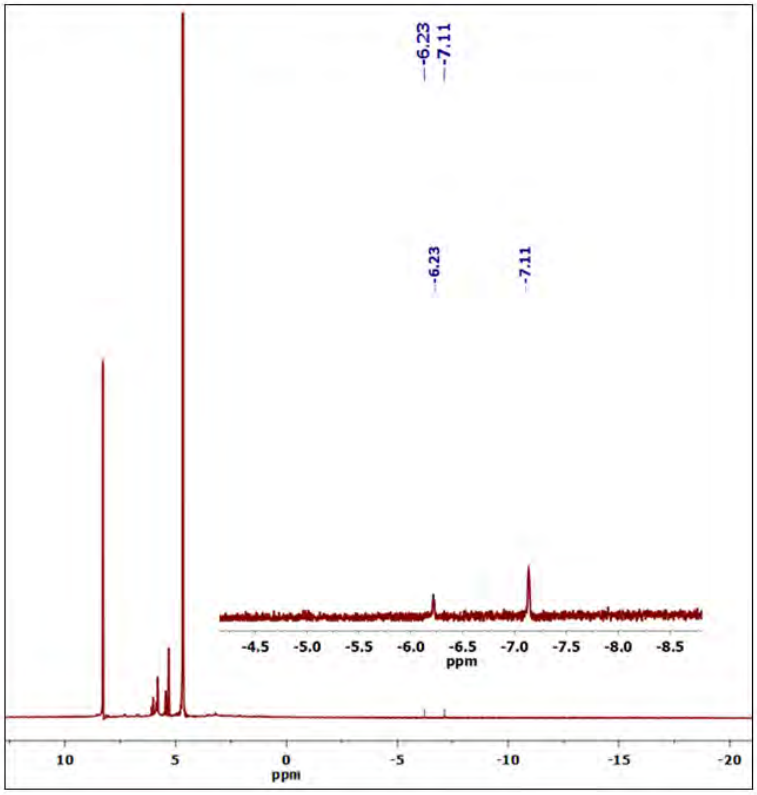

Figure E21. ^{1}H NMR of complex **1** in presence of HCOOH and HCOONa after heating at 90 °C.

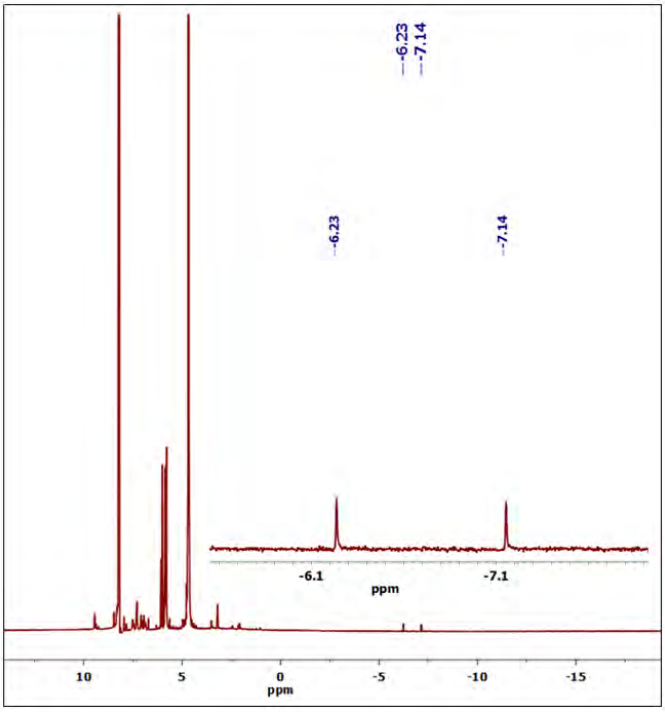

Figure E22. ^{1}H NMR of complex **2** in presence of HCOOH and HCOONa after heating at 90 °C.

Table E1. Crystal data and structure refinement for 1.

Identification code	2112742
Empirical formula	$C_{16}H_{14}NOClRu$
Formula weight	745.63
Temperature/K	293.2
Crystal system	triclinic
Space group	P-1
a/Å	7.5620(7)
b/Å	9.2366(8)
c/Å	9.7047(8)
α/°	91.151(7)
β/°	91.017(7)
γ/°	98.196(7)
Volume/Å^3	670.64(10)
Z	1
ρ_{calc}g/cm^3	1.8461
μ/mm^{-1}	1.361
F(000)	369.9
Radiation	Mo Kα (λ = 0.71073)
2Θ range for data collection/°	4.2 to 50
Index ranges	$-10 \leq h \leq 10$, $-12 \leq k \leq 12$, $-12 \leq l \leq 13$
Reflections collected	10363
Independent reflections	2331 [R_{int} = 0.0671, R_{sigma} = 0.0690]
Data/restraints/parameters	2331/0/182
Goodness-of-fit on F^2	0.989
Final R indexes [I>=2σ (I)]	R_1 = 0.0331, wR_2 = 0.0661
Final R indexes [all data]	R_1 = 0.0404, wR_2 = 0.0680

Table E2. Selected Bond Lengths for 1.

Atom	Atom	Length/Å
Ru1	N1	2.142(3)
Ru1	O1	2.051(2)
Ru1	C16	2.214(3)
Ru1	C11	2.182(3)
Ru1	C12	2.174(3)
Ru1	C13	2.169(3)
Ru1	C14	2.197(3)
Ru1	C15	2.175(3)
Ru1	Cl1	2.4180(9)

Table E3. Selected Bond Angles for 1.

Atom	Atom	Atom	Angle/°
O1	Ru1	N1	79.54(10)
C16	Ru1	N1	113.60(13)
C16	Ru1	O1	165.34(12)
C11	Ru1	N1	146.99(13)
C11	Ru1	O1	131.80(13)
C11	Ru1	C16	37.35(14)
C12	Ru1	N1	172.15(11)
C12	Ru1	O1	98.39(12)
C12	Ru1	C16	67.70(14)
C12	Ru1	C11	37.59(13)
C13	Ru1	N1	133.98(12)
C13	Ru1	O1	85.92(12)
C13	Ru1	C16	80.17(14)
C13	Ru1	C11	68.17(14)
C13	Ru1	C12	38.17(13)
C14	Ru1	N1	104.78(12)
C14	Ru1	O1	103.45(12)
C14	Ru1	C16	67.82(13)
C14	Ru1	C11	80.33(13)
C14	Ru1	C12	68.20(14)
C14	Ru1	C13	37.40(14)
C15	Ru1	N1	96.20(12)
C15	Ru1	O1	138.99(12)
C15	Ru1	C16	37.39(12)
C15	Ru1	C11	67.59(13)
C15	Ru1	C12	80.34(14)
C15	Ru1	C13	67.78(14)
C15	Ru1	C14	37.75(13)
Cl1	Ru1	N1	83.42(7)
Cl1	Ru1	O1	87.21(7)
Cl1	Ru1	C16	100.34(9)
Cl1	Ru1	C11	87.65(9)
Cl1	Ru1	C12	104.10(10)
Cl1	Ru1	C13	139.47(11)
Cl1	Ru1	C14	167.46(9)
Cl1	Ru1	C15	133.19(10)

Table E4. Crystal data and structure refinement for 2.

Identification code	2112741
Empirical formula	$C_{15}H_{14}ClNORu$
Formula weight	1435.14
Temperature/K	293.15
Crystal system	monoclinic
Space group	$P2_1/c$
a/Å	7.3837(9)
b/Å	15.434(2)
c/Å	12.6134(18)
α/°	90
β/°	117.249(10)
γ/°	90
Volume/Å^3	1277.9(3)
Z	1
ρ_{calc}g/cm^3	1.8648
μ/mm^{-1}	1.424
F(000)	707.8
Radiation	Mo Kα (λ = 0.71073)
2Θ range for data collection/°	4.48 to 50
Index ranges	$-9 \leq h \leq 9$, $-20 \leq k \leq 18$, $-17 \leq l \leq 10$
Reflections collected	5778
Independent reflections	1903 [R_{int} = 0.0349, R_{sigma} = 0.0563]
Data/restraints/parameters	1903/0/172
Goodness-of-fit on F^2	1.016
Final R indexes [I>=2σ (I)]	R_1 = 0.0378, wR_2 = 0.0665
Final R indexes [all data]	R_1 = 0.0544, wR_2 = 0.0723

Table E5. Selected Bond Lengths for 2.

Atom	Atom	Length/Å
Ru1	Cl1	2.4281(11)
Ru1	O1	2.048(3)
Ru1	N1	2.097(4)
Ru1	C13	2.168(5)
Ru1	C15	2.140(6)
Ru1	C12	2.183(5)
Ru1	C11	2.175(5)
Ru1	C10	2.155(6)
Ru1	C14	2.175(5)

Table E6. Selected Bond Angles for 2.

Atom	Atom	Atom	Angle/°
O1	Ru1	Cl1	87.08(9)
N1	Ru1	Cl1	85.00(10)
N1	Ru1	O1	78.61(13)
C13	Ru1	Cl1	90.17(16)
C13	Ru1	O1	153.3(2)
C13	Ru1	N1	127.6(2)
C15	Ru1	Cl1	150.1(3)
C15	Ru1	O1	122.0(3)
C15	Ru1	N1	93.8(2)
C15	Ru1	C13	67.0(3)
C12	Ru1	Cl1	94.10(15)
C12	Ru1	O1	117.0(2)
C12	Ru1	N1	164.3(2)
C12	Ru1	C13	36.7(2)
C12	Ru1	C15	79.2(2)
C11	Ru1	Cl1	121.79(19)
C11	Ru1	O1	92.29(18)
C11	Ru1	N1	151.5(2)
C11	Ru1	C13	66.9(2)
C11	Ru1	C15	68.0(3)
C11	Ru1	C12	36.9(2)
C10	Ru1	Cl1	159.4(2)
C10	Ru1	O1	94.6(2)
C10	Ru1	N1	115.4(2)
C10	Ru1	C13	79.2(2)
C10	Ru1	C15	37.7(3)
C10	Ru1	C12	66.9(2)
C10	Ru1	C11	37.7(3)
C14	Ru1	Cl1	113.1(2)
C14	Ru1	O1	159.6(3)
C14	Ru1	N1	99.3(2)
C14	Ru1	C13	36.8(2)
C14	Ru1	C15	37.6(3)
C14	Ru1	C12	66.6(3)
C14	Ru1	C11	79.9(2)
C14	Ru1	C10	67.8(3)

CHAPTER 7

This chapter is based on the summary of the thesis.

Chapter 7

Summary and Future scope

7.1 Summary

The present thesis synthesizes and characterizes ruthenium-based molecular catalysts for catalyzing the water oxidation and dehydrogenation of formic acid. The water oxidation was studied in both acidic and deionized water using ceric ammonium nitrate as an oxidant. The complexes also show electrochemical water oxidation with low overpotential and high faradaic efficiency. The dehydrogenation of formic acid was studied in sodium formate as the base at different temperatures for the generation of H_2 and CO_2.

All the complexes $[Ru(Fc\text{-}tpy)(bpy)Cl]^+$ **(1)** $[Ru(Fc\text{-}tpy)(bpy)(OH_2)]^{2+}$ **(2)**, $[Ru((\eta^6-benzene)(hdm)]^+$ **(3)**, $[Ru(2py\text{-}tpy)(DQN)Cl]^+$ **(4)**, $[Ru((\eta^6-benzene)(2M8hq)Cl]$ **(5)** and $[Ru((\eta^6-benzene)(8hq)Cl]$ **(6)** complexes were successfully synthesized and characterized by different spectroscopic techniques and the structure of the complexes **(1)**, **(3)**, **(4)**, **(5)** and **(6)** were characterized using a single crystal XRD technique.

The complexes of $[Ru(Fc\text{-}tpy)(bpy)Cl]^+$ and $[Ru(Fc\text{-}tpy)(bpy)(OH_2)]^{2+}$ were synthesized and characterized by various techniques. The catalytic activity of the complex $[Ru(Fc\text{-}tpy)(bpy)(OH_2)]^{2+}$ was investigated towards water oxidation. This complex shows water oxidation in the presence of ceric ammonium nitrate (CAN) in triflic acid at pH 1.0. The catalytic efficiency of the complex was compared with its parent complex $[Ru(tpy)(bpy)(OH_2)]^{2+}$ and it was observed that the parent complex shows a lower TON of 10 for the chemical water oxidation. The $[Ru(Fc\text{-}tpy)(bpy)(OH_2)]^{2+}$ complex shows electrochemical water oxidation with low overpotential of 230 mV as compared to the parent complex. The Fe(II) center of ferrocene moiety (Fc) undergoes protonation to generate the Fe(IV)hydrido species Fe(IV)-H (FcH^+) under highly acidic conditions. The introduction of the ferrocene moiety in the 'tpy' scaffold behaves as an electron-donating group due to the oxidation of Fe^{II} to Fe^{III}. The Pourbaix diagram indicates the existence of $H^+/2e^-$ PCET at pH 1.0 between $[Fc^+\text{-}Ru^{III}\text{-}OH]^{3+} \rightarrow [Fc^+\text{-}Ru^{V}{=}O]^{4+} + H^+ + 2e^-$. The stoichiometric changes in the absorbance spectra of the intermediate species involved in the water oxidation catalytic process were predicted through the SVD analysis with an appropriate model fitting in ReactLab kinetics Bundle version 1.1 software. This case indicates that $[Ru^{VI}{=}O]^{3+}$ is active species in the kinetic process for O_2 evolution. The spectra evolved from the reaction mixture indicated that $[Fc^+\text{-}Ru^{VI}{=}O]^{5+}$ generates $[Fc^+\text{-}Ru^{IV}\text{-}O\text{-}OH]^4+$ in the presence of H_2O. Further $[Fc^+\text{-}Ru^{IV}\text{-}O\text{-}OH]^{4+}$

converts into $[Fc^{+}\text{-}Ru^{V}\text{-}O\text{-}O]^{4+}$ in the presence of Ce^{4+}, which is the rate-determining step (RDS) with $k_{RDS} = 6.0 \times 10^{-4}\ M^{-1}\ s^{-1}$. The $[Fc^{+}\text{-}Ru^{V}\text{-}O\text{-}O]^{4+}$ species releases O_2 in the presence of H_2O. The O···O bond formation ($k_{O\cdots O}$) and O_2 evolution (k_{O2}) are $8.1 \times 10^{-3}\ s^{-1}$ and $8.9 \times 10^{-4}\ s^{-1}$.

The complex $[Ru((\eta^6 -\text{benzene})(hdm)]^{+}$ was synthesized and successfully employed as an active precatalyst for the catalytic activity towards chemical water oxidation in the deionized water using ceric ammonium nitrate as an oxidant at pH 6.6. The complex undergoes degradation under extremely harsh conditions of acidic pH in the presence of an oxidant and doesn't exhibit O_2 evolution. The kinetics of chemical water oxidation reveals the rate of O_2 evolution is 1st order dependent on CAN and catalyst concentration. The complex shows electrochemical water oxidation with 98 % Faradaic efficiency at pH 6.6 in phosphate buffer. The electrochemical water oxidation was performed in different complex concentrations and different pH. During the chemical water oxidation, the complex undergoes decomposition resulting in the formation of insoluble particles due to a highly acidic pH of 1.35 after the addition of CAN in deionized water. The formation of insoluble particles in the reaction mixture and a coating over the surface of the silicone rubber septum has been observed and analyzed through FE-SEM, EDX, XPS, and HR-TEM analysis. From the XPS of the reaction mixture and the solid particles deposited over the septum, it was observed that catalyst remains in Ru^{IV}=O and Ru^{VI}=O during the water oxidation reaction and becomes Ru^{VI}=O at the end of the reaction.

The complex $[Ru((\eta^6 -\text{benzene})(hdm)]^{+}$ complex also shows activity towards the decomposition of formic acid in the presence of sodium formate as the base for the production of hydrogen and carbon dioxide in a 1:1 ratio. The dehydrogenation of formic acid was studied from lower to higher temperatures, and it was observed that the reaction rate is elevated at a higher temperature. In this case, the activation energy required for dehydrogenation of formic acid is calculated from the Arrhenius plot was 11.6 kJ/mol. In contrast, the reaction is endergonic with the $\Delta G = 81.642$ kJ at 298 K calculated from the Eyring plot. The isotopic labeling experiment indicates that the rate of gas evolution is slower in heavy water than deionized water. The kinetics of the dehydrogenation reaction was studied by varying the concentration of the complex, acid, and base. The gas evolved was also confirmed from the Gas Chromatography. The dehydrogenation reaction was also studied at different pH, and it was observed that the dehydrogenation of formic acid efficiently shows gas evolution at pH 7.0. The stability of the catalyst towards dehydrogenation was examined by the iterative

addition of formic acid and sodium formate in a different set of reactions. The formation of intermediate species Ru-formate was confirmed from the HRMS analysis.

The complex [Ru(2py-tpy)(dqn) Cl]$^+$ **(**where dqn = 2,3-di(pyridine-2-yl) quinoxaline) was synthesized and characterized by various spectroscopic techniques. The complex was successfully utilized to study the dehydrogenation of formic acid using sodium formate as a base in deionized water. The dehydrogenation of formic acid was studied at different concentrations of acid, base, and complex and from lower to a higher temperatures to determine the kinetics of the reaction. The dehydrogenation of formic acid was also performed at different pH values from 2.0 to 11.0. The dehydrogenation of formic acid at different temperatures reveals that activation energy required for the dehydrogenation of formic acid was 31.45 kJ / mol, and ΔG was estimated to be 81.33 kJ. The composition of gas was detected from the TCD and FID detectors of the Gas Chromatograph. The catalytic stability of the complex towards dehydrogenation was examined by iterative addition of formic acid and sodium formate in a different set of reactions. The formation of intermediate species during the decomposition of formic acid was confirmed from the HRMS analysis, and the mass shows the peak for the formation of formate species.

The two half sandwich complexes [Ru(η^6-benzene)(L)Cl]$^+$ (where L = 2-Methyl 8-hydroxy quinoline **1** and 8-hydroxy quinoline **2**) were synthesized and employed to study the dehydrogenation of formic acid. These complexes show dehydrogenation of formic acid in sodium formate as a base in deionized water. The catalytic activity towards dehydrogenation of formic acid was compared between complexes **1** and **2**. For studying the kinetics of the dehydrogenation reaction, the reactions were performed with various concentrations of acid, base, and complex and by varying the temperature. The reaction rate depends on acid, base, and complex concentration and follows the first-order kinetics. The dehydrogenation of formic acid was also studied at different pH from highly acidic to highly basic medium. The dehydrogenation of formic acid at different temperatures reveals that activation energy required for the dehydrogenation of formic acid was 29.81 kJ / mol and ΔG was estimated to be 90 kJoules for the complex **1,** and activation energy needed for the dehydrogenation of formic acid was 29.83 kJ / mol and ΔG was found to be 83 kJoules for the complex **2**. The composition of gas was examined from the TCD and FID detectors of the Gas Chromatograph. The catalytic stability of the complex towards dehydrogenation was examined by repetitive addition of formic acid and sodium formate in a different set of reactions. The formation of different intermediate species during the decomposition of formic acid were confirmed from the ^{1}H

NMR and HRMS analysis. The ^{1}H NMR analysis shows the formation of hydride species, and the HRMS analysis shows the formation of formate species in both complexes.

The catalytic activity of the complexes was successfully studied towards water oxidation and dehydrogenation of formic acid. From the above observations, it was revealed that:

- $[Ru(Fc\text{-}tpy)(bpy)OH_2]^{2+}$ complex was utilized for the water oxidation, and its activity is compared with the parent complex $[Ru(tpy)(bpy)OH_2]^{2+}$. The $[Ru(Fc\text{-}tpy)(bpy)OH_2]^{2+}$ complex shows chemical water oxidation in the presence of CAN with a TON of 12 in triflic acid at pH 1.0.
- $[Ru(\eta^6\text{-benzene})(hdm)]BF_4$ complex was successfully employed for the chemical water oxidation using ceric ammonium nitrate (CAN) as the sacrificial oxidant in deionized water.
- $[Ru(Fc\text{-}tpy)(bpy)OH_2]^{2+}$ is highly active towards water oxidation as compared to the $[Ru(\eta^6\text{-benzene})(hdm)]BF_4$. The $[Ru(\eta^6\text{-benzene})(hdm)]BF_4$ complex undergoes decomposition after the addition of CAN as oxidant leading to the formation of insoluble particles.
- $[Ru(\eta^6\text{-benzene})(hdm)]BF_4$, $[Ru(2py\text{-}tpy)(dqn)Cl]^{2+}$ and $[Ru(\boldsymbol{\eta}^6\text{-benzene})(2M8hq)Cl]$ $[Ru(\boldsymbol{\eta}^6\text{-benzene})(8hq)Cl]$ complexes have successfully catalyzed the dehydrogenation of formic acid in the presence of sodium formate as the base in deionized water. All three complexes efficiently catalyze the dehydrogenation of formic acid in neutral pH rather than in highly acidic or basic pH.
- The formation of intermediates species during dehydrogenation of formic acid was confirmed from the ^{1}H NMR and HRMS analysis.

7.2. Future Scope

These studies may inspire the researchers to explore the activity of Ru-based polypyridyl and half-sandwich complexes towards water oxidation and towards dehydrogenation of formic acid. These types of ligands enhance the catalytic activity of the metal center and increase the solubility of the complex in the aqueous medium. More of such catalysts can be designed by taking these points into consideration:

- The catalyst must be stable in reaction conditions.
- The catalyst must have higher TOF.

- It should have low overpotential.
- The catalyst must be stable in a higher oxidation state.
- The complexes that are not stable in harsh conditions or strong oxidizing conditions should be studied in an aqueous medium with other oxidizing agents.
- These studies also provide the path for studying and designing Ru-based dehydrogenation of formic acid, catalyzed mainly by utilizing the Ir-based catalysts.

List of Publications

1. **Vatsa, A.** and Padhi, S. K. *Catalytic Water Oxidation by a Single Site [Ru(Fc-tpy)(bpy)OH$_2$]$^{2+}$ Complex and it's Mechanistic Study*, ***Inorg. Chim. Acta***, 2020, *504*, 119444.

2. **Vatsa, A.** and Padhi, S. K. *Catalytic Water Oxidation by a Ru^{II} Half Sandwich Complex*, ***Eur. J. Inorg. Chem***., 2021, *2021(34)*, 3499-3505.

3. **Vatsa, A.** and Padhi, S. K. *Dehydrogenation of Formic Acid by a Ru^{II} Half Sandwich Catalyst* , ***ChemistrySelect.***, 2021, *6(35)*, 9447-9452.

4. **Vatsa, A.** and Padhi, S. K. *Dehydrogenation of formic acid using mononuclear Ruthenium (II) [Ru(2py-tpy)(dqn)Cl]$^{+}$ complex. Manuscript under preparation.*

5. **Vatsa, A.** and Padhi, S. K. *Dehydrogenation of Formic Acid by Half Sandwich [Ru(η6-benzene)(L)Cl]$^{+}$catalysts: L = 8-Hyroxyquinoline and 8-Hydroxy-2-methyl quinoline. Manuscript under preparation.*
6. Patel, J.; Majee, K.; Ahmad, E.; **Vatsa, A**.; Das, B.; and Padhi, S. K. *Electronic Effect on Catalytic Water Oxidation by Single Site [Ru(QCl-tpy)(bpy)(OH$_2$)]$^{2+}$ Catalyst*, ***ChemistrySelect.***, 2017, *2*, 123-129.
7. Patel, J.; Majee, K.; Raj, M.; **Vatsa, A**.; Rai, S.; and Padhi, S. K. *Effect of Quinoline Substitution on Water Oxidation by [Ru(Ql-tpy)(bpy)(OH$_2$)](PF$_6$)2 Catalyst*, ***ChemistrySelect.***, 2017, *2*, 3053-3059.

List of Conferences:

1. **A. Vatsa** and S. K. Padhi, Chemical Water Oxidation Mediated by an Efficient Single Site [Ru(QCl-tpy)(bpy)OH$_2$]$^{2+}$ Catalysts. WOC 2017, IIT(ISM) Dhanbad.
2. Conference on "Recent Advances in Materials for Substainable Enegry" (RAMSE) 2018, IIT(ISM) Dhanbad.